# MODEL-BASED HIGH-DENSITY FUNCTIONAL DIFFUSE OPTICAL TOMOGRAPHY OF HUMAN BRAIN

by

YUXUAN ZHAN

A thesis submitted to the
University of Birmingham
For the degree of
DOCTOR OF PHILOSOPHY

School of Computer Science
College of Engineering and Physical Sciences
University of Birmingham
September 2013

# Abstract

Functional diffuse optical tomography (fDOT) of the human brain is an emerging functional neuroimaging technology that allows non-invasive imaging of human brain functions by injecting near infrared (NIR) light into the human head and taking optical measurements on the human scalp. Compared with the 'gold standard' in functional neuroimaging, namely functional magnetic resonance imaging (fMRI), fDOT has the advantages of cost efficiency, portability, and comprehensive haemodynamic imaging capability. However widespread acceptance of fDOT in the functional neuroimaging community has so far been hampered by as yet insufficient spatial resolution, limited depth penetration, restricted field of view, and a lack of reliable and repeatable functional mapping. The aims of this thesis are to enhance current understandings and knowledge of fDOT image quality and to improve on its imaging performance using a model-based approach. Specifically we have established a computationally efficient finite element method (FEM)-based routine to conduct MRI-guided fDOT simulation studies. Based on this framework, we have performed the first realistically noise-added point spread function (PSF) analysis for the entire field of view (FOV) of a high-density (HD) imaging system, and have demonstrated that HD-fDOT is capable of imaging focal haemodynamic response up to 18 mm depth below the human scalp surface at 10 mm image resolution and localisation accuracy, allowing distinguishability of gyri. As an extension of this work, we next investigated the effects of uncertainty in the background tissue optical property on HD-fDOT image quality, as well as the use of background absorption fitting schemes in minimising such effects. Our multi-model comparative study has concluded that the use of a homogeneous background absorption fitting scheme in HD-fDOT can minimise the chances of obtaining sub-optimal image quality due to uncertainty in background tissue optical properties. Finally we have addressed and resolved a regularisation

problem that can result in increased imaging crosstalk between the recovered parameters in spectral fDOT that was previously not understood. Our proposed singular-decomposition-based (SVD-based) regularisation method has been shown to reduce imaging crosstalk observed in both spectral and non-spectral fDOT.

# Acknowledgements

First and foremost, I would like to give my sincere thanks to Dr Hamid Dehghani. Hamid has dedicated a considerable amount of time and energy to the supervision of my research. He has helped me to evaluate my work critically and to express my results clearly. More importantly, he has encouraged me to explore and realise new research ideas as well as my own potentials. For this, I am very grateful.

Thanks also go to the many others who have helped me along the way: particularly to Dr Iain Styles and Prof Ela Claridge, for their regular and constructive feedback in my Thesis Group meetings; to our American collaborators who are on the other side of the North Atlantic Ocean, Dr Adam Eggebrecht and Prof Joseph Culver, for their seamless response to any question I had, as well as inviting me to their imaging lab in St Louis; and to my office mates, Hector Basevi, James Guggenheim, James Brown and Xue Wu, for their active participations in numerous afternoon discussions on the whiteboard.

Finally I would like to thank my parents Weiqiang Zhan and Qingjun Yan among other lovely members of my family for supporting me in everything I have chosen to do.

But after all, reader, this is also dedicated to you.

# Contents

## List of Figures

# List of Tables

## List of Notations

$\mu$ : Optical Property (in general)

$\mu_a$ : Absorption Coefficient

$\mu_s$ : Scattering Coefficient

$\mu_s'$ : Reduced Scattering Coefficient

$D$ : Diffusion Coefficient

$A$ : Total Light Attenuation

$G$ : Light Attenuation due to Scattering

$c$ : Speed of Light

$\varepsilon$ : Molar Extinction Coefficient

$L$ : Energy Radiance

$\Phi$ : Light Intensity (or Fluence Rate, Photon Density)

$\vec{J}$ : Flux (or Photon Current)

$\chi$ : Objective (or Minimisation) Function

$I$ : Identity Matrix

$J$ : Jacobian Matrix

$\lambda$ : Wavelength

$\alpha, \beta, \rho$ : Regularisation Parameters

$S$ : Diagonal Matrix (that contains singular values)

$U, V$ : Orthonormal Matrices

$\sigma$ : Singular Value

$\kappa$ : Condition Number

## List of Abbreviations

AD: Alzheimer's Disease

APD: Avalanche Photo Diode

BOLD: Blood Oxygen Level Dependent

CBF: Cerebral Blood Flow

CSF: Cerebral Spinal Fluid

CW: Continuous Wave

DA: Diffusion Approximation

DCS: Diffuse Correlation Spectroscopy

DOT: Diffuse Optical Tomography

DP: Differential Pathlength

DPF: Differential Pathlength Factor

EEG: Electroencephalography

FD: Frequency Domain

fDOI: functional Diffuse Optical Imaging

fDOT: functional Diffuse Optical Tomography

FEM: Finite Element Method

fMRI: functional Magnetic Resonance Imaging

fNIRS: functional Near Infra Red Spectroscopy

FOV: Field Of View

FVHM: Full Volume Half Maximum

FWHM: Full Width Half Maximum

$HbO_2$: Oxygenated Haemoglobin

HbR: Deoxygenated Haemoglobin

HbT: Total Haemoglobin

HD: High Density

LM: Levenberg-Marquardt

LVHM: Localised Volume Half Maximum

MC: Monte Carlo

MEG: Magnetoencephalography

MRI: Magnetic Resonance Imaging

MSR: Magnetically Shielded Room

NN: Number of Nodes

NM: Number of Measurements

NIR: Near Infra Red

NR: Number of Regions

PET: Positron Emission Tomography

PMT: Photo Multiplier Tube

PSF: Point Spread Function

RF: Radio Frequency

ROI: Region Of Interest

RSFC: Resting State Functional Connectivity

RTE: Radiative Transfer Equation

SNR: Signal to Noise Ratio

SVD: Singular Value Decomposition

TD: Time Domain

TMS: Transcranial Magnetic Stimulation

TPFS: Temporal Point Spread Function

VFT: Verbal Fluency Test

## List of Publications

Some portions of this thesis are also parts of the following publications.

**Journal publications**

- Y. Zhan, A. T. Eggebrecht, J. P. Culver, and H. Dehghani, "Singular value decomposition based regularisation prior to spectral mixing improves crosstalk in dynamic imaging using spectral diffuse optical tomography," Biomed. Opt. Express 3, 2036-2049 (2012)
- Y. Zhan, A. T. Eggebrecht, J. P. Culver, and H. Dehghani, "Image quality analysis of high-density diffuse optical tomography incorporating a subject-specific head model," Front. Neuroenergetics 4, 6 (2012).
- T. Eggebrecht, B. R. White, S. L. Ferradal, C. Chen, Y. Zhan, A. Z. Snyder, H. Dehghani, and J. P. Culver, "A quantitative spatial comparison of high-density diffuse optical tomography and fMRI cortical mapping," Neuroimage 61, 1120-1128 (2012).

**Refereed conference proceedings**

- Y. Zhan, A. T. Eggebrecht, J. P. Culver, and H. Dehghani, "Spectrally constrained functional diffuse optical tomography of the adult brain, " in Biomedical Optics, OSA Technical Digest (Optical Society of America, 2012), paper JM3A.68.
- T. Eggebrecht, B. R. White, S. L. Ferradal, Y. Zhan, A. Z. Snyder, H. Dehghani, and J. P. Culver, "A quantitative spatial comparison of high-density diffuse optical tomography and fMRI cortical mapping, " in Biomedical Optics, OSA Technical Digest (Optical Society of America, 2012), paper BSu4A.2.
- Y. Zhan, A. T. Eggebrecht, J. P. Culver, and H. Dehghani, "Quantitative evaluation of systematic imaging error due to uncertainty in tissue optical properties in high-density diffuse optical tomography, ". Proc. SPIE 7896 (2011), 78960O.
- Y. Zhan, H. Dehghani, B. R. White, and J. P. Culver, "Application of Subject Specific Models for Mapping Brain Function with Diffuse Optical Tomography, " in Biomedical Optics, OSA Technical Digest (CD) (Optical Society of America, 2010), paper JMA62.

# CHAPTER 1

# INTRODUCTION

## 1.1 Functional diffuse optical imaging

Functional neuroimaging is the imaging of human brain functions. It utilises functional neuroimaging technologies to reveal the spatial distribution and connectivity of localised brain regions that are functionally distinct or associated with performing specific tasks. Such information is important as it not only broadens and deepens our understanding and knowledge in cognitive neuroscience and the psychology of healthy humans, but also provides useful guidance for the diagnosis, prognosis and treatment of psychological diseases.

Over the years various types of functional neuroimaging technologies have been developed based on different imaging principles and possess their own characteristics. One category known as functional diffuse optical imaging (fDOI) utilises near infrared (NIR) light as its physical mean of imaging [1] and has some unique advantages over other categories: first, fDOI is non-invasive and non-ionising as compared to positron emission tomography (PET), which ensures the health and safety of the imaging subjects and is well-suited for continuous daily monitoring and imaging; second, fDOI is free from 'electromagnetic interferences' such as transcranial magnetic stimulation (TMS), metallic implant or artificial pacemaker as in electroencephalography (EEG), magnetoencephalography (MEG) and functional magnetic resonance imaging (fMRI); third, fDOI instruments are generally portable, accessible, highly wearable and insensitive to motion artefacts, which offer great flexibility regarding the

subjects' physical and medical conditions, such as for patients in the intensive care unit (ICU) or infants who require sedation; fourth, fDOI allows simultaneous recording of changes in both oxygenated haemoglobin ($\Delta HbO_2$) and deoxygenated haemoglobin ($\Delta HbR$), providing more comprehensive haemodynamic imaging capability than fMRI. Until recently the most successful fDOI technique has been functional near infrared spectroscopy (fNIRS), which has found widespread applications in cognitive neuroscience and psychiatry studies [2, 3]. However at the same time fNIRS is also known for its insufficient lateral resolution and limited depth information. The need for the development of a more advanced fDOI technology that could provide three-dimensional (3D) tomographic imaging capability at improved lateral resolution and localisation accuracy is highly demanding. With decades of numerous efforts in instrumentation design, modelling theory and software solution, this vision eventually became a reality. The technique is known as functional diffuse optical tomography (fDOT), and is the main topic that we are going to focus on in this thesis.

## 1.2 Research questions and thesis outline

Despite having all the inherent advantages of a fDOI technique, plus 3D volumetric (or tomographic) image reconstruction capability, widespread acceptance of fDOT in the functional neuroimaging community has so far been hampered by as yet insufficient spatial resolution, limited depth penetration, restricted field of view, and lack of reliable and repeatable functional mapping. Through literature review we have identified the following factors that have been well-regarded as the causes of sub-optimal image quality in previous fDOT studies:

- Sparsely arranged optical source and detector probes on the imaging array, resulting in limited spatial sampling of the underlying brain tissues [4-6].

- Model mismatch in terms of the spatial distribution and numerical accuracy of tissue optical properties, between *in vivo* head anatomy ('the ground truth') and the anatomical model used for image reconstruction [6, 7].
- Imaging crosstalk between recovered changes in oxygenated haemoglobin ($\Delta HbO_2$) and deoxygenated haemoglobin ($\Delta HbR$), which is highly dependent on the selection of imaging wavelengths [4, 8, 9]. In addition as demonstrated later in **Chapter 7**, such crosstalk can also be introduced by mathematical regularisation performed during image reconstruction.

In regard to the above-mentioned factors, the aim of this thesis is to improve the image quality of fDOT by addressing and resolving these issues selectively and collectively. Specifically we have proposed the following solutions to achieve this aim:

- Utilisation of a high-density imaging array, as opposed to sparse imaging arrays, providing higher spatial sampling of the underlying brain tissues.
- Utilisation of MRI-guided head models, as opposed to simplified head models, reducing model mismatch in terms of the spatial distribution of tissue optical properties between *in vivo* head anatomy and the anatomical model used for image reconstruction.
- Utilisation of subject-specific head tissue optical properties derived from measurements taken from the subject, as opposed to literature published generic values, reducing model mismatch in terms of the numerical accuracy of tissue optical properties between *in vivo* head anatomy and the anatomical model used for image reconstruction.

- Utilisation of novel regularisation method in spectrally-constrained fDOT image reconstruction, reducing imaging crosstalk between the recovered $\Delta HbO_2$ and $\Delta HbR$ images.

These proposals have been implemented, evaluated and presented in this thesis, which is organised as follows:

**Chapter 2** introduces the concepts of human brain function and functional neuroimaging, summarises five mainstream functional neuroimaging techniques and their applications in cognitive neuroscience and psychiatric studies.

**Chapter 3** focuses on functional diffuse optical imaging (fDOI) and describes its imaging principle, system design, imaging mode and the associated image quality analysis.

**Chapter 4** is dedicated to functional diffuse optical tomography (fDOT) with a model-based approach. Starting with the establishment of a finite element method (FEM)-based fDOT workflow, the chapter then discusses specific modelling issues within the workflow in greater detail.

**Chapter 5** presents the first realistically noise-added point-spread-function (PSF) analysis in MRI-guided HD-fDOT studies and demonstrates achievable image quality throughout the field of view (FOV) of a realistic imaging system.

**Chapter 6** investigates the effects of uncertainty in the background tissue optical properties on HD-fDOT image quality, as well as the proposed use of background absorption fitting scheme in minimising such effects.

**Chapter 7** describes a novel regularisation scheme that reduces imaging crosstalk between $\Delta HbO_2$ and $\Delta HbR$ images using spectral fDOT image reconstruction.

Finally we conclude in **Chapter 8**, followed by **Appendices** and **Bibliography**.

# CHAPTER 2

# FUNCTIONAL NEUROIMAGING

## 2.1 Physiology

The human brain is an extremely complex information processor. The cerebral cortex contains around 15-33 billion information processing units known as the neurons [10]. Neurons are electrically active cells that are primarily responsible for human brain functional activities. A typical neuron is composed of three parts: a cell body, dendrites and an axon. Neurons can create electrical membrane potentials known as the action potentials, which propagate from one neuron to another along the axon in the form of electrical impulses. Once the impulse arrives at the synapse at the axon terminal, neurotransmitter molecules are released upon specific receptor on the dendrite of the postsynaptic neuron. The neurotransmitter-receptor interaction causes membrane current flows within the dendrite or cell body of the neuron, which then sum up to generate the post-synaptic neuronal action potential for further transmission, as shown in **Figure 1**.

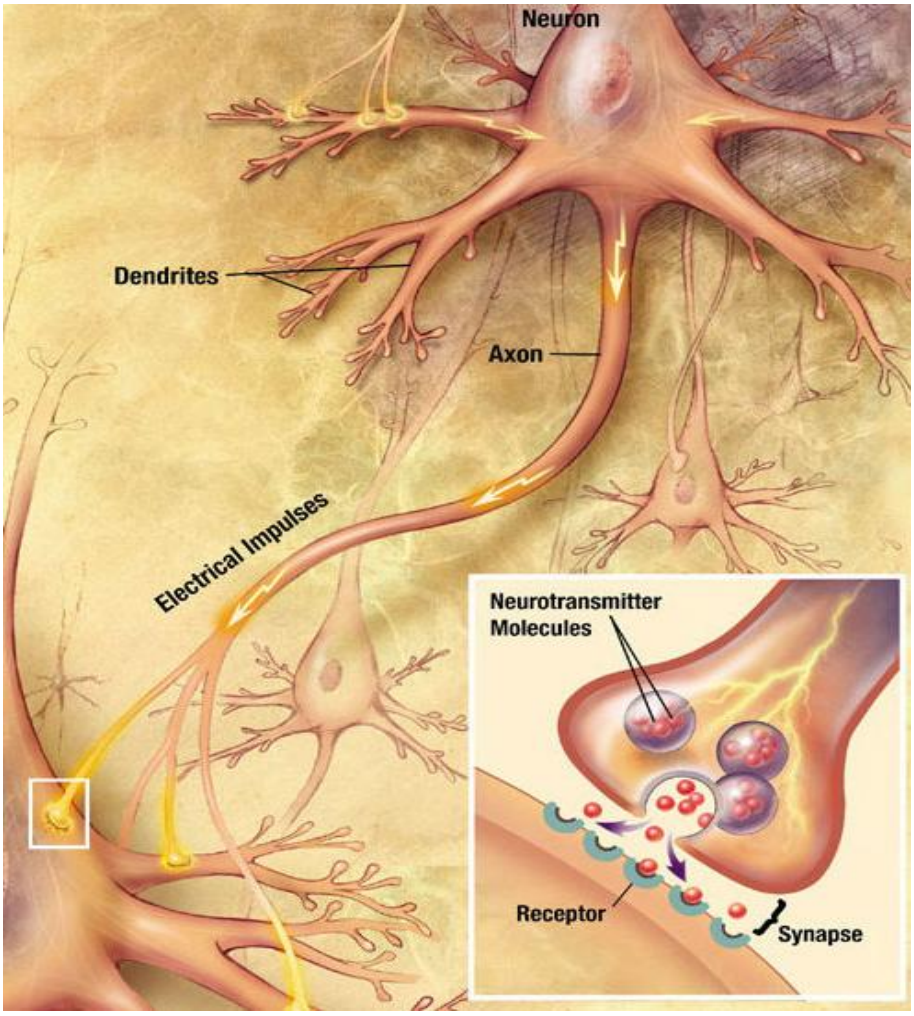


**Figure 1 Synaptic transmission between neurons via axon [11].**

It is worth noting that during a synaptic transmission, energy is required to be consumed at or around synapses. As the neurons themselves do not contain sufficient energy sources, neuronal activation is accompanied by increased regional cerebral blood flow (rCBF) for greater local deliver of oxygen and glucose. This phenomenon is known as the 'neurovascular coupling effect' [12, 13].

## 2.2 Functional neuroimaging technology

From the imaging point of view, the electrical pulse provides a direct and explicit measure of the underlying neuronal activities in the human brain, whereas the blood flow offers an

indirect and implicit yet effective indication of those activities through neurovascular coupling. Based on the type of physiological phenomenon to be measured, two streams of functional neuroimaging techniques have been developed, each possessing their own characteristics in terms of temporal and spatial resolution. On one hand, direct (or electro-magnetic) techniques such as electroencephalography (EEG) or magnetoencephalography (MEG) allow direct measure of the electrical neural signals induced by neuronal activities in real time, offering millisecond imaging temporal resolution. On the other hand, indirect (or haemodynamic) techniques such as functional magnetic resonance imaging (fMRI), positron emission tomography (PET), and functional diffuse optical imaging (fDOI) detect the much slower vascular signals that accompany the neuronal activities (normally 2 to 5 seconds after the neuronal signal), but at higher spatial resolution than direct techniques. Interestingly there have also been attempts to use fDOI to detect a much faster type of optical signal (10 to 100 milliseconds after the neuronal signals) known as the 'fast signals', which was thought to be induced by changes in scattering due to cell conformation and swelling during neuronal activities. Unfortunately the topic later became controversial when the magnitude of the signal was thought to be too small to be reliably detectable [14, 15]. Here we describe five mainstream functional neuroimaging technologies as mentioned previously in greater detail and summarise them in **Table 1**:

- **Electroencephalography (EEG)**

EEG measures excitatory postsynaptic potential (EPSP) caused by extracellular volume current. This is measured by multiple electrodes placed on the scalp. **Figure 2** illustrates its signal basis and a subject wearing a standard EEG imaging cap.

**The advantages:** EEG is a non-invasive and non-ionising technique. It offers high temporal resolution (at milliseconds) because of its direct measure of the primary electrical neural

signals. In addition modern EEG instruments are portable, accessible and affordable (at tens of thousands of pounds).

**The disadvantages:** The availability of boundary-only measurements means limited depth penetration as signal sources located at deeper depth are measured at weaker strength. In addition, EEG signal is measured through intervening tissues such as meninges, cerebral spinal fluid (CSF) and skull, which possess low conductivity that distorts and affects the signal-to-noise ratio (SNR) of the measurement, thereby limiting the spatial resolution of scalp EEG to centimetres [16]. One approach to avoid such intervention is to remove the scalp and place the electrodes directly on the cortex of the brain, which is a sub-branch of EEG known as Electrocorticography (ECoG). However such an invasive procedure is impractical for most human subject studies. Furthermore, even if access to quality EEG signals can be obtained, it is theoretically possible that several currents produce potentials that cancel each other out, which suggests that reconstruction of a unique intracranial current source from a given EEG signal is mathematically infeasible [17].

**Figure 2 (a) Schema of EEG signal basis: both tangentially (grey arrows) and radially (yellow arrows) oriented current can be picked up by EEG electrodes placed on the scalp; (b) a human subject wearing an EEG imaging cap. EEG signals are detected by the electrodes fixed at specified locations on the black imaging cap, and transmitted to the EEG machine via EEG leads (red wires) [18].**

- **Magnetoencephalography (MEG)**

MEG records magnetic field produced by intracellular current flowing in the dendrites of neurons during synaptic transmission. **Figure 3** illustrates its signal basis and a subject sitting in an MEG scan.

**The advantages:** MEG is also non-invasive and non-ionising, and offers millisecond temporal resolution like EEG. Since the magnetic field measured by MEG is not affected by the intervening tissues between the measuring probe and the brain, MEG has higher spatial resolution (at millimetre) than EEG [16].

**The disadvantages:** MEG signal magnitude is in the order of femtotesla (fT, $10^{-15}$) as compared to the microtesla (μT, $10^{-6}$) of the earth's magnetic field. For this reason, modern MEG systems are equipped with arrays of highly sensitive superconducting quantum interference device (SQUID) magnetometers and must be operated in a magnetically shielded

room (MSR), thus making the cost of an entire MEG system setup stands at millions of pounds, which in turn constrain its availability and accessibility. Furthermore MEG measurement sensitivity decreases even more rapidly with source depth than EEG [16], and magnetic fields generated by radially oriented current cannot be picked up by MEG [19], which limits its field of view.

**Figure 3 (a) Schema of MEG signal basis: MEG can pick up the magnetic field (red ellipse) induced by tangentially (yellow arrows) oriented current, but is insensitive to radially (grey arrows) oriented current; (b) a human subject sitting in a MEG system located in a MSR [18].**

- **Functional magnetic resonance imaging (fMRI)**

fMRI utilises strong magnetic fields to measure blood magnetic susceptibility. Specifically, the imaging subject is placed under a strong static magnetic field generated by a magnet and a smaller varying gradient magnetic field generated by a gradient coil. A radiofrequency (RF) coil then generates a pulse and detects the resultant resonance frequency signal, as illustrated in **Figure 4**. Since oxygenated haemoglobin ($HbO_2$) is diamagnetic while deoxygenated haemoglobin (HbR) is paramagnetic [12], the fMRI signal varies with local blood oxygenation level and owns its name as the 'BOLD (blood oxygen level dependence) signal'.

However because the BOLD contrast depends on the combined effect of vascular oxygen level and rCBF, it does not provide a direct measure of $\Delta HbO_2$ and $\Delta HbR$. While the paramagnetic nature of HbR suggests a strong correlation between $\Delta HbR$ and BOLD, experimental confirmation of this remains controversial as better correlations between BOLD and either haemoglobin have been reported (BOLD-$\Delta HbO_2$: [20, 21]; BOLD-$\Delta HbR$: [22, 23]).

**The advantages:** fMRI is non-invasive and non-ionising, and is capable of three-dimensional tomographic imaging at high spatial resolution (at millimetre resolution) with large field of view (good depth penetration throughout the brain). For these reasons, fMRI has been widely regarded as the 'gold standard' in functional neuroimaging.

**The disadvantages:** Being a haemodynamic technique means that fMRI has a compromised temporal resolution compared to EEG and MEG, characterised by a typical 2-5 seconds 'haemodynamic lag'. An fMRI instrument is also large in terms of both physical scale and financial cost, which limits its availability and accessibility. Magnetic interferences such as TMS, metallic implants and artificial pacemakers are prohibited during fMRI scans. The magnet in the machinery generates loud acoustic noise during operation, which is unsuited for subjects who require sedation. The technique is also sensitive to head motions by the imaging subject, which can result in significant imaging artefacts that require postprocessing for motion correction [12].

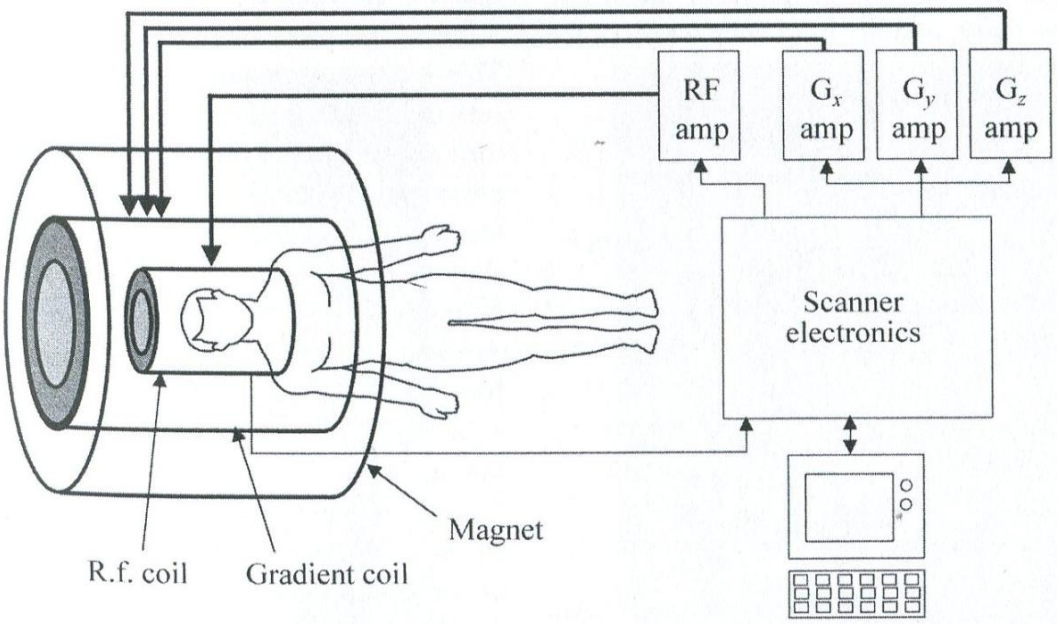


**Figure 4 (a) Schema of a fMRI scanner. The scanner consists of a magnet, a gradient coil and a radiofrequency (RF) coil. The magnet generates a strong static magnetic field. The gradient coil generates a smaller varying gradient magnetic field to provide spatial-encoding. The RF coil generates a pulse and detects the resultant resonance frequency signal [12].**

- **Positron emission tomography (PET)**

PET requires a short-lived radioisotope to be injected into the human body to provide radioactive labelling of biologically active molecules such as fluorodeoxyglucose (FDG). The radioisotope undergoes positron emission decay, in which a positron is emitted. When the positron collides with an electron in the body, a process known as annihilation takes place, which produces a pair of gamma photons travelling in opposite directions. These photons are detected by photomultiplier tubes (PMTs) located around the imaging subject in a ring-shape configuration, as shown in **Figure 5**. Since PET images are most useful when aligned and displayed over the underlying anatomy, modern brain scanners often combine PET with MRI to build the so-called "PET/MRI" system [24, 25].

**The advantages:** PET provides high spatial resolution (at millimetre).

**The disadvantages:** PET is invasive and ionising in the sense that external material must be injected and ionising radiation is emitted within the human body. In addition, signal attenuation occurs when the emitted gamma photons are absorbed by the surrounding tissues with unknown absorptions before reaching the detector. The instruments are expensive (typically hundreds of thousands of pounds) and even more so when combined with an MRI machine. Due to the existence of alternative non-invasive and non-ionising technique such as fMRI, approvals for human subject PET studies have become increasingly difficult.

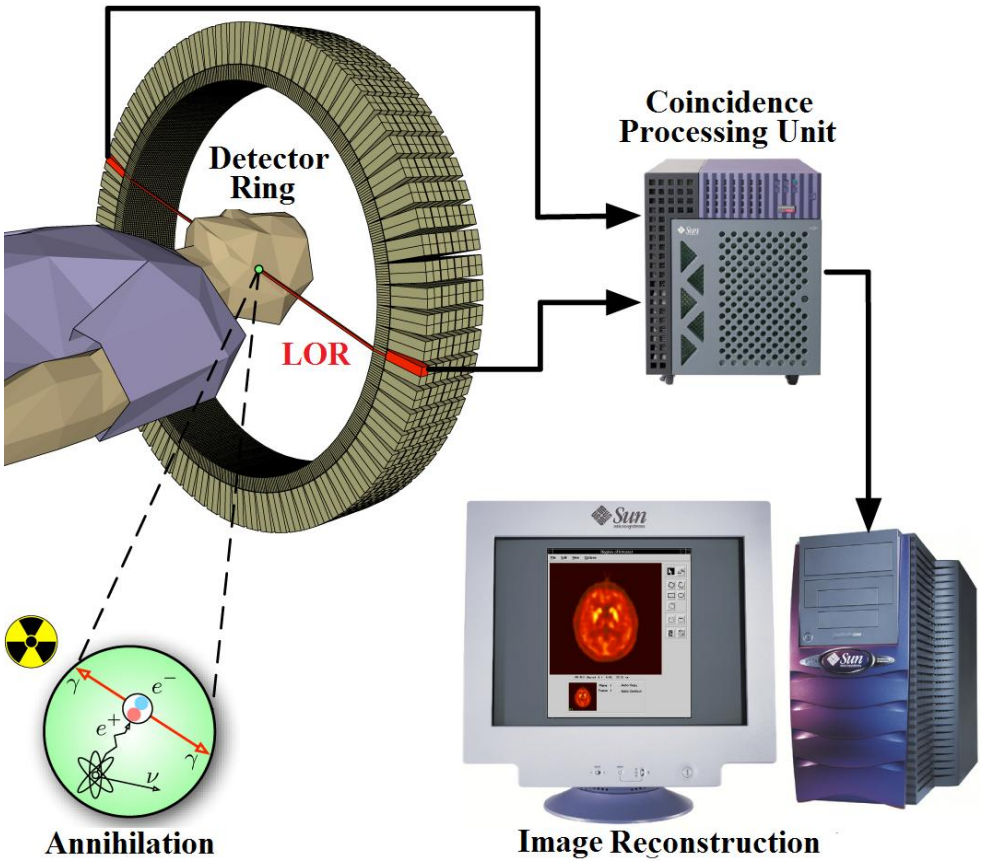


**Figure 5 Schema of a PET scanner as modified from [26]. When the positron emitted from the injected radioisotope encounters the electron in the brain, annihilation takes place (shown in bottom-left figure). The process produces a pair of gamma photons travelling in opposite directions, which are captured by the detector ring and recorded in the coincidence processing unit to localise the source along the straight line of response (LOR, shown in red in upper-left figure) and then reconstruct an image (bottom-right).**

- **Functional diffuse optical imaging (fDOI)**

fDOI makes use of the relatively low optical attenuation of human tissue in the near infra red (NIR) spectrum between 650 and 950 nm. Specifically photons are injected into the head from optical sources such as light-emitting diodes (LEDs) or laser diodes placed on the scalp, and a portion of them (known as the exit photons) would be collected by optical detectors such as avalanche photodiodes (APDs) or PMTs placed at other locations on the scalp, typically at a few centimetres away from the sources. Given that the exit photons have propagated through the brain tissues, they are encoded with optical information of the brain, which can be further interpreted into physiological and functional information. According to the 'Handbook of Biomedical Optics' [27], fDOI can be categorised into 'dynamic' and 'static' regimes. Diffuse correlation spectroscopy (DCS) for instance, which measures the dynamic motion of the flowing scatters in the brain (in this case the red blood cells, or RBCs) and provides an indication of the rCBF, is considered as a 'dynamic' method; Functional near-infrared spectroscopy (fNIRS) on the other hand, which measures 'the amount of variations in tissue scattering and absorption' rather than the dynamic scattering motion, and provides an indication of the amount of changes in oxygenated and deoxygenated haemoglobin concentrations during brain activities, is regarded as a 'static' technique. Furthermore indocyanine green (ICG) has been used as a standard contrast agent for fDOI signal enhancement [28, 29]. It is worth noting that there exists an alternative definition of the words 'dynamic' and 'static' in diffuse optics literature. For instance in [30] the phrase 'dynamic imaging' was used to refer to techniques that measure the differential change in haemoglobin concentration between two functional states, and will be referred to as 'differential imaging' in this thesis; the phrase 'static imaging' was used to describe techniques that measure the absolute value of haemoglobin concentration, for instance in diffuse optical breast imaging to

characterise breast cancer [31], and will be referred to as ‘absolute imaging’ in this thesis. A more extensive review on fDOI will be given in the next chapter (**Chapter 3)**.

**The advantages:** In comparison with the four above-mentioned neuroimaging techniques, fDOI possesses many advantages: first of all, fDOI is non-invasive and non-ionising as compared to PET, which ensures the health and safety of the imaging subjects; second, fDOI is free from ‘electromagnetic interferences’ such as TMS [32], metallic implant or artificial pacemaker as in EEG, MEG and fMRI; third, fDOI instruments are portable, accessible, highly wearable and insensitive to motion artefacts, allowing much greater flexibility regarding the subjects’ physical and medical conditions, for example for patients in the intensive care unit (ICU), or infants who require sedation for the otherwise fMRI scans; fourth, fDOI allows simultaneous recording of changes in both oxygenated haemoglobin ($HbO_2$) and deoxygenated haemoglobin (HbR), offering more comprehensive haemodynamic imaging capability than the ‘gold standard’ fMRI.

**The disadvantages:** The diffuse nature of photon propagation in human tissue results in rapid degradation of spatial resolution with increasing depth into the brain, constraining the penetration depth of fDOI. Specifically the optical measurements provide limited tissue sampling at deeper signal locations, which results in the so-called ‘partial volume effect’, where the quantified haemoglobin response represents an underestimated (in image contrast) and broadened (in image resolution) version of the actual response [4]. In addition, the collected optical measurements (or exit photons) contain functional information regarding not only the brain but also the intervening tissues such as the scalp and the skull, therefore requiring postprocessing signal regression to remove the so-called ‘superficial signals’.

**Table 1 Comparison of five functional neuroimaging techniques. All haemodynamic techniques have a typical 2-5 seconds temporal lag.**

| Criteria | Electro-magnetic | | Haemodynamic | | |
|---|---|---|---|---|---|
| Technique | EEG | MEG | fMRI | PET | fDOI |
| Temporal resolution | millisecond | millisecond | second | second | hundreds of millisecond to second |
| Spatial resolution | centimetre | millimetre | millimetre | millimetre | milli to centimetre |
| Invasive & Ionising | No | No | No | Yes | No |
| Cost scale | ~£10,000 | ~£1,000,000 | ~£1,000,000 | ~£100,000 | ~£10,000 |
| Experimental flexibility | Movement permitted | Not permitted | Not permitted | Not permitted | Movement permitted |
| Signal index | Extracellular (secondary) current | Magnetic field generated by intracellular (primary) current | Blood oxygenation level dependent (BOLD) | Regional cerebral blood flow (rCBF) | Optical absorption of haemoglobin / rCBF |
| Signal purity | Affected by intervening tissues | Unaffected | Unaffected | Affected by intervening tissues | Affected by intervening tissues |

## 2.3 Functional neuroimaging application

The advent of functional neuroimaging technology has revolutionised a number of neuroscience disciplines, most notably cognitive neuroscience in healthy human beings, and psychiatric research in patients. To demonstrate the widespread applications of functional neuroimaging techniques in clinical studies, we herein review a number of selected examples from both cognitive neuroscience and psychiatry.

### 2.3.1 Cognitive neuroscience

Briefly speaking cognitive neuroscience relates cognitive functions to specific regions of the brain. The availability of functional neuroimaging techniques has allowed neuroscientists to directly visualise regions that are functionally active while the subject is performing certain cognitive operations. A number of classic cognitive functions have been established in the field of cognitive neuroscience, which have been extensively investigated by various functional neuroimaging modalities over the past few decades. Here we review selected applications in some of these classic cognitive functions. Note that the phrases 'fNIRS', 'functional diffuse optical topography' and 'fDOT' as mentioned below are three types of imaging mode within fDOI, which will be explained in greater detail in **Section 3.3**.

- **Vision**

Vision is mainly related to the primary visual cortex (V1), which is located in the occipital lobe in the back of the brain. It is found that the human visual cortex consists of four quadrants, which map to their respective functional quadrants in a contralaterally reversing manner. Retinotopic mapping of the human visual cortex has been extensively conducted in early evaluation of PET [33] and fMRI [34, 35], and more recently in fDOT standalone validation [36, 37], as shown below in **Figure 6**, as well as with fMRI [38].

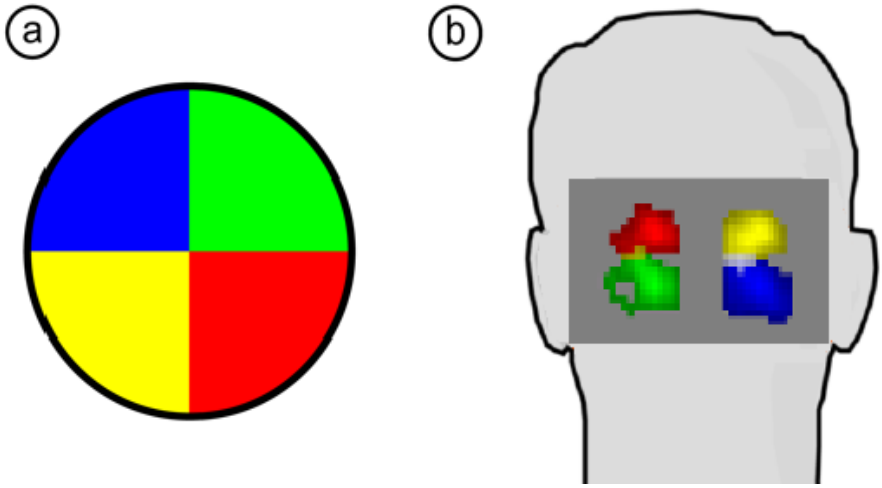


**Figure 6 (a) The 4 quadrants which are colour-coded illustrate the 4 possible positions at which the visual stimuli can be displayed; (b) The corresponding quadrant activations recorded using fDOT [37].**

- **Somatosensory activity**

Somatosensory activity is mainly associated with the primary somatosensory cortex (S1) which is located in the lateral post-central gyrus. Its organisation is also well studied by PET [39] , fMRI [40], and more recent standalone fDOT validation [41] as reported in **Figure 7**, as well as with fMRI [42].

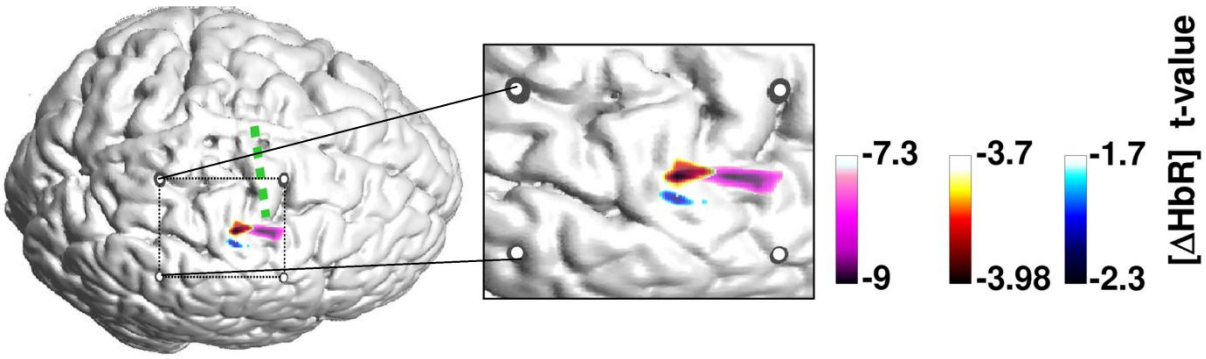


**Figure 7 fMRI activation maps (HbR t-value maps) for finger tapping (pink), vibrotactile stimulation of first (blue) and fifth (red) finger respectively, are superimposed on the anatomical brain [41]. The t-value provides a measure of the significance of the change (or difference) between one set of HbR concentration data measured during a baseline state (when no finger tapping or no vibrotactile stimulation is performed) and another set of HbR concentration data obtained during an activation state (when finger tapping or vibrotactile stimulation is performed). The value is calculated using the t-test which takes the standard deviation of each dataset into account. The negative t-values shown in the graph indicate negative ΔHbR, or decrease in HbR concentration from baseline to activation state.**

- **Motor activity**

Motor activity is related to the primary motor cortex (P1) which is located in the pre-central gyrus. Simple motor tasks such as finger tapping are often used to stimulate motor activation which can be well imaged by fMRI and fNIRS [43] as illustrated in **Figure 8**, which shows a good correspondence of the measured BOLD signal with fNIRS derived data, as well as the advantage of quantifying the related changes in total, oxygenated and deoxygenated haemoglobins.

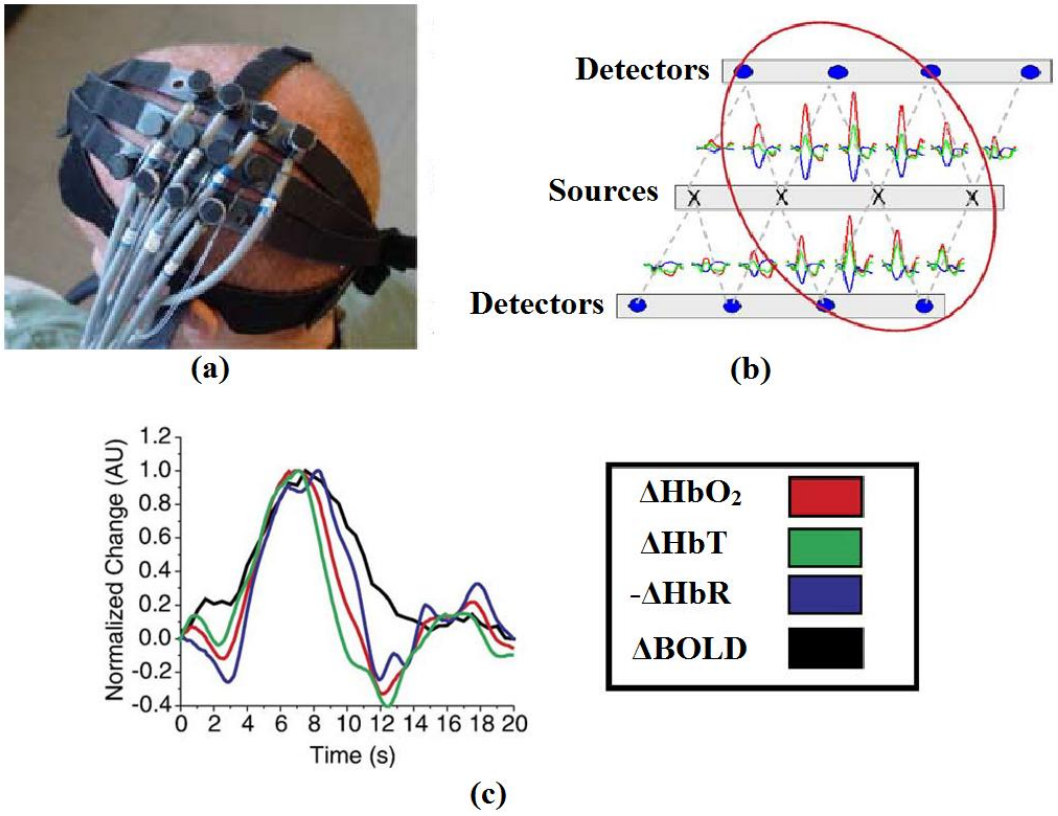


**Figure 8 (a) Experimental setup of the fNIRS probes on the imaging subject; (b) schema of the probes (sources and detectors) and the patterns of recovered change in chromophore concentrations for each channel; (c) normalised change (averaging across all channels) of $\Delta HbO_2$, $\Delta HbR$ and $\Delta HbT$ ($=\Delta HbO_2+\Delta HbR$) from fNIRS and $\Delta BOLD$ from fMRI [43].**

- **Resting state functional connectivity (RSFC)**

RSFC is the correlation of haemodynamic activities between distinct regions of the human brain at the resting state. PET and fMRI studies have revealed that in absence of overt tasks there exists spontaneous low-frequency fluctuation (sLFF<0.08 Hz) in brain activity that are correlated across functional related regions [44]. More recent fDOT studies have demonstrated the capability of reproducing the RSFC [45, 46]. **Figure 9** reveals the spatial similarity of the fDOT and fMRI functional connectivity maps for the visual and motor cortex seeds [45].

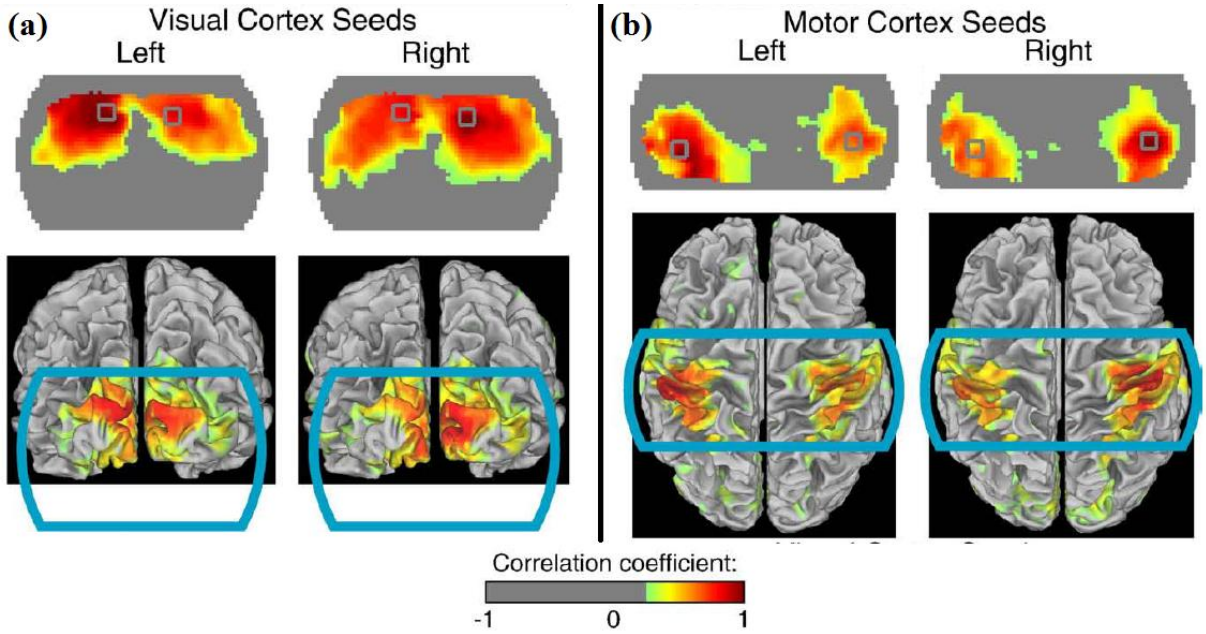


**Figure 9 fDOT (upper row) and fMRI (lower row) functional connectivity map: (a) using left and right visual cortex seed; (b) using left and right motor cortex seed [45].**

### 2.3.2 Psychiatry

The main role of functional neuroimaging in psychiatry is to characterise the neurobiological features of psychiatric disorder at various stages (early to late) for the purpose of diagnosis, prognosis and treatment. This has been done by comparing functional neuroimaging data collected from healthy and patient subjects during a variety of designated tests or cognitive paradigms, such as the verbal fluency test (VFT) where the participants are instructed to say as many words as possible within a pre-specified context (a certain category or word starting with certain letter). Here we review selected examples of functional neuroimaging application in the studies of psychiatric disorder.

- **Schizophrenia**

Schizophrenia is a mental (or psychiatric) disorder characterised by disorganised locomotion, speech and emotion. PET, fMRI [47] as well as fNIRS [48, 49] studies have observed task-

dependent hypo-functionality in the frontal cortex. **Figure 10** shows significantly reduced frontal activations in schizophrenic patients during a VFT task.

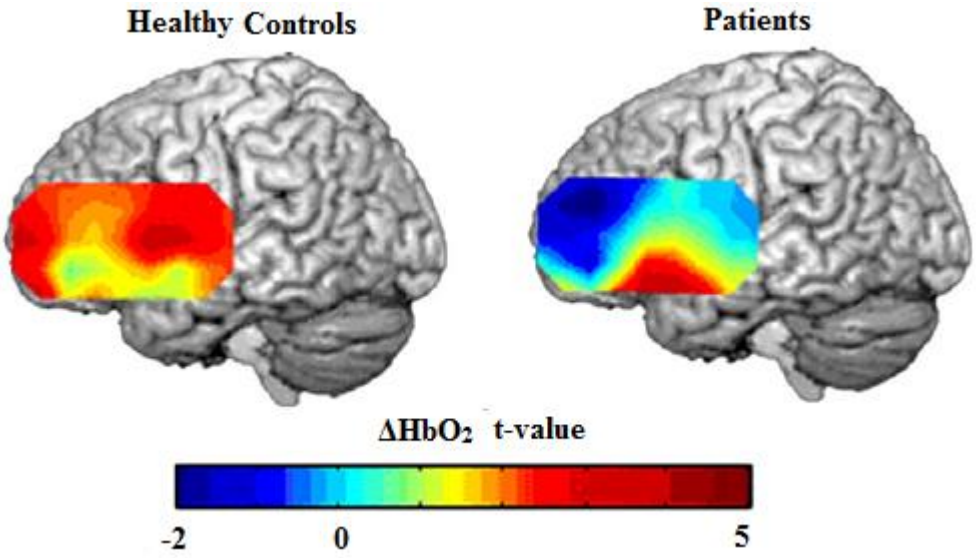


**Figure 10 Functional response of healthy controls (left) versus schizophrenic patients (right) to a VFT task. The t-value provides a measure of the significance of the change (or difference) between one set of $HbO_2$ concentration data measured during a baseline state (when the healthy control or patient is performing a control task) and another set of HbR concentration data obtained during an activation state (when the healthy control or patients is performing the VFT). The negative t-values shown in the frontal cortex of the patients as compared to positive t-values of the healthy controls, indicate significantly reduced frontal activations in the patients. [49].**

- **Alzheimer's disease (AD)**

AD is the most common type of dementia. It is a neurodegenerative process of the brain due to aging, characterised by reduced activation and cognitive functional losses. Both PET [50] (**Figure 11**) and fMRI [51] reported reduced parietal activity in AD patients, and further fNIRS studies [52, 53] confirm reduced task-related $\Delta HbO_2$ (increase in $HbO_2$).

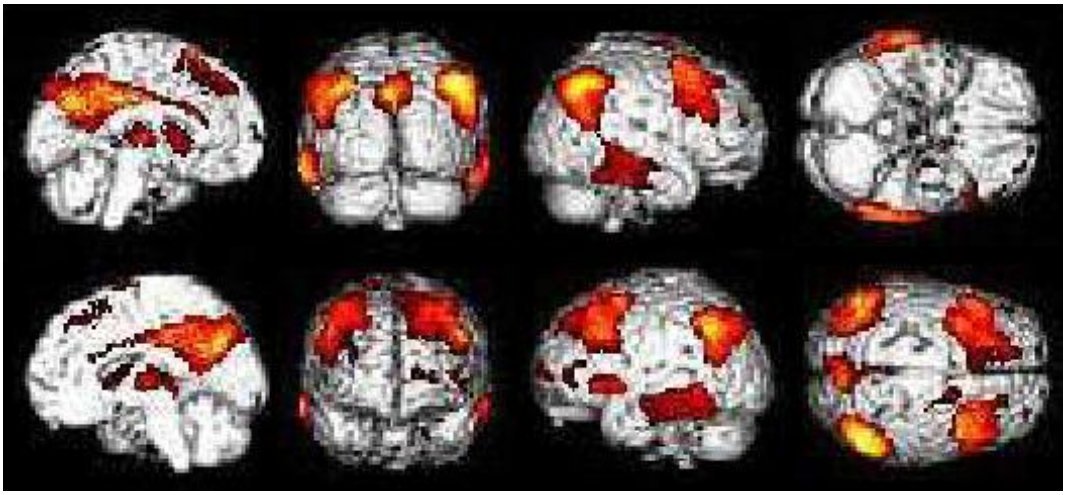

**Figure 11 Hypo-metabolic regions (shown in warm colour) found in patients with probable AD as compared to healthy controls. These regions include the bilateral posterior cingulated and media parietal cortex, temporal-parietal associated with occipital cortex, prefrontal cortex and temporal cortex [50].**

- **Addiction**

Addiction has been thought to relate to hyper activation within the reward system located in the ventral striatum. Recent fNIRS studies on alcohol dependent patients [54] observed reduced prefrontal activations as compared to healthy subjects (**Figure 12**), suggesting the hyper-activation of the reward system is likely to be based on reduced inhibitory control by the prefrontal cortex region [3].

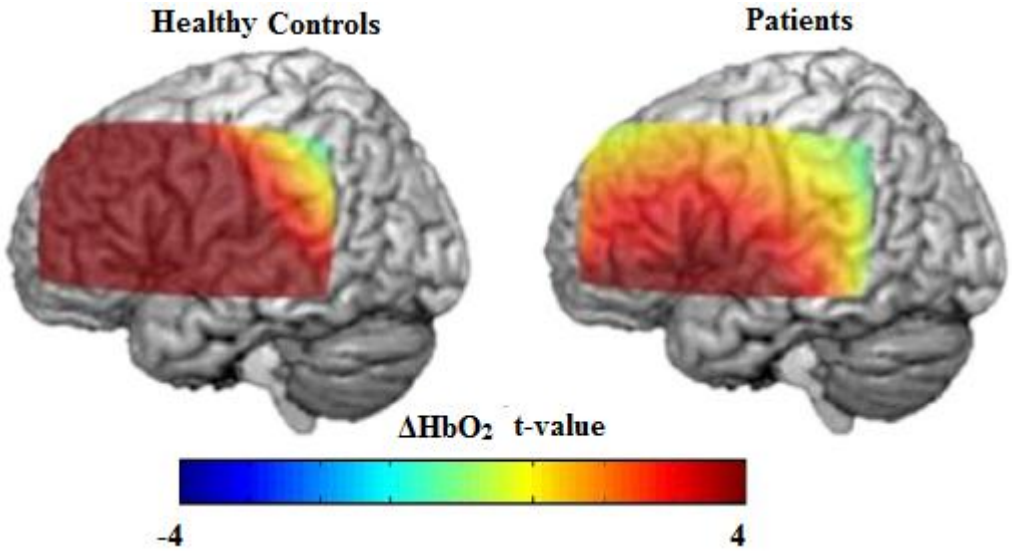


**Figure 12 Functional response of healthy controls (left) versus alcohol dependent patients (right) to a VFT task. The t-value provides a measure of the significance of the change (or difference) between one set of $HbO_2$ concentration data measured during a baseline state (when the healthy control or patient is performing a control task) and another set of HbR concentration data obtained during an activation state (when the healthy control or patients is performing the VFT). The positive t-values shown in the prefrontal cortex of the patients are less in magnitude than the positive t-values of the healthy controls, indicating reduced prefrontal activations in the patients [54].**

- **Repetitive transcranial magnetic stimulation (rTMS)**

TMS is a technique that utilises an electromagnetic coil to stimulate neurons in the human brain. Specifically the coil is placed on the human scalp, producing rapidly changing magnetic pulses to generate electrical fields that can depolarise the neurons. Most notably it was found that such procedure when repeated on a daily basis (known as repetitive TMS or rTMS) on the prefrontal cortex can provide treatment for depression, making rTMS a therapeutic tool [55, 56]. In order to further evaluate and optimise the treatment procedure, an objective measure of the impact of rTMS on the functionality of the brain is required and was recently realised using fNIRS [57] and functional diffuse optical topography [32], as demonstrated in **Figure 13** below.

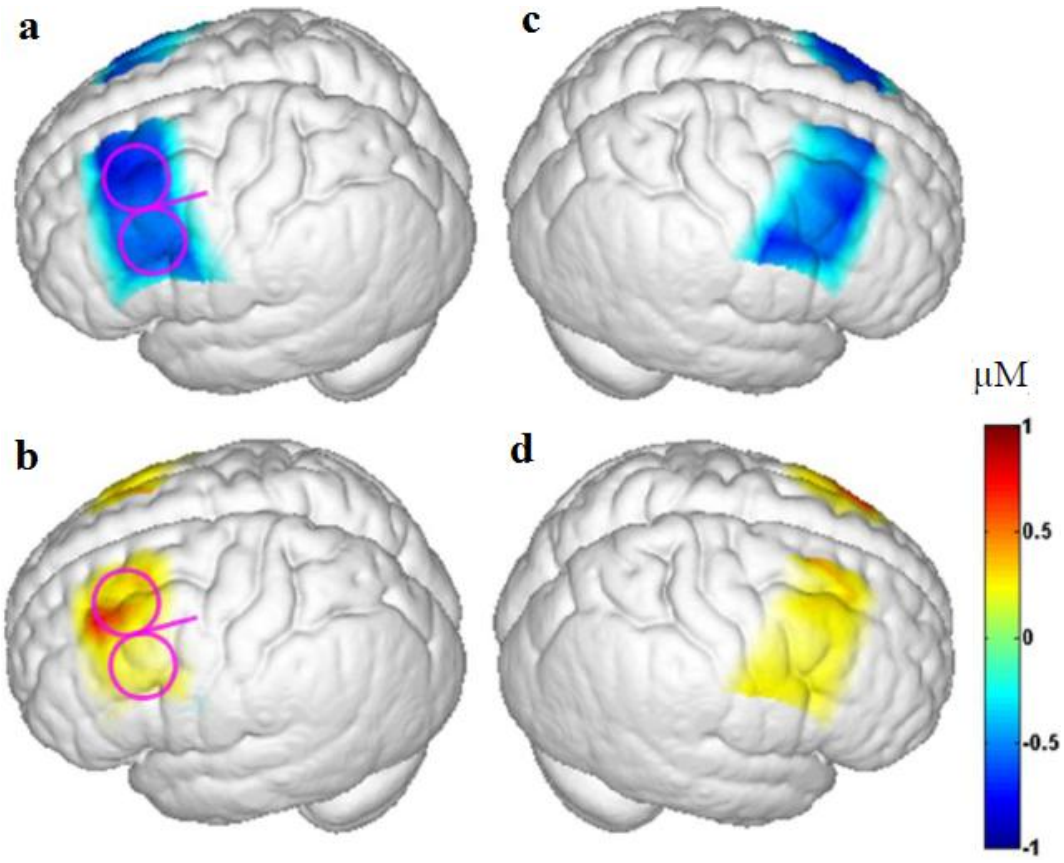


**Figure 13 Averaged topographic images at the prefrontal cortex: (a) $\Delta HbO_2$ and (b) $\Delta HbR$ in the ipsilateral hemisphere (with respect to the site of the TMS coil, indicated by the pink circles), as well as (c) $\Delta HbO_2$ and (d) $\Delta HbR$ in the contralateral hemisphere [32].**

## 2.4 Summary

This chapter has provided a background introduction for functional neuroimaging and set the scene for the rest of the thesis. We started by describing the physiology behind neuronal activation, which is fundamentally an electrical transmission process. We then brought in the energy perspective of this process, which requires additional energy to be supplied and consumed at or near the site of transmission. Physiologically this is achieved by increased regional cerebral blood flow (rCBF) that allows greater local delivery of oxygen and glucose (as the energy source), and this phenomenon is known as the 'neurovascular coupling effect'.

By understanding the physiology of neuronal activation, we then described five mainstream functional neuroimaging technologies that have been developed by making use of these physiological phenomena. After illustrating their respective working principles, we discussed the advantages and disadvantages of each technique, and emphasised the strengths of diffuse optical imaging (fDOI), notably in non-invasiveness, accessibility and comprehensive haemodynamic imaging capability.

To further demonstrate the usefulness of these functional neuroimaging techniques in the study of cognitive neuroscience and psychiatry, we then reviewed selected examples among their widespread applications in the monitoring of neuronal activities in both healthy and patient subjects, and highlighted the comprehensive haemodynamic imaging capability of fDOI, which could provide helpful indications and guidance for the diagnosis, prognosis and treatment of mental illnesses. These set the motivation for the continuous and ongoing efforts in the development of fDOI techniques, which are to be discussed in the next chapter.

# CHAPTER 3

# INTRODUCTION TO fDOI

## 3.1 Principle of fDOI

Functional diffuse optical imaging (fDOI) utilises near infra red (NIR, 650nm to 950nm) light to measure physiological changes in the human brain during neuronal activities. In a standard experimental setup, an imaging array which contains optical sources (or emitting probes) such as LEDs or laser diodes, and optical detectors (or detecting probes) such as APDs or PMTs, are placed over and in contact with the human scalp. Any blockage between the probes and the scalp by the human hairs should preferably be avoided as they could significantly affect the strength of the signal and reduce the signal to noise ratio (SNR) of the measurement. During the imaging session, the source probes emit photons into the head while the detecting probes measure any photons that exit from the head at the detector locations. The measurement is denoted by $\Phi$, meaning light intensity (or fluence rate). Photon propagation in head tissues (and biological tissues in general) is predominantly characterised by two physical phenomena: scattering and absorption, as illustrated in **Figure 14 (a)**. The optical properties (denoted by $\mu$) that are commonly used in literature to quantify these phenomena are the scattering coefficient $\mu_s$ and the absorption coefficient $\mu_a$, which represent the average number of scattering and absorption events occurring per unit distance travelled by a photon, respectively. Since the injected photons undergo hundreds if not thousands of scattering and absorption events before being collected by the detectors, the exit photons are

'encoded' with information regarding the optical properties of the underlying imaging domain. In addition, because the size of an adult head (approximately 8 cm in radius) is most likely to be much larger than the source-detector distance (typically no longer than 5 cm [4, 38]), fDOI measurements are mostly reflectance rather than transmittance (however on a side note, transmittance measurement is possible with new born babies [58-60]). This means that the overall shape of the optical path of the exit photons is curved backwards like a banana [61] as shown in **Figure 14 (a)**, and so is the resultant measurement sensitivity as shown in **Figure 14 (b-c)**. The measurement sensitivity has the notation $\frac{\partial \Phi}{\partial \mu}$, which represents the sensitivity of boundary measurement to change in the underlying optical property. It is also commonly known as the Jacobian $J$ [62], which will be discussed in greater detail in **Section 4.3.1.3** later. It is worth noting that the human head consists of various tissue types, which are sampled at different proportion by measurements of different source-detector distances: at shorter distance, the scalp and the skull contribute the majority of the measurement sensitivities, as shown in **Figure 14 (b);** only at sufficiently long distance does the cortex be sampled more substantially, as illustrated in **Figure 14 (c).** This implies two things in practice: first, source-detector distance should not be shorter than (typically) 2 cm in order to receive sufficient signal from the brain; and second, measurements at any source-detector distance would have signal contamination from the scalp and the skull. In *in vivo* fDOI experiments, two approaches have been commonly taken to attenuate the so-called 'superficial signals' which include respiratory waves and cardiac signals in the scalp and the skull among other sources of contamination. The first and most basic approach applies a band-pass filter (typically between 0.01 and 0.2Hz) to remove noises that are outside the specified bandwidth, such as respiratory wave (>0.2 Hz), cardiac signal (>0.5 Hz) and long-term drift (<0.01 Hz) [41, 42, 45, 46]; the second and more advanced approach makes use of

the short distance measurements like the one shown in **Figure 14 (b),** which provide a direct measure of the superficial signals in the scalp and skull. Thus it has become a standard *in vivo* practice to directly subtract the average of the short distance data (differential measurements) from all signal channel data (differential measurements) to accomplish the task of superficial signal filtering [37, 38, 45]. There also exist other sources of interference such as head motions, and as a result more sophisticated image processing techniques have been developed for noise reduction in optical signals. A comprehensive review on this topic can be found in [63].

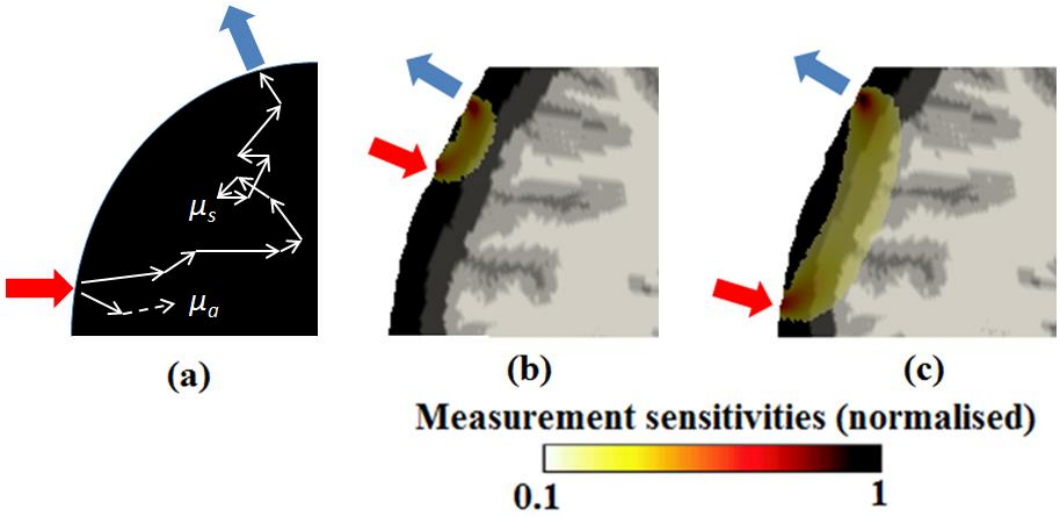


**Figure 14 (a) Schema of the optical paths of injected photons illustrating tissue absorption (dashed arrow), and scattering (solid arrow) phenomena; (b-c) Measurement sensitivities (normalised to 1) of a (b) shorter (1.3 cm) and (c) longer (4 cm) source-detector pair. The red arrow presents photons enter-in from the source, and the blue arrow presents photon exit-out to the detector.**

Depending on the 'feature' or the type of physiology information one wishes to extract, fDOI can be further categorised into 'dynamic' and 'static' techniques [27]. 'Dynamic' technique, such as diffuse correlation spectroscopy (DCS), focuses on measuring the motions of the scattering red blood cells (RBCs) in the cerebral blood flow (CBF) by looking at the fluctuation (or autocorrelation in mathematical sense) of the measurements [64-66]. 'Static'

techniques such as functional diffuse optical imaging (fDOI) on the other hand, focus on quantifying the amount of differential change in the tissue absorption between two functional states, i.e. a 'baseline state' and an 'activation state', by looking at the amplitude or phase changes of the measurements (more of these will be discussed immediately after this in **Section 3.2.1**). For the interest of this thesis we focus on the latter technique which is static (or differential) fDOI.

## 3.2 System design for fDOI

### 3.2.1 Probe type

Over the years numerous fDOI instruments have been developed. Depending on the principle of operation and the type of probe (including both source and detector probe) equipped, these systems can be categorised into three types: continuous wave (CW), time domain (TD) and frequency domain (FD) [2, 67-69], which are discussed in order below.

- **Continuous wave (CW) system**

In CW systems, the source probes (LEDs or laser diodes) emit monochromatic light of constant intensity or modulated at a low frequency (in the order of kilohertz), and the detector probes (avalanche photodiodes, also known as APDs) measure transmitted light intensity only, **Figure 15 (a-b)**. The idea on which CW systems are based is to extract the optical properties of the imaging domain by which the amplitude of light intensity gets attenuated, most commonly using the modified Beer-Lambert law to be discussed in **Section 3.3.1**.

**The advantages:** CW system hardware is inexpensive to build, the data collection and analysis is relatively straightforward to perform, and yet useful information can be extracted from CW data as demonstrated in clinical applications [1]. For these reasons, CW systems have been the most widely used and commercialised system type in the fDOI research

community. In fact the system we used across our studies as presented later in **Chapter 5-7** is a CW system [36], which reflects the mainstream approach in the community.

**The disadvantages:** First, CW measurement provides poor depth localisation capability due to its banana-shaped measurement sensitivity distribution as shown in **Figure 14** [70]. The ultra-high sensitivity near the source and the scalp surface often result in untruthfully reconstruction of a deep target at a more superficial depth, and for instance has led to the development of depth compensation algorithm [71]. Second, CW measurement from a single wavelength is unable to distinguish between the effects of tissue absorption and scattering [72]. This is because an increase in scattering would lengthen the average total path length of the exit photons, and lead to a reduction in the boundary intensity which may also appear as an increase in absorption. Third, the measured light intensity is highly sensitive to surface coupling, which can be affected by the presence of hair, local variation in skin colour and the firmness of the contact between the sources and the skin. However in the fDOI applications that we are interested in in this thesis, where the differences between two sets of measurements recorded at separate time instances are used, such unknown coupling effects can be assumed to be cancelled out [67].

**Example systems:** CW4-6 (TechEn, USA) [73], DYNOT (NIRx, USA) [74], NIRO-200NX (Hamamatsu, Japan) [75], ETG-4000 (Hitachi, Japan) [76], INVOS 5100C (Somanetics, USA) [77].

- **Time domain (TD) system**

TD systems are equipped with pulsed laser source probes that produce light pulses of picoseconds in duration, and detector probes (PMTs) that measure the temporal (or full time-of-flight) distribution of the exit photons, also known as the temporal point spread function

(TPSF). The TPSF is a delayed, broadened and attenuated version of the light pulse, and normally extends over several nanoseconds, as shown in **Figure 15 (c-d).**

**The advantages:** The lack of depth information in the CW data is resolved in the TD data, which contains the flight time of the exit photon that is proportional to the distance and depth it has travelled through the imaging medium. It has been shown that the additional temporal information available in TD data can result in improved lateral resolution and depth localisation as compared to CW data alone [78, 79]. Furthermore, knowledge of the TPSF can help discriminate between absorption and scattering effects [80]. Specifically, increasing scattering delays and broadens the TPSF, because this would cause the exit photons travel further on average. On the other hand, increasing absorption attenuates the signal intensity and steepens the trailing edge (i.e. the slope of the TPSF tail in **Figure 15 (d)**), because photons with longer path length are now more likely to be absorbed and never exit the boundary [81]. The system can also be used to measure and derive the differential pathlength (*DP*) as required for fNIRS analysis as discussed later in **Section 3.3.1** [82]**.**

**The disadvantages:** Although recent advances in pulsed laser diode and PMT hardware have significantly reduced the cost as well as system complexity of TD systems, they are still comparably more expensive than CW and FD systems and require more sophisticated analysis.

**Example systems:** TRS-20 (Hamamatsu, Japan) [83].

- **Frequency domain (FD) system**

FD systems produce continuous intensity-modulated and high-frequency (a few hundred MHz) light via a laser diode driven by a radio-frequency (RF) oscillator, and measure the reduction in modulation amplitude and phase shift of the transmitted signal via APDs, as

illustrated in **Figure 15 (e-f)**. The attenuation in amplitude is caused by tissue absorption (as in CW measurement), whereas the shift in phase is dependent on the photon pathlength.

**The advantages:** FD systems utilise largely the same source and detector probes as CW systems (thus two systems are often combined as in [84]), which are less expensive than TD systems but still capable of extracting temporal information such as measuring differential pathlength [85]. In addition, FD systems are capable of rejecting temporally uncorrelated background illumination often presented in clinical environment by the use of lock-in amplifiers [67].

**The disadvantages:** Although FD and TD measurements can be mutually translated using the Fourier (and its inverse) transform, one TD measurement contains information at all frequencies whereas one FD measurement contains information at only one frequency. Therefore FD measurements have to be taken at several modulation frequencies in order to achieve comparable amount of information to an equivalent TD measurement [2].

**Example systems:** OxiplexTS (ISS, USA) [86].

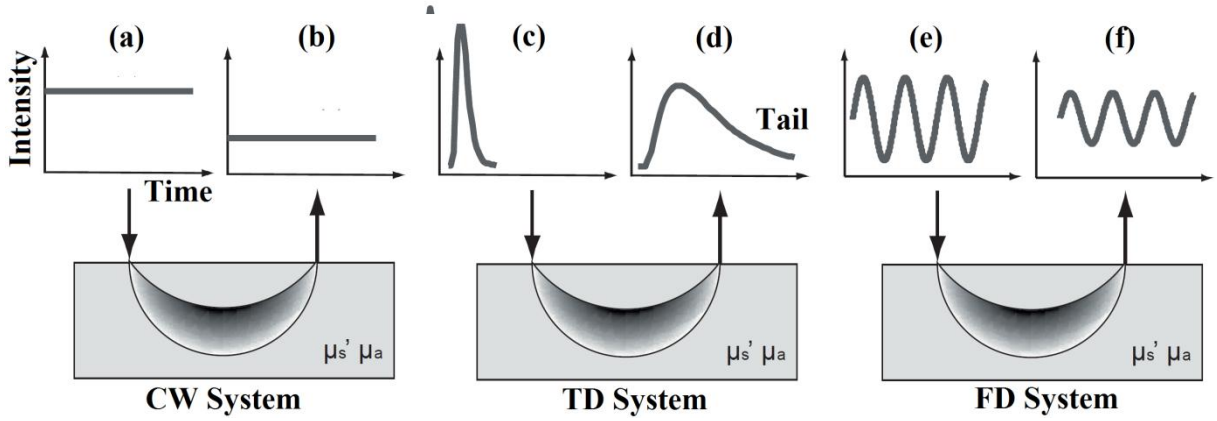


**Figure 15 Illustration of different waveforms of incident light (from source probe) and transmitted light (measured by detector probe) in CW, TD and FD system. In CW system, both (a) incident and (b) transmitted light have constant intensity; in TD system, (c) incident light pulse is injected and (d) transmitted temporal point spread function (TPSF) is recorded; in FD system, (e) incident amplitude modulated waveform and (f) transmitted waveform representing intensity reduction and phase shift from (e) [2].**

### 3.2.2 Probe arrangement

Another aspect of fDOI system design is the arrangement of imaging probes (both sources and detectors), which has been found to have significant effect on image quality [5, 6]. The arrangement of the probes has been largely related to the number of probes equipped in the system, which is dependent on the data acquisition capabilities (memory and speed) of the hardware. Over the years continuous technological advancement has allowed the single source-detector configuration of the early days to evolve into the sparsely-arranged imaging arrays that contain multiple source-detector pairs, and further into the high-density imaging arrays that have been popularised in recent years. This evolution also affects the imaging mode that can be operated in fDOI studies, from fNIRS to fDOT with increasing computational complexity, as discussed next in **Section 3.3**. Here we review three types of probe arrangement that have been frequently mentioned in previous literature.

- **Square sparse imaging array**

A square sparse imaging array arranges source and detector probes in square patterns where each ‘square’ has two sources and detectors facing each other diagonally, **Figure 16 (a)**. This geometry has been commonly used in topographic fDOI, including visual pattern study of awake infants [87], and visual word recognition study of adults [88]. In these studies, the recovered chromophore concentrations are directly displayed or interpolated on the subject’s scalp surface, providing spatial information that does not exceed the inter-probe distance, which are 2 cm [87] and 3 cm [88]. White et al. [5] further demonstrated that the resolution of this array, even at tomographic mode, is almost equal to its inter-probe distance (3 cm).

- **Triangular sparse imaging array**

A triangular sparse imaging array characterises an arrangement where one array of sources aligns between two arrays of detectors, **Figure 16 (b)**. This has proven to be one of the most widely used configurations in the fDOI community, with typical source-detector distance of 3 cm, and inter-source (detector) distance ranging from 1.84 to 2.6 cm [4, 5, 32, 43, 46, 89]. Again image quality analysis has shown that its resolution does not go beyond the 3 cm source-detector distance limit [5].

- **High-density imaging array**

High-density imaging arrays have been utilised more recently than those sparse imaging arrays owing to faster and larger data acquisition capability of the imaging system. This arrangement effectively stacks multiple triangular sparse imaging arrays at shorter inter-probe spacing to create high-density coverage of the underlying region. A major advantage of this configuration is the possibility of utilising overlapping measurements that allows a more uniform, comprehensive and potentially deeper sampling of the underlying brain tissue. The

probe arrangement chosen in our works as presented later in **Chapter 5-7** is a high-density imaging array consisting of 24 sources and 28 detectors as shown in **Figure 16 (c)**. This array has been previously tested in *in vivo* visual cortical mapping studies [36-38] and evaluated in simulation studies [5, 6] in fDOT, and demonstrated a level of image quality that was inaccessible with sparse imaging arrays. For systematic management of overlapping measurements, the concept of '$n^{th}$ nearest neighbour' has been introduced. Under this configuration, the first, second and third nearest neighbour measurements for a given source are defined for all detectors as 1.3 cm, 3 cm and 4 cm distances away from it, respectively as shown in **Figure 16 (d)**. This gives rise to a total of 84, 128, and 48 first, second and third nearest neighbour measurements respectively.

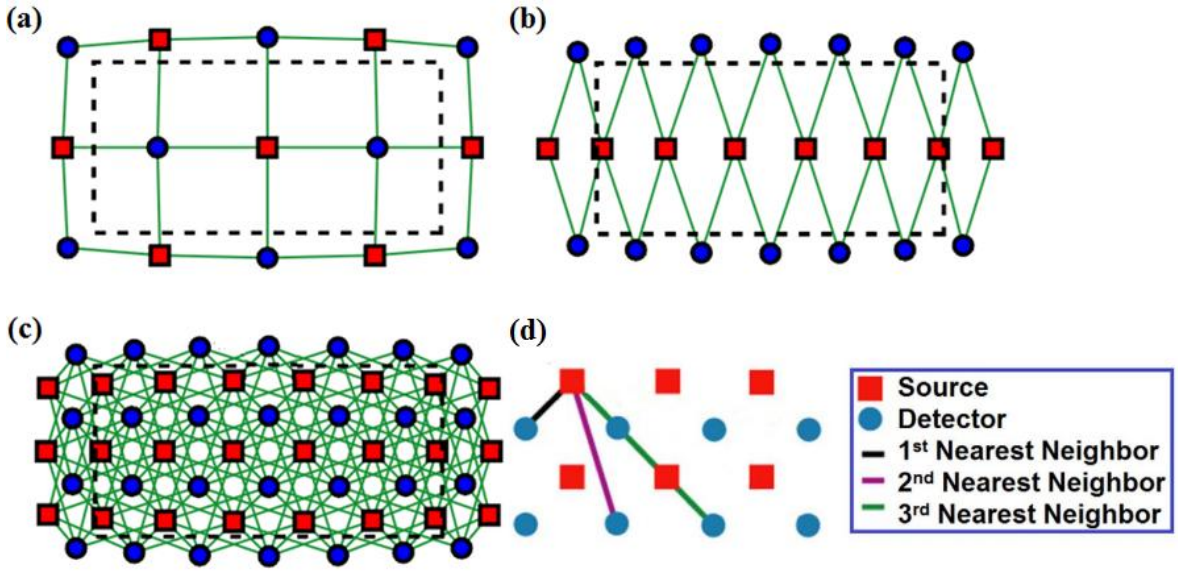


**Figure 16 Schematic (sources are red squares, detectors are blue circles) of: (a) square sparse imaging array; (b) triangular sparse imaging array; (c) high-density imaging array [5]; (d) first to third nearest neighbour measurements defined by source-detector distance of 1.3, 3, 4 cm respectively under the configuration in (c).**

## 3.3 Imaging mode of fDOI

As mentioned previously, the phrase ‘functional diffuse optical imaging’ (‘fDOI’) actually refers more to an imaging category than a specific imaging technique. In fact the more frequently appearing phrases (or words) in the literature are functional near infrared spectroscopy (fNIRS), functional diffuse optical topography, and functional diffuse optical tomography (fDOT), which we regard as three different imaging modes (and techniques) under fDOI. For instance, the first fDOI study which was performed by Jobsis to measure blood and tissue oxygenation in a cat brain [90], was conducted in the spectroscopic mode, or fNIRS. The more sophisticated topographic and tomographic modes were only realised later when more advanced fDOI instruments, powerful computers and enhanced software solutions became available. Below we review each of these techniques in greater detail.

### 3.3.1 Spectroscopic mode: functional near infrared spectroscopy (fNIRS)

fNIRS is the simplest of the three modes, which only requires single source-detector probe configuration, and returns quantitative numbers regarding the global change of the underlying tissue absorption, but no image or spatial information can be revealed. This is based on the so-called modified Beer-Lambert law of the following form [82, 91]:

$$A = \log\left(\frac{\Phi_0}{\Phi}\right) = DP \cdot \mu_a + G \tag{1.1}$$

which states that the total attenuation $A$ of incident $\Phi_0$ and transmitted $\Phi$ light is the sum of attenuation due to absorption $DP \cdot \mu_a$ and due to scattering $G$. Both $\Phi_0$ and $\Phi$ are light intensity (or fluence rate), which can be detected using a CW or FD system. $DP$ is the distance travelled by the light from the emitting source to the receiving detector known as the differential pathlength and can be obtained from a TD or FD system. For computational

convenience, literature [82] has related *DP* to the straight-line distance *r* between the source and the detector by publishing the so-called 'differential pathlength factor' (*DPF*), defined as $DPF = DP / r$ . *DPF* is wavelength-dependent and values have often been reported at several discrete wavelengths in the literature. In general it was found that the neonatal head on average has a lower *DPF* than adult's, which is attributed to its lower scattering coefficient [85].

In the context of functional neuroimaging, where we are concerned with changes rather than absolute values of tissue absorption, we have:

$$\Delta A = DP \cdot \Delta \mu_a + \Delta G \tag{1.2}$$

Assuming attenuation due to change in scattering is negligible, i.e. $\Delta G = 0$, we arrive at the equation:

$$\Delta \mu_a = DP / \Delta A \tag{1.3}$$

Moreover, since the primary interest of functional neuroimaging are changes in oxyhaemoglobin ($\Delta HbO_2$) and deoxyhaemoglobin ($\Delta HbR$) concentration rather than absorption, a further 'spectral decomposition' step is required. Although the main absorbing chromophores of NIR in tissue are $HbO_2$, HbR, water and lipid (**Figure 17**), only the concentrations of the two haemoglobins are assumed to be variable during neuronal activities, or at least are the main contributors of the signal change. Thus the change in absorption is expressed as a linear summation of $\Delta HbO_2$ and $\Delta HbR$:

$$\Delta \mu_a(\lambda) = \varepsilon_{HbO_2}(\lambda) \cdot \Delta HbO_2 + \varepsilon_{HbR}(\lambda) \cdot \Delta HbR \tag{1.4}$$

where $\varepsilon$ is the molar extinction coefficient. Since $\varepsilon_{HbO_2}$ and $\varepsilon_{HbR}$ have distinct molar extinction coefficients in the NIR spectrum (**Figure 17**), measurements at two wavelengths

are typically sufficient to recover the changes in the concentration of both chromophores [4]. In the case of a dual-wavelength system, **Equation (1.4)** can be rewritten in matrix form [65]:

$$\begin{bmatrix} \Delta\mu_a(\lambda_1) \\ \Delta\mu_a(\lambda_2) \end{bmatrix} = \begin{bmatrix} \varepsilon_{HbO_2}(\lambda_1) & \varepsilon_{HbR}(\lambda_1) \\ \varepsilon_{HbO_2}(\lambda_2) & \varepsilon_{HbR}(\lambda_2) \end{bmatrix} \cdot \begin{bmatrix} \Delta HbO_2 \\ \Delta HbR \end{bmatrix} = M_S \cdot \begin{bmatrix} \Delta HbO_2 \\ \Delta HbR \end{bmatrix} \tag{1.5}$$

where the matrix $M_S$ is also referred as the 'spectral prior' to be discussed later in **Section 4.3.3**. Thus the recovery of chromophore concentrations from absorption is a simple matrix inversion of $M_S$:

$$\begin{bmatrix} \Delta HbO_2 \\ \Delta HbR \end{bmatrix} = M_S^{-1} \cdot \begin{bmatrix} \Delta\mu_a(\lambda_1) \\ \Delta\mu_a(\lambda_2) \end{bmatrix} \tag{1.6}$$

In fact most existing fDOI systems including those mentioned in **Section 3.2.1** are dual-wavelength systems, for example the CW4 and CW5 (690 and 830 nm) [14, 46, 92], Hitachi ETG-4000 (695 and 830 nm) [88], the DYNOT (760 and 830 nm) [41, 46, 93], Hitachi Medical NIR OT instrument (780 and 830 nm) [87], as well as the high-density-DOT imaging system at Washington University School of Medicine (750 and 850 nm) [36, 37, 45, 94] that we are modelling in this thesis.

In addition it is worth mentioning that all these systems select one wavelength from each (left or right hand) side of the intersection point at about 795 nm (blue dot in **Figure 17**), i.e. one wavelength is longer and the other is shorter than 795 nm. This is to ensure the contribution from each of the two chromphores (i.e. $HbO_2$ and HbR) to both wavelength measurements is as equal (or similar) as possible. Within the concept of wavelength optimisation theory [8], such wavelength selection would result in a much smaller condition number of matrix $M_S$ than if both wavelengths are longer or shorter than 795 nm.

The advantage of fNIRS lies in its computational simplicity, i.e. no anatomical model of the imaging domain is required while quantitative $\Delta HbO_2$ and $\Delta HbR$ are obtainable. Although such quantification is rather 'global' with no spatial information included, it has proven to be sufficiently useful in neuroscience research.

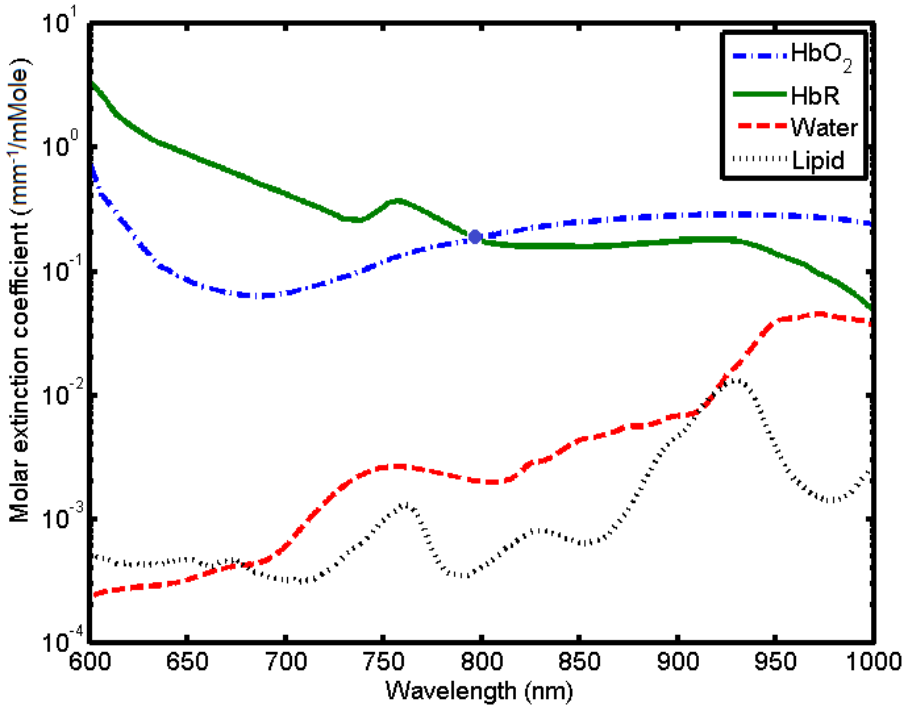


**Figure 17 Molar extinction coefficient (in $mm^{-1}$/mMole) for oxyhaemoglobin ($HbO_2$), deoxyhaemoglobin (HbR), water and lipid in the NIR spectrum [95, 96].**

### 3.3.2 Topographic mode: functional diffuse optical topography

Functional diffuse optical topography is more advanced than fNIRS in the sense that two-dimensional (2D) projection images are obtained, therefore providing lateral spatial information. This mode utilises multiple but non-overlapping measurements to be taken from an imaging array such as the ones descried in **Figure 16**, from which 'global' $\Delta HbO_2$ and $\Delta HbR$ values can be computed for each channel using fNIRS (here a channel refers to a measurement taken from a specific source-detector pair). For this reason, the topographic mode is also known as multichannel-fNIRS [87]. Given the known or approximated position

of sources and detectors, and consequently of the channels (the position of a channel is normally approximated as the half-way point between the source-detector pair), these global values can be spatially interpolated and projected onto a 2D plane that is parallel to the scalp surface. However such linear interpolation procedures limit the spatial resolution of diffuse optical topography to no better than the nearest source-detector distance, which is typically no less than 2 cm. This is because the detector needs to be placed at sufficient distance away from the source in order to receive photons that have propagated deep enough to sample the brain tissue as already illustrated in **Figure 14**.

### 3.3.3 Tomographic mode: functional diffuse optical tomography (fDOT)

fDOT is the most advanced imaging mode of fDOI, which utilises more rigorous mathematical models to describe light propagation in human tissue than the modified Beer-Lambert law as expressed by **Equation (1.1)**. It also requires a three-dimensional (3D) anatomical model of the underlying imaging domain. There are a number of other modelling issues surrounding fDOT which will be covered extensively in the next chapter. In return for such computational complexity, fDOT allows 3D volumetric optical and functional data of the imaging domain to be recovered at higher lateral and depth resolution than in fNIRS and topographic mode. Although there is no minimum requirement for the number of probes or probe arrangement, it is always desirable to utilise a high-density probe configuration and overlapping measurements to further improve the image quality [5, 97]. In our works as presented in **Chapter 5-7**, the high-density imaging array is used together with the tomographic imaging mode to achieve the most optimised image quality possible.

## 3.4 Image quality analysis of fDOI

A crucial objective (if not the ultimate goal) for the development of an emerging imaging technology is its widespread acceptance and establishment as a reliable imaging tool in the clinical research community. To do that, the clinicians or users must acquire sufficient knowledge regarding the achievable image quality of the technique in order to make judgement on whether images obtained from such technique can reveal clinically meaningful information. Image quality analysis therefore plays an important role as it provides both qualitative and quantitative information regarding the image quality of the underlying technique, and therefore directly helps the clinicians to make the judgement.

Based on our literature research, image quality analyses of fDOI have been mainly conducted in tomographic mode or fDOT. This is understandable since fNIRS does not produce an image, and while topographic fDOI does, its 2D topographic image has unquantifiable depth accuracy and lateral resolution that is known to be no better than the nearest source-detector distance (as discussed in **Section 3.3.2**). Furthermore since our main interest in this thesis is fDOT, our review on image quality analysis in this section has been limited to fDOT studies only. From these studies we have summarised previous image quality analyses into two categories: experiment-based analysis in which the results are evaluated against images obtained from another imaging modality (often the 'gold standard' in the field), or simulation-based analysis in which the results are evaluated against simulated known targets, or the 'ground truth'. Here we review selected examples from both categories.

### 3.4.1 Experiment-based analysis

To date, the number of experiment-based image quality analysis studies of fDOT have been limited, due to the demanding requirement for a multi-modal imaging system or procedure

that allows simultaneous data recording by at least two different imaging modalities (one being fDOT) of the same subject in order to make a fair comparative evaluation. Recent literature has reflected on fDOT-fMRI as the mainstream dual-modality approach, which include studies of human motor [45, 98], somatosensory [42] and visual system [38, 45]. In one of our publications on visual cortical mapping [38], we reported an average centre-of-mass localisation error of 5±1 mm between fDOT and fMRI, which is within the size of a gyral ridge. Another study on the somatosensory cortex [42], as shown in **Figure 18**, demonstrated qualitatively similar activation patterns between fDOT and fMRI, and also observed less than 10 mm lateral localisation error between the two modalities in seven out of ten subjects. These results have demonstrated gyral specificity in fDOT technique, which provides sufficient image quality to be useful as a surrogate for fMRI in both clinical and basic neuroscience study. The continuous advancement in multi-modal fDOT imaging system development should also encourage more frequent experiment-based image quality analysis studies of fDOT to be conducted in future.

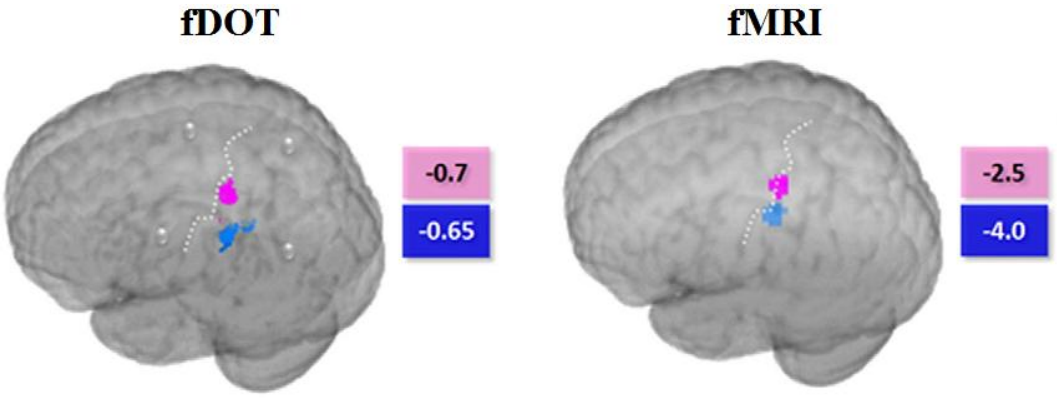


**Figure 18 fDOT and fMRI activation map (t-map) of a subject performing 1st finger tapping (pink) and 5th finger tapping (blue) [42]. The t-value provides a measure of the significance of the change (or difference) between one set of data (HbR data in fDOT, or BOLD data in fMRI) measured during a baseline state (when no finger tapping is performed) and another dataset obtained during an activation state (when finger tapping is performed). The value is calculated using the t-test which takes the standard deviation of each dataset into account. The negative t-values shown in the graph indicate negative ΔHbR, or decrease in HbR concentration from baseline to activation state.**

### 3.4.2 Simulation-based analysis

Simulation-based image quality analysis of fDOT can be further divided into point-based analysis and region-based analysis, which have their respective advantages. In the point-based approach, a 'single-pixel' activation (or perturbation) is simulated and then reconstructed within a defined region of interest (ROI), which is often the field of view (FOV) of the imaging array, as shown in **Figure 19**. Since the reconstructed image for a given perturbation is also known as the point spread function (PSF) of that perturbation, this analysis has also been referred to as the PSF analysis in the literature [5]. The main advantage of the PSF analysis is that it allows the theoretical 'image resolution', namely the area or volume per single pixel, to be quantified and displayed across the entire imaging system FOV, along with localisation accuracy, as shown in **Figure 20**. Specifically in [5], White et al. conducted comparative PSF analysis between the sparse and high-density imaging arrays as mentioned

in **Section 3.2.2**, and demonstrated dramatic improvement in image quality. Quantitatively speaking there is a five-fold improvement in localisation accuracy, where localisation error reduced from 5.3±2.0 mm (square sparse) and 5.3±2.0 mm (triangular sparse) to 1.0±0.9 mm (high density), and two-fold improvement in lateral resolution, where FVHM reduced from 21.6±4.6 mm (square sparse) and 20.9±4.3 mm (triangular sparse) to 12.1±1.4 mm (high density) [5]. Nevertheless this study has several limitations: the PSF analysis was performed on a simplified head geometry of spherical shape where the FOV was a smooth 2D plane representing a simplified version of the cortical surface. In addition, the data used for image reconstruction were noise-free. Therefore in order to provide more realistic image quality evaluation, we have extended the PSF analysis to anatomically more accurate subject-specific head geometries with a realistic level of noise added to the data, to be presented in **Chapter 5 and 6**.

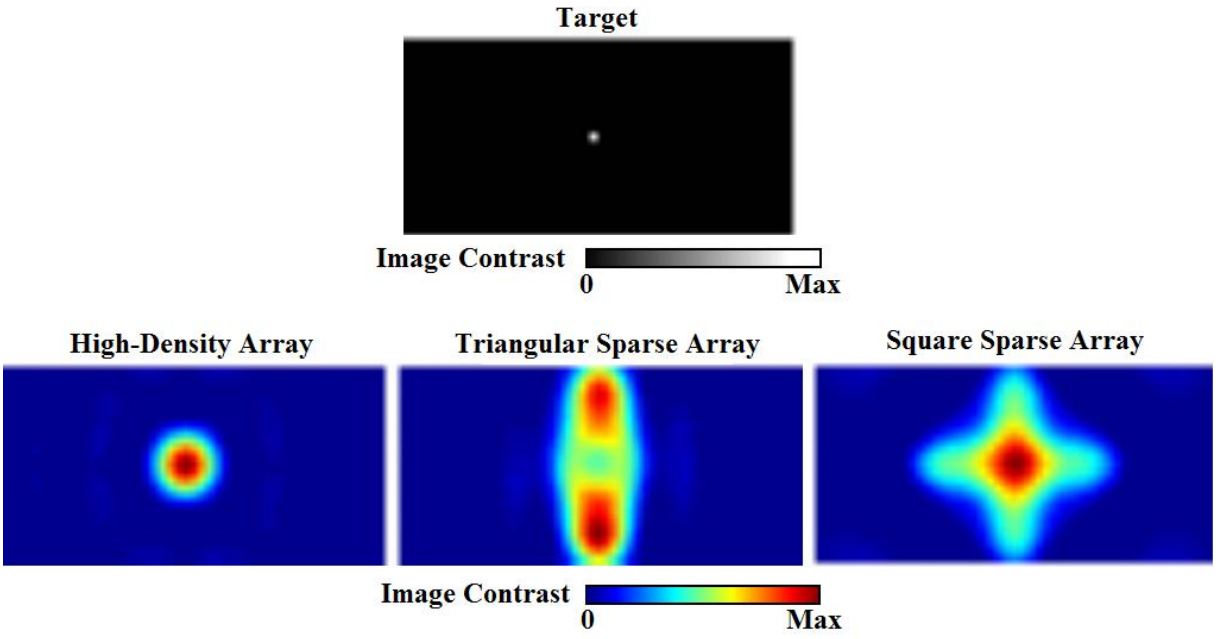


**Figure 19 A simulated target point activation (perturbation) and its reconstructed point spread function using the sparse and high-density image arrays as mentioned in Section 3.2.2, displayed on a 2D topographic plane within a defined field of view (FOV) [5].**

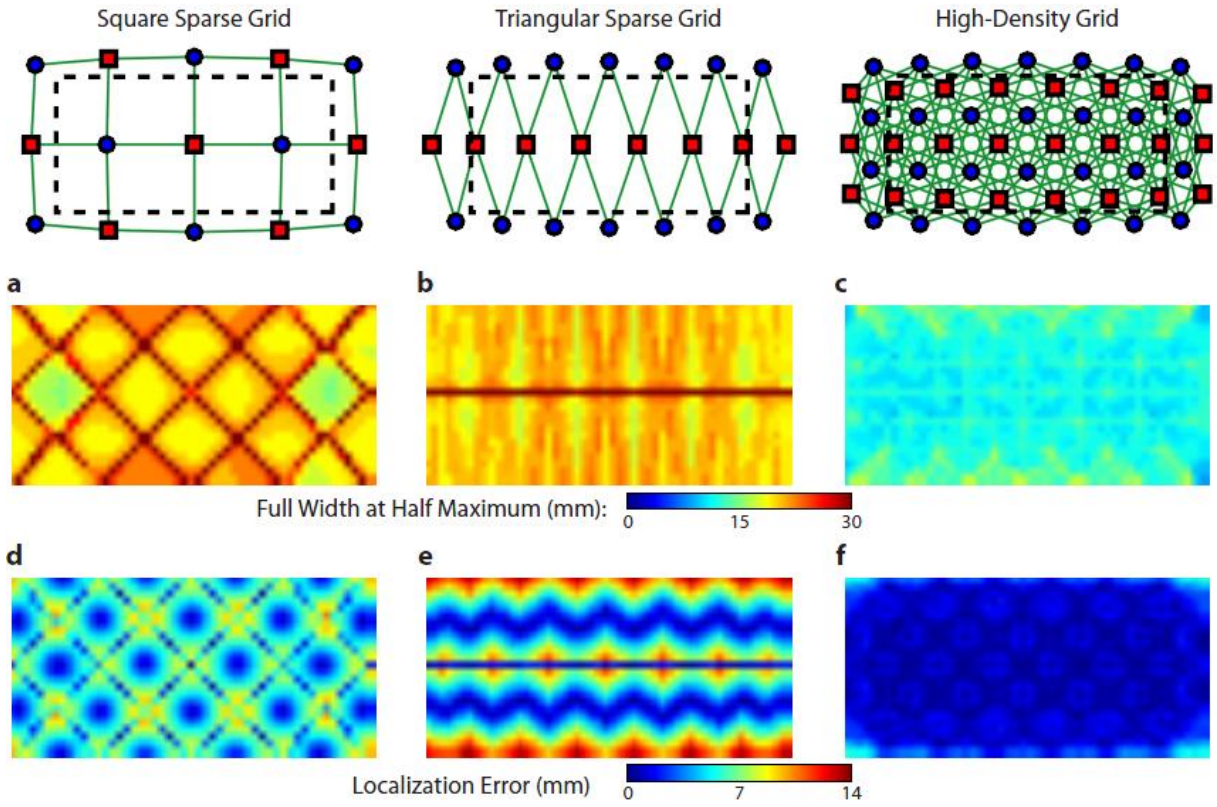


**Figure 20 Top row: schema (source as red square, detector as blue circle) of the three different probe arrangements as previously discussed in Section 3.2.2 (left to right): square sparse imaging array, triangular sparse imaging array and high-density imaging array; middle row: full-width half max (FVHM) map on the FOV of the three imaging arrays, where FWHM is a metric to measure lateral resolution; bottom row: localisation error map on the FOV of the three imaging arrays, where localisation error is a metric to measure localisation accuracy [5].**

The region-based approach on the other hand, serves as an intermediary approach between *in silico* PSF analysis and *in vivo* experiment-based approach. In this case, regional activations are simulated in order to mimic neuronal activation patterns observed in *in vivo* experiments. Consequently the reconstructed images are also expected to be similar to those obtained from *in vivo* experiments, but have the additional advantage of knowing the exact 'ground truth', namely the simulated regional activations. This allows not only the quantification of localisation accuracy and image resolution, but also imaging contrast [6, 7, 70]. For instance,

the results shown in **Figure 21** as presented by Heiskala et al. quantified a localisation error of 2.7 mm and peak contrast of 64% for the activation on the left, and a localisation error of 2.2 mm and peak contrast of 73.3% for the activation on the right, demonstrating good localisation accuracy at slightly compromised imaging contrast [6]. However there are also limitations associated with this approach. First of all it can be difficult to simulate regional activations that are rightly justifiable as 'similar to actual activations observed at *in vivo* experiments', especially on realistically segmented head models. This is because the brain activations to be imaged (at least within fDOI applications) only occur at the grey matter (or cerebral cortex), which is the outermost sheet of the brain that has a thin, complex and layered geometry, as shown later in **Figure 29-30** in **Chapter 5**. The 'blobs' as presented in **Figure 21** however are spheres of 4.3 mm in radius and the existence of such activations in *in vivo* studies can be arguable. Moreover, this would add further difficulty if one seeks to extend the region-based approach across the entire system FOV as in the point-based approach. Thus region-based image quality analyses are often presented with limited cases and scenarios for 'proof of concept' rather than provide a comprehensive description of image quality across the entire FOV. In **Chapter 7** where we present our novel regularisation technique, we have taken the region-based approach for our 'proof of concept' analysis.

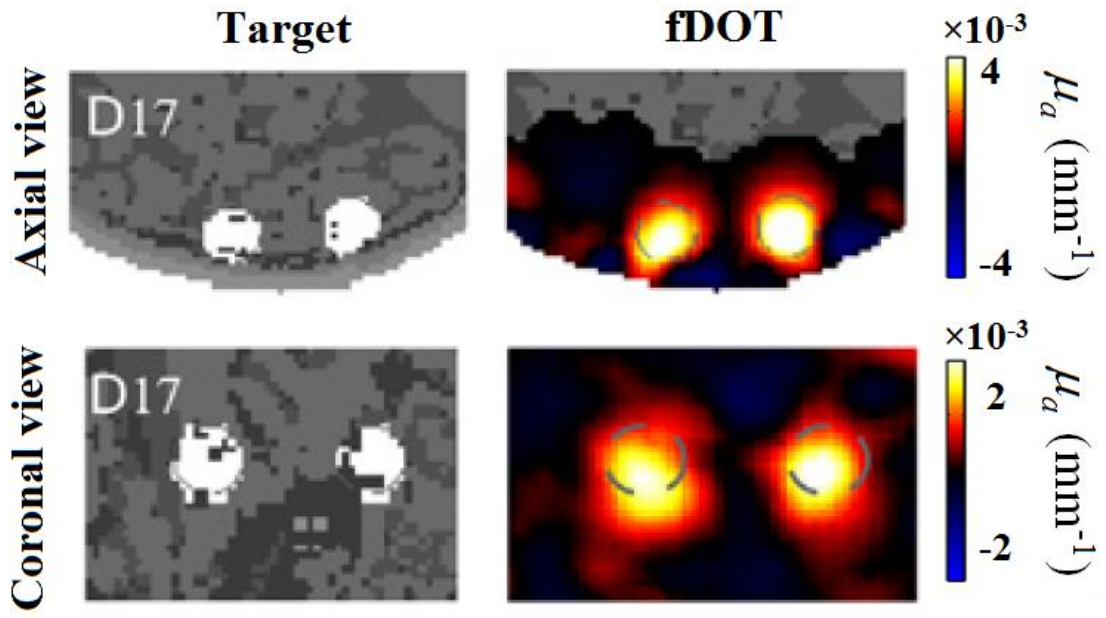


**Figure 21 A pair of simulated spherical activations (left column) of 4.3 mm in radius and 17.3 mm (centre-to-centre distance) apart with $\Delta\mu_a$ =8×10$^{-3}$ mm$^{-1}$ and their fDOT reconstructed images (right column) [7].**

### 3.5 Summary

In comparison with **Chapter 2** where we reviewed functional neuroimaging in a general and broad context, this chapter has provided a focused background review on optics-based neuroimaging techniques, namely functional diffuse optical imaging (fDOI). We started by describing the working principle of fDOI, which involves injecting photons into the human head, and measuring exit photons that are encoded with optical and functional information regarding the brain. Because photon propagation in head tissues is predominantly characterised by the physical phenomena of scattering and absorption, the primary parameters of optical properties are the scattering coefficient $\mu_s$ and the absorption coefficient $\mu_a$. We next reviewed fDOI instrumentation in terms of probe type and arrangement, and highlighted the cost-efficiency and wide-commercialisation of CW systems as well as the improved sampling coverage of the high-density imaging array. Building from these, we introduced

three different imaging modes of fDOI in the order of increasingly instrumental and computational complexity, namely spectroscopic mode (fNIRS), topographic mode (functional diffuse optical topography), and tomographic mode (fDOT). While in multichannel-fNIRS or topographic mode, 2D projection images with limited lateral spatial and unquantifiable depth information can be achieved with the use of modified Beer-Lambert law and linear interpolation, we highlighted the capability of reconstructing three-dimensional (3D) volumetric images with improved lateral resolution and depth localisation when operating in the tomographic mode. All of these have provided the justification for the approach we are taking in our work, namely utilising a high-density, CW imaging system and performing tomographic image reconstruction, as presented later in **Chapter 5-7**. However before we reach there, the workflow of fDOT needs to be introduced and comprehensively explained, as detailed in the next chapter.

# CHAPTER 4

# MODELLING IN fDOT

## 4.1 Workflow of fDOT

In the previous chapter we have reviewed the principles behind fNIRS and functional diffuse optical topography, which suffered from limited image resolution and non-quantified depth information. This chapter focuses on a more advanced fDOI mode or technique known as functional diffuse optical tomography (fDOT), which allows three-dimensional (3D) volumetric images to be reconstructed at improved image resolution and depth localisation, owing to the utilisation of more complex modelling theories and tools. To help illustrate various modelling issues arising at different stages of a standard fDOT workflow and understanding their relationship to each other, a block diagram that describes the fDOT modelling workflow is drawn below in **Figure 22**. A feature of this diagram is that each modelling issue to be discussed in a later section in this chapter is represented by a block in the workflow with the corresponding section number enclosed, thereby providing a more organised overview to the reader. As shown in **Figure 22**, these blocks can be grouped into three larger (red) blocks, namely ‘experiment’, ‘forward problem’ and ‘inverse problem’. As we have covered the ‘experiment’ part in the last chapter, this chapter focuses on the ‘forward and inverse problem’. It is also worth mentioning that this schema should be applicable to any imaging problems in general, which can be described as follows: Given a set of measurements $y$ taken during an experiment from an imaging domain of properties $x$, the forward problem

derives $y$ from $x$ via a forward operator $f$ in the form of $y = f(x)$, and the inverse problem recovers the properties $x$ from measurements $y$ in the form of $x = f^{-1}(y)$ [99]. From the modelling perspective, there are three types of models involved in the forward problem, namely the mathematical forward model, the anatomical model, and the computational model that implements the forward problem. These are discussed in order in **Section 4.2**. With regard to the inverse problem, there are also three models that we would like to discuss within the scope of this thesis, namely the mathematical inverse problem, and inclusions of structural prior and spectral prior, to be described in **Section 4.3**.

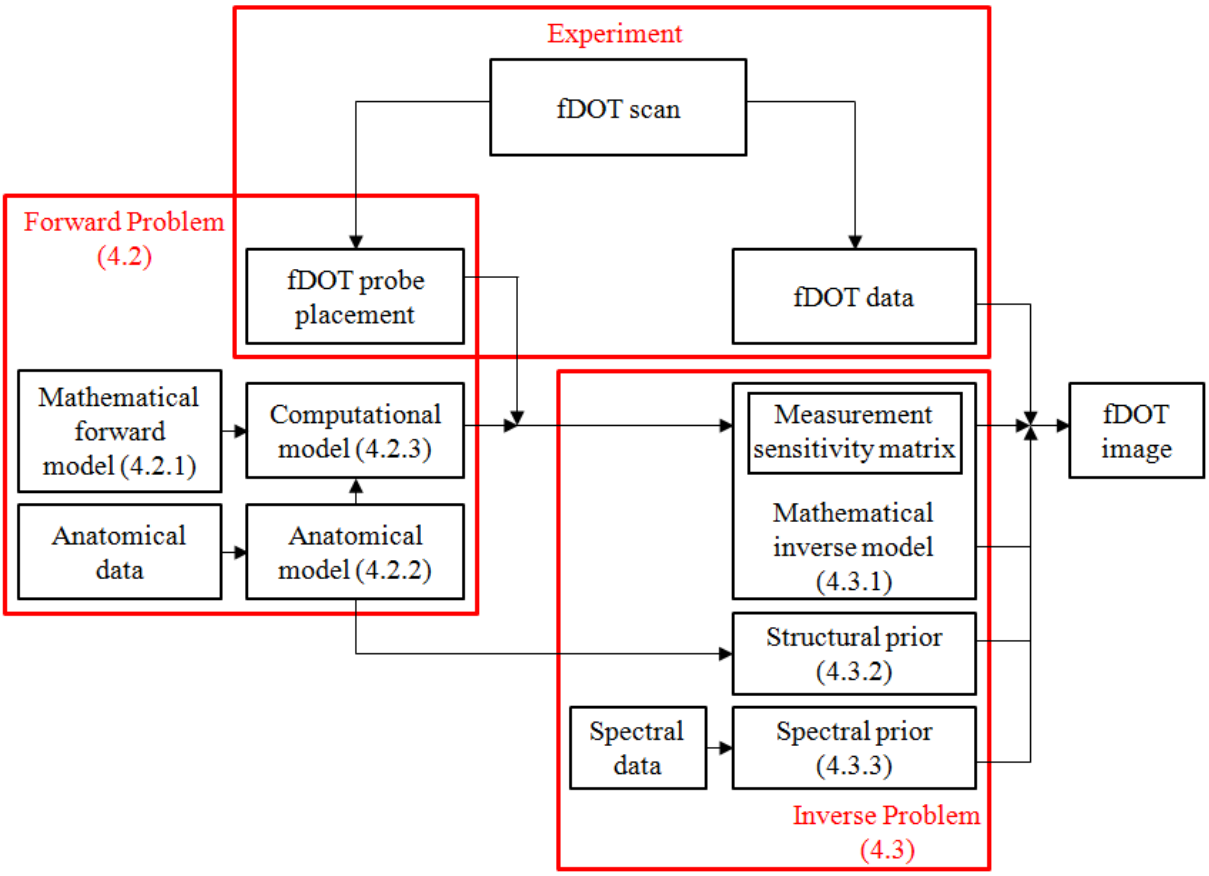


**Figure 22 The fDOT modelling workflow.**

## 4.2 The forward problem

### 4.2.1 The mathematical model

In the previous chapter we have seen the use of the modified Beer-Lambert law in fNIRS as well as in topographic mode, which is a relatively simple and fast mathematical model for functional diffuse optical imaging but results in limited image resolution and non-quantified depth information. In this section we introduce two more complex mathematical forward models that have been used to recover 3D volumetric images in tomographic mode, namely the radiative transfer equation (RTE), and a more computationally efficient approximation (first spherical harmonic expansion) of the RTE known as the diffuse approximation (DA) at the expense of the requirement for certain assumptions.

#### 4.2.1.1 Radiative transfer equation

The radiative transfer equation (RTE) is a mathematical model to describe the conservation of energy at a position $\vec{r}$ in direction $\vec{e}_s$ at time *t* in the medium [62]:

$$\begin{aligned} &\frac{1}{c}\frac{\partial L}{\partial t} + \vec{e}_s \cdot \nabla L(\vec{r},t,\vec{e}_s) + (\mu_a + \mu_s) L(\vec{r},t,\vec{e}_s) \\ &= \mu_s \int_{4\pi} f(\vec{e}_s,\vec{e}_{s'}) L(\vec{r},t,\vec{e}_{s'}) d^2\vec{e}_{s'} + q(\vec{r},t,\vec{e}_s) \end{aligned} \tag{1.7}$$

where $L(\vec{r},t,\vec{e}_s)$ is the energy radiance at position $\vec{r}$ in direction $\vec{e}_s$ at time *t*; *c* is the speed of light in the medium; $\mu_s$ and $\mu_a$ are the scattering and absorption coefficients respectively as introduced in the previous chapter; $f(\vec{e}_s,\vec{e}_{s'})$ is the single scattering phase function which describes the probability density of a photon scattering from direction $\vec{e}_{s'}$ into direction $\vec{e}_s$; $q(\vec{r},t,\vec{e}_s)$ is the light source. The first term represents change of energy radiance with time, the second term represents change of radiance due to energy flow, the third term represents

radiance loss due to absorption and scattering, the fourth term represents radiance gain due to scattering from direction $\vec{e}_{s'}$ into direction $\vec{e}_s$, and the final term represents radiance due to a source. Note that these terms are also wavelength dependent and the equation here assumes monochromatic light at a given wavelength. This is a conservation equation which describes the loss of radiance due to absorption and scattering, and its gain due to scattering and the source. Although the RTE does not model wave effects, it is generally sufficient for modelling light propagation in the context of diffuse optical imaging, where the wavelength of NIR light (650nm to 950nm) is much smaller than the imaging object.

#### 4.2.1.2 Diffusion approximation

Solving the RTE is computationally expensive and not favorable for numerical modelling. The standard approach to simplify the RTE is to express $L(\vec{r},t,\vec{e}_s)$ in its first spherical harmonics $P_1$ approximation. Specifically:

$$L(\vec{r},t,\vec{e}_s) = \frac{1}{4\pi}\Phi(\vec{r},t) + \frac{3}{4\pi}\vec{J}(\vec{r},t)\cdot\vec{e}_s \tag{1.8}$$

where $\Phi(\vec{r},t)$ is the fluence rate (or photon density), and $\vec{J}(\vec{r},t)$ is the flux (or photon current), in the following forms:

$$\Phi(\vec{r},t) = \int_{4\pi} L(\vec{r},t,\vec{e}_s)d^2\vec{e}_s \tag{1.9}$$

$$\vec{J}(\vec{r},t) = \int_{4\pi} L(\vec{r},t,\vec{e}_s)\cdot\vec{e}_s d^2\vec{e}_s \tag{1.10}$$

Similarly the $P_1$ approximation for $q(\vec{r},t,\vec{e}_s)$ is:

$$q(\vec{r},t,\vec{e}_s) = \frac{1}{4\pi}q_o(\vec{r},t) + \frac{3}{4\pi}q_1(\vec{r},t)\cdot\vec{e}_s \tag{1.11}$$

where $q_o(\vec{r},t)$ is an isotropic source of photons, and $q_1(\vec{r},t)$ is a linearly anisotropic source.

Substituting **Equation (1.8)** and **(1.11)** into **(1.7)**:

$$\begin{aligned}&\left(\frac{1}{c}\frac{\partial}{\partial t}+\vec{e}_s\cdot\nabla+\mu_a+\mu_s\right)\left(\Phi(\vec{r},t)+3\vec{J}(\vec{r},t)\cdot\vec{e}_s\right)\\&=\mu_s\int_{4\pi} f(\vec{e}_s,\vec{e}_{s'})\left(\Phi(\vec{r},t)+3\vec{J}(\vec{r},t)\cdot\vec{e}_s\right)d^2\vec{e}_{s'}+q_0(\vec{r},t)+3q_1(\vec{r},t)\cdot\vec{e}_s\end{aligned}\tag{1.12}$$

Integrating **Equation (1.12)** over $\vec{e}_s$ arrives at the continuity equation:

$$\frac{1}{c}\frac{\partial\Phi}{\partial t}+\nabla\cdot\vec{J}(\vec{r},t)+\mu_a\Phi(\vec{r},t)=q_0(\vec{r},t)\tag{1.13}$$

Multiplying **Equation (1.12)** by $\vec{e}_s$ and integrating over $\vec{e}_s$ gives another equation:

$$\left(\frac{1}{c}\frac{\partial}{\partial t}+\mu_a+(1-g)\mu_s\right)\vec{J}(\vec{r},t)+\frac{1}{3}\nabla\Phi(\vec{r},t)=q_1(\vec{r},t)\tag{1.14}$$

where $g$ is average cosine of the scattering angle. $\mu_s'=(1-g)\mu_s$ is also referred to as the reduced scattering coefficient. Assuming an isotropic source:

$$q_1(\vec{r},t)=0\tag{1.15}$$

And also:

$$\frac{1}{c}\frac{\partial\vec{J}(\vec{r},t)}{\partial t}\ll\left(\mu_a+\mu_s'\right)\vec{J}(\vec{r},t)\tag{1.16}$$

Letting:

$$D=\frac{1}{3\left(\mu_a+\mu_s'\right)}\tag{1.17}$$

where $D$ is also known as the diffusion coefficient, we have Fick's law:

$$\vec{J}(\vec{r},t)=-D\nabla\Phi(\vec{r},t)\tag{1.18}$$

Substituting **Equation (1.18)** into **(1.13)** arrives at the diffuse approximation (DA) equation:

$$\frac{1}{c}\frac{\partial\Phi(\vec{r},t)}{\partial t} - \nabla \cdot D\nabla\Phi(\vec{r},t) + \mu_a\Phi(\vec{r},t) = q_0(\vec{r},t) \quad (1.19)$$

Numerical and experimental results [100, 101] have demonstrated the validity of the DA under the condition that $\mu_s' >> \mu_a$, which limits its application to highly scattering mediums only, such as most human tissues. However in the application of functional neuroimaging there exists a 2-4 mm [102] thin non-scattering or low scattering layer known as the cerebral spinal fluid (CSF), which occupies the region between the skull and grey matter. While earlier literature proposed more complex hybrid models such as the hybrid radiosity-DA model [103, 104] and hybrid RTE-DA [105] model to deal with the presence of such local and non-scattering region in a largely high-scattering domain, more recent simulations [106, 107] and experimental studies [38] explored the idea of setting the CSF $\mu_s'$ to any value between zero and the inverse of the CSF layer thickness ($1/\text{thickness}_{CSF}$ = 0.3 $mm^{-1}$ approximately) under the DA model. Their results suggested that such an approach, although possibly not sound in principle, could provide a sufficiently accurate approximation for fDOT applications.

### 4.2.2 The anatomical model

Another aspect of modelling in the fDOT forward problem is the anatomical model of the underlying imaging domain, i.e. the human head. Such model incorporates the spatial distribution of different anatomical regions that are characterised by their distinctive optical properties $\mu$. This in turn affects the spatial distribution of the measurement sensitivity, denoted by $\frac{\partial\Phi}{\partial\mu}$, which is also known as the Jacobian *J*. Since the Jacobian *J* is used directly for image reconstruction as discussed later in **Section 4.3**, the accuracy of the anatomical model therefore has a direct impact on the image quality of the reconstructed fDOT images. Furthermore knowing the anatomical information would allow the incorporation of additional

constraint (known as structural prior, see **Section 4.3.2**) in solving the inverse problem, which has been shown to improve the accuracy of the solution [70]. In the early days of fDOT the lack of subject-specific anatomical data as well as modelling software solution limited the anatomical models used in most studies to simply-shaped and homogenous geometries. But in recent years the increasing accessibility of anatomical data such as CT and MRI, as well as the rapid development of anatomical modelling software solutions have allowed more complex anatomical modelling approaches to be taken. Here we review some of the most commonly used anatomical models in the literature.

- **Slab model**

When the true surface geometry of the human head is unknown, a common approximation is to assume a slab geometry. This assumption becomes even more valid when the region of imaging interest is relatively small as compared to the size of the head, which is similar to the analogy that the earth may be assumed to be flat at a small regional level. Because the slab geometry is relatively straightforward to generate while also allowing sophisticated description regarding its internal structure (**Figure 23**), it has proven to be suitable and very popular in proof-of-concept evaluation of fDOT versus back projection [97], TD-fDOT versus CW-fDOT [78] and validation of the depth compensation algorithm (DCA) [108], as well as in preliminary investigations on the effect of internal refractive index [109] and the presence of the CSF layer in fDOT [110].

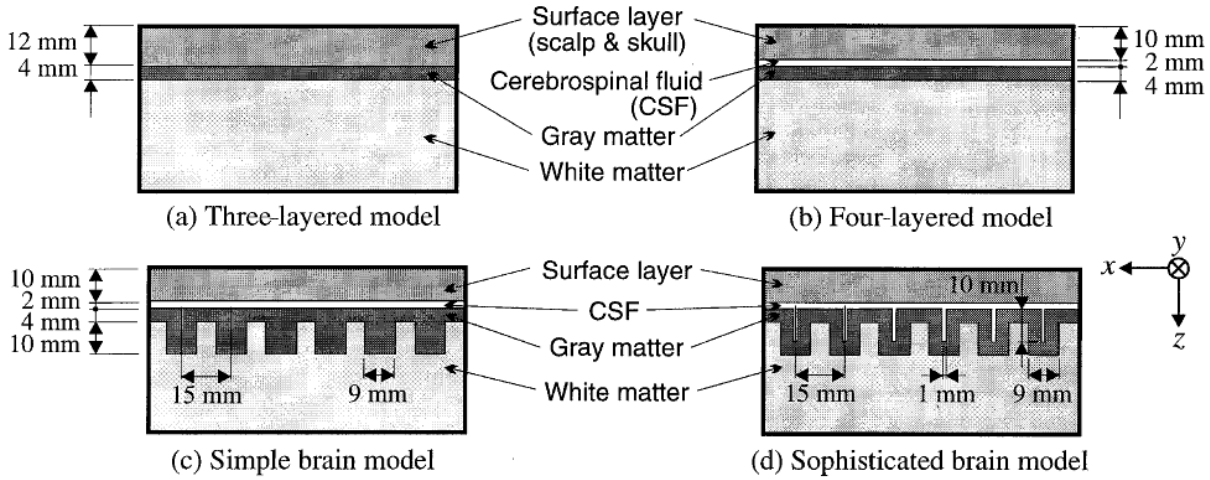


**Figure 23 Schema designs of four slab models for adult head. (a) smoothly three-layered model; (b) smoothly four-layered model (added CSF layer); (c) more realistic white matter layer than (b); (d) more realistic grey matter layer than (c) [110].**

- **Spherical model**

The lack of accounting for the curvature of the human head in the slab model approach has led to the use of another basic but more realistic head modelling geometry, which is the sphere (or hemisphere). The radius of the sphere should be specified such that its surface contour provides a close fit to the human head that it attempts to model, as illustrated in **Figure 24 (a-b)**, and may vary between subjects [111]. Furthermore, a brain region and an outer intervening tissue layer can be specified as in **Figure 24 (c)** [5]. This geometry is considered to be much more realistic than the slab approach and it has indeed produced encouraging results in the tomographic mode [5, 36, 37, 45]. However without knowing the true head anatomy of the subject, these fDOT results are still crude estimations of the functional maps of the human visual cortex, and do not provide a like-for-like comparison with fMRI data.

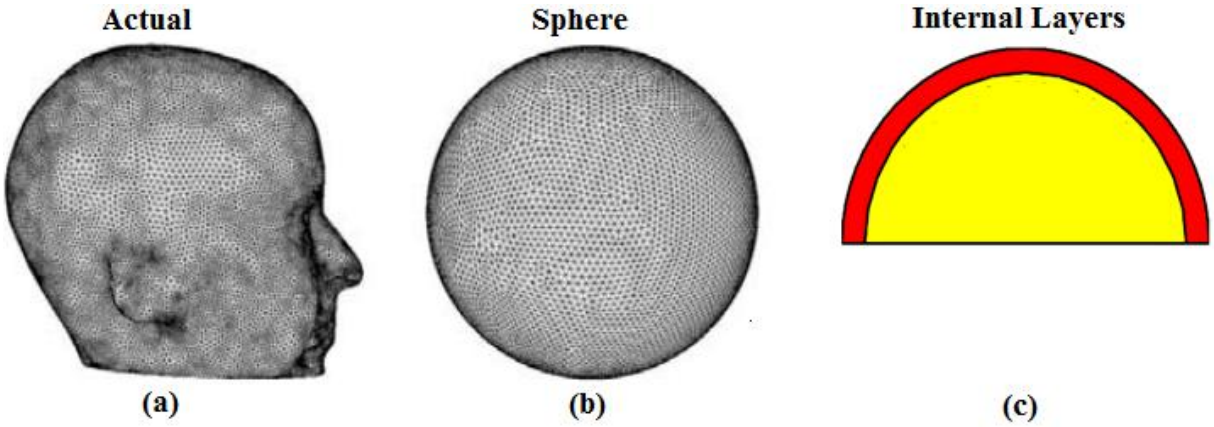


**Figure 24 (a) A realistic human head model, and (b) a sphere that provides a good approximation of (a) [111]; (c) cross section of a hemispherical head model (8 cm in radius) illustrating a two-layer internal structure: an inner brain region (yellow, 7 cm in radius) surrounded by an outer skin/skull layer red, 1 cm thick) [5].**

- **Realistically-segmented model**

Simple geometries as mentioned above provide an easy-to-implement yet crude approximation of the actual head anatomy. The use of realistically-segmented head models would not only improve the reconstructed image quality by contributing to a more accurately described forward model of light propagation in the subject, but also allow reconstructed functional data to be overlaid (or co-registered) on the actual geometry as in fMRI, providing like-for-like comparison with the gold standard. However to improve on the level of anatomical details at subject-specific level inevitably requires a significant amount of extra information and resources. Fortunately in recent years, with the increasing availability of subject-specific anatomical data such as CT and MRI, as well as the rapid development of efficient anatomical modelling software solutions (for tissue segmentation and mesh generation), the construction of realistically-segmented subject-specific head models that incorporate sub-millimetre-scale anatomical details has become a reality. Besides it is worth mentioning a parallel effort that has been working on the so-called atlas-based approach,

which makes use of realistically-segmented generic atlases (head anatomies) in subject-specific studies with appropriate deformations. The atlas could be a standard (averaged) anatomy such as the Collins head dataset [112] or the Chinese visible human dataset [113]), or even just another subject-specific anatomy. To improve the subject-specificity of the atlas, surface-based (or landmark-based) co-registrations (or deformations) of the atlas are often used, where the landmarks can be measured on the head of the subject at the scene [7, 89]. The merit offered by this approach is that when the anatomical data of the imaging subject is unavailable, the deformed atlas could still provide a 'second-to-best approximation' of the actual anatomy. Nevertheless regardless whether a subject-specific or atlas-based approach is used, there are two procedures that are always required for the construction of a realistically segmented head model, namely tissue segmentation and mesh generation, which are discussed below.

#### 4.2.2.1 Tissue segmentation

Tissue segmentation is the task of clustering pixels that belong to the same tissue type on the anatomical images. The clustered pixels of each tissue type are often highlighted with a unique colour (or grey scale intensity) for distinction. The level of difficulty for tissue segmentation is highly dependent on the number of tissue types required to be segmented out, as well as the number and types of anatomical data set available for use. At present the mainstream approach in fDOT studies is five-tissue-segmentation, namely the scalp, skull, CSF, grey matter and white matter, which is generally thought to be sufficient, although more types should always help to improve the accuracy of the model in principle [114]. In terms of the type of the anatomical data needed, T1-MRI has become the minimum requirement to perform head tissue segmentation. However T1-MRI provides high contrast between the scalp, grey matter and white matter but almost no contrast between the skull and CSF [115].

Possible solutions include co-registering the T1-MRI dataset with a secondary anatomical modality, such as CT which provides high contrast for the skull, **Figure 25** [116], or with T2-MRI which provides distinctive contrast for the CSF [38], as shown later in **Figure 29** .

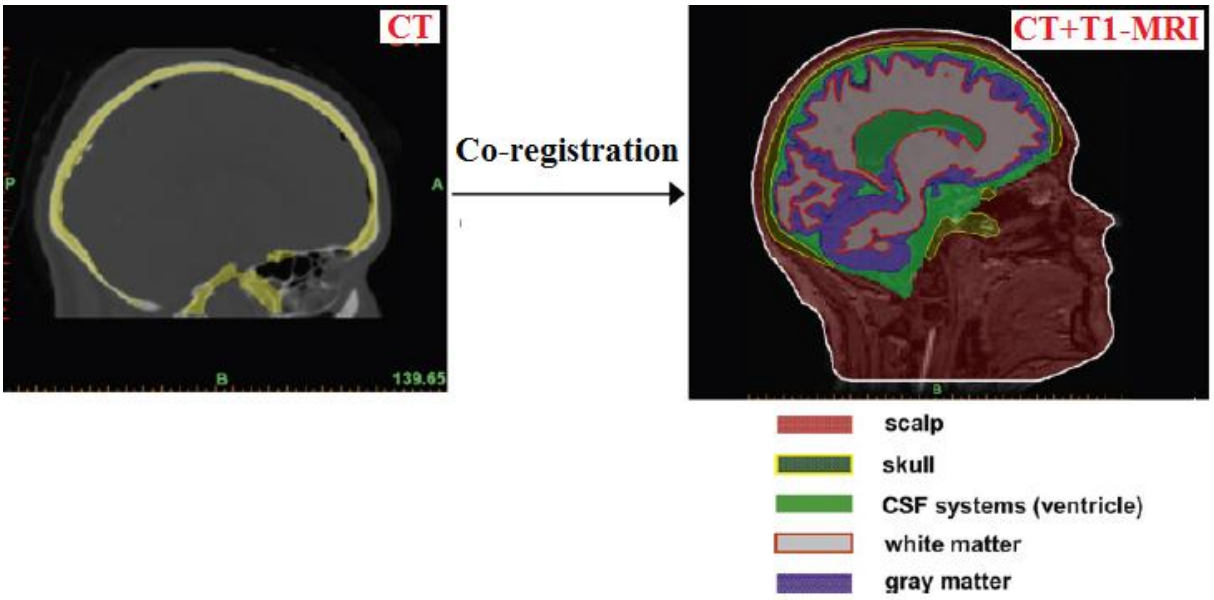


**Figure 25 Left: CT image of human head with yellow mask representing the skull; Right: Five-tissue-segmented image from T1-MRI co-registered with CT [116].**

However in the absence of additional imaging modalities, contrast-based (or threshold-based) segmentations are generally not sufficient and more sophisticated methods are required. The most widely used approach is known as statistical atlas-based segmentation, which utilises another pre-segmented head atlas anatomy to provide a statistical estimation for the spatial distributions of the underlying tissue types that are indistinguishable contrast-wise. A number of MRI-based neuroimaging software packages have incorporated this segmentation functionality, such as FreeSurfer (MGH, USA) [117] and SPM (UCL, UK) [118]. A brief tutorial on statistical atlas-based segmentation using SPM is described in **Appendix A**.

#### 4.2.2.2 Mesh generation

First of all it is worth noting that the mesh generation procedure as discussed in this section has been particularly relevant to one type of computational models named the finite element method (or FEM, as described later in **Section 4.2.3.3**). In the FEM, a finite element mesh that consists of a finite number of non-overlapping and small elements is required. For 3D realistic head models, the elements should be volumetric, i.e. three-dimensional, and the tetrahedron is regarded as the standard geometry element (although other geometries are also common). This means that each element contains 4 nodes (or vertices), and the surface of the mesh is represented by triangles. There exist a number of commercial mesh generation software packages such as Mimics (Materialise, Belgium) and Simpleware (Simpleware, UK), as well as open-source software such as Nirfast [119] and iso2mesh [120]. A major challenge in FEM-based fDOT studies is to generate these finite elements in a way that could adequately reflect the heterogeneity as well as the complex internal and external geometries of the human head. The procedure can sometimes be extremely computationally expensive, and there are in general two approaches for mesh generation, as described below.

- **Surface-based mesh generation**

This approach consists of two steps: surface mesh extraction and volumetric mesh generation. First of all, the surface mesh (consisting of triangles) of each tissue type must be specified, which describes the boundary between different tissue regions. The volumetric (tetrahedral) elements are then generated by 'growing' upon these surface triangles to fill the volumes in-between the boundaries. This means that the quality of the volumetric element is highly dependent on the quality of the surface element. A major computational burden in this procedure is the refinement of the white and grey matter surface meshes due to their complex and micro-millimetre-scale structures [116]. For instance the automatic mesh quality

optimisation tools in Mimics [121] are often found to be insufficient to provide a workable mesh, and additional manual or semi-automatic correction is required, which further increases the complexity and human subjectivity of the task. A common solution in earlier studies has been to apply smoothing operations on the brain surface, which inevitably introduces anatomical modelling error [122, 123]. **Figure 26** shows an example where a work-around approach was taken in the Collins head: the grey matter surface in **Figure 26 (c)** appears smoother than it should be, and is actually a 1-2 pixel expansion of the segmented grey matter surface. This is to prevent mesh creation failure caused by the so-called triple-surface (of the CSF, grey matter, white matter surfaces) intersection problem, which happens when the classified CSF, grey matter and white matter pixels appear to be inter-connected with each other (often at a local site) on the segmented image. In standard human brain anatomy, since the grey matter is the outermost layer of the brain, the white matter should not be directly exposed to the CSF. Therefore such scenario is often considered to be the result of segmentation errors.

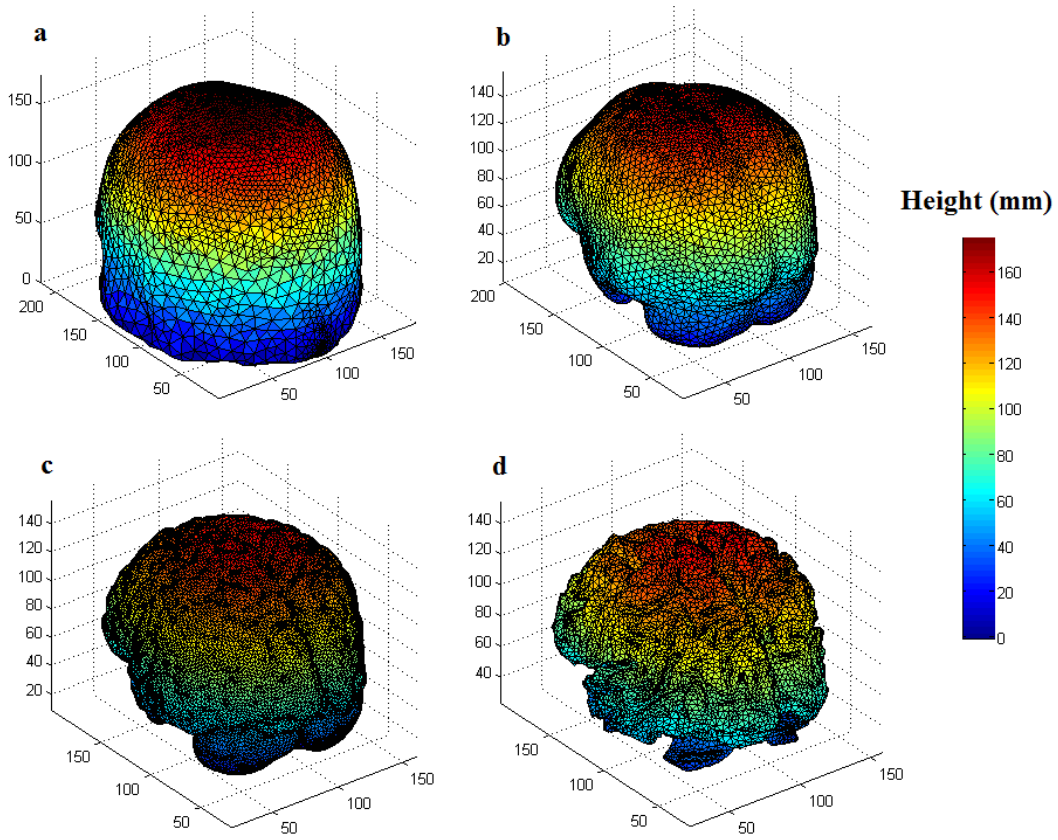


**Figure 26 Surface of (a) scalp; (b) CSF; (c) grey matter; (d) white matter of the 'Collins head' [112] generated by Fang [124].**

- **Non-surface-based mesh generation**

This approach consists of two steps: volumetric mesh generation and region labelling. In this case, volumetric tetrahedral elements are first generated by growing inwards upon the triangular surface mesh of the scalp, regardless of the internal heterogeneity of other tissue types. The 3D finite element head model is then co-registered with the segmented head anatomy, and each node or element within the model is assigned to a unique tissue type based on a 'look up' on the segmented anatomy. This procedure effectively eliminates the computational burden for the refinement of high quality surface meshes for each tissue while maintaining the capability of describing heterogeneity within the head model. Although such description may not be as accurate as the surface-based approach, especially when the mesh

resolution is low, it was found that a mesh resolution of 1-2 mm was sufficient for fDOT studies [38]. Furthermore this procedure can be fully automatic without hand corrections. Brief tutorials on non-surface-based mesh generation using Mimics and Nirfast are given in **Appendix B**.

### 4.2.3 The computational model

The role of the computational model is to implement the mathematical forward model on the anatomical model, so as to provide a model-specific description of photon propagation in the underlying imaging subject. In general there are three types of computational modelling approaches to be taken, namely analytical modelling, statistical (or stochastic) modelling, and deterministic modelling. For the scope of this thesis we review one selected example from each approach as described below.

#### 4.2.3.1 Analytical model: Green's function

Green's function can be used as a numerical as well as analytical tool to solve partial differential equations (PDE) such as the RTE and DA, which involves a source condition: the solution is Green's function when the source is a dirac delta function. Since the pulsed laser source equipped in time-domain (TD) systems provides a sufficient approximation to the dirac delta function, the application of Green's function is therefore valid in this case [99]. The solution for any other types of sources could then be computed using convolution. While analytical solutions for the RTE as well as heterogeneous and irregularly shaped geometries remain scarce, solutions that use the Green's function to solve the DA for homogeneous and simple geometries such as slab, cylinder and sphere geometry have been published [125], and are often chosen as the benchmarks to validate statistical and deterministic models [126-128].

#### 4.2.3.2 Statistical model: Monte Carlo method

The Monte Carlo (MC) method is the most well-known and widely used statistical model in fDOI literature, and has been generally regarded as the 'gold standard' for the validations of other computational methods in heterogeneous and irregularly shaped geometries. In MC simulation, an individual photon is injected into the region of interest and its trajectory is modelled and recorded until it escapes from the object or is absorbed. This process is repeated until the required counting statistics are obtained, which allows the probability density function of photon propagation to be estimated. This method tolerates heterogeneity and flexible shape for the medium and allows reasonably low level of statistical error when executed in a controlled manner. A Monte Carlo code for planar multi-layered tissue (known as the 'MCML') was developed by Wang et al. [128]. Later Boas et al. released a more advanced code (known as 'tMCimg') that deals with arbitrary boundaries and spatial variation in the optical properties of the imaging medium, including applications to the human head [127]. More recently the MC approach has been used in the investigations of anatomical atlas-based fDOT for both *in silico* [7] and *in vivo* studies [89]. Although historically MC was known for its high computational time and cost, recent advancement in parallel computing [129] as well as mesh-based MC ('MMCM') [124] have dramatically reduced the computational burden it once posed. For instance, Fang [124] reported that it takes MMCM 40 minutes to simulate $3\times10^7$ photons for a time-window of 0-3 nanosecond on a head mesh that consists of 69,865 nodes and 425,224 elements using 4 CPU cores.

#### 4.2.3.3 Deterministic model: Finite element method

The finite element method (FEM) is a numerical technique for the solution of partial differential equations (PDE) such as the RTE and DA, and is the most commonly used deterministic model in the diffuse optical imaging literature. In principle, FEM discretises the

original continuous imaging domain into a finite number of non-overlapping and small elements based on some basis functions, with the most commonly used one being the simplest, namely piecewise linear basis function. The problem can then be described in matrix form and solved using matrix algebra. Similar to Monte Carlo, FEM is also capable of dealing with heterogeneity in arbitrary geometries, at higher speed but compromised solution accuracy. Arridge et al. [126] introduced the application of FEM in solving the forward problem using the DA, and demonstrated good agreement with both analytical and MC model, especially when the mesh resolution is high. Since then several FEM package have been developed, including Nirfast [119] and TOAST [126, 130]. It is worth noting that we have selected FEM as our choice of computational model and used the Nirfast package to compute our forward models for our work to be presented later in **Chapter 5-7**. The Nirfast package has also been used in numerous diffuse optical imaging studies including prostate [131], breast [132-134], and brain function imaging [5, 36, 37, 45, 94, 123].

## 4.3 The inverse problem

As seen from the DA, **Equation (1.19)**, the relationship between the measurement of absolute light intensity (or fluence rate) $\Phi$ and the optical property $\mu$ is nonlinear. However, in the application of fDOT where we are concerned with relatively small differential changes in both fluence rate $\Delta\Phi$ and optical property $\Delta\mu$, the problem can assumed to be linear [62]. In this section, we first review the nonlinear optimisation method [31] that is commonly used to reconstruct $\mu$ from $\Phi$ in traditional nonlinear (or absolute) DOT inverse problems, and then its linearised version [5, 37, 45, 123] that recovers $\Delta\mu$ from $\Delta\Phi$ in the linear (or differential) fDOT inverse problem.

### 4.3.1 The mathematical model

#### 4.3.1.1 The Levenberg-Marquardt nonlinear optimisation

The problem of recovering optical property $\mu$ from measured fluence rate $\Phi$ is not linear and can be solved using nonlinear optimisation method. An optimisation problem is to search for the 'most appropriate' solution out of all possible answers. The 'appropriateness' is called the objective function, and 'all possible answers' define the feasible space of the solutions. In the context of nonlinear optimisation, the objective of the nonlinear image reconstruction problem is to search (or recover) for $\mu$ such that the difference between measured (observed) fluence rate $\Phi^M$ at the tissue surface, and the calculated data $\Phi^C$ from the forward solver, is minimised. Thus the objective function is given by:

$$\chi^2 = \min_{\mu}\left\{\sum_{i=1}^{NM}\left(\Phi_i^M - \Phi_i^C\right)^2\right\} \tag{1.20}$$

One way to derive the solution is called the Tikhonov approach, where an additional penalty term is added to the objective function in **Equation (1.20)**:

$$\bar{\chi} = \min_{\mu}\left\{\sum_{i=1}^{NM}\left(\Phi_i^M - \Phi_i^C\right)^2 + \rho\sum_{j=1}^{NM}\left((\mu)_j - (\mu_0)_j\right)^2\right\} \tag{1.21}$$

where $\rho$ is a damping factor that tends to minimise the difference between the current and the initial estimate of optical properties, $\mu$ and $\mu_0$, thereby reducing the oscillations during convergence. Since minimisation of $\bar{\chi}$ with respect to $\mu$ means that its first derivative equals to zero, we want to find $\mu$ such that:

$$\frac{\partial\bar{\chi}}{\partial\mu} = 0 \tag{1.22}$$

From Newton's method, we have the iterative update equation:

$$\mu_{i+1} = \mu_i - \frac{\partial \bar{\chi}}{\partial \mu}\left[\frac{\partial}{\partial \mu}\left(\frac{\partial \bar{\chi}}{\partial \mu}\right)\right]^{-1} \tag{1.23}$$

Calculating the first and second derivative of **Equation (1.21)**:

$$\frac{\partial \bar{\chi}}{\partial \mu} = 2\left(\frac{\partial \Phi^C}{\partial \mu}\right)^T \left(\Phi^M - \Phi^C\right) - 2\rho(\mu - \mu_0) \tag{1.24}$$

$$\frac{\partial}{\partial \mu}\left(\frac{\partial \bar{\chi}}{\partial \mu}\right) = 2\left(\frac{\partial \Phi^C}{\partial \mu}\right)^T \left(\frac{\partial \Phi^C}{\partial \mu}\right) + 2\left(\frac{\partial \Phi^C}{\partial \mu}\right)^T \left(\Phi^M - \Phi^C\right) - 2\rho \tag{1.25}$$

Substituting **Equation (1.24)** and **(1.25) into (1.23):**

$$\begin{aligned}\mu_{i+1} = \mu_i - &\left[2\left(\frac{\partial \Phi^C}{\partial \mu}\right)^T \left(\Phi^M - \Phi^C\right) - 2\rho(\mu - \mu_0)\right] \cdot \\ &\left[2\left(\frac{\partial \Phi^C}{\partial \mu}\right)^T \left(\frac{\partial \Phi^C}{\partial \mu}\right) + 2\left(\frac{\partial \Phi^C}{\partial \mu}\right)^T \left(\Phi^M - \Phi^C\right) - 2\rho\right]^{-1}\end{aligned} \tag{1.26}$$

The contribution of the second derivative term $2\left(\frac{\partial \Phi^C}{\partial \mu}\right)^T \left(\Phi^M - \Phi^C\right)$ is considered small and therefore discarded:

$$\mu_{i+1} - \mu_i = \left[\left(\frac{\partial \Phi^C}{\partial \mu}\right)^T \left(\Phi^M - \Phi^C\right) - \rho(\mu - \mu_0)\right]\left[\left(\frac{\partial \Phi^C}{\partial \mu}\right)^T \left(\frac{\partial \Phi^C}{\partial \mu}\right) + \rho\right]^{-1} \tag{1.27}$$

Assuming $\mu_{i+1} - \mu_i = \mu - \mu_0 = \delta\mu$:

$$\left[\left(\frac{\partial \Phi^C}{\partial \mu}\right)^T \left(\frac{\partial \Phi^C}{\partial \mu}\right) + \rho\right]\delta\mu = \left(\frac{\partial \Phi^C}{\partial \mu}\right)^T \delta\Phi - \rho\delta\mu \tag{1.28}$$

Using standard terminology Jacobian $J = \frac{\partial \Phi^C}{\partial \mu}$:

$$\left(J^T J + 2\rho\right)\delta\mu = J^T \delta\Phi \tag{1.29}$$

Letting $2\rho = \bar{\rho}$, we arrive at the familiar form of the Levenberg-Marquardt (LM) method:

$$\delta\mu = \left(J^T J + \bar{\rho} I\right)^{-1} J^T \delta\Phi \tag{1.30}$$

Or equivalently:

$$\delta\mu = J^T \left(JJ^T + \bar{\rho} I\right)^{-1} \delta\Phi \tag{1.31}$$

where $I$ is the identity matrix, and $\bar{\rho}$ is chosen to be arbitrarily large at the first iteration to stabilise potential oscillations due to poor initial estimate $\mu_0$, and will either decrease iteratively along with the objective function $\bar{\chi}$ to accelerate convergence, or increase iteratively along with $\bar{\chi}$ to further reduce oscillations.

#### 4.3.1.2 Tikhonov linear inverse

The nonlinear problem as describe above can be linearised if $\Delta\mu$ and $\Delta\Phi$ is small, which is assumed to be the case in the application of functional diffuse optical tomography (fDOT). Therefore by letting $\Delta\mu = \delta\mu$, $\Delta\Phi = \delta\Phi$ and replacing $\bar{\rho}$ with the Tikhonov regularisation parameter $\alpha_\lambda{}^2$, we arrive at the linearised Tikhonov version of **Equation (1.31)** for single-wavelength $\lambda$ [135]:

$$\Delta\mu_\lambda = J_\lambda{}^T (J_\lambda J_\lambda{}^T + \alpha_\lambda{}^2 I)^{-1} \Delta\Phi_\lambda \tag{1.32}$$

The role of Tikhonov regularisation parameter $\alpha_\lambda{}^2$ will be discussed in detail in **Section 4.3.1.4**.

#### 4.3.1.3 The Jacobian

From **Equation (1.32)** it can be seen that solving the inverse problem requires the computation of the Jacobian $J = \dfrac{\partial\Phi^C}{\partial\mu}$, or measurement sensitivity, which has the dimension of NM (number of measurements) by NN (number of nodes), and represents the sensitivity of

measurements to changes in the underlying optical properties. In general there are three ways of calculating the Jacobian *J*. The first is the perturbation method, in which separate sets of measurements $\Phi$ are calculated before and after a perturbation $\delta\mu$ occurs in the imaging domain in order to derive $\frac{\partial\Phi^C}{\partial\mu}$, and to do so for each of the NN total number of nodes in the FEM mesh requires (NN+1) number of forward calculations (given CW measurement and absorption $\mu_a$ only); the second is the direct method, which involves the differentiation of the DA, or **Equation (1.19)** with respect to $\mu_a$, and again to do for the entire mesh would result NN number of forward calculations; the third and quickest is the adjoint method [136], which makes use of the reciprocity theorem that states that the measurement of the flux at location *x* that is due to a source at location *y* is equivalent to the measurement of the fluence rate at location *y* that is attributed to a source at location *x*. This allows only (NS+ND) number of forward calculations to be computed in order to derive the Jacobian, where NS and ND stand for the number of sources and detectors respectively [62].

Given the imaging application that we are mostly concerned with in this thesis, namely intensity-only measurements, absorption-only reconstruction problem, and finite element modelling, the Jacobian (or measurement sensitivity) at single wavelength $\lambda$ has the following matrix form:

$$J_\lambda(\text{Born form}) = \frac{\partial\Phi}{\partial\mu} = \begin{bmatrix} \frac{\delta\Phi_1}{\delta\mu_1} & \cdots & \frac{\delta\Phi_1}{\delta\mu_{NN}} \\ \vdots & \ddots & \vdots \\ \frac{\delta\Phi_{NM}}{\delta\mu_1} & \cdots & \frac{\delta\Phi_{NM}}{\delta\mu_{NN}} \end{bmatrix} \tag{1.33}$$

where $\frac{\delta\Phi_i}{\delta\mu_j}$ defines the change in amplitude of the $i^{th}$ measurement among NM measurements arising from a small change in $\mu$ ($\mu$ represents $\mu_a$ from this point onwards) at the $j^{th}$ node among NN nodes in the mesh. **Equation (1.33)** is also known as the Born approximation form, as compared to the Rytov approximation of the following form:

$$J_\lambda(\text{Rytov form}) = \frac{\partial \ln(\Phi)}{\partial \mu} = \begin{bmatrix} \frac{\delta \ln(\Phi_1)}{\delta \mu_1} & \cdots & \frac{\delta \ln(\Phi_1)}{\delta \mu_{NN}} \\ \vdots & \ddots & \vdots \\ \frac{\delta \ln(\Phi_{NM})}{\delta \mu_1} & \cdots & \frac{\delta \ln(\Phi_{NM})}{\delta \mu_{NN}} \end{bmatrix} \quad (1.34)$$

Literature suggested the use of logarithmic intensity $\ln(\Phi)$ as in the Rytov form allows for a larger dynamic range of measurements and was found to provide considerable improvement in imaging performance as compared to the use of absolute intensity $\Phi$ as in Born form [137-139]. For this reason, the Rytov form has been used throughout our studies as presented later in **Chapter 5-7**.

#### 4.3.1.4 Ill-condition and regularisation methods

As mentioned previously, in nonlinear optimisation problems the damping parameter $\bar{\rho}$ in **Equation (1.31)** is utilised to reduce the oscillations during convergence. Similarly in linear problems (such as fDOT), the Tikhonov regularisation parameter $\alpha_\lambda^2$ is used to stabilise the Jacobian matrix inversion by reducing the condition number of the problem. The inverse problem (**Equation (1.32)**) is said to be ill-conditioned if the solution $\Delta\mu$ is not stable, i.e. a small error in $\Delta\Phi$ would propagate to or result in a large error in $\Delta\mu$, suggesting that the reconstructed images are extremely sensitive to noise in the measurements. The scale of such

error propagation can be characterised by the singular value decomposition (SVD) of the Jacobian matrix $J_\lambda$ which yields a triplet of matrices:

$$J_\lambda = USV^T = Udiag(\sigma_i)V^T, i = 1:rank(J) \tag{1.35}$$

Where $U$ and $V$ are orthonormal matrices containing the singular vectors of $J_\lambda$, and $S$ is a diagonal matrix that contains the singular values of $J_\lambda$, i.e. $\sigma_i$. The ratio of the maximum and minimum (also the first and last) singular values, denoted by $\frac{\sigma_1}{\sigma_{rank(J)}}$ and also known as the condition number $\kappa$, provides an indication of error propagation from $\Delta\Phi$ to $\Delta\mu$. The higher the condition number is, the more severe the error propagation, and the inverse problem is said to be more ill-conditioned.

As shown in **Equation (1.32)**, the Tikhonov regularisation parameter $\alpha_\lambda^2$ is added to the $J_\lambda J_\lambda^T$ term. If we apply SVD on $J_\lambda J_\lambda^T$, we have:

$$J_\lambda J_\lambda^T = USV^T(USV^T)^T = US^2U^T \tag{1.36}$$

After Tikhonov regularisation is applied, the relationship becomes:

$$J_\lambda J_\lambda^T + \alpha_\lambda^2 I = US^2U^T + U\alpha_\lambda^2 IU^T = U[S^2 + \alpha_\lambda^2 I]U^T \tag{1.37}$$

From **Equation (1.36)** and **(1.37)**, effectively by adding $\alpha_\lambda^2 I$ to the $J_\lambda J_\lambda^T$ term, the singular values of $J_\lambda$ change from $\sigma_i$ to $\sqrt{\sigma_i^2 + \alpha_\lambda^2}$. Consequently the condition number of $J_\lambda$ reduces from $\frac{\sigma_1}{\sigma_{rank(J)}}$ to $\sqrt{\frac{\sigma_1^2 + \alpha_\lambda^2}{\sigma^2_{rank(J)} + \alpha_\lambda^2}}$, thus the inverse solution $\Delta\mu_\lambda$ becomes more stable and the reconstructed images are more robust against noise in the measurements.

A similar technique to improve the ill-condition-ness of the problem is the SVD based truncation method [140]. This method reduces the condition number of $J_\lambda$ by setting all $\sigma_i$ below a predetermined threshold to zero. An illustrative example of the effect of Tikhonov regularisation and SVD based truncation on the singular value spectra of the original matrix are shown below in **Figure 27**.

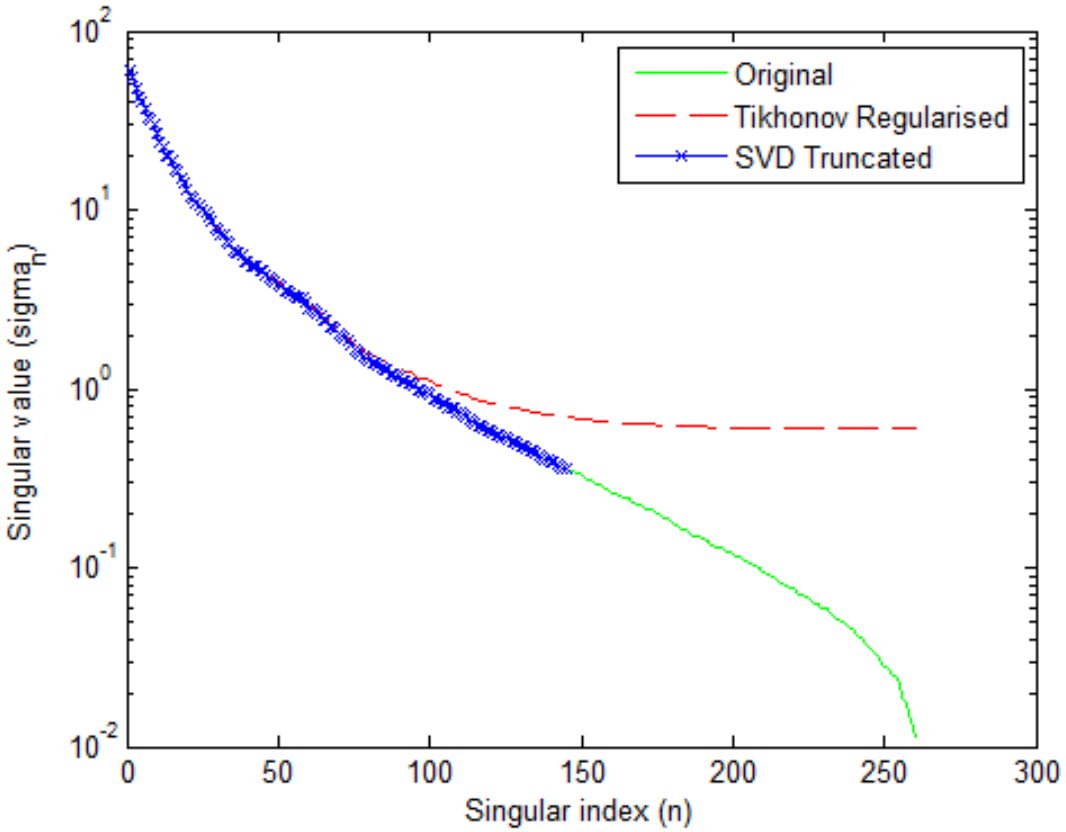


**Figure 27 Singular value spectra of an example Jacobian matrix of size 256 (number of measurements) by 1,087,223 (number of nodes), showing the original matrix (green), its Tikhonov regularised version (red), and SVD truncated version (blue) respectively. The rank of the original matrix is 256, which is the same as the number of measurements, meaning each of the 256 measurements carries some unique information regarding the imaging domain.**

Although the use of Tikhonov regularisation parameter $\alpha_\lambda^2$ improves the robustness of the recovered images against measurement noise, on the other hand it has been shown that the

value of $\alpha_\lambda^2$ is inversely proportional to the reconstructed image resolution, i.e. higher $\alpha_\lambda^2$ yields lower resolution and vice versa [141]. Therefore the selections of $\alpha_\lambda^2$ require a good balance between image resolution and image sensitivity to noise, which have shown to be empirically determined and application-dependent in *in vivo* literature [5, 142-144].

#### 4.3.1.5 Back projection method

In addition to the Tikhonov linear inverse, a back projection method has also been mentioned in previous fDOT literature [4, 97], with the following reconstruction equation:

$$\Delta\mu = (J \cdot C)^T \cdot \Delta\Phi \tag{1.38}$$

where $C$ is a diagonal matrix that performs column normalisation on $J$. In this case the inverse of $J$ has been approximated by $(J \cdot C)^T$, namely $J^{-1} \simeq (J \cdot C)^T$, which is valid if $J$ is an orthogonal matrix. This means that $J$ or $J \cdot C$ needs to be a square matrix whose columns and rows are orthogonal unit vectors. However under current fDOT applications, first, the number of measurements are far less than the number of nodes, and second, all measurement sets are unlikely to be orthogonal to each other. Therefore $J$ is not an orthogonal matrix, and this method was found to only serve as a fast solution to provide qualitative images [145], as compared to the more accurate Tikhonov linear inverse which offers better image quality [98].

### 4.3.2 Structural prior

The utilisation of structural priors in fDOT was first described by Boas [70]. The idea is that based on the internal structural information regarding the distribution of different tissues in the head, one can constrain the image reconstruction problem to a smaller region of interest, i.e. the cortex (or grey matter), where functional activations are expected to be recovered but

not in elsewhere. This not only imposes a meaningful constraint to the inverse problem that could potentially lead to more accurate solution, but also simplifies the problem by reducing its computational complexity. Specifically the sensitivity matrix $J_\lambda$ is 'segmented' into two parts: $J_{cortex}$ which contains the sensitivity values of all the nodes in the cortex (grey matter), and $J_{noncortex}$ which includes the sensitivities of all the nodes in the rest of the head mesh (white matter, CSF, skull and scalp). By using $J_{cortex}$ instead of $J_\lambda$ in the image reconstruction step as expressed by **Equation (1.32)**, the image recovery problem is effectively constrained to the cortex (or grey matter), therefore this is also known as 'cortically constrained' image reconstruction. It is worth noting that the application of such a constraint is only applicable when the sources of the signal are known to be located within the constrained region, i.e. the cortex. However as we discussed in **Chapter 3**, the raw boundary measurements would always contain superficial noises from various sources of contamination, therefore the importance of noise filtering and the integrity (or purity) of the signal becomes even more critical in this type of application. In addition, the utilisation of a 'cortical constraint' requires accurate tissue segmentation as well as mesh representation of the white matter, which is highly dependent on segmentation and mesh generation methods. In **Chapter 5-7** we present a 'whole brain constraint' that allows for more tolerance of tissue segmentation error, and evaluate its image performance on realistic subject-specific head geometries.

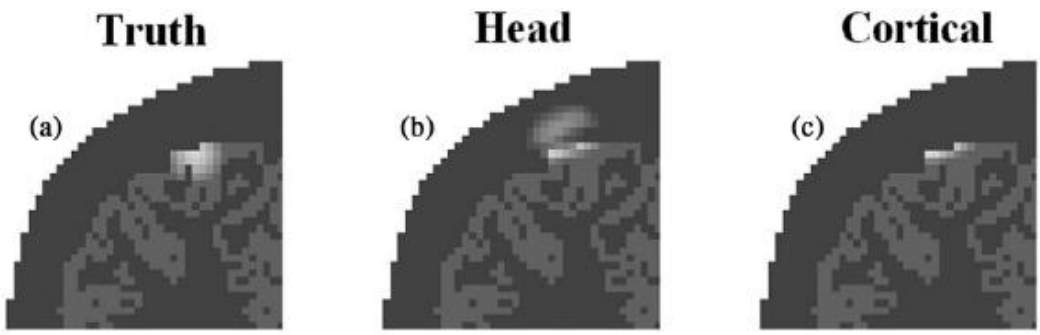


**Figure 28 Coronal slice of (a) a simulated cortical activation and its fDOT reconstructed image (b) without and (c) with cortical constraint [70].**

### 4.3.3 Spectral prior

The spectrally constrained image reconstruction method was first described by Corlu et al. in nonlinear (or absolute) DOT [8, 146], and later extended to linear (or differential) DOT [142]. Prior to their works, DOT image reconstruction was performed in 'non-spectral' mode which consists of two steps: the first step is expressed by **Equation (1.32)**, which is the recovery of absorptions from measurements; the second step is expressed by **Equation (1.6)**, which recovers chromophore concentrations from absorptions. Spectrally constrained image reconstruction is simply to incorporate or merge the 'spectral prior', or $M_S$ in **Equation (1.5)** into the wavelength dependent Jacobian in **Equation (1.32)** to form a 'multi-spectral Jacobian' matrix $J_S$ of the following form:

$$J_S = \begin{pmatrix} J_{\lambda_1} \cdot \varepsilon_{c_1,\lambda_1} & J_{\lambda_1} \cdot \varepsilon_{c_2,\lambda_1} \\ J_{\lambda_2} \cdot \varepsilon_{c_1,\lambda_2} & J_{\lambda_2} \cdot \varepsilon_{c_2,\lambda_2} \end{pmatrix} \tag{1.39}$$

By doing so, the forward problem can be described as:

$$\begin{pmatrix} \Delta\Phi_{\lambda_1}{}^T \\ \Delta\Phi_{\lambda_2}{}^T \end{pmatrix} = J_S \begin{pmatrix} \Delta HbO_2{}^T \\ \Delta HbR^T \end{pmatrix} \tag{1.40}$$

and the spectral image reconstruction using conventional Tikhonov regularisation becomes:

$$\begin{pmatrix} \Delta HbO_2^{\,T} \\ \Delta HbR^{T} \end{pmatrix} = J_S^{\,T}\left(J_S J_S^{\,T} + \alpha_S^{\,2} I\right)^{-1} \begin{pmatrix} \Delta\Phi_{\lambda_1}^{\,T} \\ \Delta\Phi_{\lambda_2}^{\,T} \end{pmatrix} \tag{1.41}$$

where $\alpha_S^{\,2}$ is the spectral Tikhonov regularisation parameter. Here it is worth noting that the weight of regularisation is directly associated with image resolution [141]. Previous works have found that $\alpha_S^{\,2}$ (in **Equation (1.41)**) must be smaller than $\alpha_\lambda^{\,2}$ (in **Equation (1.32)**) in order to achieve equivalent image resolution between non-spectral and spectral methods [143]. The spectral method allows a direct mapping between changes in measurements and changes in chromophore concentrations, bypassing the absorption-based transition step in the non-spectral method. Furthermore, measurements at multiple wavelengths are utilised simultaneously and absorption coefficients are correlated across these wavelengths within the image reconstruction. However, as our work in **Chapter 7** later points out, the regularisation technique utilised here regularises not only the underlying wavelength dependent Jacobian matrices $J_\lambda$ but also the spectral prior information $M_S$ (**Equation (1.5)**) incorporated within the spectral Jacobian matrix $J_S$, which results in numerical error in the form of crosstalk on the reconstructed images. In **Chapter 7** we present a singular value decomposition based regularisation method for spectral fDOT that dramatically reduces such crosstalk effect.

## 4.4 Summary

In **Chapter 3** we reviewed functional diffuse optical imaging (fDOI), which includes three operating modes: spectroscopic mode (fNIRS), topographic mode, and tomographic mode (fDOT). In this chapter we have further constrained our scope of literature review into functional diffuse optical tomography (fDOT) only. We started by establishing the entire workflow of fDOT (**Figure 22**), specifying various modelling issues arising throughout the

workflow, and grouping them into the forward problem and the inverse problem, which were then discussed separately in **Section 3.2 and 3.3**.

The forward problem can be further broken down into the mathematical model, anatomical model and computational model. We first described the two most well known mathematical models for fDOT, which are the radiative transfer equation (RTE) and its first spherical expansion known as the diffusion approximation (DA). We highlighted the advantage of the DA as being its computational simplicity over the RTE at the cost of certain assumptions, most notably that $\mu_s' >> \mu_a$, but reassured its validity in the application of fDOT of human brain, which mostly deals with highly scattering human tissues. For the exceptional non-scattering or low scattering cerebrospinal fluid (CSF) which occupies the void region between the skull and grey matter, we have reviewed literature that supports the use of DA with a $\mu_s'$ lower than 0.3 $mm^{-1}$ as sufficient approximation for *in vivo* fDOT studies.

Next we moved into the anatomical model and reviewed its historical trend of utilising increasingly complex and realistic head models owing to the greater accessibility of subject-specific anatomical data such as CT and MRI, as well as the rapid development of efficient anatomical modelling software solutions. We described two current approaches in building realistically-segmented head models, namely subject-specific and atlas-based approaches, and also two major challenges to build such models, namely tissue segmentation and mesh generation, in greater detail.

Building from these, we discussed the last model in the forward problem, which is the computational model that implements the mathematical model on the anatomical model. We described three of the most cited models in fDOT literature, namely the analytical approach using Green's function, the statistical approach using Monte Carlo simulation, and the

deterministic approach using Finite Element Modelling. We highlighted the advantages of FEM in geometry flexibility as well as computational efficiency, which also justified our use of Nirfast (a FEM package) for our studies to be discussed in **Chapter 5-7**.

After explaining the forward problem, we moved into the second part of the workflow, which is the inverse problem. We started by describing the mathematical aspect of the model, which is fundamentally a nonlinear optimisation problem, and derived the Levenberg-Marquardt (LM) equation (**Equation (1.30)** or **(1.31)**) as the solution. Then, given the application of fDOT where we are interested in relatively small changes of fluence rate $\Delta\Phi$ and optical property $\Delta\mu$, the LM equation can be linearised and we arrived at the Tikhonov linear inverse equation, **Equation (1.32)**, which is the standard inverse equation appearing in most fDOT literature. Building from this, we further discussed the inclusion of structural and spectral prior in the inverse problem through additional manipulations of **Equation (1.32).**

This chapter should have provided sufficient background knowledge and mathematical foundation for the reader to understand the entire fDOT workflow, upon which our work to be presented in the next three chapters have been built.

# CHAPTER 5

# POINT-SPREAD-FUNCTION ANALYSIS FOR MRI-GUIDED HD-fDOT

## 5.1 Introduction

As introduced in **Chapter 3**, a recent advancement in fDOT system design is the development of high-density (HD) imaging arrays, also known as HD-fDOT. This configuration encourages the utilisation of overlapping measurements, which improves the spatial sampling of brain tissue. Initial efficacy of HD-fDOT has been demonstrated through *in vivo* studies including retinotopic mapping of adult human visual cortex [36, 94], somatotopic mapping of the sensor motor cortex [41], resting-state mapping of functional connectivity [45], and phase-encoded retinotopic mapping [37]. In these studies HD-fDOT images have shown a level of detail that was previously inaccessible via sparsely arranged imaging arrays [5, 6]. On another front following the trend in diffuse optical tomography of breast cancer imaging [62, 147], more recent fDOT studies of the human brain have taken an MRI-guided approach in which a realistically-segmented subject-specific head model is constructed [70]. The realistic representation of the anatomical model provides not only the external and internal structure necessary for an accurate description of light propagation within the imaging subject, but also the possibility of incorporating anatomically derived spatial constraints into the image reconstruction algorithm [70]. Literature review has shown that the performance of HD-fDOT

was evaluated by Dehghani et al. [123] and Heiskala et al. [7] with anatomically realistic head models. However both studies only considered a limited number of simulated focal activations and neither provided a quantitative evaluation of the point-spread-function (PSF) analysis throughout a defined field of view (FOV), as conducted by Boas et al. [97] and White et al. [5] whom themselves were limited to simplified head models and noise-free analysis. In this work, we provide a realistic-noise-added PSF analysis of HD-fDOT on six anatomically realistic head models derived from their corresponding MRI datasets, with and without an anatomically based 'whole brain' spatial constraint for image recovery. Specifically the PSF analysis is performed throughout the visual cortex within a specified region of interest (ROI), corresponding to the total FOV of an experimental HD-fDOT system for the visual cortex [36].

## 5.2 Method

### 5.2.1 Dataset

For this study we use the anatomical MRI datasets from five healthy adults (Subject 1-5, aged 21-30). For each subject, T1-weighted MPRAGE (echo time (TE) = 3.13 ms, repetition time (TR) = 2400 ms, flip angle = 8°, 1 × 1 × 1 mm isotropic voxels, 176 slices) and T2-weighted (TE = 84 ms, flip angle = 120°, 1 × 1 × 4 mm voxels, 32 slices) scans are collected on a Siemens Trio (Erlagen, Germany) 3T scanner. For simplicity we refer them as T1 and T2 in the rest of this thesis. The scan session is approved by the Human Research Protection Office at Washington University School of Medicine [38].

### 5.2.2 Head tissue segmentation

An in-house automated algorithm is developed to perform five-tissue-segmentation, namely the scalp, skull, CSF, grey matter and white matter. The algorithm performs a series of

iterative thresholding, region grow, and masking operations that rely on the high contrast specificity of the scalp, grey matter and white matter on the T1 dataset and the CSF on the T2 dataset, as shown in **Figure 29.** The algorithm outputs 176 segmented slices (same as the number of T1 slices) of the head for each subject in .bmp format. An observation we made on these auto-segmented results is the false-negative errors of the CSF accompanied by the true-negative of the grey matter, i.e. regions that belong to the CSF are classified as the grey matter, as shown in **Figure 30 (a-b)**. This is potentially due to the lower resolution of the T2 than the T1, which are used for CSF segmentation. Therefore in a separate case, we hand-corrected the auto-segmented results from Subject 1 for a more accurate modelling of the CSF, **Figure 30 (c)**. Consequently we have obtained six segmented datasets from five sets of subject-specific MRIs.

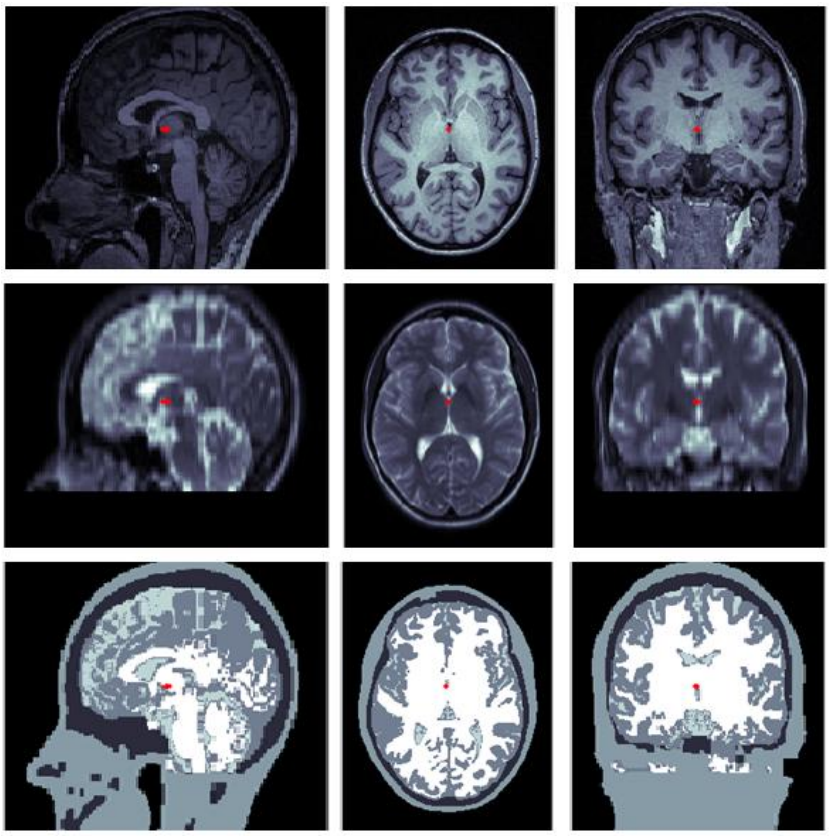

**Figure 29 Sagittal (left column), axial (middle column) and coronal (right column) slice of T1 (upper row), T2 (lower row) scan and auto-segmented anatomy of Subject 1.**

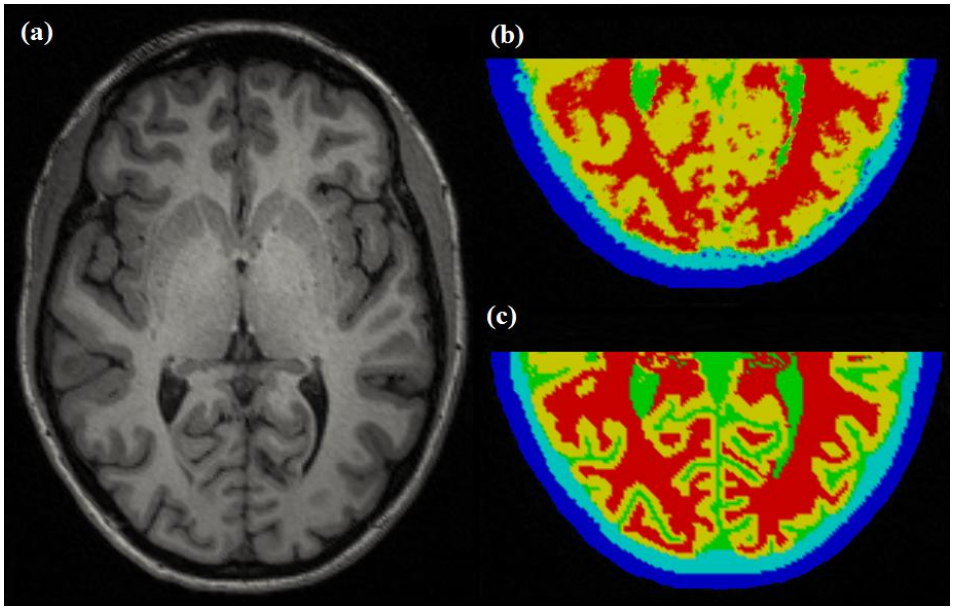


**Figure 30 An example showing an axial slice of Subject 1: (a) original grey-scale MRI; (b) auto-segmented and (c) 'auto-segmented + hand-corrected' anatomy showing colour-coded: white matter (red), grey matter (yellow), CSF (green), skull (cyan) and scalp (blue). Note the expanded region of CSF (green) and reduced area of grey matter (yellow) in (c) as compared to (b).**

### 5.2.3 Head mesh generation

Two different mesh generation software packages have been used for head mesh generation. While both packages implement the non-surface-based mesh generation as described in **Section 4.2.2.2**, Mimics [121] produces voxel-based (cube-based) tetrahedral elements of uniform size and shape (each voxel or cube consists of six tetrahedral elements), whereas Nirfast [119] generates non-uniform tetrahedral elements that satisfy a specified shape quality (e.g. minimum facet angle of 25 degrees). Tutorials for both software packages are given in **Appendix B**. Affected by the different availabilities of our mesh generation and tissue segmentation tools during the course of the study, we have used Mimics to perform mesh generation on the hand-corrected dataset of Subject 1 and named it 'Subject 1a', and used Nirfast for the other five auto-segmented datasets and named them 'Subject 1b' to '5b' respectively. We have imposed the same 1-mm-mesh-resolution constraint (as part of the

mesh generation parameter settings) when using both software packages in order to ensure the size of the tetrahedral element generated by them are comparable. Since our imaging region of interest is the visual cortex located at the back of the brain, we crop the anterior part of head and only use the posterior part for mesh generation. **Table 2** summarises the number of nodes and elements as well as total volume contained in each of the six subject head meshes. Once the volumetric mesh generation is completed, both software packages then perform region labelling based on a 'look up' of the segmented anatomy, which turn the homogeneous model into five-region, heterogeneous finite element mesh that provides realistic description of tissue distribution in the human head.

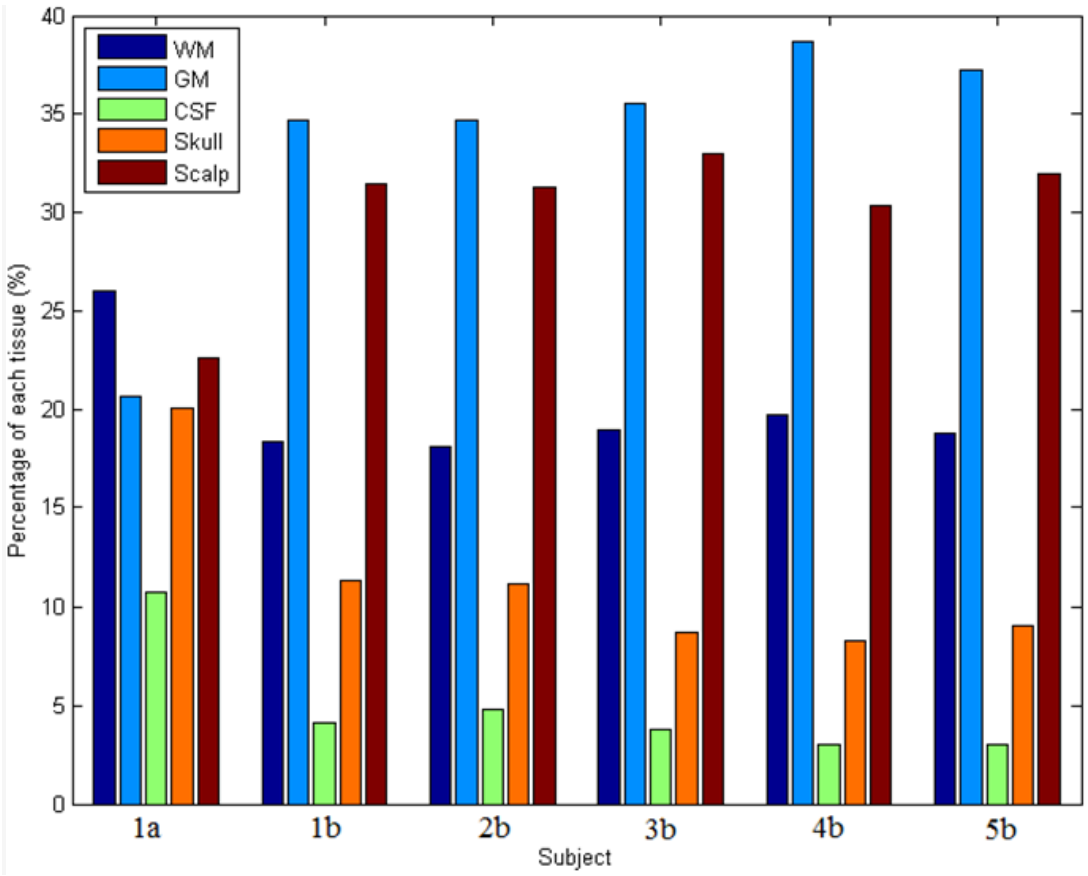


**Figure 31 Percentage of each tissue type in the segmented head mesh across six subjects. The decreased percentage in grey matter and increased percentage in CSF between Subject 1a and 1b are in good agreement with our observations made in Figure 30.**

**Table 2 Mesh information for each of the six subject meshes.**

| Subject | Number of nodes | Number element | Total volume ($cm^3$) |
|---|---|---|---|
| 1a | 1,087,223 | 6,289,566 | 1047.7 |
| 1b | 684,367 | 4,075,648 | 946.5 |
| 2b | 661,025 | 3,932,397 | 913.3 |
| 3b | 675,530 | 4,019,166 | 933.0 |
| 4b | 657,131 | 3,910,566 | 908.1 |
| 5b | 647,954 | 3,863,967 | 894.7 |

On a side note, it would also be interesting to consider 'Subject 1a' (**Figure 30 (c)**) as an 'aged version' of 'Subject 1b' (**Figure 30 (b)**). This is because earlier studies have reported a strong positive correlation between the human age and the corresponding CSF thickness, revealing that aged human brains are characterised by expanded layer of the CSF due to brain shrinkage [102].

### 5.2.4 Optical description

Tissue optical properties assigned to the head model were values estimated at 750 nm (**Table 3**), which is one of the primary wavelengths used in our current system [5] and can be adapted to other wavelengths. These values were estimated by applying a linear line-fitting scheme on values published at other available wavelengths [106, 148, 149].

**Table 3 Tissue optical properties used for 750 nm.**

| Tissue | $\mu_a$ ($mm^{-1}$) / $\mu_s'$ ($mm^{-1}$) |
|---|---|
| Scalp | 0.0170 / 0.74 |
| Skull | 0.0116 / 0.94 |
| CSF | 0.004 / 0.3 |
| Grey Matter | 0.0180 / 0.8359 |
| White Matter | 0.0167 / 1.1908 |

### 5.2.5 Probe arrangement

The high-density (HD) imaging array used for the data simulation consists of 24 sources and 28 detectors, which has been previously described in **Section 3.2.2**. The HD imaging array is modelled on the scalp surface over the visual cortex, and a region of interest (ROI) is defined as the volume up to 40 mm under the posterior FOV of the HD imaging array, as shown in **Figure 32**. The posterior FOV has been selected to focus on the visual cortex region under the array with the highest sensitivities and lowest image artefacts [5]. In this study all measurements detected within 4 cm from each source, i.e. first, second, and third nearest neighbours are taken, which give rise to a total of 260 independent measurements. It is assumed that only intensity data (as available from a CW system) measured at 750 nm are used to provide maps of optical absorption related changes only.

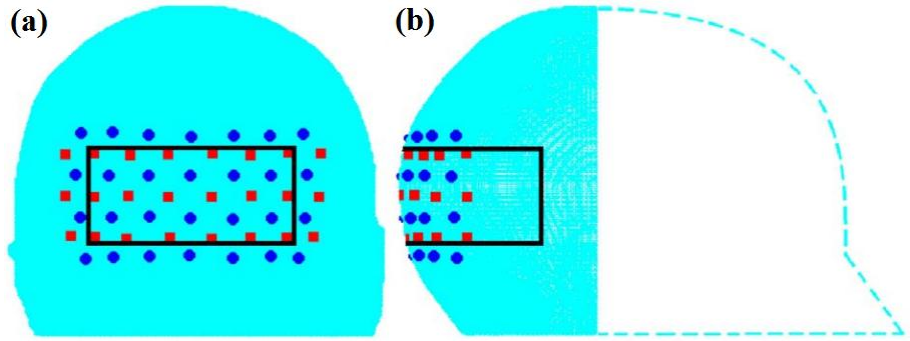


**Figure 32 (a) Posterior and (b) lateral schematic view showing the placement of the high-density imaging array over the visual cortex of Subject 1a with 24 sources (red squares) and 28 detectors (blue circles).**

### 5.2.6 Forward light modelling

Forward modelling of light propagation within the head model is performed using Nirfast [119] which is a modelling and image reconstruction toolbox based on the Diffusion Approximation. Nirfast is used to generate the wavelength dependent Jacobian matrix $J_\lambda$ in its Rytov approximation form as presented by **Equation (1.34)** in **Section 4.3.1.3**. It takes

approximately 28 minutes on average to generate the Jacobian matrix for one head mesh across all six subject models on a quad-core CPU, which is still much faster than the 40 minutes time that took MMCM [124] to simulate $3\times10^7$ photons for a time-window of 0-3 nanosecond on a coarser head mesh that consists of 69,865 nodes and 425,224 elements (~one tenth of the number of nodes and elements of our meshes) using 4 CPU cores, as mentioned in **Section 4.2.3.2**.

### 5.2.7 Image reconstruction

Image reconstruction is performed based on the Tikhonov inverse formula described by **Equation (1.32)** in **Section 4.3.1.2**. However instead of using the original $J_\lambda$, we have applied additional spatial regularisation to regularise the hyper sensitivities often observed in regions near the probes [70, 114], allowing a more homogenous spatial distribution of the measurement sensitivity. The spatially-regularised $J_\lambda$, denoted by $\bar{J}_\lambda$, has the following form:

$$\bar{J}_\lambda = \frac{J_\lambda}{\sqrt{J_\lambda J_\lambda{}^T + \beta(\max(diag(J_\lambda J_\lambda{}^T)))}} \tag{1.42}$$

where $\beta$ is the spatial regularisation factor. The optimal values chosen in this work are $\alpha$ $=10^{-2}\times$the maximum singular value of $J_\lambda$, and $\beta=10^{-2}$, which are found to provide a good balance between image resolution and robustness to measurement noise in our previous human [5] and animal [144] fDOT studies.

Furthermore we also include a scenario where structural prior is applied in image reconstruction. Here we apply a 'whole brain constraint' $J_b$ which limits the image recovery to both grey and white matter, allowing more degrees of freedom than the 'cortical constraint' $J_{cortex}$ as described in **Section 4.3.2**. A key issue with the cortical constraint is that it requires

accurate subject-specific grey matter segmentation. In comparison, the whole brain constraint as applied in this work should in principle be more robust with respect to tissue segmentation inaccuracy, most notably false-negative errors of the grey matter.

### 5.2.8 Total spatially-regularised sensitivity

The total spatially-regularised sensitivity $\bar{J}^{total}$ (for either $\bar{J}_\lambda$ or $\bar{J}_b$) is calculated as the sum of the spatially-regularised sensitivity over all measurement pairs at each node within the model. This is effectively the sum of the elements in each column of the spatially-regularised sensitivity matrix $\bar{J}$:

$$\bar{J}_j^{total} = \sum_{i=1}^{NM} \bar{J}_{i,j} \tag{1.43}$$

where $\bar{J}_j^{total}$ is the total spatially-regularised sensitivity at node *j*, and $\bar{J}_{i,j}$ is the spatially-regularised sensitivity at node *j* due to source-detector pair measurement *i* for a total number of NM measurements. This provides a measure of the system's sensitivity profile throughout the imaging domain.

### 5.2.9 Point-spread-functional analysis

The image quality of HD-fDOT is evaluated by performing point-spread-function (PSF) analysis at each grey matter (visual cortex) nodes within the ROI as defined in **Figure 32**. The simulated absorptive perturbation, $\Delta\mu$, is assumed to come from a small (a single node) focal haemodynamic visual response located within the visual cortex. The magnitude of the perturbation is determined such that a perturbation at 10 mm below the scalp would give a maximum $\Delta\ln(\Phi)$ of ~0.05 (or 5%), which was observed in the acquired measurements in *in vivo* studies [36]. This magnitude is kept constant for all perturbations, therefore $\Delta\ln(\Phi)$ reduces accordingly as the perturbation locates at deeper depths. For each simulated focal

activation, the equation $\Delta\ln(\Phi)(noiseless) = J \cdot \Delta\mu$ is used to compute the noiseless differential measurements. In line with our current *in vivo* performance, 0.1%, 0.14% and 1% Gaussian random noise is added to first, second and third nearest neighbours to provide realistic-noise-added differential measurements, $\Delta\ln(\Phi)$ . Specifically our noise model consists of two components: first, a constant noise floor, $n_1$, due to detector hardware (also known as the 'dark noise'), which are modelled as 0.001%, 0.1% and 1% of the first, second and third nearest neighbour measurement intensity $\Phi$ respectively based on our *in vivo* data [36]. The reason that such constant noise floor is accounted in ascending percentage of the first to third nearest neighbours, is because the measured absolute intensity $\Phi$ decreases as the source-detector distance increases; second, there is another 0.1% signal level dependent noise (the 'shot noise'), $n_2$, which is empirically determined from our *in vivo* data. Since the sources of these two noise components are independent, they are added in quadrature, i.e. $n_{total} = \sqrt{n_1^2 + n_2^2}$, to provide the total noise level. It can be seen that the shot noise is the dominant source of noise in the first nearest neighbour measurements, but the dark noise takes over gradually as source-detector increases. In order to mimic our current data collection strategy (whereby data is collected from each patient at a sampling rate of 10 Hz and then appropriately block averaged), ten sets of noise added data are generated for each perturbation activation. These are then appropriately block averaged and images are reconstructed with and without the application of whole brain constraint to produce the final point spread function images.

### 5.2.10 Metrics of image quality

Consider an example perturbation target and two reconstructed activations as shown in **Figure 33**. It is clearly evident that in Case A, whereby a single activation has been recovered

using full head reconstruction, the use of localisation error (displacement between actual and recovered peak value) is an intuitive and common image quality metric. Additionally for Case A, the use of full volume half maximum (FVHM) is an appropriate evaluation of the spread (size) of the recovered activation. There exists however scenarios, such as demonstrated in Case B, whereby multiple activations are reconstructed instead of the expected single activation, using whole brain constrained reconstruction. As such the use of localisation error and FVHM alone is not straightforward because it is not clear which recovered activation should be used for accurate analysis. To this end, we will next define and clearly state the specific image quality metrics utilised in this work, which aims to minimise the uncertainty due to multiple recovered activations.

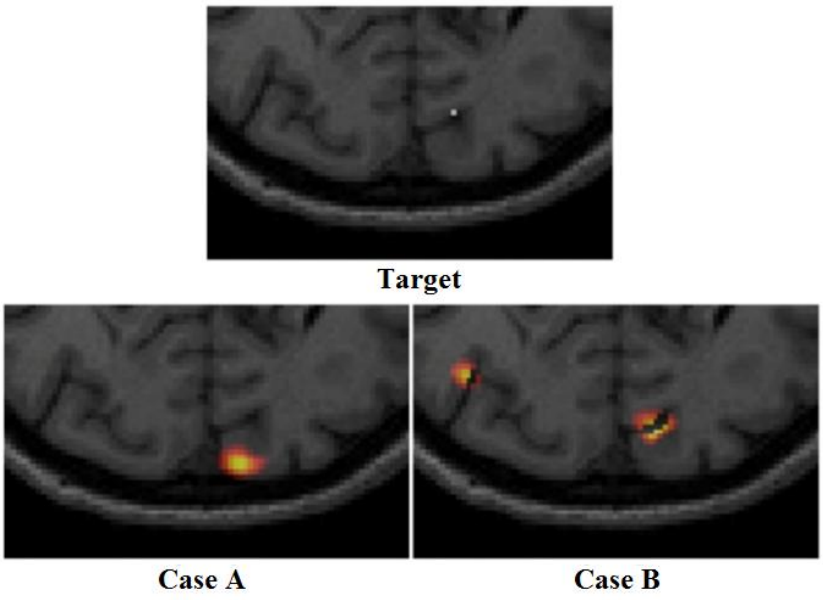


**Figure 33 An example of a 'target' focal activation on the cortical surface and two examples of reconstructed activations: Case A where a single activation is recovered using full head reconstruction, and Case B where multiple activations are recovered using whole brain constrained reconstruction.**

Following from above, three metrics are utilised to provide a quantitative measure of the imaging performance. First the localised full volume half maximum (LVHM) is defined as the

single volume enclosing the peak-response node in the PSF as well as other contiguous nodes having a value above half of the peak response. In case A of **Figure 33**, this would correspond to the FVHM of the single recovered activation, whereas in Case B, it corresponds to the single volume that contains the peak-response node. Second, the localisation error is defined as the Euclidian difference between the peak-response node in the LVHM (which is considered as the PSF) and the target node:

$$\text{localisation error} = \sqrt{(x_{peak} - x_{target})^2 + (y_{peak} - y_{target})^2 + (z_{peak} - z_{target})^2} \quad (1.44)$$

where ($x$, $y$, $z$) represents the nodal coordinate in the standard x-y-z 3D coordinate system. By such definitions it is assumed that the LVHM reveals useful localisation information about the actual target, which may not be valid when multi-regional artefacts are reconstructed due to low sensitivity and/or poor signal to noise ratio (SNR). Since the presence of imaging artefacts could affect the integrity of the localisation error and LVHM as quantified above, we introduce the third metric named 'focality', given by:

$$\text{focality} = \frac{\text{LVHM}}{\text{FVHM}} \quad (1.45)$$

where full volume half maximum (FVHM) is defined as the total (sum) volume enclosing all nodes having a value above half of the maximum reconstructed response. The 'focality' metric serves for two purposes: one is to reflect on the level of integrity of the corresponding localisation error and FVHM, and the other is to reflect on the SNR and the effect of noise on the image quality. While 1 indicates a single-regional PSF, a focality value above 0.5 describes a reconstructed activation well separated from the background artefacts, assuring a good level of integrity in the corresponding localisation error and LVHM and also reflecting a signal-dominating-over-noise situation; inversely a focality value below 0.5 suggesting a noise-dominating-over-signal scenario. As in Case A of **Figure 33**, the focality value is

clearly equal to 1, whereas in Case B, it would correspond to a value of less than 1. It is also important to note that the 0.5 minimum focality tolerance may not be directly applicable for the whole brain constrained PSF, since in cases where the focal activation lies within a fold of the visual cortex, the recovered activation using the whole brain constraint may be 'split' across this fold, thereby decreasing the calculated 'focality' metric (see Y in **Figure 40 (Brain)** for an example). Since a reasonable objective within the field of functional neuroimaging is 10 mm resolution, we set the maximum tolerance for localisation error at 10 mm, and 1000 $mm^3$ for LVHM [5].

## 5.3 Results

### 5.3.1 Total spatially-regularised sensitivity

**Figure 34** shows the spatial distribution of the total spatially-regularised sensitivity (from **Equation (1.42) and (1.43)**) of Subject 1a of the full head (left column '**Head**') and of the whole brain constraint (right column '**Brain**') at three different axial slices with different positions relative to sources and detectors. Since the spatial distribution of sensitivity is highly dependent on the probe placements, variations are expected between the slices when utilising sparsely arranged imaging arrays. In **Figure 34** however the three sensitivity distributions within the same column show similar spatial coverage owing to the high spatial sampling of tissue by a large number of overlapping measurements and the spatial regularisation scheme applied in **Equation (1.42)**. Without using the whole brain constraint, the regions with larger than 50% sensitivity (indicated by warm colour in **Figure 34**) reside mainly within the scalp, skull and CSF, which is a distribution not ideally suitable for imaging visual cortex activations that take place in the grey matter. While the gyri are also well covered by high sensitivity, sulcal folds show a significant decrease in sensitivity.

On the other hand the use of the whole brain constraint produces a more gradual decay of sensitivity in the brain region as depth increases. The sensitivity profile throughout the grey matter is more uniform with the whole brain constraint, potentially indicating a better recovery of focal activations within the visual cortex both in the sulcal folds and gyri. These observations are also consistent in Subject 1b-5b.

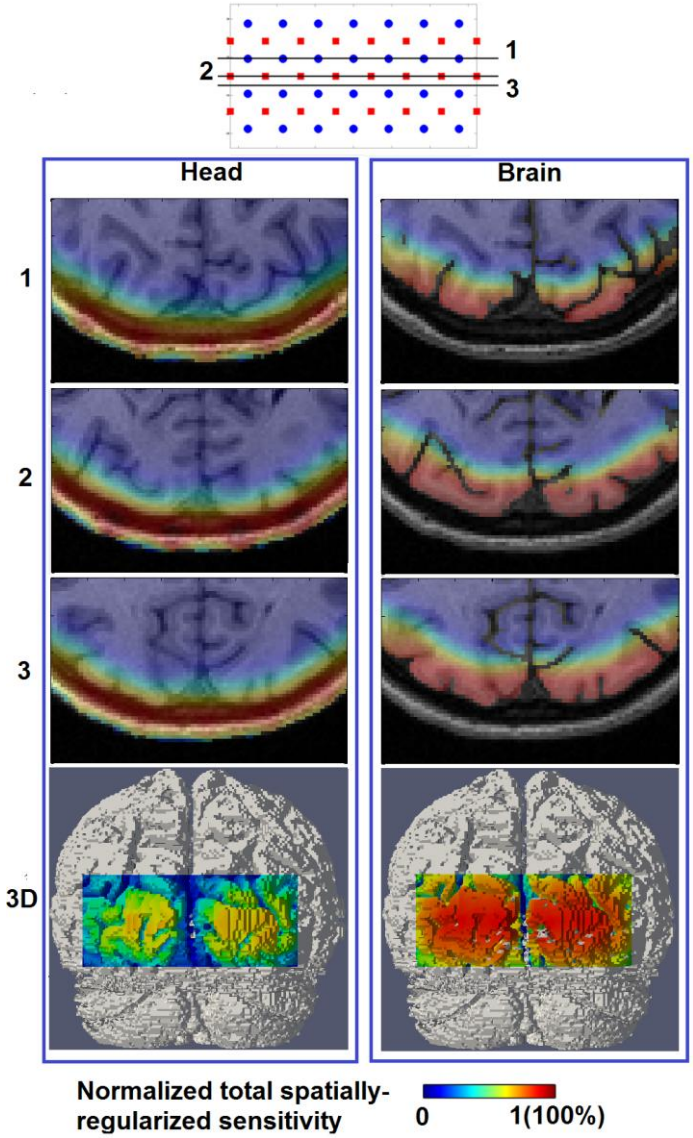


**Figure 34 Total spatially regularised sensitivity (normalised to 1) $\overline{J}_{head}^{total}$ (left column) and $\overline{J}_{brain}^{total}$ (right column) of Subject 1a are shown at three axial MR slice (1,2 and 3) with different positions relative to sources and detectors, and also at posterior view on the 3D cortical surface (bottom row).**

### 5.3.2 Subject 1a vs. Subject 1b

**Figure 35 and 36** show the colour-coded scatter plots of the three defined imaging performance metrics (localisation error, LVHM and focality) versus imaging depth using the unconstrained (Head) and structurally constrained (Brain) reconstruction methods for Subject 1a and 1b respectively. The colour-coded plots have been utilised to identify cases whereby the localisation error is either less than 10 mm (green) or greater than 10 mm (red). We also introduce the concept of 'high image quality zone', which is defined by imaging depths at which the quantified 'mean ± standard deviation' boundary of the image quality metric is within the specified tolerance. From these figures, we can see that the localisation errors between the two subjects are broadly similar: under 'Head' reconstruction, a 'high image quality zone' between 9 mm and 13 mm imaging depth can be identified where localisation error increases from (0.70±0.62) mm to (3.84±6.10) mm for Subject 1a, and (1.17±0.74) mm to (4.43±6.36) mm for Subject 1b; under 'Brain' reconstruction, the 'high image quality zone' reaches up to 13 mm imaging depth where localisation error increases from (0.54±0.67) mm to (3.84±5.97) mm for Subject 1a, and (1.46±1.06) mm to (3.22±8.02) mm for Subject 1b. The integrity of these data is ensured by the focality plots, which are also comparable and consistently above 0.5.

With regard to LVHM: under 'Head' reconstruction, LVHM increases from (563±59) $mm^3$ to (897±215) $mm^3$ for Subject 1a, and (461±59) $mm^3$ to (515±114) $mm^3$ for Subject 1b in the high quality zone; under 'Brain' reconstruction, LVHM increases from (95±42) $mm^3$ to (286±119) $mm^3$ for Subject 1a, and (49±30) $mm^3$ to (158±89) $mm^3$ for Subject 1b. Although in this metric, the numerical values obtained from Subject 1b (as well as Subject 2b-5b, see **Appendix C** for more details) are significantly smaller than those from Subject 1a, it is worth noting that these values are in the '$mm^3$' unit. Specifically if we approximate the PSF under

'Head' reconstruction as a sphere (see **Figure 40** and **41**), then we can convert LVHM into the more conventional full-width-half-max (FWHM) based on the equation for calculating the volume of a sphere:

$$\mathrm{LVHM} = \frac{4}{3}\pi\left(\frac{\mathrm{FWHM}}{2}\right)^3 \tag{1.46}$$

After conversion, under 'Head' reconstruction, FWHM increases from (10.24.±0.35) mm to (11.9±0.9) mm for Subject 1a, and (9.6±0.4) mm to (9.9±0.7) mm for Subject 1b, revealing an average difference of less than 2 mm in FWHM between the two subjects. We believe this scale of differences can be well expected, given the additional hand-correction procedure on tissue segmentation for Subject 1a, as well as the distinctive mesh generation routine used for Subject 1a and 1b. A summary of the above quantified image metrics of the two subjects is provided in **Table 4** below.

**Table 4 Summary of HD-fDOT image quality at the two boundary depths of the 'high image quality zone' (i.e. 9 mm and 14 mm for Head reconstruction; 9 mm and 13 mm for Brain reconstruction) for subjects 1a and 1b respectively.**

| Recon. method | Imaging depth (mm) | Subject 1a | | | Subject 1b | | |
|---|---|---|---|---|---|---|---|
| | | Localisation (mm) | FVHM ($mm^3$) | Focality | Localisation (mm) | FVHM ($mm^3$) | Focality |
| Head | 9 | 0.70±0.62 | 563±59 | 1.00±0.00 | 1.17±0.74 | 461±59 | 1.00±0.00 |
| | 14 | 3.84±6.10 | 897±215 | 0.98±0.09 | 4.43±6.36 | 515±114 | 0.97±0.12 |
| Brain | 9 | 0.54±0.67 | 95±42 | 0.99±0.05 | 1.46±1.06 | 49±30 | 1.00±0.00 |
| | 13 | 3.84±5.97 | 286±119 | 0.76±0.21 | 3.22±8.02 | 158±89 | 0.86±0.21 |

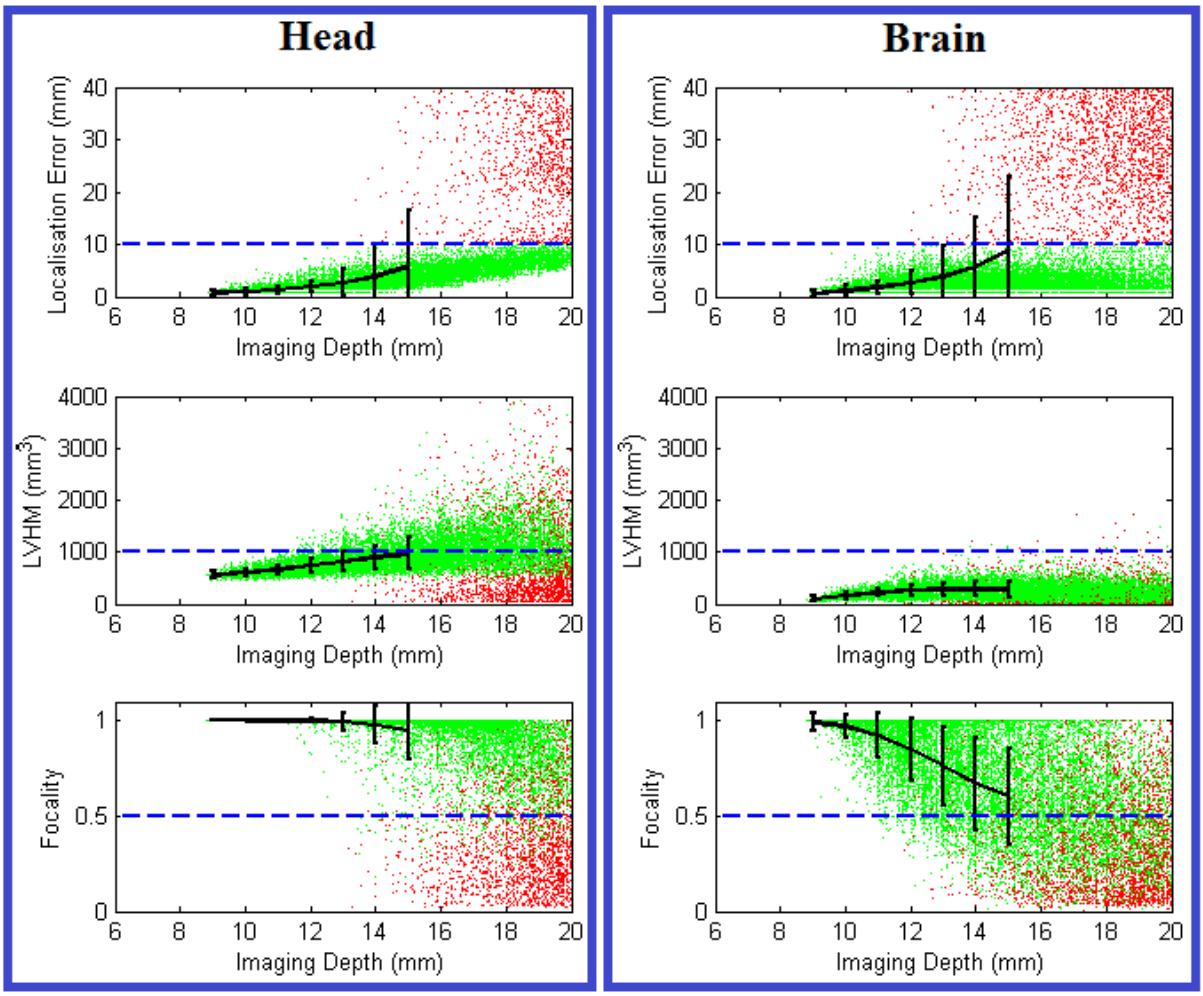


**Figure 35 Scatter plots of localisation error, LVHM and focality versus imaging depth (up to 20 mm) for all PSFs of Subject 1a reconstructed with full head [column (Head)] and whole brain constraint [column (Brain)]. Each dot, which represents a reconstructed PSF, is colour-coded in green if its localisation error is less than 10 mm or otherwise in red. The mean plus/minus standard deviations are reported at 1 mm imaging depth interval (black solid plot) up to 15 mm. The blue dashed line in each figure represents tolerance level for each metric as stated in Section 5.2.10 "Metrics of Image Quality". In all cases the x-axis has been limited to 20 mm for conciseness.**

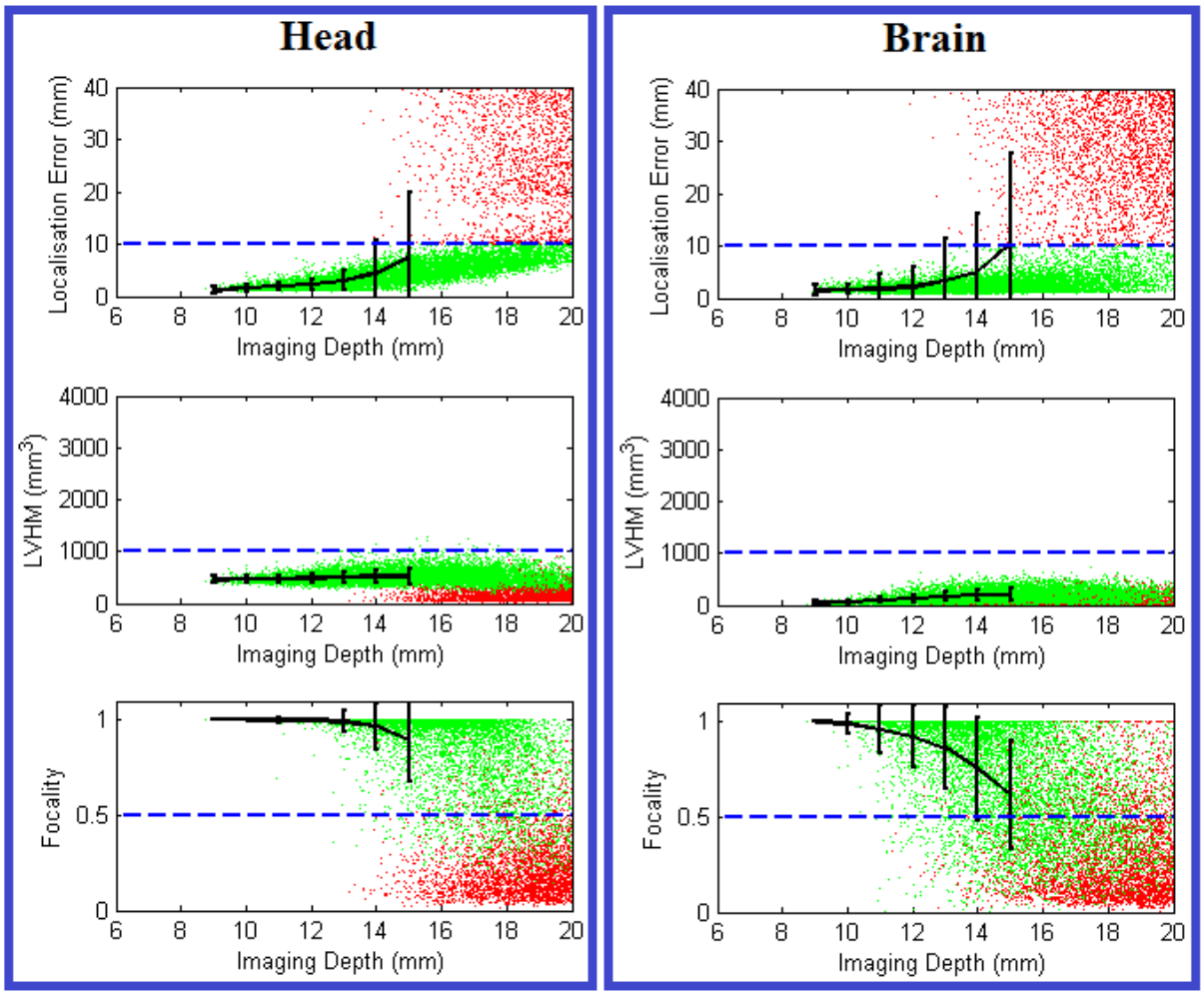


**Figure 36 Same as the last figure, but of Subject 1b.**

### 5.3.3 Head vs. Brain

In **Figure 37**, the scatter plots of metrics of image quality of the six subjects are combined to provide an averaged statistical analysis of image quality across all available subjects. It can be seen that similar to our individual subject plots in **Figure 35** and **36**, within the 'high image quality zone', that is from the cortical surface (from 7 mm imaging depth) up to 13 mm imaging depth, localisation error increases from (1.18±0.77) mm to (3.30±5.37) using 'Head' reconstruction, and from (0.89±0.91) mm to (3.65±8.71) mm using 'Brain' reconstruction. The cortical surface of this figure starts from approximately 7 mm rather than 9 mm as in **Figure 35-36,** because we have included four other subjects (Subject 2b-5b) into the graphs,

which all have different starting depths of the cortical surface. Specifically, the depth from which grey matter node begins to appear for Subject 1a, 1b-5b are 8.8 mm, 8.7 mm, 8.2 mm, 7.1 mm, 7 mm and 8.5 mm respectively (see **Appendix C** for more details). Beyond the 13 mm depth there is a growing number of poor quality PSFs (red dots) appearing in the form of high localisation error, low LVHM and more crucially lower focality, indicating a gradual takeover by imaging artefacts due to poor signal to noise ratio at deeper depths. A summary of the quantified image metrics is provided in **Table 5** below.

**Table 5 Summary of HD-fDOT image quality at the two boundary depths of the 'high image quality zone' (i.e. 7 mm and 13 mm for both Head and Brain reconstructions) of all six subjects combined.**

| Reconstruction Method | 7 mm | | | 13 mm | | |
|---|---|---|---|---|---|---|
| | Localisation (mm) | FVHM ($mm^3$) | Focality | Localisation (mm) | FVHM ($mm^3$) | Focality |
| Head | 1.19±0.78 | 410±65 | 1.00±0.00 | 3.30±5.37 | 564±171 | 0.88±0.24 |
| Brain | 0.89±0.92 | 35±25 | 0.99±0.06 | 3.65±8.71 | 215±113 | 0.62±0.28 |

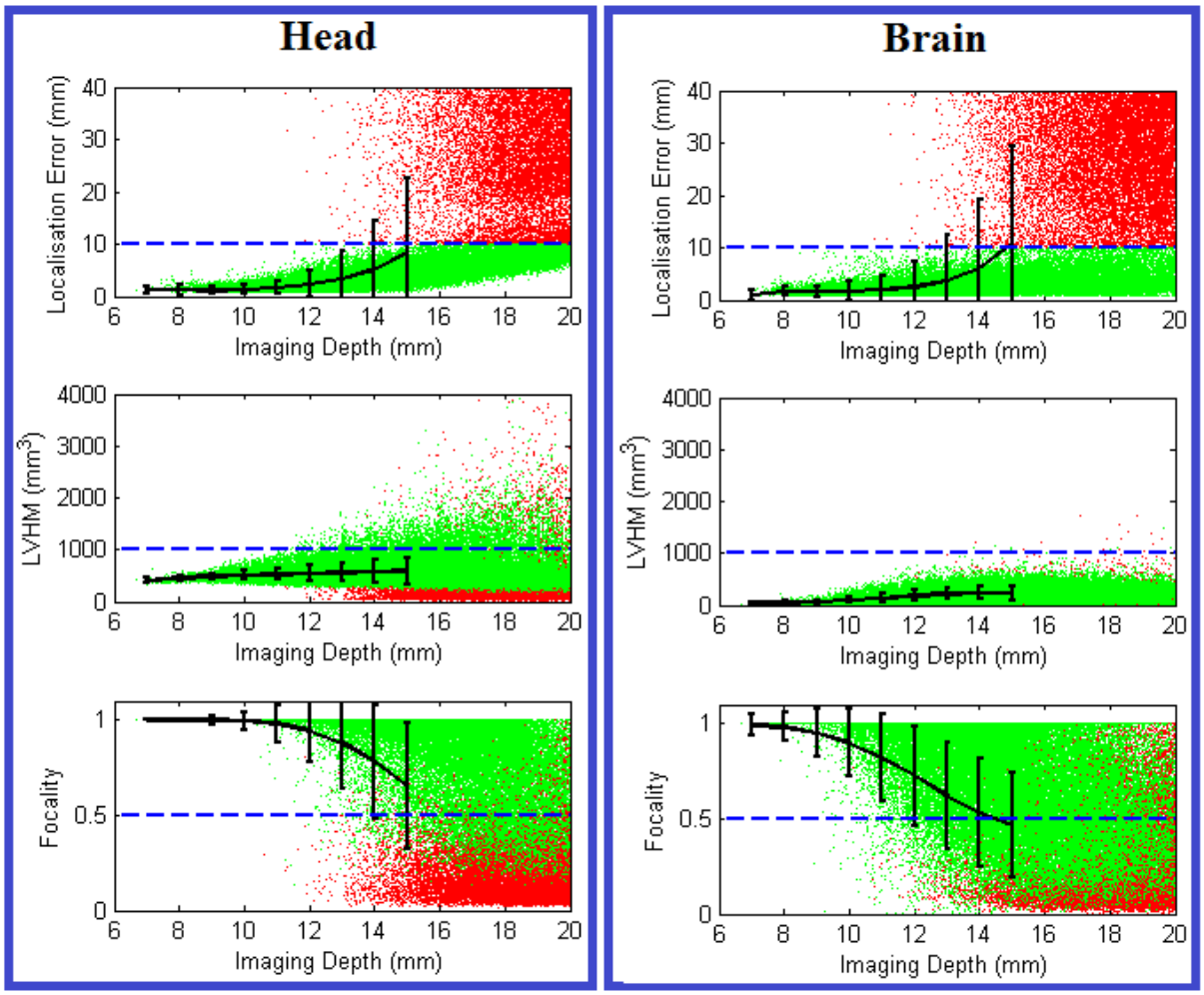


**Figure 37 Same as the last figure, but plotting the PSFs of all six subjects on the same graph. Therefore the mean plus/minus standard deviations statistics quantified in this graph can be considered as the 'average' image quality across all six subjects.**

As an illustrative example, **Figure 38 (Head)** displays the spatial distribution of localisation errors over the corresponding MRI for Subject 1a, where the white solid and dashed lines represents a depth of 13 mm and 18 mm respectively below the scalp. These data points have high integrity because all of the displayed results have a focality value above 0.5 as evident in **Figure 35 (Head)**. A key observation in both **Figure 35 (Head)** and **38 (Head)** is that the localisation error is low and constant for depths up to 13 mm, but increases linearly beyond this depth. This reflects a depth related imaging error, which is also qualitatively demonstrated by selected examples in **Figure 40** and discussed later.

**Figure 38 (Brain)** shows that localisation error of less than 10 mm covers up to 18 mm below the scalp surface with better and more uniform localisation accuracy beyond the 13 mm contour as compared to **Figure 38 (Head),** owing to the improved depth sensitivity. It is worth noting the existence of minor variations in localisation accuracy between spatial locations of the same depth, as revealed in **Figure 38 (Brain),** which is likely to be due to the complicated surface geometry (folds) of the brain (and hence of the applied constraint).

**Figure 39** shows the spatial distribution of LVHM of Subject 1a up to 1000 $mm^3$ on top of the corresponding MRI, where the white solid and dashed lines represent a depth of 13 mm and 18 mm below the scalp respectively. It can be seen that when compared with non-constrained reconstruction, the utilisation of the whole brain constraint dramatically reduces the magnitude of the LVHM throughout the visual cortex. This is substantially evident in the 3D cortical surface maps (**Figure 39**, bottom row), which is in line with the scatter plots shown in **Figure 35**.

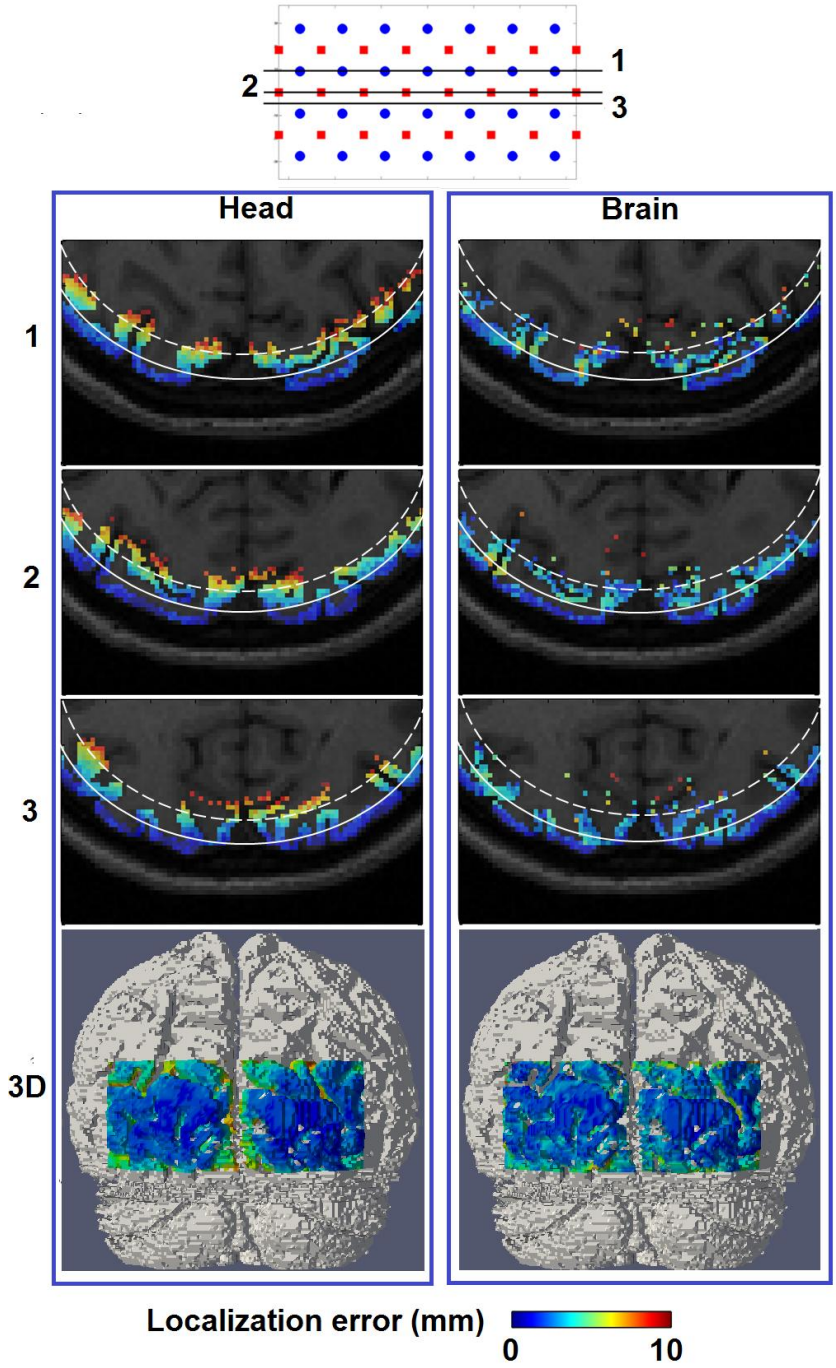


**Figure 38 Spatial distribution of localisation error of Subject 1a with full head (left column) and whole brain constrained (right column) reconstruction. Three axial MRI slices (1, 2 and 3) with different positions relative to sources and detectors are shown, as well as a posterior view on the 3D cortical surface (bottom row). The white solid contour on each MRI slices represents imaging depth of 13 mm below the scalp while the white dashed contour represents imaging depth of 18 mm below the scalp.**

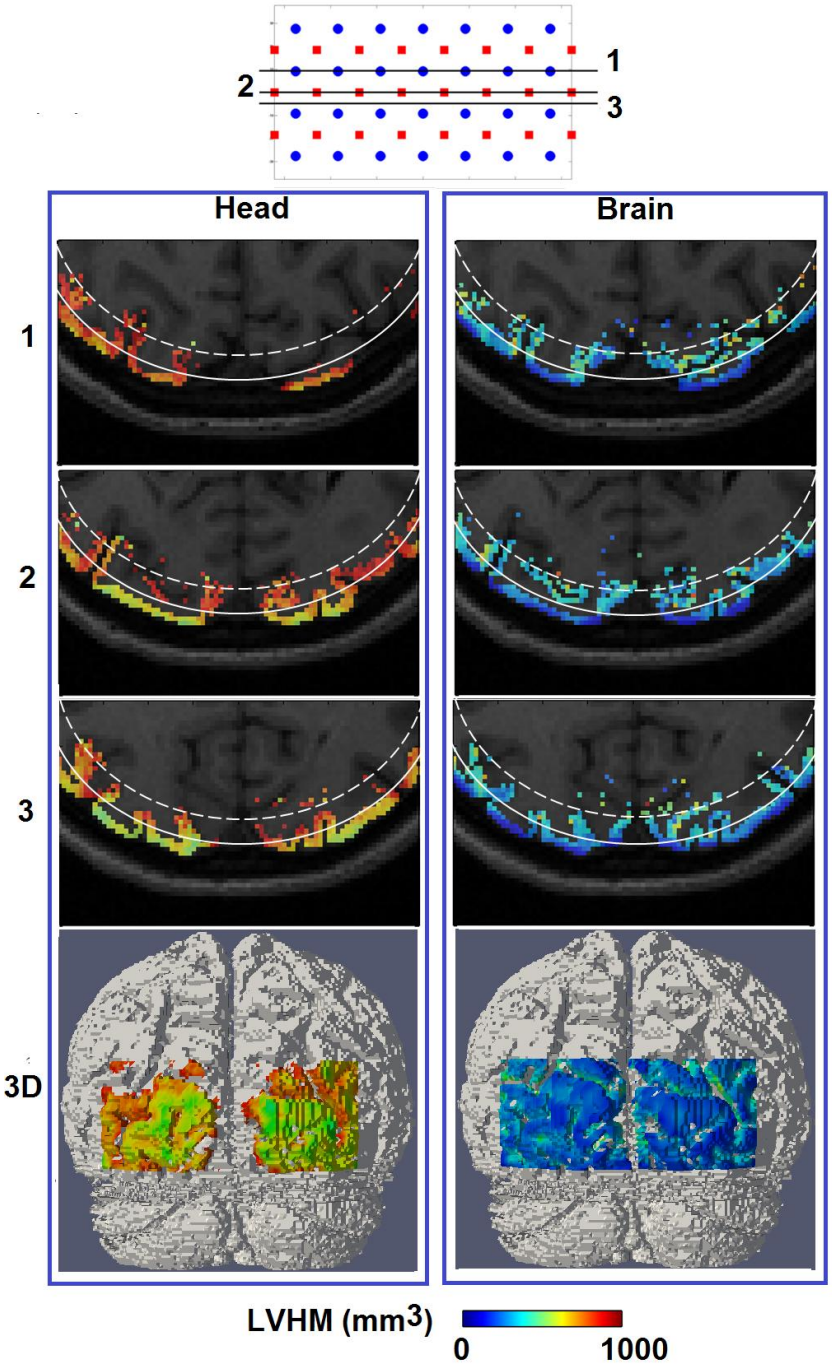


**Figure 39 Same as the last figure but for spatial distribution of localised volume half maximum of Subject 1a.**

## 5.4 Discussions

In this work we have presented a FEM-based routine for conducting subject-specific HD-fDOT studies, and quantitatively evaluated the corresponding image performance throughout the FOV of a realistic imaging system on the visual cortex across six subject head models. The first step of the routine is to construct a high-resolution 3D finite element head model that incorporates realistically segmented tissue spatial information, which requires both T1 and T2 (MRI datasets) from the subject and an appropriate tissue segmentation procedure, as shown in **Figure 29-30**. Comparing with using simplified generic head models [5, 36, 37, 45], this approach reduces the systematic imaging error due to model mismatch between the *in vivo* anatomy and the anatomical model used for image reconstruction. After a spatial regularisation scheme is applied, the full head total sensitivity is shown to have high sensitivities (larger than 50% of maximum value) covering non-brain regions and no further than superficial regions of the cortex (**Figure 34 (Head)**). This reveals a deeper sensitivity coverage than the Dehghani et al. study which reported total sensitivity on the cortical surface at 10% of maximum value [123]. However the head model used in that study was based on fewer segmented regions, which were also less complex in structure.

The reconstructed PSF for each grey matter node within the FOV is evaluated by three metrics of image quality. Traditionally FVHM and localisation error have been the standard metrics for evaluating imaging quality. We have demonstrated that in presence of noise where multi-regional activations are reconstructed, the FVHM may not be the best metric as it is not trivial to isolate the true recovered activation from background noise and artefacts. Therefore we have introduced two other metrics, namely LVHM and focality, which aim to provide a more comprehensive and systematic approach in the evaluation of the image quality. We have found that in presence of noise these parameters provide a more consistent evaluation of

image quality when used in conjunction with localisation error, as compared to FVHM and localisation error only.

Across all six subjects we have reported a 'high quality region' down to 13 mm imaging depth below the scalp (**Figure 37**), based on defined thresholds of each image quality metric. Localisation error and FWHM (as derived from LVHM using **Equation (1.45)**) at 10 mm imaging depth are (1.31±0.76) mm and (9.92±0.6) mm respectively, which are within good agreement with White et al.'s findings on a simplified head model [5].

When a whole brain constraint is applied within the image recovery algorithm, the total sensitivity yields a more homogenous spread of sensitivities on the 3D cortical FOV (**Figure 34 (Brain)**). Consequently focal activation up to 18 mm below the scalp can be better localised as shown quantitatively by metrics of image quality in **Figure 38 (Brain)**. This improvement in localisation depth has not been evaluated in any other previous study, highlighting the utility and benefit of this approach.

If an image quality goal is set at better than 10 mm in localisation accuracy and image resolution, these comprehensive simulations suggest that HD-fDOT is capable of imaging focal activations within the visual cortex up to 13 mm below the scalp using full head reconstruction (**Figure 38-39 (Head))**, and up to 18 mm using whole brain constrained reconstruction (**Figure 38-39 (Brain))**. Both depths roughly correspond to the 30% contour in their respective total spatially-regularised sensitivity as illustrated in **Figure 34**.

It can also be observed that the lack of spatial constraint pulls the activations towards the scalp surface where the measurement sensitivities are higher, sacrificing 5 mm imaging depth capability and image resolution which is also in line with previous study [70]. Such phenomena can be qualitatively demonstrated in **Figure 40 (Head)**: while a perturbation

moves from location X to Z, its recovered location stops moving beyond the 13 mm contour. Effectively at location Z the PSF is pulled towards the skull/scalp region where the sensitivities are much higher (see **Figure 34 (Head)**). Thus the degradation in localisation accuracy after 13 mm imaging depth as observed in **Figure 35 (Head)** and **38 (Head)** represents a stronger effect on the depth accuracy than the lateral localisation accuracy. On the other hand, localisation error at given depths (regardless of lateral locations), shows good consistency in **Figure 38 (Head). Figure 41 (Head)** confirms this finding by showing the recovered activations at three similar depths but different lateral location (I, J, K). Specifically **Figure 41 (Brain)** demonstrates that while the whole brain constraint biases the recovery of activations towards a deeper depth, their localisation errors are 5.8 mm (I), 2.8 mm (J) and 3.0 mm (K) respectively, all below the 10 mm tolerance.

In terms of imaging resolution, when using the whole brain constraint for image recovery, a more homogenous distribution of LVHM at lower than 1000 $mm^3$ up to 18 mm imaging depth, as evident in **Figure 35 (Brain)** and **39 (Brain)**, provides the capability to distinguish between gyri as shown by activation X in **Figure 40 (Brain),** and between gyrus and sulcus as shown by activation K in **Figure 41 (Brain)**. Finally the 3D cortical surface maps of localisation error and LVHM in **Figure 38-39 (Brain)** also illustrate a much more homogeneous distribution of image accuracy and resolution throughout the FOV on the visual cortex as compared with **Figure 38-39 (Head).**

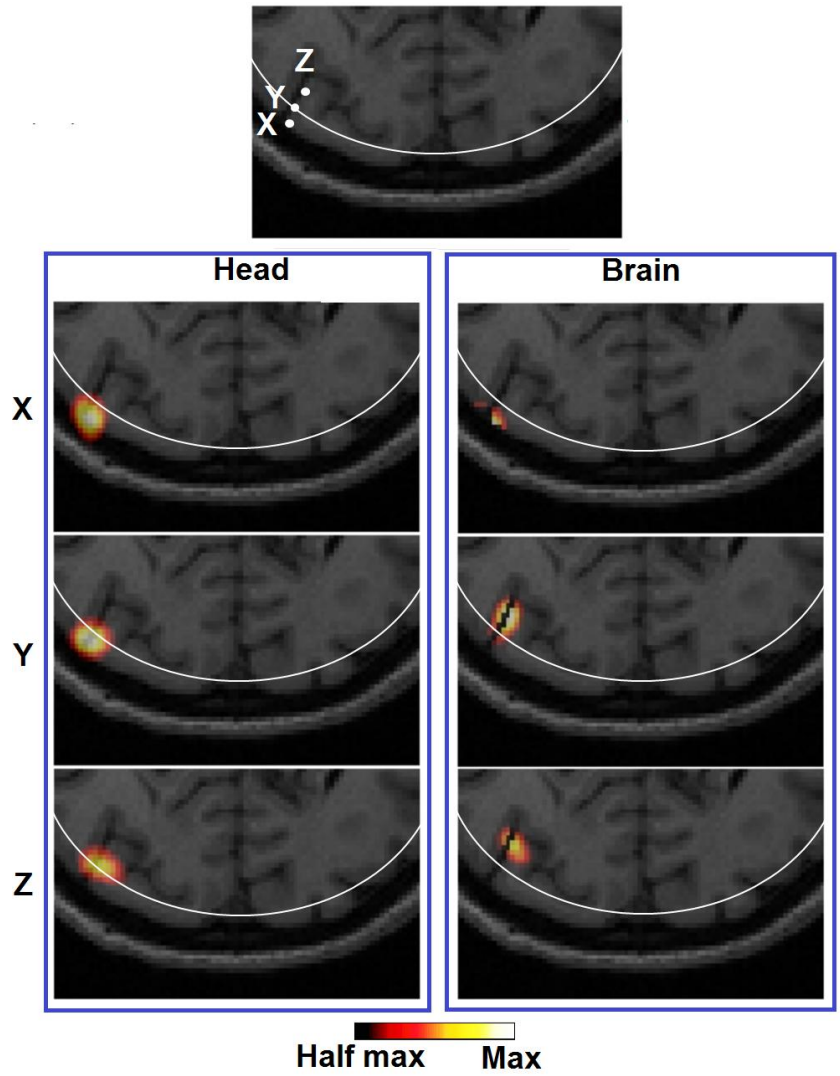


**Figure 40 Image of three target perturbations located along the same cortical fold but different depth in Subject 1a: 10.22 mm (X), 13.14 mm (Y), and 18.13 mm (Z), and the corresponding PSFs shown at FVHM using full head [column (Head)] and 'whole brain constraint' (column [Brain]) reconstruction. The white contour on each MRI slice represents the 13 mm imaging depth.**

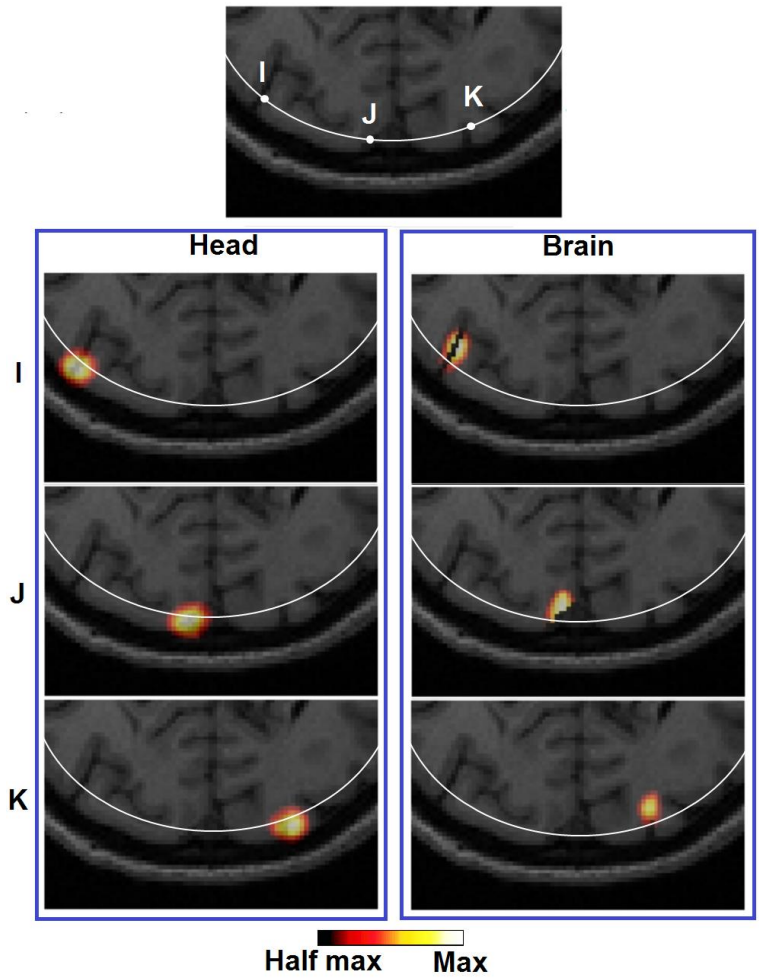


**Figure 41 Image of three target perturbations located at different lateral positions but similar depth in Subject 1a: 13.14 mm (I), 13.01 mm (J), and 13.07 mm (K), and the corresponding PSFs shown at FVHM using full head [column (Brain)] and whole brain constrained [column (Head)] reconstruction. The white contour on each MRI slice represents the 13 mm imaging depth.**

The work presented in this study, for conciseness, is limited to a single NIR wavelength, and parameters relating to errors such as probe placements and variations to underlying optical properties are ignored. The choice of using single wavelength (750 nm in the presented work) is appropriate, since most systems rely on single wavelength measurements for the recovery of optical parameters and the methods and findings can easily be expanded to other wavelengths (for example, to 800 nm and 850 nm in later **Chapter 6** and **7** respectively). In

addition, the image performances (i.e. all three image quality metrics) as reported herein, are directly associated with the values of the spatial and Tikhonov regularisation parameters being used as stated in **Section 5.2.7**. Therefore we expect the image performance to vary should these regularisation parameters change. Although the assumptions regarding the probe placements, and underlying tissue optical properties (which will be investigated in the next chapter), are important when relating any findings to clinical applications, it is critically important to understand the underlying physical limits of optical parameters recovery when utilising HD-fDOT for functional neuroimaging studies, as presented in this study.

## 5.5 Conclusions

Our multi-subject simulation studies have shown that HD-fDOT methods that incorporate realistically-segmented subject-specific head models are capable of imaging focal haemodynamic response up to 18 mm below an adult human scalp using whole brain constrained reconstruction within 10 mm localisation accuracy and image resolution, which would allow the distinguish-ability of gyri. Yet further yield in image quality can be expected via the utility of more overlapping measurements, for instance up to fourth and fifth nearest neighbours, as the dynamic range of future HD-fDOT systems increases, or imaging on subjects with less optically absorptive head tissues, e.g. neonates and young children. The results presented herein provide the first comprehensive study in evaluating the image resolution and localisation accuracy of HD-fDOT with subject-specific head models and the use of whole brain constrained reconstruction. This work can serve as guidance on what image quality to expect throughout the cortical folds and approaches that might be taken to validate with fMRI.

# CHAPTER 6

# EFFECT OF UNCERTAINTY IN TISSUE OPTICAL PROPERTY – BACKGROUND ABSORPTION FITTING SCHEME

## 6.1 Introduction

fDOT image reconstruction accuracy depends on multiple factors, such as system design, data processing, computational model and inverse formula, which have been comprehensively discussed in **Chapter 4**. One of the concerning issues is the anatomical model of the human head, which has evolved from the homogeneous slab geometry of the early days into the increasingly popular realistically-segmented subject-specific head model, as reviewed in **Section 4.2.2**. Specifically in magnetic resonance imaging (MRI)-guided HD-fDOT as described in the last chapter, where both T1 and T2-weighted datasets are available, three-dimensional (3D) anatomical head models containing up to five segmented tissue types can be utilised as the underlying anatomical model for image reconstruction. With disregard to misclassification of head tissues, or assuming that perfect tissue segmentation is possible, the uncertainty in the numerical value of tissue optical property becomes the dominant cause of systematic error in the predicted measurement sensitivity and the reconstructed images.

Current practice as documented in *in vivo* fDOT literature, which selects or derives numerical value of tissue optical property from other literature-based data, does not account for the following three aspects of uncertainty or variability. First of all, literature-published values are derived by interpreting measurements obtained through specific experimental procedures and based on certain photon transport models. Consequently there is an inherent degree of uncertainty in the value being derived, which is highly dependent on specific model assumptions, measurement techniques, experimental apparatus, calibration scheme, and biological heterogeneity [150]. This means that optical properties obtained through different procedures, even from the same subject, could vary. Secondly, variation between subjects is also expected (due for examples to demographics), and the direct use of literature-based data in subject-specific studies does not account for subject variability. Third, literature often reports data at limited choices of wavelengths [148, 149], and linear interpolation has been utilised to approximate values at other wavelengths [5, 36], which inevitably introduces another degree of uncertainty to the final numerical values used for image reconstruction. In this work we propose the use of background absorption fitting schemes with measurements obtained directly from the imaging subject during a typical fDOT scan and at no extra cost on data collection, which provides a procedure-specific, subject-specific and wavelength-specific approach that effectively eliminates the three uncertainty issues surrounding the current literature-based practice.

The effect of uncertainty in the optical properties of background media in the linear (or differential) DOT problem was initially investigated by Cheng and Boas [151], who focused on the imaging error in the recovered image contrast rather than image resolution and localisation accuracy. Pei et al. [30] further demonstrated a robust variation tolerance of (nearly) ±100% in either background absorption $\mu_a$ or scattering $\mu_s'$ that would still allow

qualitatively similar images to be produced in linear (or differential) DOT simulations. However the study was limited to a two-dimensional simple circular model, and both transmittance and reflectance measurements were used for noise-free image reconstruction. More recently Heiskala et al. [6] investigated the topic more purposefully for the application of fDOT of the human brain, but only considered a limited number of simulated focal activations. More importantly, none of these studies include the scenario of structural-constrained image reconstruction, which has been shown to demonstrate improved localisation accuracy and image resolution in HD-fDOT from our findings in the last chapter.

In this work we extend the realistic-noise-added PSF analysis in **Chapter 5** to a multi-model comparative study that provides a more comprehensive investigation in the effect of uncertainty in background optical properties on HD-fDOT image quality, with and without the inclusion of whole brain constraint in image reconstruction. In additional, we are also interested in validating our hypothesis for the use of background absorption fitting schemes, which hypothesizes that the schemes can be applied to derive tissue optical properties that result in better HD-fDOT image quality than literature-based approaches. There are five models included in this comparative study, which represent the following scenarios: (A) precisely correct background optical properties (‘ground truth’), (B) homogeneous optical properties derived from our homogeneous background absorption fitting scheme, (C) heterogeneous optical properties derived from our heterogeneous background absorption fitting scheme, (D) homogeneous optical properties cited from literature [42], (E) heterogeneous optical properties cited from literature [152]. Each scenario is evaluated using the three image quality metrics described in the last chapter to provide comprehensive and systematic comparison of image quality between each other.

## 6.2 Method

### 6.2.1 Homogeneous background absorption fitting scheme

The homogeneous absorption fitting scheme was originally described in nonlinear (absolute) DOT of breast imaging in [31]. The role of the scheme was to provide a 'good homogeneous initial guess' $\mu_0$ of the underlying tissue optical properties for the Levenberg-Marquardt nonlinear optimisation procedure (as reviewed in **Section 4.3.1.1**) so that the minimisation function is likely to converge quickly in fewer iterations. In fDOT application of human brain, we propose the use of homogeneous background absorption fitting scheme to provide a fast yet subject-specific approximation of the underlying head tissue optical properties to minimise the uncertainty in literature-based background optical properties and the resulting systematic imaging error .

Specifically the scheme is applied to fit a homogeneous background absorption value for the underlying imaging subject based on a single set of measurements from the subject, that is, one data per measurement channel across all available channels. In order to improve the robustness of this scheme against measurement noise, this single dataset is often computed as the averaged data across multiple sets of measurements in diffuse optical breast imaging [31, 153]. In our case where a participant is sitting for a visual stimulation experiment while all data channels of the fDOT imaging system are taking continuously data recording throughout the time course of the experiment, we have proposed a similar procedure that computes this dataset as the averaged data over the recorded time trace at each channel, which potentially implies averaging over thousands sets of data, given a data collection rate of 10 Hz and an imaging session of 10 minutes, for instance.

For our simulation study, we have modelled the same high-density imaging system as used in **Chapter 5** except changing the measuring wavelength from 750 nm to 800 nm. This is because one set of literature-based data as used later in our multi-model comparative study (model E in **Table 7**) are values at 800 nm, which constrains our selection to this wavelength only. The corresponding head tissue optical properties used for 800 nm wavelength are listed in **Table 6** under 'Ground truth', which are linearly interpolated values from [38]. To generate realistic-noise-added measurements for our background absorption fitting scheme, we have taken the following steps: first, the noiseless boundary measurements $\ln(\Phi)(noiseless)$ are generated using the forward solver ('femdata' function) in Nirfast [119]. Next, 0.1%, 0.14% and 1% Gaussian random noise are added to first, second, and third nearest neighbours in $\ln(\Phi)(noiseless)$ to produce $\ln(\Phi)(baseline)$, which represent the data collected from a realistic imaging system at a 'baseline' functional state, that is, when no visual stimulus is shown to the participant. We then compute the realistic-noise-added differential measurement $\Delta\ln(\Phi)$ as described previously in **Section 5.2.9**, which represent the differential change in the measured data between the 'baseline', and an 'activation' functional state, which could be when visual stimuli are displayed and perceived by the participant. Therefore by combining $\Delta\ln(\Phi)$ with $\ln(\Phi)(baseline)$ we can derive $\ln(\Phi)(activation)$, which is the noise-added boundary data collected at certain 'activation' functional state. We repeat this for all simulated perturbations within the system FOV on the visual cortex (as in the last chapter), which should reflect on all possible sets of measurements contained within the recorded data time trace during a standard *in vivo* visual stimulation experiment. Finally we compute the average of the 'baseline' dataset $\ln(\Phi)(baseline)$ and all available 'activation' datasets $\ln(\Phi)(activation)$ as the single set of measurements to be used for background absorption

fitting scheme. **Figure 42 (a) and (b) 'Original'** show the averaged dataset derived from Subject 1b, and the procedures are repeated for all six subjects (Subject 1a, 1b-5b).

After this, the homogeneous background absorption fitting scheme is performed. In this case we assume a constant global background reduced scattering coefficient $\mu_s'$ of 1.0 $mm^{-1}$, which was commonly applied in human tissue optics studies [42, 98, 151]. In principle, the scheme derives the global absorption coefficient $\mu_a$ by fitting for the slope of the log of intensity times distance $\ln(\Phi * r)$ with respect to the straight-line source-detector distance *r*, denoted by $\phi = \frac{d\ln(\Phi * r)}{dr}$, as shown in **Figure 42 (a)**. This is based on the following analytical expression derived for infinite medium and CW measurements, which suggests that $\mu_a$ is proportional to $\phi$ given a constant $\mu_s'$ [153]:

$$\phi = \frac{d\ln(\Phi * r)}{dr} = \sqrt{\frac{\mu_a}{D}} \tag{1.47}$$

where *D* is the diffusion coefficient as described in **Chapter 4**. In practice, the scheme consists of two stages. The first stage fits for $\mu_a$ based on the analytical solution as expressed by **Equation (1.47)**. This value is then taken as an initial guess into the second stage, which is an iterative fitting process where $\phi$ is calculated through linear regression to boundary data generated from our subject-specific head model using the Nirfast forward solver, as shown in **Figure 42 (b) 'Fitted'**. This iterative fitting utilises Newton's method of the following form:

$$\mu_{a,i+1} - \mu_{a,i} = \delta\mu_a = \frac{\phi(\mu_{a,i}) - \phi(\mu_{a,i+1})}{\frac{\partial\phi(\mu_{a,i})}{\partial\mu_a}} \tag{1.48}$$

where $\frac{\partial\phi(\mu_{a,i})}{\partial\mu_a}$ is approximated numerically by $\frac{\phi(\mu_{a,i})-\phi(\mu_{a,i}+\delta)}{\delta}$ and $\delta$ is set to be 0.0001. This two-stage fitting scheme is implemented in the 'fit_data_cw' function in Nirfast and the iteration terminates when the change in the fitted $\mu_a$ between two iterations is less than 0.1%. This takes approximately 1 hour on average for each subject and the results are summarised in **Table 6**. We can see that the fitted background absorption coefficients across all subjects are closely comparable, with a mean value of 0.0122 $mm^{-1}$ and standard deviation of 1.2%.

**Table 6 Homogeneous background absorption fitting assuming $\mu_s'$ of 1.0 $mm^{-1}$.**

| $\mu_a$ ($mm^{-1}$)/ $\mu_s'$ ($mm^{-1}$) | **Ground truth** | 1a | 1b | 2b | 3b | 4b | 5b | **Mean±Std** |
|---|---|---|---|---|---|---|---|---|
| Scalp | **0.018/ 0.69** | 0.0119/ 1.0 | 0.0121/ 1.0 | 0.0122/ 1.0 | 0.0122/ 1.0 | 0.0123/ 1.0 | 0.0123/ 1.0 | **0.0122±1.2%/ 1.0** |
| Skull | **0.01275/ 0.89** | | | | | | | |
| CSF | **0.004/ 0.3** | | | | | | | |
| Grey Matter | **0.0186/ 0.75425** | | | | | | | |
| White Matter | **0.01875/ 1.1** | | | | | | | |

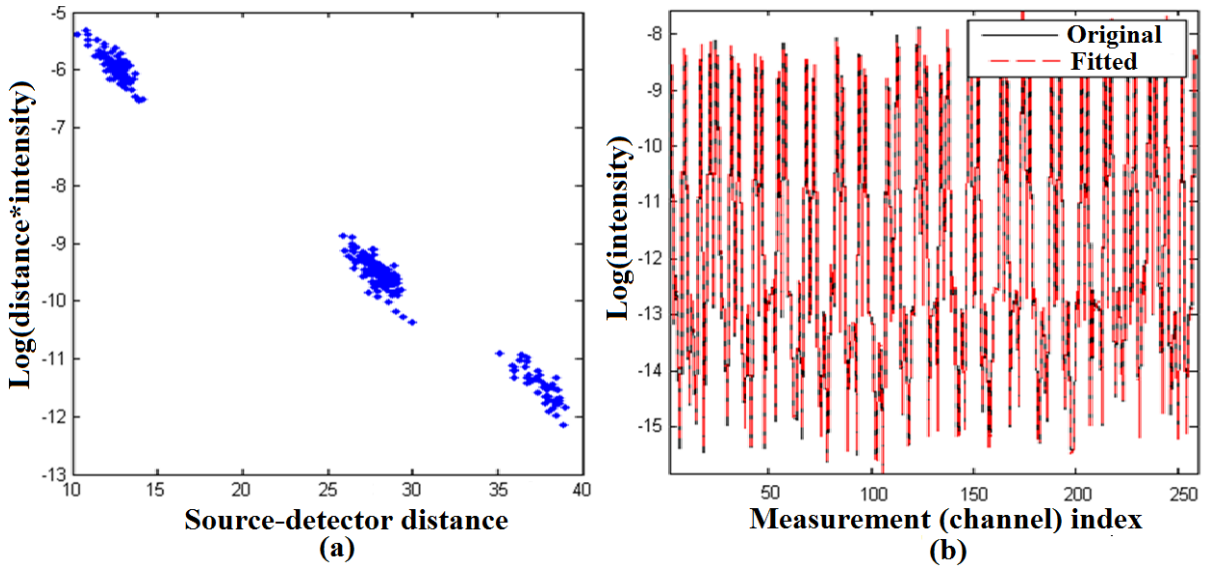


**Figure 42 Subject 1b: (a) Scatter plot of log of source-detector distance times intensity versus source-detector distance; (b) simulated noise-added average log intensity for each of the 260 measurements ('Original') and corresponding homogeneous fitted measurements ('Fitted').**

### 6.2.2 Heterogeneous background absorption fitting scheme

In addition to the homogenous background absorption fitting scheme, we have also tested a heterogeneous background absorption fitting scheme using the 'reconstruct_stnd_cw_region' function in Nirfast. This is also known as the 'hard prior' image reconstruction in nonlinear DOT (such as breast imaging), where a region-based approach is taken to reduce the recovered parameter space to the number of specified regions in the imaging domain [154]. Specifically, tissue absorptions are still recovered iteratively using the LM method given by **Equation (1.30)** or **(1.31)** but with a new, region-based Jacobian $\tilde{J}$ having the dimension of NM by NR (number of regions) instead of NM by NN as $J$ in **Equation (1.33)** or **(1.34)**. This is achieved by multiplying $J$ with a region mapping matrix $R$:

$$\tilde{J} = J \cdot R \tag{1.49}$$

where $R$ has the dimension of NN by NR. Effectively $R$ adds the sensitivity of all the nodes that belong to each specific region in $J$ to produce $\tilde{J}$. In our application of MRI-guided HD-fDOT study, this scheme would fit an absorption value for each of the five head tissue regions iteratively until the change in projection error (projection error is defined by the difference between the fitted measurements, **Figure 42 (b) 'Fitted'**, and the original measurements, **Figure 42 (b) 'Original'**) between two iterations is less than 2%. We first validate the scheme with the correct $\mu_s'$ in each tissue region, which takes on average 5 hours per subject. Although this takes significantly longer time than the homogeneous fitting scheme, the fitted absorption values are within 2.5% variation of the ground truth across all subjects as shown in **Table 7**, which are promising. The largest variation of 2.5% comes from the fitted CSF of Subject 3b, where the correct value is 0.004 $mm^{-1}$ and the fitted value is 0.0039 $mm^{-1}$.

**Table 7 Heterogeneous background absorption fitting assuming correct $\mu_s'$ in each region.**

| $\mu_a$ ($mm^{-1}$)/ $\mu_s'$ ($mm^{-1}$) | **Ground truth** | 1a | 1b | 2b | 3b | 4b | 5b |
|---|---|---|---|---|---|---|---|
| Scalp | **0.018/ 0.69** | 0.018/ 0.69 | 0.018/ 0.69 | 0.018/ 0.69 | 0.018/ 0.69 | 0.018/ 0.69 | 0.018/ 0.69 |
| Skull | **0.01275/ 0.89** | 0.0128/ 0.89 | 0.0128/ 0.89 | 0.0128/ 0.89 | 0.0128/ 0.89 | 0.0128/ 0.89 | 0.0128/ 0.89 |
| CSF | **0.004/ 0.3** | 0.004/ 0.3 | 0.004/ 0.3 | 0.004/ 0.3 | 0.0039/ 0.3 | 0.004/ 0.3 | 0.004/ 0.3 |
| Grey Matter | **0.0186/ 0.75425** | 0.0186/ 0.75425 | 0.0186/ 0.75425 | 0.0186/ 0.75425 | 0.0186/ 0.75425 | 0.0186/ 0.75425 | 0.0186/ 0.75425 |
| White Matter | **0.01875/ 1.1** | 0.0188/ 1.1 | 0.0188/ 1.1 | 0.0188/ 1.1 | 0.0188/ 1.1 | 0.0188/ 1.1 | 0.0188/ 1.1 |

However it is important to realise that under *in vivo* experimental circumstances, the correct value of $\mu_s'$ for each tissue type in the imaging subject is unlikely to be available. Therefore we further test the heterogeneous fitting scheme with the generic global $\mu_s'$ of 1.0 $mm^{-1}$ used

previously for the homogeneous fitting scheme. In this case it takes less time (approximately 3 hours on average) but the fitted $\mu_a$ values are significantly different from the ground truths as shown in **Table 8**. Specifically, the largest mismatch between the correct value and the average fitted value across all subjects comes from the scalp at -43% (the correct value is 0.018 $mm^{-1}$ and the average fitted value is 0.0102 $mm^{-1}$). However it is worth noting that such variation in the fitted absorption values should be well expected, since the precondition of setting a global $\mu_s'$ of 1.0 $mm^{-1}$ has posed a mismatch in the scattering parameter. In the case of the scalp, the mismatch in $\mu_s'$ is greater than +75% (the correct value is 0.69 $mm^{-1}$ and the assumed generic value is 1.0 $mm^{-1}$), which explains the variation in absorption. It can also be seen that the standard deviation across all subjects increases with tissue depth, from 3% for the scalp to 37% for the white matter, except the CSF which has ultra low absorption and scattering properties compared to other tissue types and therefore more difficult to recover anyway. These suggest that the derived absorption parameters have lower cross-subject variation for the superficial tissues (standard deviation: scalp: 3%; skull: 8%) where the measurement sensitivity is higher, than the deeper tissues (standard deviation: grey matter: 12%; white matter: 37%) where the measurement sensitivity is lower, which is intuitive.

**Table 8 Heterogeneous background absorption fitting assuming homogeneous $\mu_s'$ of 1.0 mm$^{-1}$.**

| $\mu_a$ (mm$^{-1}$)/ $\mu_s'$ (mm$^{-1}$) | **Ground truth** | 1a | 1b | 2b | 3b | 4b | 5b | **Mean±Std** |
|---|---|---|---|---|---|---|---|---|
| Scalp | **0.018/ 0.69** | 0.0098/ 1.0 | 0.01/ 1.0 | 0.0107/ 1.0 | 0.0102/ 1.0 | 0.0104/ 1.0 | 0.0102/ 1.0 | **0.0102±3%/ 1.0** |
| Skull | **0.01275/ 0.89** | 0.0122/ 1.0 | 0.0119/ 1.0 | 0.0096/ 1.0 | 0.0116/ 1.0 | 0.0106/ 1.0 | 0.0113/ 1.0 | **0.0112±8%/ 1.0** |
| CSF | **0.004/ 0.3** | 0.0006/ 1.0 | 0.0083/ 1.0 | 0.0092/ 1.0 | 0.0067/ 1.0 | 0.0077/ 1.0 | 0.0003/ 1.0 | **0.0055±73/ 1.0** |
| Grey Matter | **0.0186/ 0.75425** | 0.0169/ 1.0 | 0.0162/ 1.0 | 0.0164/ 1.0 | 0.0123/ 1.0 | 0.0167/ 1.0 | 0.018/ 1.0 | **0.016±12%/ 1.0** |
| White Matter | **0.01875/ 1.1** | 0.0114/ 1.0 | 0.0157/ 1.0 | 0.0161/ 1.0 | 0.0293/ 1.0 | 0.0133/ 1.0 | 0.0164/ 1.0 | **0.017±37%/ 1.0** |

### 6.2.3 Model description

As briefly described in the Introduction, there are five models to be presented in this work and the tissue optical properties used for each model are listed in **Table 9** below. Specifically, model A is a heterogeneous model that represents the ground truth with optical properties derived from [38] at 800 nm wavelength; model B is a homogeneous model with optical properties derived using the homogeneous background absorption fitting scheme from model A, **Table 6**; model C is a heterogeneous model with optical properties derived using the heterogeneous background absorption fitting scheme from model A, **Table 8**; model D is a homogeneous model with optical properties cited from literature [42]; model E is a heterogeneous model with optical properties cited from literature [152]. Here it is worth noting that model D represents a case in which tissue absorptions (except CSF) have been severely underestimated, as compared to the ground truth (model A). On the other hand, model E represents a scenario where both absorption and scattering (except CSF absorption and scattering, and white matter absorption) have been significantly overestimated against

model A. Nevertheless all three datasets can be rightly justified based on their respective literature, which provides further evidence of the uncertainty issues in background tissue optical properties that surround current literature-based approaches.

**Table 9 The five hypothetical models presented with optical properties at 800 nm.**

| $\mu_a$ (mm$^{-1}$)/ $\mu_s'$ (mm$^{-1}$) | A (Ground truth [38]) | B (Homog 1) | C (Heterog 1) | D (Homog 2 [42]) | E (Heterog 2 [110]) |
|---|---|---|---|---|---|
| Scalp | 0.018/ 0.69 | 0.0122/ 1.0 (From **Table 6**) | (Depending on subject as shown in **Table 8**) | 0.006/ 1.0 | 0.04/ 2.0 |
| Skull | 0.01275/ 0.89 | | | | 0.04/ 2.0 |
| CSF | 0.004/ 0.3 | | | | 0.001/ 0.01 |
| Grey Matter | 0.0186/ 0.75425 | | | | 0.025/ 2.5 |
| White Matter | 0.01875/ 1.1 | | | | 0.005/ 6.0 |

### 6.2.4 Comparative point-spread-functional analysis

Detailed procedures of performing our realistic-noise-added PSF analysis on a single model have been described in **Chapter 5**. However in this five-model comparative study, since the aim is to investigate the effect of uncertainty (or inaccurate) in background tissue optical properties on the resultant image quality, we need to mimic the scenario where the differential data $\Delta\ln(\Phi)$ and the measurement sensitivity matrix $J$ to be used for image reconstruction come from mismatched models. Specifically in this study, we let $\Delta\ln(\Phi)$ used in the PSF analysis for all five models (model A-E) to be the same, which is generated from model A (the 'ground truth'). In this case, the reconstructed result from model A is also known as the 'inverse crime'.

## 6.3 Results

### 6.3.1 Head reconstruction

In **Figure 43**, the scatter plots of metrics of image quality of the six subjects are combined to provide an average statistical analysis of image quality for model A-E (See **Appendix D.1** for individual Subject 1a, 1b-5b). Similar to the last chapter, we define 'high image quality zone' as imaging depths up to which the quantified 'mean ± standard deviation' boundary of the image quality metric is within the specified tolerance. Across all three image quality metrics, we have observed extremely similar imaging performance among models A, B and C. Specifically, a 'high image quality zone' up to 13 mm imaging depth can be defined among models A to C, where the localisation error at 13 mm image depth is (3.45±5.67) mm for model A, (3.30±5.42) mm for model B, and (3.75±6.06) mm for model C; the FVHM at 13 mm image depth is (569±178) $mm^3$ for model A, (596±182) $mm^3$ for model B, and (410±234) $mm^3$ for model C; the focality at 13 mm image depth is (0.86±0.25) for model A, (0.86±0.26) for model B, and (0.88±0.22) for model C, which are all within their respective tolerance levels (blue dotted lines). These are also evident in **Figure 44-46, A-C**, where the three image quality metrics are plotted spatially over the corresponding MRI slices, and the graphs between model A, B and C in these figures are visually difficult to distinguish.

Model D, as compared to model A-C, demonstrate improved localisation accuracy but worsen image resolution. Quantitatively, the localisation error at 13 mm image depth is (2.67±5.28) mm for model D, which is lower than model A-C, but the FVHM is (711±187) $mm^3$ ,which is higher than model A-C. Focality-wise, model D is (0.86±0.26) at 13 mm image depth, which is the same as model B, and comparable to model A and C. These findings are also in agreement with **Figure 44-46**, where model D shows more extensive and deeper coverage of the cortical surface by the blue colour (representing low localisation accuracy) than Model A-

C in **Figure 44** (localisation error), less colour-coded regions in **Figure 45** (FVHM), and visually indistinguishable patterns in **Figure 46** (focality).

While model A-D have demonstrated a depth related variation across all image quality metrics, model E on the other hand, reveals a non-depth related spatial distribution of imaging performance throughout the imaging FOV as qualitatively illustrated in **Figure 44-46, E**. This is also reflected in **Figure 43, E**, where at as early as 7 mm image depth, the localisation error for model E is (6.65±3.38) mm, the FVHM is (277±210) $mm^3$, and the focality is (0.94±0.11), which all have a significantly larger standard deviation than the metrics of model A-D at the same depth. Given that the PSF analysis are performed across all models with the same level of measurement noise, these results have shown that model E is more sensitive to noise and the resultant imaging artefacts. This is further confirmed by three example perturbations I, J, K and their reconstructed PSFs in **Figure 47**, where model A-D show PSFs that are qualitatively similar in both size and location, but model E produces imaging artefacts appearing in the scalp (**Figure 47**, **model E**, **perturbation I**), and the shapes of the PSFs are also strongly distorted (**Figure 47**, **model E**, **perturbation J-K**). A summary of the quantified image metrics for models A-E using Head reconstruction is provided in **Table 10** below.

**Table 10 Summary of HD-fDOT image quality at the two boundary depths of the 'high image quality zone' (i.e. 7 mm and 13 mm) of all six subjects combined for models A-E using Head reconstruction.**

| Model | 7 mm | | | 13 mm | | |
|---|---|---|---|---|---|---|
| | Localisation (mm) | FVHM ($mm^3$) | Focality | Localisation (mm) | FVHM ($mm^3$) | Focality |
| A | 1.32±0.88 | 426±73 | 1.00±0.00 | 3.45±5.67 | 569±178 | 0.86±0.25 |
| B | 1.54±1.03 | 451±63 | 1.00±0.00 | 3.30±5.42 | 596±182 | 0.86±0.26 |
| C | 1.12±0.77 | 284±37 | 0.99±0.00 | 3.75±6.06 | 410±234 | 0.88±0.22 |
| D | 1.72±1.17 | 529±80 | 0.99±0.00 | 2.67±5.28 | 711±187 | 0.86±0.26 |
| E | 6.65±3.38 | 277±210 | 0.94±0.11 | 6.82±5.54 | 428±261 | 0.79±0.24 |

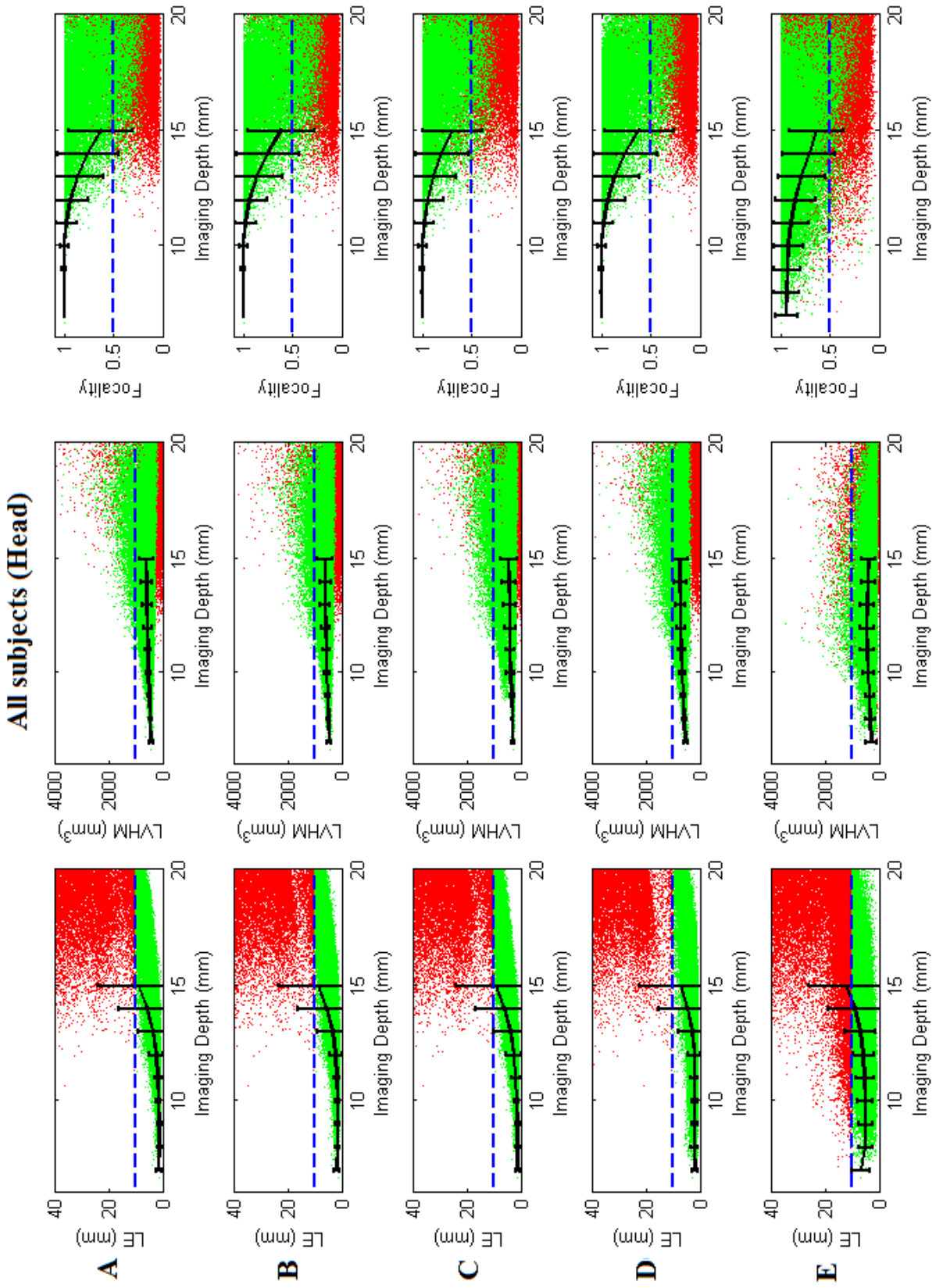


**Figure 43 Scatter plots of localisation error, LVHM and focality versus imaging depth (up to 20 mm) of all six subjects using full head reconstruction in model A-E.**

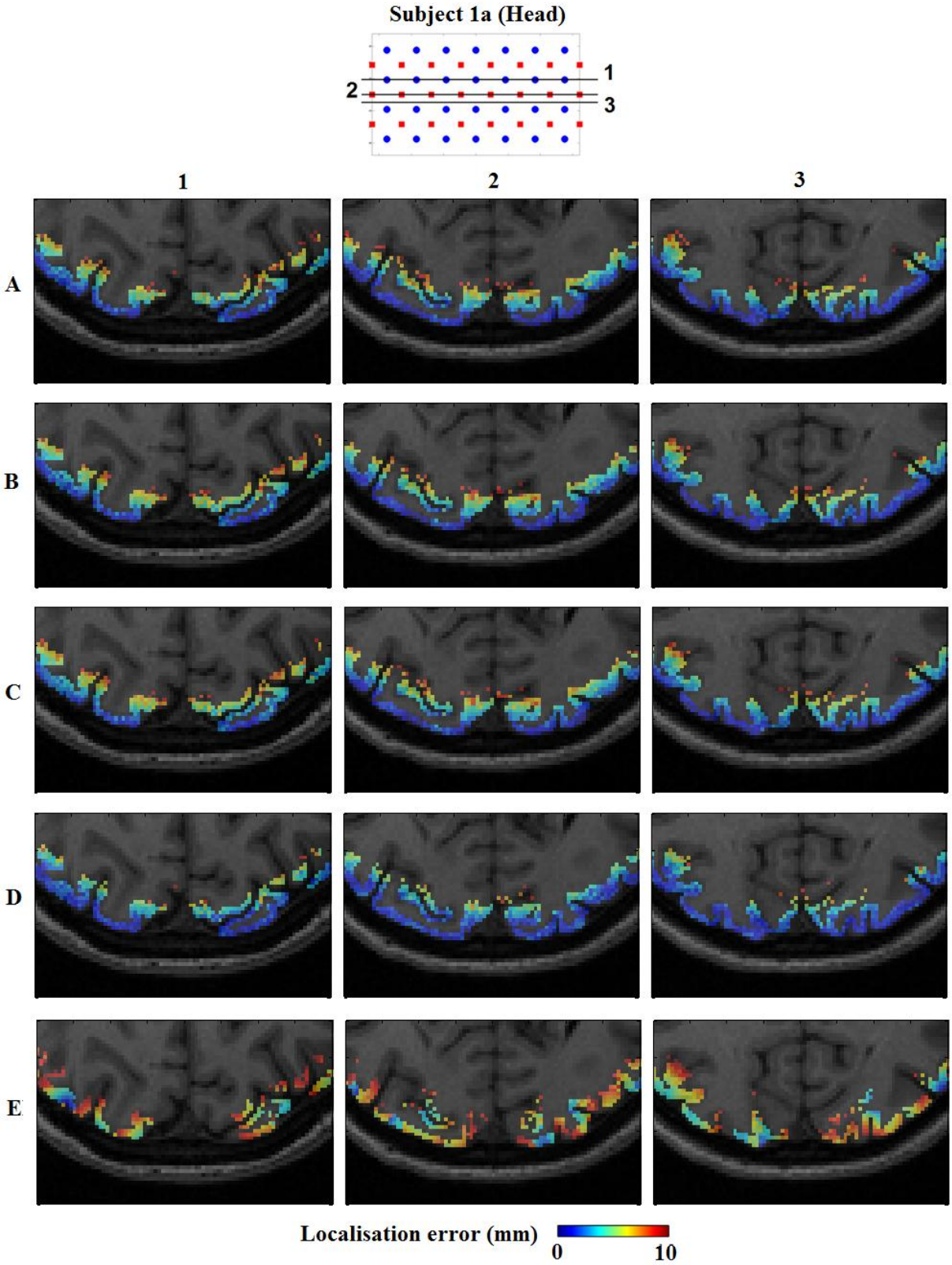


**Figure 44 Spatial distribution of localisation error of Subject 1a using full head reconstruction in model A-E. Three axial MRI slices (1, 2 and 3) with different positions relative to sources and detectors are shown.**

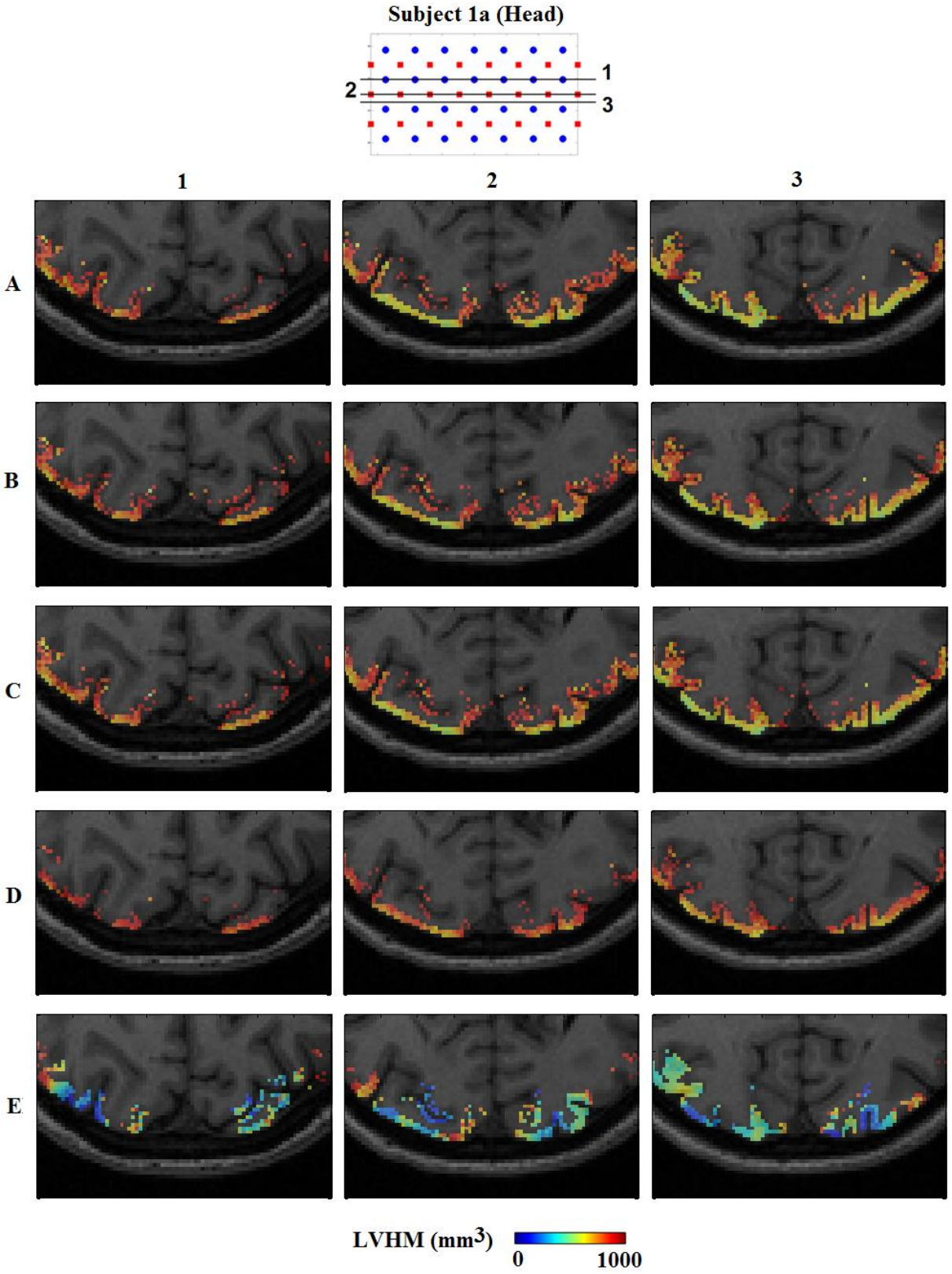


**Figure 45 Same as the last figure, but of FVHM.**

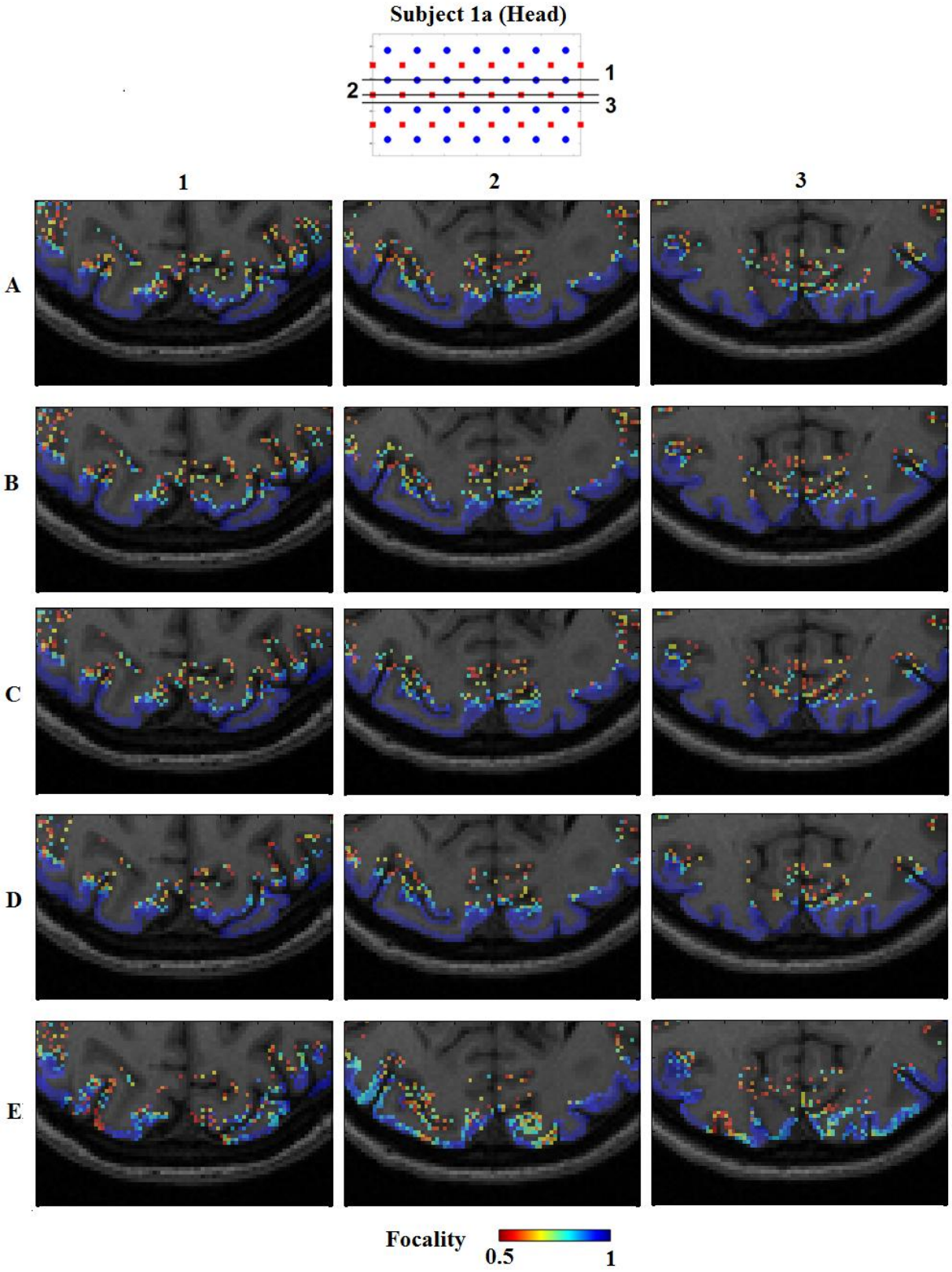


**Figure 46 Same as the last figure, but of focality.**

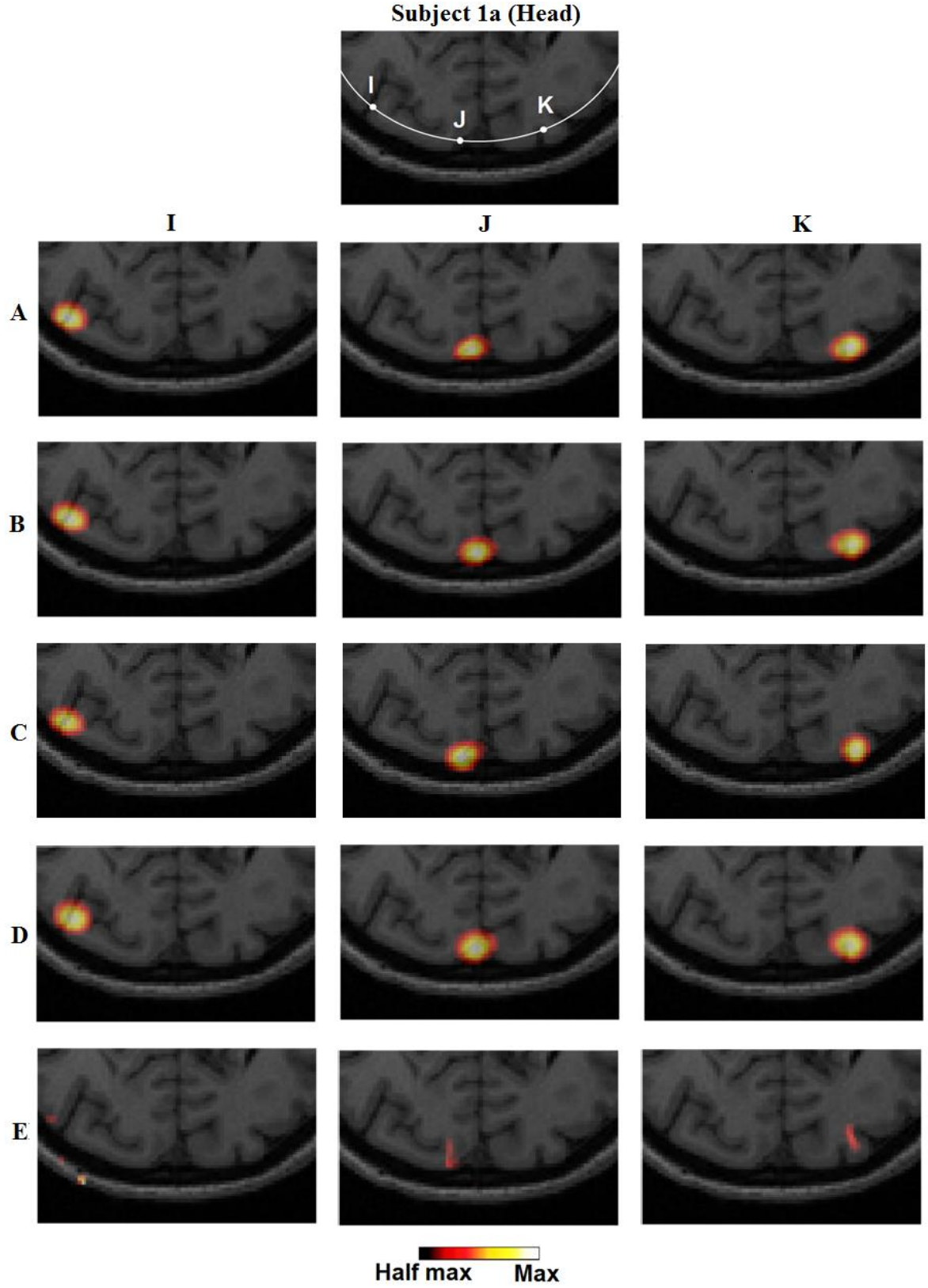


**Figure 47 Image of three target perturbations located at different lateral positions but similar depth in Subject 1a: 13.14 mm (I), 13.01 mm (J), and 13.07 mm (K), and the corresponding PSFs shown at FVHM using full head reconstruction in Model A-E.**

### 6.3.2 Brain reconstruction

The scatter plots of metrics of image quality of the six subjects using whole brain constrained reconstruction are shown in **Figure 48** (See **Appendix D.2** for individual Subject 1a, 1b-5b). Similar to our observations in the full head reconstruction, the image quality between model A-C are comparable. Specifically, a 'high image quality zone' up to 12 mm imaging depth can be defined among model A to C, where the localisation error at 12 mm image depth is (2.70±6.00) mm for model A, (3.22±6.96) mm for model B, and (2.66±6.04) mm for model C; the FVHM at 12 mm image depth is (178±103) $mm^3$ for model A, (205±120) $mm^3$ for model B, and (163±100) $mm^3$ for model C; the focality at 12 mm image depth is (0.68±0.27) for model A, (0.70±0.28) for model B, and (0.71±0.27) for model C, which are all within their respective tolerance except slightly not true for the focality. However as discussed before, the 0.5 focality tolerance may not always be applicable under the whole brain constrained reconstruction because the PSF may 'split' across folds (**Figure 40**, **Brain**, **Y**). These results are also in line with the spatially plots of image quality metrics over the corresponding MRI slices in **Figure 49-51, A-C**, where the distribution patterns between model A, B and C in these figures are qualitatively similar.

Model D, as compared to model A-C, demonstrates worse localisation accuracy and image resolution, but slightly more robustness to image artefacts. Quantitatively, the localisation error at 12 mm image depth is (4.86±4.93) mm for model D, which has a mean value higher than model A-C, and the FVHM is (477±146) $mm^3$, which is significantly higher than model A-C. However focality-wise, model D is (0.84±0.25) at 12 mm image depth, which is more robust than model A-C. These findings are also in agreement with **Figure 49-51**, where model D shows more extensive coverage of the cortical surface by warm colour (representing relatively high value) than Model A-C in **Figure 49** (localisation error) and **Figure 50**

(FVHM), and deeper coverage of the cortical surface by the blue colour (representing relatively high value) than Model A-C in **Figure 51** (focality).

Also similar to our observations in the full head reconstruction, Model E under whole brain constrained reconstruction reveals higher level of imaging error throughout the FOV than model A-D, but at even more severe magnitude than in the full head reconstruction. Most notably, the focality metric of model D at as early as 7 mm image depth is (0.83±0.23), reflecting dramatic sensitivity of its image quality to noise. The ultra low (as compared to model A-D) FVHMs as quantified in this case, for instance (84±121) $mm^3$ at 12 mm, are more likely to represent the resolution of the imaging artefacts due to noise rather than of the PSFs. This is further investigated by showing three example perturbations I, J, K and their reconstructed PSFs in **Figure 52**. While model A-C produce PSFs that are qualitatively similar in both size and location, model D recovers all three targets towards deeper location with a larger spread of PSF, which are in good agreement with our previous findings from **Figure 48-51**. For model E, the PSF is either reconstructed completely off the correct axial slice (**Figure 52**, **model E**, **perturbation I**), or severely dislocated towards deeper locations with reduced spread (**Figure 52**, **model E**, **perturbation J-K**). A summary of the quantified image metrics for models A-E using Brain reconstruction is provided in **Table 11** below.

**Table 11 Summary of HD-fDOT image quality at the two boundary depths of the 'high image quality zone' (i.e. 7 mm and 12 mm) of all six subjects combined for models A-E using Brain reconstruction.**

| Model | 7 mm | | | 12 mm | | |
|---|---|---|---|---|---|---|
| | Localisation (mm) | FVHM ($mm^3$) | Focality | Localisation (mm) | FVHM ($mm^3$) | Focality |
| A | 0.93±0.98 | 36±25 | 0.99±0.07 | 2.70±6.00 | 178±103 | 0.68±0.27 |
| B | 0.98±0.95 | 33±22 | 0.99±0.06 | 3.22±6.96 | 205±120 | 0.70±0.28 |
| C | 0.92±0.96 | 29±22 | 0.96±0.11 | 2.66±6.04 | 163±100 | 0.71±0.27 |
| D | 1.22±1.12 | 49±35 | 0.98±0.07 | 4.86±4.93 | 477±146 | 0.84±0.25 |
| E | 2.86±2.74 | 31±37 | 0.83±0.23 | 6.75±5.16 | 85±121 | 0.79±0.27 |

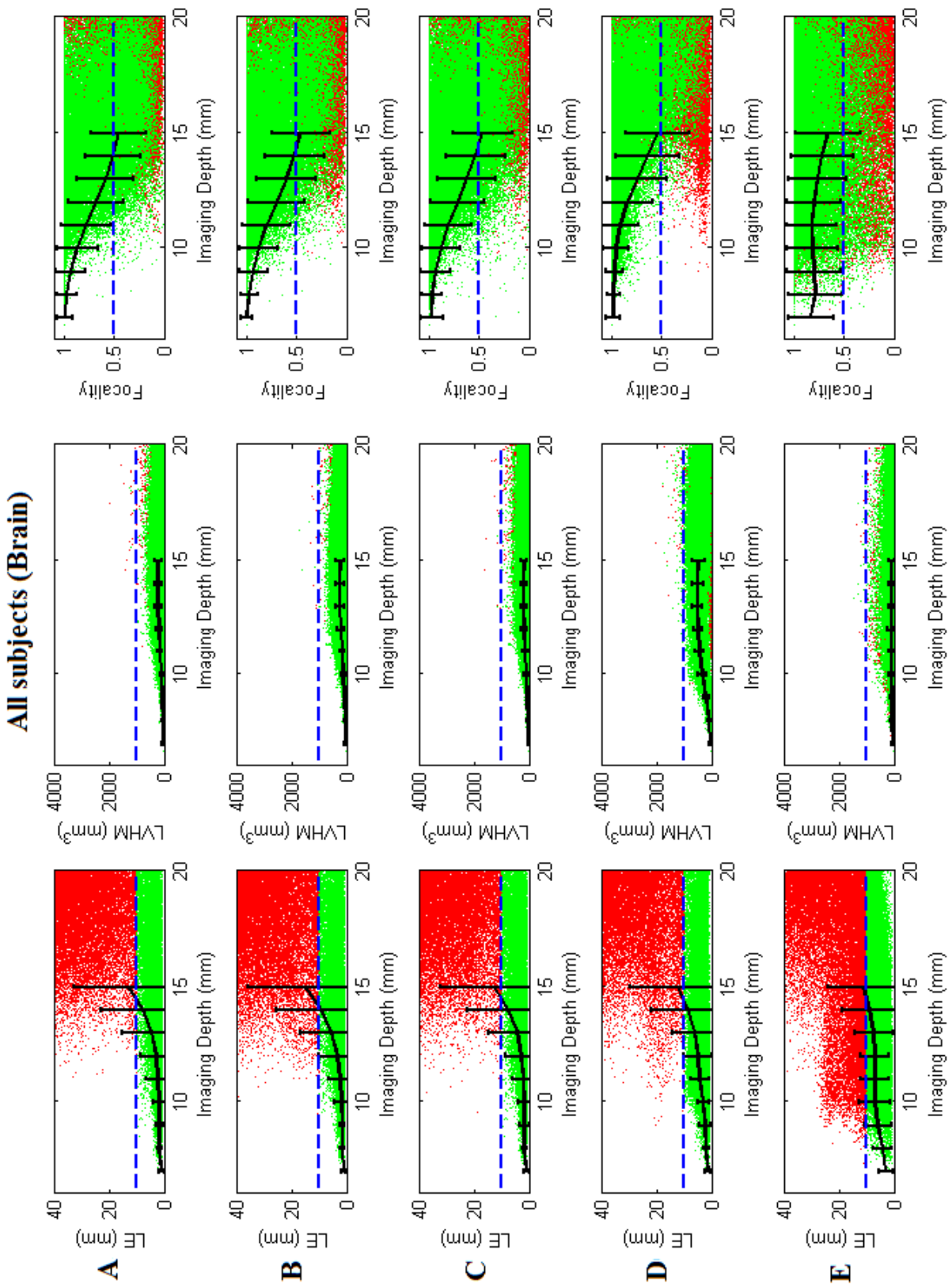


**Figure 48 Scatter plots of localisation error, LVHM and focality versus imaging depth (up to 20 mm) of all six subjects using whole brain constrained reconstruction in model A-E.**

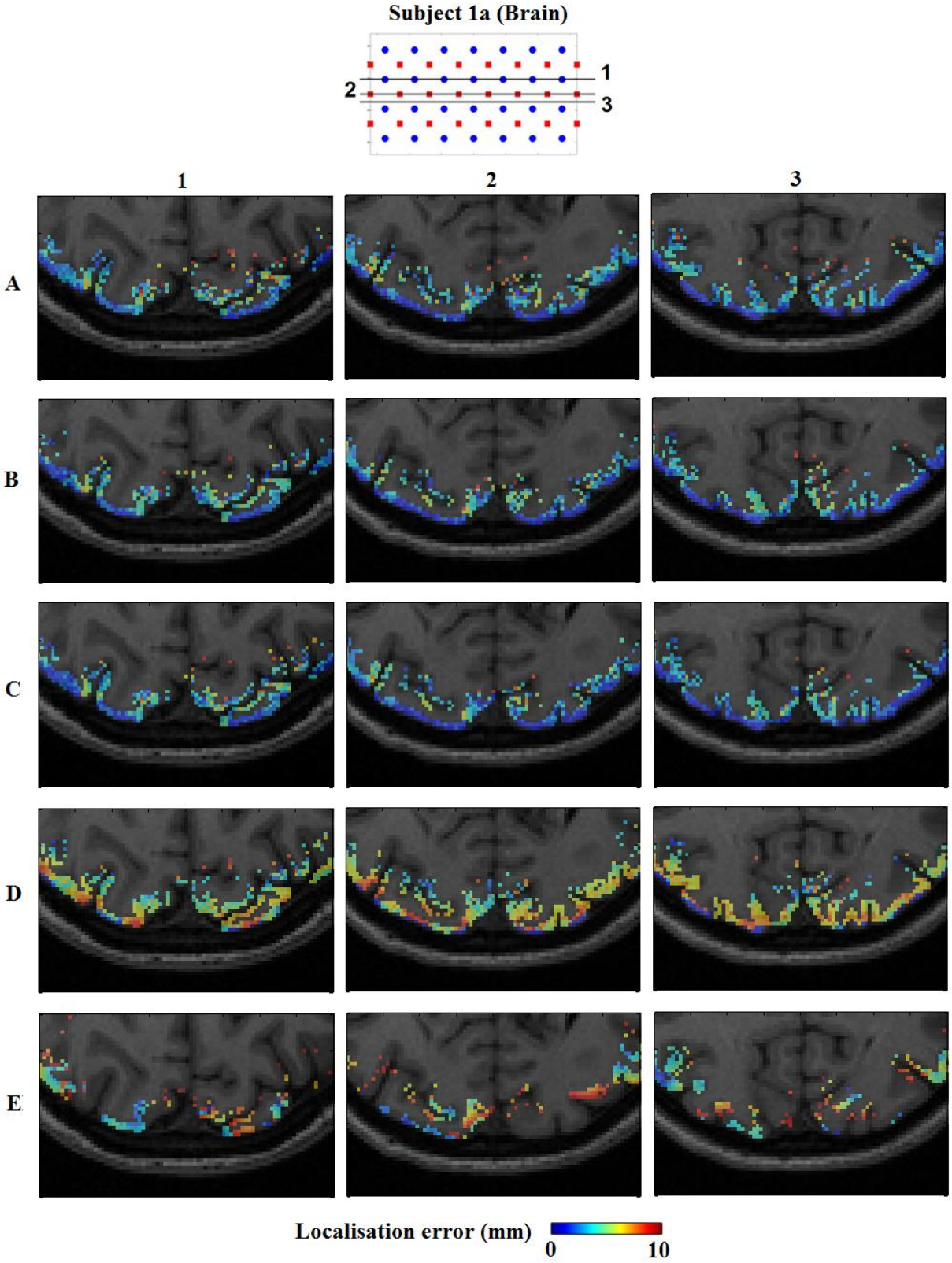


**Figure 49 Spatial distribution of localisation error of Subject 1a using whole brain constrained reconstruction in model A-E. Three axial MRI slices (1, 2 and 3) with different positions relative to sources and detectors are shown.**

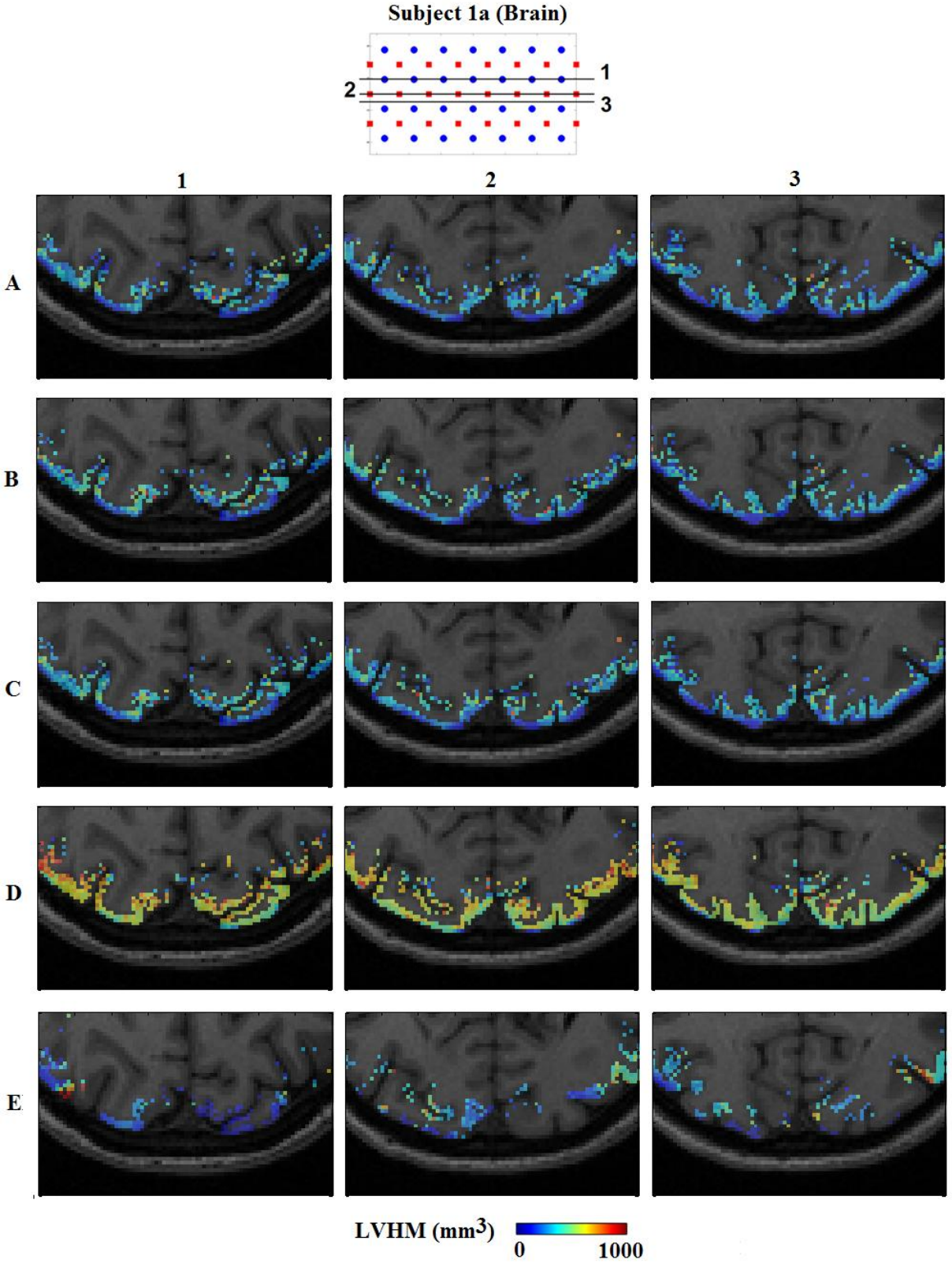


**Figure 50 Same as the last figure, but of FVHM.**

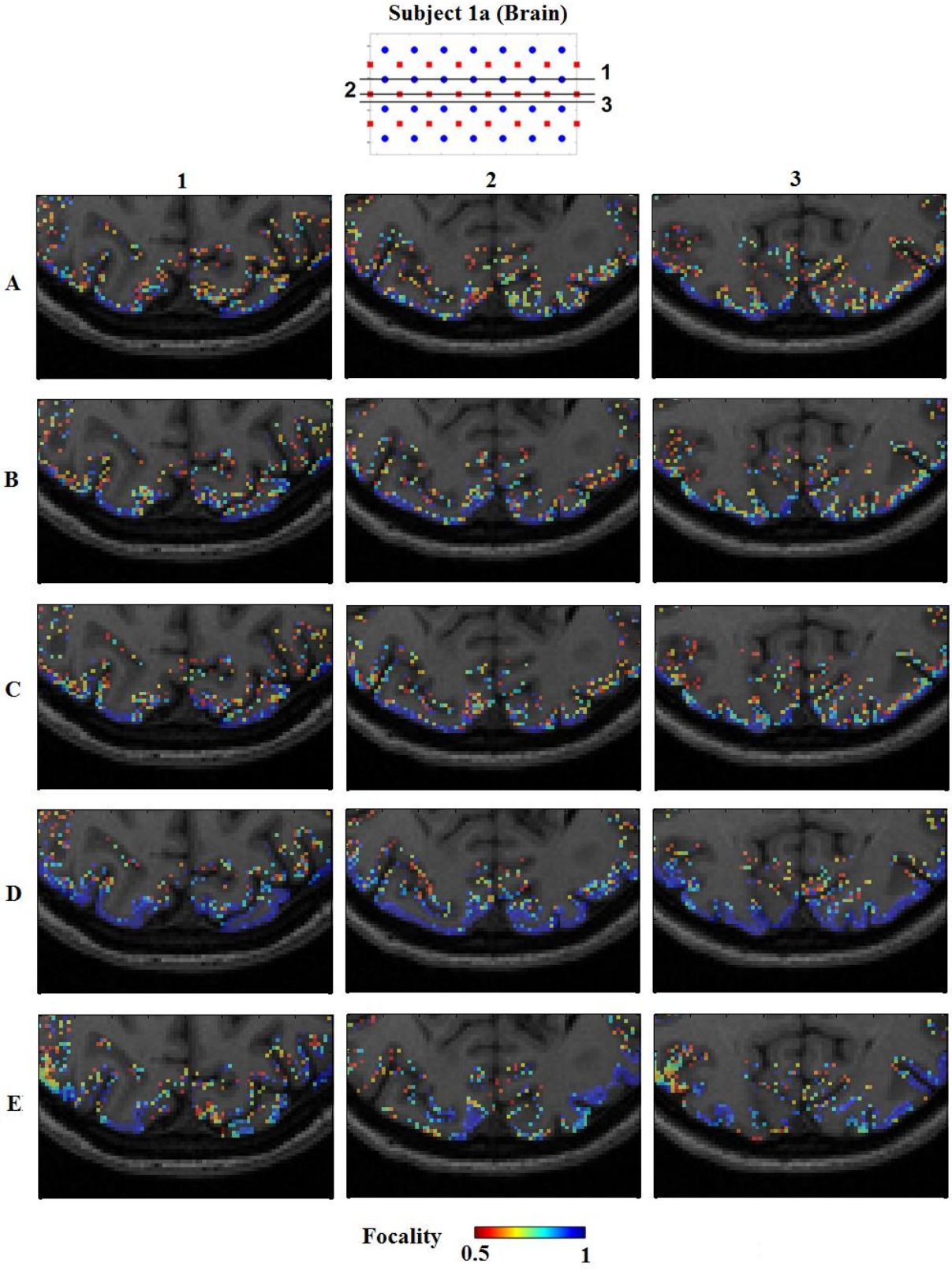


**Figure 51 Same as the last figure, but of focality.**

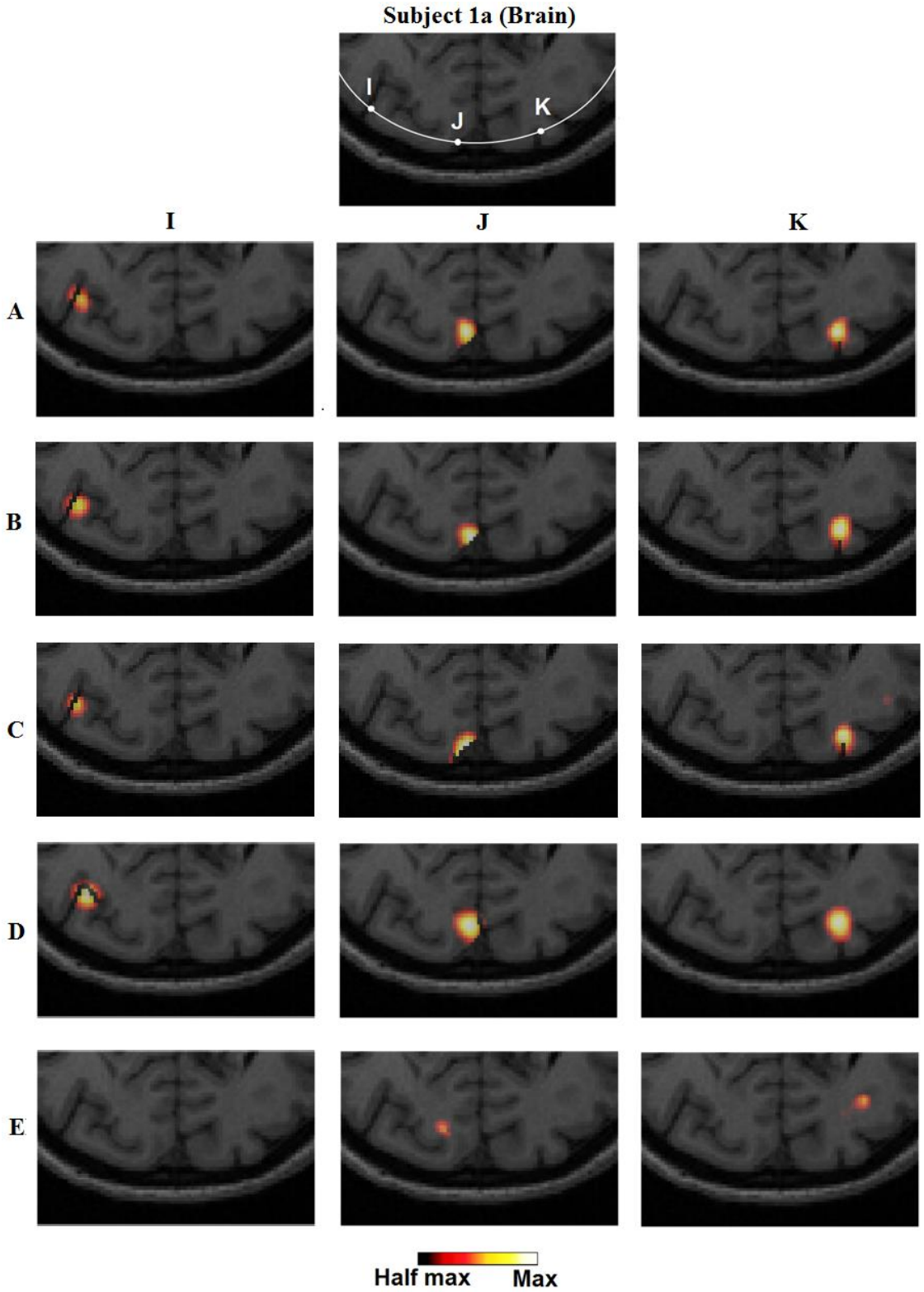


**Figure 52 Image of three target perturbations located at different lateral positions but similar depth in Subject 1a: 13.14 mm (I), 13.01 mm (J), and 13.07 mm (K), and the corresponding PSFs shown at FVHM using whole brain constrained reconstruction in Model A-E.**

## 6.4 Discussions

In this work, we have presented a multi-model comparative study to investigate the effect of uncertainty in background tissue optical properties within the context of HD-fDOT of human brain, and for the first time analysing its effect in structurally-constrained image reconstruction. This topic is important, since current practice as documented in *in vivo* fDOT literature relies on background tissue optical properties published or used in other literature, which contain three degrees of uncertainty in terms of procedure-specificity, subject-specificity, and wavelength-specificity. This is also evident in three of our tested models (model A, D and E), which have distinctive optical properties yet are all justifiable from their respective literature. In addition, we have also validated our hypothesis for the use of background absorption fitting schemes by including two more hypothetical models (model B and C). The purpose of proposing the schemes is to provide a fast, reliable and most importantly procedure-specific, subject-specific and wavelength-specific approximation of the underlying head tissue optical properties that effectively eliminates the uncertainty issues surrounding current literature-based approach, and at no extra cost of data collection.

We first test the homogeneous background absorption fitting scheme using realistic-noise-added intensity measurements generated from model A (the ground truth) across six subject head models (Subject 1a, 1b-5b), assuming a commonly-used generic global $\mu_s'$ of 1.0 $mm^{-1}$. The fitted background absorption coefficients from these subjects have a standard deviation of 1.2%, demonstrating reliable cross-subject consistency. We further test a heterogeneous background absorption fitting scheme with the same global $\mu_s'$, and find low cross-subject variation in the superficial tissue (scalp: 3%; skull: 8%), but higher uncertainty in the deeper tissues (grey matter: 12%; white matter: 37%), which are acceptable and intuitive results. It is

worth noting that given the validation of using a generic $\mu_s'$ =0.3 mm$^{-1}$ for the CSF in fDOT studies (**Section 4.2.1.2**), it may be more intuitive to apply this value instead of 1.0 mm$^{-1}$ as used in our heterogeneous background absorption fitting scheme. While this matter requires further analysis and investigation, we expect the improvement in the fitted $\mu_a$ values to be dependent on the accuracy of the spatial distribution of the CSF (from tissue segmentation), and the resultant improvement in image quality to be incremental.

Further from these, we established the five models to be evaluated by the PSF analysis, where model B uses the fitted absorption values from the homogeneous background fitting scheme, and model C uses the fitted absorptions from the heterogeneous background fitting scheme.

In the case of full head reconstruction, namely no structural constraint is applied, the imaging performances from our background absorption fitting schemes (model B-C) demonstrate consistently comparable imaging performance with the inverse crime (model A). It is also interesting to note that the optically underestimated homogeneous model (model D) reveals better localisation accuracy even than the inverse crime albeit at worse image resolution. A similar phenomenon was also reported in one of our publications with noise-less simulations and different regularisation parameters in the inverse equation [155]. Our explanation for this is actually intuitive: the underestimation of tissue optical properties has allowed deeper-than-expected coverage of high measurement sensitivity throughout the imaging domain, thereby resulting a better-than-inverse-crime localisation accuracy at deeper imaging depth but not necessarily for the image resolution. On the other hand, when a significantly overestimated heterogeneous model (model E) is used, the image quality becomes sensitive to noise in the measurements, specifically in the form of imaging artefacts (**Figure 47, model E, perturbation I**), or activation distortion but within acceptable localisation accuracy (**Figure**

**47, model E, perturbation J-K**). We believe the reason is that the overestimation of tissue optical properties effectively attenuates the measurement sensitivity within the superficial tissues such as the scalp, and therefore less-than-expected measurement sensitivity on the brain, which results in a higher sensitivity of image quality to noise.

In the case of whole brain constrained reconstruction, similar results are found for the use of our background absorption fitting schemes (model B-C), which provide consistently similar imaging performance with the inverse crime (model A). However, the underestimated homogeneous model (model D) now underperforms in both localisation accuracy and image resolution. Specifically the localisation error mainly comes from a deeper-than-expected reconstruction location rather than error of lateral resolution. This could be explained by the combined effect of the deeper-than-expected measurement sensitivity distribution as discussed in the last paragraph, and the application of the whole brain constraint, which turns to bias the activation towards a slightly deeper location, as shown in **Figure 41, Brain** in **Chapter 5**. Finally when using a significantly overestimated heterogeneous model (model E) for image reconstruction, the results demonstrate hyper-sensitivity of image quality to noise in the measurements even at superficial imaging depths (<10 mm). As a result, the activation is either failed to be picked up (**Figure 52, model E, perturbation I**), or appears in a location that is beyond our localisation accuracy tolerance (**Figure 52, model E, perturbation J-K**), and thus does not provide clinically useful information regarding the activation.

Overall, we have shown that in non-structurally-constrained HD-fDOT image reconstruction, it is possible to achieve comparable image quality to the ‘inverse crime’, even with another model (model B-D) that has distinctive optical properties than the ‘ground truth’ (model A). This is in good agreement with Heiskala et al. [6] who reported a ~1 mm difference in localisation error between the ground truth and a homogeneous model (which is neither an

underestimation nor an overestimation of the ground truth, and similar to our model A and model B here) in a simulated spherical activation reconstruction study. In additional, we have demonstrated compromised image quality in the form of increasing imaging artefacts, activation distortions and dislocations when using a significantly overestimated model (model E). While the scenario of overestimation of optical property was not included in [6], it was comprehensively evaluated by Pei et al. [30] but only in noise-free simulations using 2D simplified geometry, and is therefore not comparable with our findings here.

In the case of whole brain constrained reconstruction, the models (model B and C) derived from our background absorption fitting schemes perform consistently comparable with the 'inverse crime' (model A). On the other hand, both underestimated model (model D) and overestimated model (model E) underperform in localisation accuracy, especially in model E where imaging artefacts and severe activation dislocations are observed across the entire FOV. These results have provided full validation for our hypothesis for the use of background absorption fitting schemes in HD-fDOT studies.

## 6.5 Conclusions

Our multi-model multi-subject comparative studies have shown that uncertainty in background tissue optical properties arisen from current literature-based approaches, can affect the reconstructed image quality significantly in the application of HD-fDOT of human brain, especially when whole brain constrained reconstruction is performed. In response, we have proposed the use of a homogeneous or a heterogeneous background absorption fitting scheme that effectively eliminates such uncertainty, and both have shown to provide consistently comparable image quality to the 'inverse crime' scenario. Given that the homogeneous fitting scheme takes less time (1 hour) to perform than the heterogeneous scheme (3 hours), our analysis suggests that future *in vivo* HD-fDOT studies should highly

consider the use of homogeneous background absorption fitting scheme in order to ensure optimal image quality.

# CHAPTER 7

# SINGULAR-VALUE-DECOMPOSITION BASED SPECTRAL HD-fDOT

## 7.1 Introduction

The spectrally constrained image reconstruction method was first documented by Corlu [8] in nonlinear (or absolute) DOT, wherein absolute concentrations of chromophores are solved iteratively with a minimisation function [62] as described in **Section 4.3.1.1**. When compared with non-spectral methods, whereby images of absorption and scattering coefficients are first recovered and then un-mixed to provide chromophore concentrations, spectrally constrained reconstruction techniques are found to suppress artefacts in water and scattering power images, and also reduce crosstalk between chromophores and scatter parameters in breast imaging [133, 156, 157]. However the success of spectral method in nonlinear DOT studies has concealed an underlying numerical operation that in fact increases (rather than reduce) crosstalk between chromophores, but the issue was not known prior to our study. This was evident in literature where Li et al. [142] originally claimed that the use of spectral method in linear (or differential) DOT had led to crosstalk reduction between reconstructed $\Delta HbO_2$ and $\Delta HbR$, but later [143] reported an increase in crosstalk between the two chromophores that could not be explained. In fact, as we now know, such crosstalk is partially due to the sub-optimal regularisation and update of the Jacobian matrix as pointed out by Eames et al. [96],

who proposed a Jacobian normalisation technique in nonlinear DOT that allows for more uniform regularisation and parameter update in image reconstruction, hence reducing imaging crosstalk. However in fDOT of brain function where the imaging problem is linear and measurements are mostly reflectance rather than transmittance, such normalisation techniques would inappropriately bias the measurement sensitivities towards deeper regions in the brain and cause significant imaging error.

In this work we address and resolve this crosstalk issue by proposing a novel regularisation technique based on the singular value decomposition (SVD). While previous DOT literature has focused on using the SVD as a tool to understand the relationship between DOT measurements (in terms of probe number and location) and image quality [158] in order to guide optimisation of detector placement [109, 141], the approach we are taking is to integrate the SVD directly into the image reconstruction algorithm. Previous applications in the use of SVD-based truncation methods for Jacobian inversion are well documented [140], however our approach are different in that we are not using the SVD approach to achieve a pseudo-inverse of the spectral Jacobian, but instead using it to regularise the wavelength dependent Jacobian, and then calculate the pseudo-inverse of its spectral counterpart.

Qualitative and quantitative evaluations are conducted among non-spectral method and spectral method (using conventional and SVD-based regularisation respectively) first on a two dimensional (2D) circular model and then on a three dimensional (3D) subject-specific head geometry. The 2D model provides an initial proof-of-concept analysis whereas the 3D model has more degrees of freedom, is highly ill-determined and more realistic to *in vivo* diffuse optical tomography of human brain studies.

## 7.2 Spectral method using SVD based regularisation

Instead of constructing the spectral Jacobian matrix $J_s$ first and performing the regularisation second as mentioned in **Equation (1.41)**, we propose an alternative regularisation technique that reverses the order of these two operations. This is achieved by utilising the relationship described in **Equation (1.37)**: since applying Tikhonov regularisation of weight $\alpha^2$ changes the singular values of $J_\lambda$ from $\sigma_{\lambda,i}$ to $\sqrt{{\sigma_{\lambda,i}}^2+\alpha^2}$, we can recompose the regularised $J_\lambda$, denoted by $\hat{J}_\lambda$ as:

$$\hat{J}_\lambda = U\sqrt{S\cdot S + diag({\alpha_\lambda}^2)}V^T \tag{1.50}$$

We can then construct the regularised $J_S$, denoted by $\hat{J}_S$ as:

$$\hat{J}_S = \begin{pmatrix} \hat{J}_{\lambda_1}\cdot\varepsilon_{c_1,\lambda_1} & \hat{J}_{\lambda_1}\cdot\varepsilon_{c_2,\lambda_1} \\ \hat{J}_{\lambda_2}\cdot\varepsilon_{c_1,\lambda_2} & \hat{J}_{\lambda_2}\cdot\varepsilon_{c_2,\lambda_2} \end{pmatrix} \tag{1.51}$$

The inverse problem therefore becomes:

$$\begin{pmatrix} \Delta HbO_2^T \\ \Delta HbR^T \end{pmatrix} = {J_S}^T\left(\hat{J}_S{\hat{J}_S}^T\right)^{-1}\begin{pmatrix} {\Delta\Phi_{\lambda_1}}^T \\ {\Delta\Phi_{\lambda_2}}^T \end{pmatrix} \tag{1.52}$$

The advantage here is that regularisation is applied to the Jacobian matrix while the spectral prior information $M_S$ is exactly preserved and therefore contains all information needed for the wavelength unmixing operation. In addition, ${\alpha_\lambda}^2$ in the non-spectral method is now directly used in the spectral method, avoiding the operation to find an equivalent ${\alpha_S}^2$ for comparative studies which can be problematic due to its subjective choice [142, 143].

## 7.3 Method and results

### 7.3.1 Two-dimensional circular model

To compare the image performance on crosstalk among non-spectral, conventional spectral, and our newly proposed SVD-based spectral methods, a set of proof-of-concept simulations are carried out on a 2D circular model. Using a well defined numerical model has the benefit of knowing the exact location and magnitude of the targets, allowing accurate analysis of the reconstructed images. The simulated 2D model consists of a uniform circular mesh of radius 43 mm with 1785 nodes corresponding to 3418 linear triangular elements. Sixteen co-located source/detector fibres are modelled equidistant on the external boundary and are used for continuous-wave data collection, giving rise 240 (16×15 where the source fibre is not used for detection) differential measurements per wavelength (**Figure 53**). The model is assumed to be homogeneous with $\mu_a$ = 0.017 mm$^{-1}$, $\mu_s'$ = 0.74 mm$^{-1}$ at 750 nm, and $\mu_a$ = 0.019 mm$^{-1}$, $\mu_s'$ = 0.64 mm$^{-1}$ at 850 nm. The background chromophore concentrations of $HbO_2$ and HbR are both 0.5 mM. The molar extinction coefficients used are 0.1193 mm$^{-1}$/mM and 0.3236 mm$^{-1}$/mM for $HbO_2$ and HbR respectively at 750 nm, and 0.2436 mm$^{-1}$/mM and 0.1592 mm$^{-1}$/mM for $HbO_2$ and HbR respectively at 850 nm from **Figure 17**. A target of 5 mm in radius is located at three different depths, i.e. 13 mm, 28 mm and 43 mm, corresponding to a modelled $\Delta HbO_2$ = +0.05mM (**Figure 54 (a-c), Target**). Forward data is generated using Nirfast [119]. For regularisation, we find that in order to achieve comparable image resolution and contrast between these three methods, a lower value of $\alpha$ is required for the conventional spectral method ($\alpha_S$ in **Equation (1.41)**) as compared to the non-spectral method ($\alpha_\lambda$ in **Equation (1.32)**) and the proposed SVD approach ($\alpha_\lambda$ in **Equation (1.50)**), which is in line with previous findings [143]. Specifically we chose $\alpha_\lambda$ =$10^{-2}$×the maximum singular value of

$J_\lambda$ and $\alpha_S$ =5×10$^{-3}$×the maximum singular value of $J_s$, which are found to provide a good balance between image resolution and robustness to measurement noise in this comparative study.

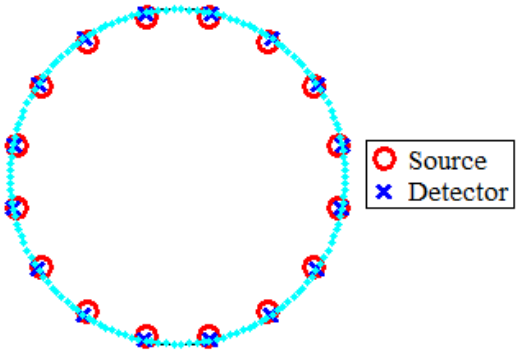


**Figure 53 Schematic view showing the placement of 16 co-located sources (red squares) and 16 detectors (blue cross) on the boundary of a 2D circular model. Note for each source excitation, the same fibre is not used as detector, giving rise to 240 differential measurements in total.**

Linear, single-step (as in fDOT) reconstructed images of haemodynamic changes using non-spectral (denoted as 'Non-Spec'), spectral with conventional regularisation ('Conv-Spec'), and spectral with SVD-based regularisation ('Svd-Spec') are shown in **Figure 54-56** with 0%, 0.2% and 0.5% added Gaussian random noise respectively. Within each figure, three scenarios/locations (a-c) having the $\Delta HbO_2$ target moving towards the centre of the circular model are presented, emulating a gradual decrease in signal-to-noise ratio (SNR) in the measurement; that is as the target moves deeper within the domain, the magnitude of the detected differential signal decreases. It is evident from **Figure 54** that in the case of 0% noise, a region of crosstalk can be easily identified in the recovered ΔHbR images along with some imaging artefacts due to the measurement sensitivity distribution in all three methods, with 'Svd-Spec' demonstrating the least magnitude of crosstalk and imaging artefacts while 'Conv-Spec' produces the most. As noise increases to 0.2% (**Figure 55**), imaging artefacts

due to noise appear although at smaller magnitudes as compared to the crosstalk. At 0.5% the noise artefacts begin to dominate the ΔHbR concentration images for both the 'Svd-Spec' and 'Non-Spec' as shown in **Figure 56**. Specifically when the target is at the centre of the model (43 mm from boundary, **Figure 56 (c)**), the recovered images from 'Svd-Spec' and 'Non-Spec' become indistinguishable. In comparison, crosstalk and imaging artefacts in 'Conv-Spec' still dominate the ΔHbR concentration images even at 0.5% noise level.

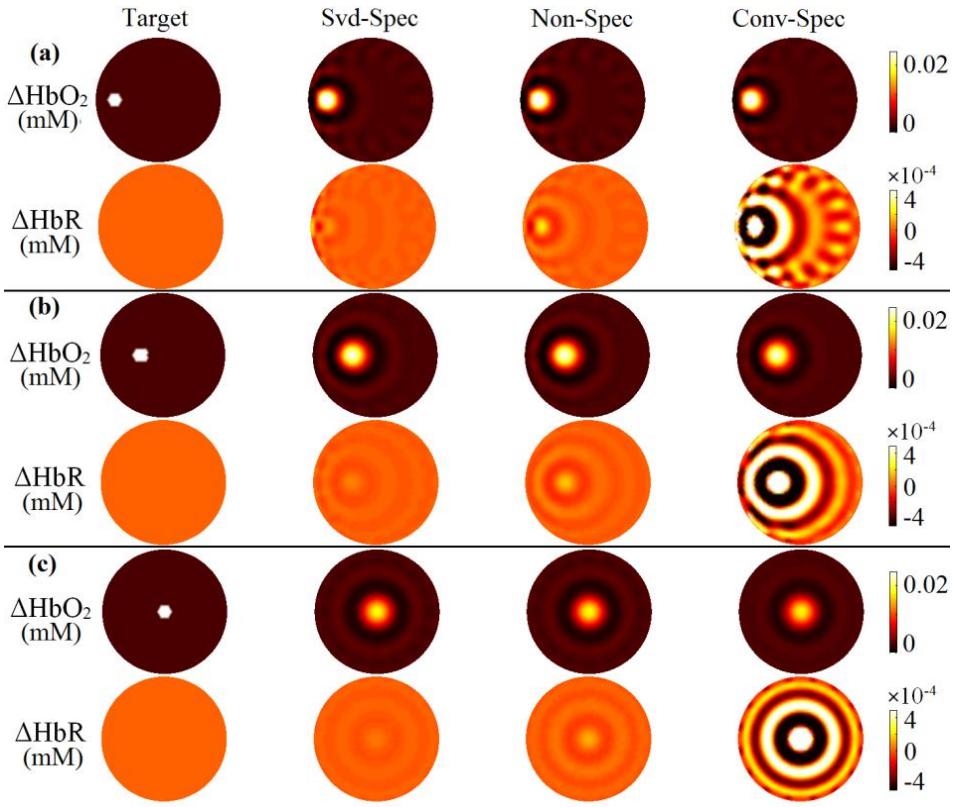


**Figure 54 Reconstructed images of $\Delta HbO_2$ (upper row) and ΔHbR (lower row) concentration at three different locations (a-c) using methods 'Svd-Spec', 'Non-Spec' and 'Conv-Spec' with 0% noise. Note that for comparative displaying purpose, the range of the colour bar has been set by the maximum and minimum values of the images from the 'Non-Spec' method. This causes colour saturation in parts of the images from the 'Conv-Spec' method, which has a colour scale of -0.001 to 0.003 (mM).**

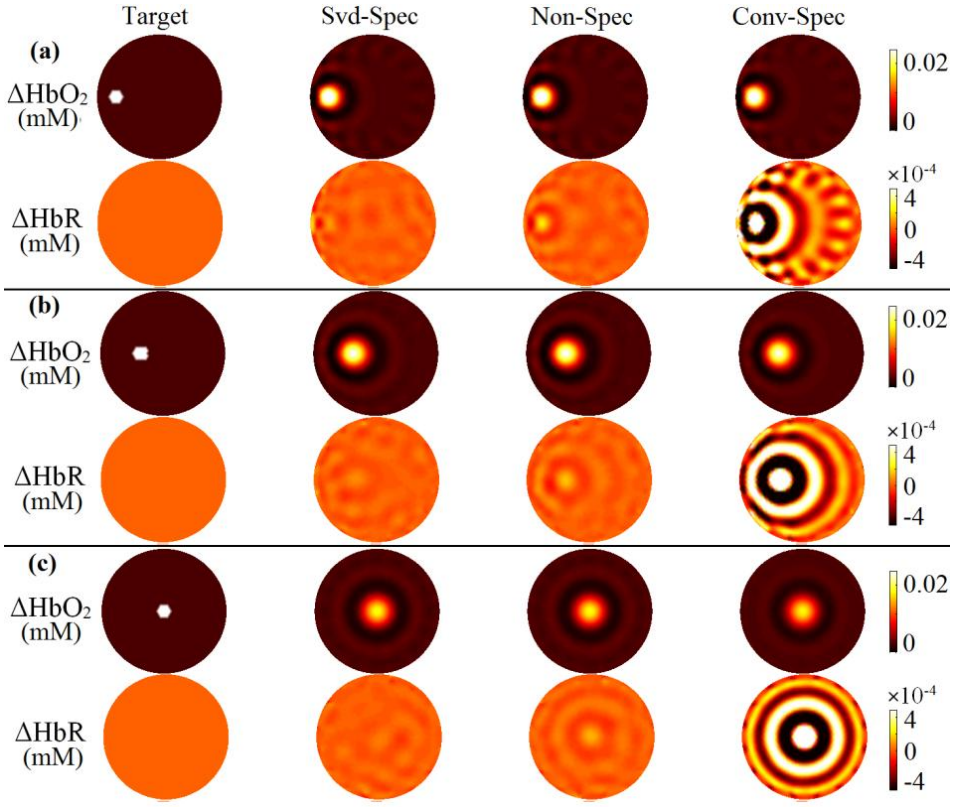


**Figure 55 Same as the last figure, but with 0.2% added noise.**

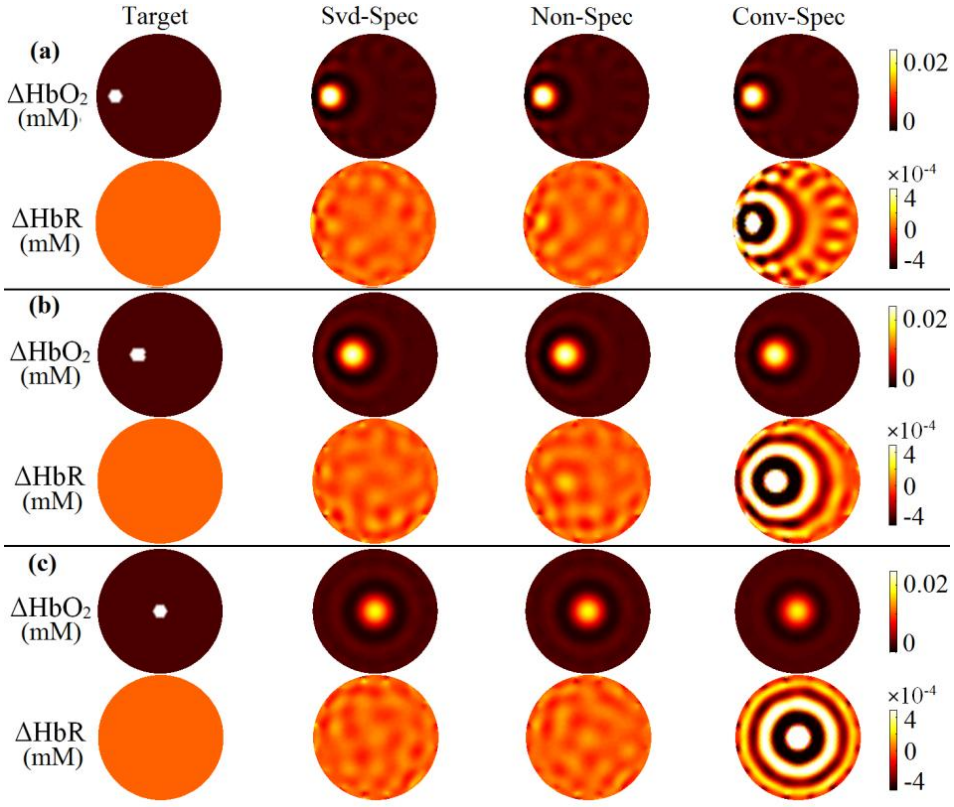


**Figure 56 Same as the last figure, but with 0.5% added noise.**

For quantitative analysis of image crosstalk, we have defined the crosstalk from $\Delta HbO_2$ into $\Delta HbR$ as the mean concentration value in the 'region of crosstalk' in the $\Delta HbR$ image divided by the mean concentration value of the known 'region of target' in the $\Delta HbO_2$ image, where the 'region of crosstalk' and 'region of target' refer to effectively the same physical region in the imaging domain. This metric measures the amount of $\Delta HbO_2$ being 'cross-talked' into the $\Delta HbR$ image as a percentage of the amount of $\Delta HbO_2$ (the target) in its own image. In **Figure 57** the plotted crosstalk versus depth of target is shown for all cases presented in **Figure 54-56**. Again it can be seen that crosstalk increases along with depth of target due to decreasing magnitude of the differential signal and/or SNR. As summarised in **Table 12**, crosstalk levels at 0.23% on average for 'Svd-Spec', representing a 59% reduction from 0.55% level of crosstalk for 'Non-Spec', and a 98% reduction from 11.7% level of crosstalk for 'Conv-Spec'. At 0.5% noise the imaging artefacts dominate over the crosstalk for both 'Svd-Spec' and 'Non-Spec', particularly when the target is located at the centre of the model (**Figure 56 (c)**), where crosstalk for both methods are approximately 0.5%, indicating little difference between the two methods, however still much better as compared to conventional spectral reconstruction, 'Conv-Spec'. These simulations were repeated with a $\Delta HbR$ target and similar results were obtained.

**Table 12 Summary of quantified crosstalk at locations (a-c) with 0%, 0.2% and 0.5% added noise in data respectively.**

| Recon. method | Location (a) | | | Location (b) | | | Location (c) | | | Average |
|---|---|---|---|---|---|---|---|---|---|---|
| | Noise free | 0.2% noise | 0.5% noise | Noise free | 0.2% noise | 0.5% noise | Noise free | 0.2% noise | 0.5% noise | |
| Svd-Spec | 0.19% | 0.21% | 0.23% | 0.20% | 0.25% | 0.15% | 0.21% | 0.26% | 0.38% | 0.23% |
| Non-Spec | 0.55% | 0.54% | 0.52% | 0.57% | 0.52% | 0.61% | 0.61% | 0.62% | 0.45% | 0.55% |
| Conv-Spec | 9.33% | 9.32% | 9.28% | 12.2% | 12.2% | 12.2% | 13.7% | 13.7% | 13.6% | 11.7% |

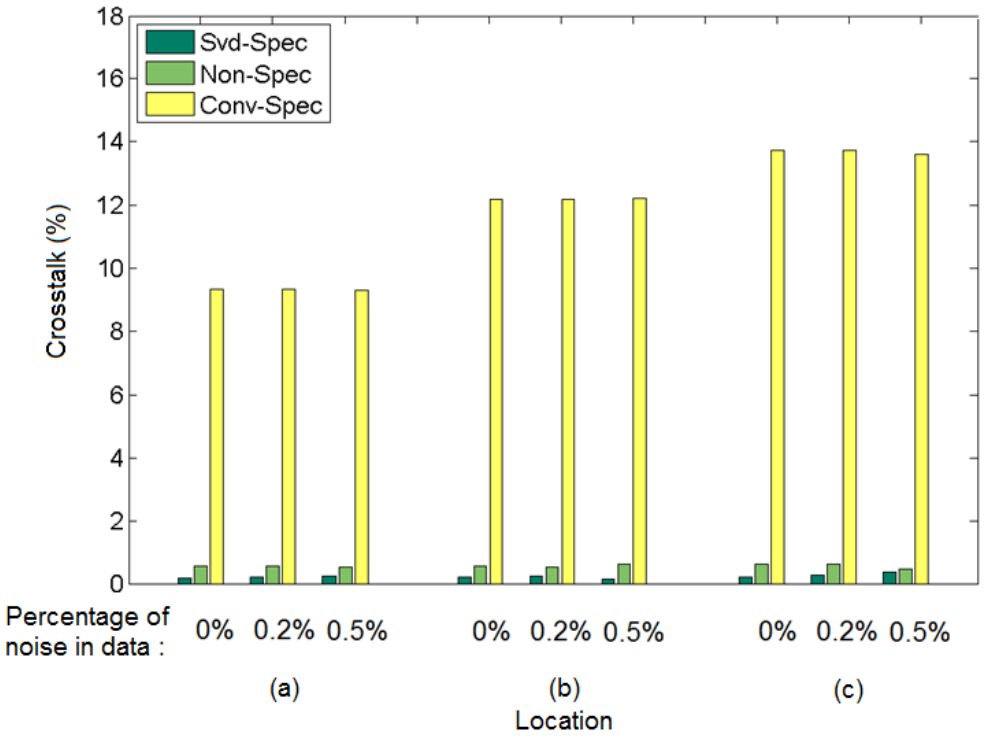


**Figure 57 Bar chart illustrating image crosstalk at locations (a-c) and 0%, 0.2% and 0.5% noise level from Table 12.**

### 7.3.2 Three-dimensional head model

Next we extend our analysis to a more realistic, three-dimensional finite element head model. Here we use the hand-corrected voxel-based head mesh 'Subject 1a' as described in **Chapter 5**. Tissue optical properties assigned to this heterogeneous head model are values used in previous *in vivo* study [94] at 750 nm and 850 nm (**Table 13**), which are the two wavelengths equipped in the current HD-DOT system at Washington University School of Medicine [5] and can be adapted to other and more wavelengths.

**Table 13 Head tissue optical properties used for 750 nm and 850 nm.**

| $\mu_a$ (mm$^{-1}$) / $\mu_s'$ (mm$^{-1}$) | 750 nm | 850 nm |
|---|---|---|
| Scalp | 0.0170 / 0.74 | 0.0190 / 0.64 |
| Skull | 0.0116 / 0.94 | 0.0139 / 0.84 |
| CSF | 0.004 / 0.3 | 0.004 / 0.3 |
| Grey Matter | 0.0180 / 0.8359 | 0.0192 / 0.6726 |
| White Matter | 0.0167 / 1.1908 | 0.0208 / 1.0107 |

Instead of presenting a $\Delta HbO_2$ concentration target as in the 2D circular model, here we model a ΔHbR concentration target for the 3D head model. To generate the forward data, we simulate a focal activation of ΔHbR=-0.01mM and 1 cm in radius on the right hemisphere of the visual cortex (**Figure 58 (a-b)**) as the type of brain activation one would expect from a retinotopic mapping study [5]. Similar to our practice in **Chapter 5**, Gaussian random noise of 0.1%, 0.14% and 1% in amplitude is added to first, second and third nearest neighbour measurements respectively to mimic our current *in vivo* performance [123] and ten sets of noise added data are generated and averaged to produce the final image. Image reconstruction is performed with the 'whole brain' structural constraint as described in **Chapter 5** which limits the recovered activation on the grey and white matter only [89, 159]. The optimal value of regularisation is $\alpha_\lambda = 10^{-2} \times$the maximum singular value of $J_\lambda$, which is found to provide good imaging quality based on our previous human [5] and animal [144] DOT studies. The conventional spectral method is excluded in this part of the study due to severe crosstalk between chromophores as already demonstrated on the 2D model.

Reconstructed chromophore concentration images of simulated brain activation using non-spectral ('Non-Spec') and spectral method with SVD-based regularisation ('Svd-Spec'), with noise free and noise added data, are displayed on the surface rendered FEM model of the

brain in **Figure 58**. Similar to our finding with the 2D model, a region of crosstalk of ΔHbR into $\Delta HbO_2$ is identified when noiseless data are used for image reconstruction, with the magnitude of crosstalk from 'Svd-Spec' significantly smaller than 'Non-Spec'. The crosstalk (same definition as in the 2D case) in **Figure 58 (c)** is 0.005% for 'Svd-Spec', representing a 95% reduction from 0.11% for 'Non-Spec'. When measurement noise based on a current imaging system specification is added, the two methods produce images that are qualitatively similar, with quantitative crosstalk both at 0.20% (**Figure 58 (d)**), showing little difference between non-spectral and spectral reconstruction techniques. A summary of the quantified crosstalk using the two methods is provided in **Table 14** below.

**Table 14 Summary of quantified crosstalk using 'Svd-Spec' and 'Non-Spec' reconstruction methods, without and with realistically added noise in measurements respectively.**

| Reconstruction method | Noise-free | Noise-added |
|---|---|---|
| Svd-Spec | 0.005% | 0.20% |
| Non-Spec | 0.11% | 0.20% |

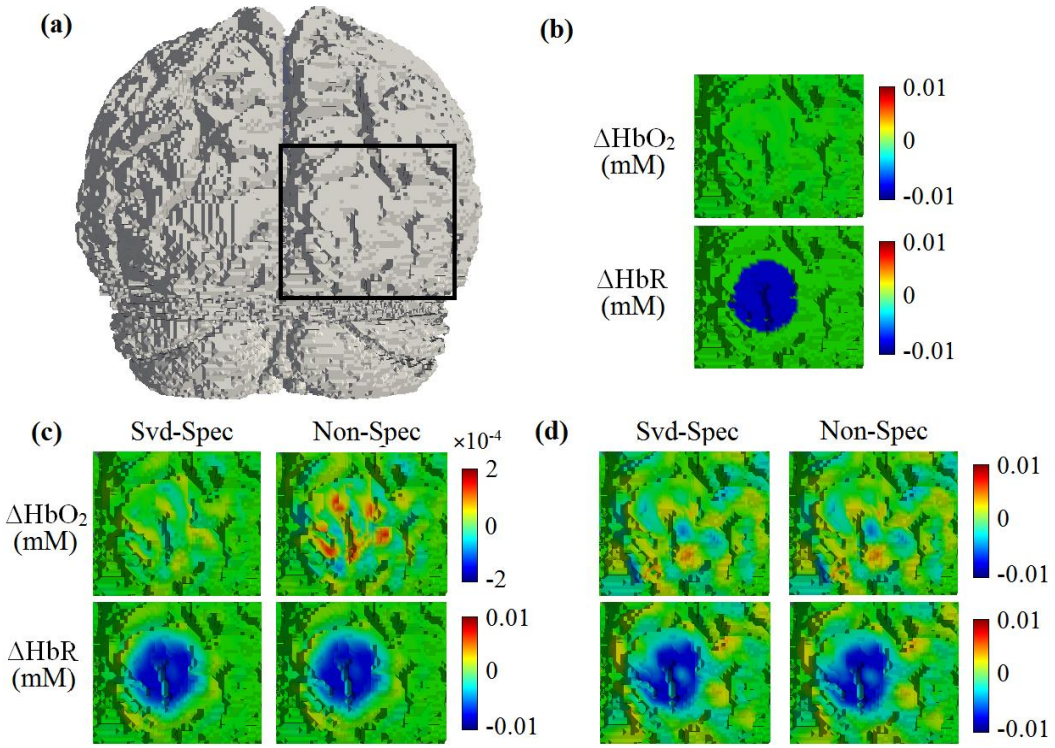


**Figure 58 (a) Posterior surface rendered view of the 3D FEM brain model, (b) a regional FOV focused on the right hemisphere of visual cortex enclosed within the black window in (a), showing simulated chromophore target, (c) reconstructed images of $\Delta HbO_2$ (upper row) and ΔHbR (lower row) concentration for 'Svd-Spec' and 'Non-Spec' method using noise free data, and (d) using noise added data.**

## 7.4 Discussions

In this study we have presented a new regularisation technique for linear image reconstruction in spectral diffuse optical tomography. This technique utilises the singular value decomposition (SVD), allowing regularisation on the spectral Jacobian matrix to be applied without altering the underlying spectral prior information. Specifically, this is achieved by regularising the wavelength dependant Jacobian matrix prior to mixing with the spectral coefficients, a completely new method where the regularisation does not affect the mapping of absorption changes onto chromophore concentrations, thereby providing a much more accurate spectral inversion technique. This method is different to previously published work, whereby the Jacobian is first spectrally mixed and then regularised and inverted.

Through a series of proof-of-concept analyses using a 2D circular model, we have shown that the SVD-based regularisation technique followed by spectral unmixing dramatically reduces the crosstalk between chromophores. While the conventional spectral method has demonstrated an average level of crosstalk at 11.7%, which could potentially lead to clinically significant mis-interpretation in *in vivo* studies, SVD-based technique has shown to reduce this metric by 98%, demonstrating only 0.23% level of crosstalk between $\Delta HbO_2$ and $\Delta HbR$ images. When compared with non-spectral method, this technique also demonstrates 59% crosstalk reduction and demonstrated consistently robust performance against crosstalk as noise increases, before the image is dominated by imaging artefacts due to poor SNR (**Figure 56 (c)**). We extended our evaluation analysis on a 3D subject-specific head model with a simulated regional activation on the visual cortex, showing 95% reduction in crosstalk from 0.11% to 0.005% when comparing the proposed algorithm with the non-spectral method using noiseless data. When mimicking realistic image system noise, both methods demonstrate 0.2% level of image crosstalk, which should have very limited impact on the significance of clinical interpretation.

In conventional spectral technique as expressed by **Equation (1.41)** where the Tikhonov parameter $\alpha_s^2$ is operated directly on the spectral Jacobian $J_s$ (one that relates a small change in measurements to a change of either oxyhaemoglobin or deoxyhaemoglobin concentrations), the regularisation or smoothing applied will also have an effect on the spectral mixing. However, using the proposed SVD-based spectral method as expressed by **Equation (1.52)**, the spectral Jacobian $\hat{J}_s$ is a pre-regularised matrix (which only relates a small change in measurements to change in absorption) and the spectral mixing is unaffected by this regularisation, implying that the latter method should provide better accuracy in parameter recovery. When comparing with the non-spectral method which consists of three matrix

inversion operations, namely applying **Equation (1.32)** twice for the recovery of absorption at wavelength $\lambda_1$ and $\lambda_2$ , and **Equation (1.6)** once for the recovery of chromophore concentration from absorption, our SVD-based spectral method requires only one inversion in **Equation (1.52),** consequently reducing the numerical error associated with the computation of matrix inversion. In the case of noise-added data, it is possible to expand **Equation (1.52)** by adding a noise term: $\begin{pmatrix} \Delta HbO_2^T \\ \Delta HbR^T \end{pmatrix} = J_S^T \left( \hat{J}_S \hat{J}_S^T \right)^{-1} \begin{pmatrix} \Delta\Phi_{\lambda_1}^T \\ \Delta\Phi_{\lambda_2}^T \end{pmatrix} + J_S^T \left( \hat{J}_S \hat{J}_S^T \right)^{-1} \begin{pmatrix} \Delta noise_{\lambda_1}^T \\ \Delta noise_{\lambda_2}^T \end{pmatrix}$. Therefore as the level of noise increases up to a point where $J_S^T \left( \hat{J}_S \hat{J}_S^T \right)^{-1} \begin{pmatrix} \Delta noise_{\lambda_1}^T \\ \Delta noise_{\lambda_2}^T \end{pmatrix}$ is greater than the improvement in solution numerical accuracy by $J_S^T \left( \hat{J}_S \hat{J}_S^T \right)^{-1} \begin{pmatrix} \Delta\Phi_{\lambda_1}^T \\ \Delta\Phi_{\lambda_2}^T \end{pmatrix}$ over the other two methods, it would appear on the recovered images that the effect of crosstalk reduction by the SVD-based spectral method is gradually minimised, and eventually diminished as the imaging artefacts due to noise become dominant, as demonstrated in **Figure 56 (c)** and **58 (d).**

Validation of the SVD-based method as presented in this paper has been limited at a specific wavelength pair, i.e. 750 and 850 nm. In this case the crosstalk between ΔHbR and $\Delta HbO_2$ is systematically small, owing to the large and opposite difference between their molar extinction coefficients at 750 and 850 nm (**Figure 17**). In the concept of wavelength optimisation [8], this means that the condition number of their spectral composition matrix $M_S$ is relatively low as compared to other wavelength pairs. Nevertheless since the crosstalk improvement by our SVD-based method relies on no assumption on either specific spectral range or specific combinations of the molar extinction coefficients, we expect the

improvement to be consistent when using other pairs of wavelengths. A full validation of this could be carried out over an extensive range of wavelength pairs as an extension of this work.

When compared with the linear spectral fDOT as presented here, nonlinear spectral DOT reconstruction has the added benefit of iteratively updating the recovered chromophore concentrations simultaneously with a minimisation function until the solution converges to a predefined threshold, as described by the Levenberg-Marquardt nonlinear optimisation in **Section 4.3.1.1**. It is also worth mentioning that the regularisation parameter would decrease over the iterations, resulting a gradual reduction in the imaging crosstalk due to conventional spectral regularisation method (as appeared in **Figure 54-56**, **Conv-Spec**), or a 'crosstalk correction' process over the iterations. However in the case of single-step, differential spectral fDOT as described in this work, appropriate regularisation method has shown to be critical to minimise crosstalk while maintaining the benefits of spectral constraints. We expect that in the presence of larger magnitude differential measurements and lower noise levels, this proposed reconstruction algorithm to be superior to non-spectral techniques.

## 7.5 Conclusions

The use of conventional regularisation techniques can result in additional crosstalk between chromophores. A novel regularisation technique that regularises the Jacobian using the singular value decomposition (SVD) prior to spectral mixing has been presented in an attempt to reduce such crosstalk effects. Simulations have shown that using SVD-based regularisation can dramatically reduce the crosstalk presented in images recovered using conventional regularisation technique in linear, single-step spectral DOT. Although our analysis has shown that given the current HD-fDOT imaging system specification, such improvement in crosstalk over the non-spectral method may not be substantial, it is evident that future instruments with higher SNR measurements would only yield better image quality for the spectral method over

the non-spectral method. The use of SVD in matrix regularisation as described in this study is also potentially applicable to other one-step linear imaging problems, offering an alternative approach to the conventional Tikhonov regularisation and should also play an important part in nonlinear spectral imaging techniques in DOT.

# CHAPTER 8

# CONCLUSIONS AND FUTURE WORKS

## 8.1 Conclusions

The keyword in this thesis is fDOT image quality. At the beginning of the thesis (**Chapter 1)**, we have identified several factors that caused sub-optimal image quality in previous fDOT studies and aimed to address and resolve these issues. This section summarises the contributions of this thesis as our solutions for improving fDOT image quality. Our main contributions include the first realistic-noise-added point-spread-function (PSF) analysis of MRI-guided HD-fDOT, the validation for the use of homogeneous background absorption fitting scheme in HD-fDOT, and the validation for the use of singular-value-decomposition-based (SVD-based) regularisation method for spectral fDOT. From our overall results it follows that: (1) HD-fDOT is capable of imaging focal haemodynamic response up to 18 mm depth below the human scalp surface at 10 mm image resolution and localisation accuracy, allowing distinguishability of gyri; (2) the use of homogeneous background absorption fitting scheme in HD-fDOT can minimise the chances of obtaining sub-optimal image quality due to uncertainty in background tissue optical property; (3) the SVD-based regularisation scheme is capable of reducing imaging crosstalk observed in both conventional spectral and non-spectral fDOT. The details of our main contributions and findings are expanded below.

### 8.1.1 PSF analysis of HD-fDOT

A recent advancement in fDOT system design is the development of high-density (HD) image array, also known as HD-fDOT (**Section 3.2.2**). This configuration allows the utilisation of overlapping measurements, providing more intensive spatial sampling of the underlying brain tissues than traditional sparse imaging arrays. The initial efficacy of HD-fDOT has been demonstrated through *in vivo* studies [36, 41, 42, 94] but there has been a lack of image quality analysis studies to demonstrate the achievable imaging performance of HD-fDOT in a realistic experimental setting. In **Chapter 5**, we have provided, to the best of our knowledge, the first realistic-noise-added point-spread-function (PSF) analysis of HD-fDOT on MRI-guided subject-specific head models, with and without the inclusion of an anatomically derived whole brain constraint. Our contributions and findings include:

- We have described and established a finite-element-method-based (FEM-based) routine to conduct MRI-guided fDOT simulation studies, which allows the construction of 1-mm high resolution (same resolution as T1-MRI, 1 × 1 × 1 mm voxels) finite element head model that provides realistic anatomical description of the underlying subject and also faster computation of the Jacobian matrix (20-30 minuses on average) than mesh-based Monte Carlo (MMCM) [124].
- We have introduced two novel image quality metrics, namely localised volume half maximum (LVHM) and focality, as compared to the conventional and standalone full volume half maximum (FVHM), in order to provide a more comprehensive and objective measure of image quality in situations where the FVHM contains multiple regions. The focality metric is mainly to assess the integrity of the other two metrics, namely whether the associated localisation error and LVHM reflect on the PSF of the target activation or the noise artefact. Therefore the focality itself also provides a

measure of the overall image quality, i.e. how 'focal' or 'spread' the recovered responses look like, and consequently an indication for the effect of noise on image quality (in the form of imaging artefacts).

- Through our realistic-noise-added point-spread-function (PSF) analysis across six subject head models and the utilisation of our novel image quality metrics, we have concluded that HD-fDOT is capable of imaging focal haemodynamic response up to 13 mm depth below the human scalp surface with no structural constrained image reconstruction, and up to 18 mm depth with the whole brain (both white matter and grey matter) constrained image reconstruction, given 10 mm localisation accuracy and image resolution that allows distinguishability of gyri.

### 8.1.2 Background absorption fitting scheme

The HD-fDOT image reconstruction accuracy depends on multiple modelling issues arising at different stages of the fDOT workflow (**Figure 22**). One of the concerning issues is the anatomical model of the human head, which has evolved from the homogeneous slab geometry of the early days into the increasingly popular realistic-five-tissue-segmented subject-specific head model (**Section 4.2.2**). The anatomical model affects the image reconstruction accuracy in that different anatomical regions are characterised by tissue types with distinct optical properties $\mu$, which in turn determine the spatial distribution of the measurement sensitivity $\frac{\partial \Phi}{\partial \mu}$ or the Jacobian $J$ that will be used in image reconstruction (**Section 4.3**). With disregard to misclassification of head tissues, or assuming that perfect tissue segmentation is possible, the uncertainty in the numerical value of tissue optical property becomes the dominant cause of systematic error in the predicted optical measurement sensitivity and the reconstructed images. However current practice as

documented in *in vivo* fDOT literature, which selects or derives numerical values of tissue optical property from other literature-based data, do not account for such uncertainty, possibility because earlier literature has demonstrated the insensitivity of linear DOT image quality to mismatches in background optical properties [30]. However the study was limited to noise-less analysis and generic two-dimensional simple geometry, and is therefore not helpful in understanding the issue in more realistic fDOT image problem. In **Chapter 6**, we have presented a multi-model comparative study to investigate the effect of uncertainty in background tissue optical properties within the context of HD-fDOT of human brain, and for the first time analysing its effect in structurally-constrained image reconstruction. We have also proposed the use of a homogeneous background absorption fitting scheme and validated its application in minimising sub-optimal image quality resulting from uncertainty in literature-based background optical properties. Our contributions and findings include:

- We have investigated the utilisation of background absorption fitting schemes in providing procedure-specific, subject-specific and wavelength-specific approximation of the underlying head tissue optical properties at no extra cost of data collection within the context of HD-fDOT of human brain. The homogenous background absorption fitting scheme takes on average 1 hour to complete and the fitted numerical values across six subjects are closely comparable (standard deviation of 1.2%). The heterogeneous background absorption fitting scheme takes on average 3 hours and the fitted numerical values are relatively consistent for the superficial tissues (standard deviation: 3% for scalp, 8% for skull, 12% for grey matter). Overall both fitting schemes have demonstrated reasonable levels of cross-subject consistency in the values they have derived.

- We have found that in non-structurally constrained HD-fDOT, when using a model that represents an underestimation of the actual tissue optical properties, the localisation accuracy outperforms the ‘inverse crime’ at deeper depth, owing to the deeper-than-expected coverage of high measurement sensitivity. On the other hand when using a model that represents an overestimation of the actual tissue optical properties, the image quality demonstrates high sensitivity to measurement noise in the form of image artefacts, activation distortions and dislocations because of the higher attenuation of measurement sensitivity within the non-brain tissues and therefore less-than-expected measurement sensitivity on the brain.
- We have also found that in whole-brain constrained HD-fDOT, which has fewer degrees of freedom than non-structurally constrained HD-fDOT, both underestimated and overestimated models show underperformed image quality. Specifically, the underestimated model demonstrates dislocation of activation towards deeper depth, while the overestimated model demonstrates hyper sensitivity of image quality to measurement noise in the form of severe imaging artefacts and activation dislocations, and in this case does not provide distinguishability of gyri.
- We have demonstrated that in both non-structurally constrained and whole-brain constrained HD-fDOT, when using a model that has optical properties derived from either homogeneous or heterogeneous background absorption fitting scheme, the image quality is consistently comparable with the ‘inverse crime’. Therefore we have successfully validated our hypothesis for the use of background absorption fitting schemes in HD-fDOT, which hypothesizes that optical properties derived from the scheme can provide better HD-fDOT image quality than literature-based approach that is likely to result either an overestimation or underestimation of the ‘ground truth’.

### 8.1.3 SVD-based spectral fDOT

The inclusion of spectral prior in nonlinear DOT image reconstruction has been shown to reduce crosstalk between chromophores. However such success has concealed the underlying Tikhonov regularisation operation that actually introduces (rather than reduces) crosstalk between chromophores, and the problem was not known prior to our study in **Chapter 7**. In response to this, we have proposed, implemented and validated a novel singular-value-decomposition-based (SVD-based) regularisation method for spectral fDOT that aims to resolve such crosstalk issue. Our contributions and findings include:

- We have provided the theoretical explanation for the increased crosstalk between $\Delta HbO_2$ and $\Delta HbR$ observed in [143] where the authors could not justify. The explanation is that the applied Tikhonov regularisation has modified the underlying spectral prior information, therefore introducing numerical errors in the form of imaging crosstalk (**Section 4.3.3**). This also means that the results and conclusions given in [142] are strongly misleading.
- We have proposed a novel SVD-based regularisation that operates on individual wavelength dependent sensitivity matrix independently (**Section 7.2**), thereby preventing the modification of the underlying spectral relationship between chromophores. We have provided an initial validation for the SVD-based spectral method on a two-dimensional simple model, which demonstrates 60% and 98% crosstalk reduction as compared to the non-spectral and conventional spectral method respectively in noise-less simulation.
- We have further validated the efficacy of the SVD-based spectral method in the context of HD-fDOT of human brain and reported 95% crosstalk reduction as compared to the non-spectral method in noise-less simulation. When realistic-noise

based on a current HD-fDOT imaging system is added to the analysis, we have found the effect of crosstalk reduction is overwhelmed by imaging artefacts due to the noise. Therefore we have concluded that the benefit of SVD-based spectral method will be more substantial when the signal-to-noise ratio (SNR) improves in future HD-fDOT instruments.

## 8.2 Future work

Possible directions of future work include:

- **Full head point-spread-function analysis.** The analyses as presented in this thesis have been limited to the primary visual cortex due to the size of the high-density imaging array [36]. However there has been an on-going effort at Washington University in St Louis to design a larger imaging pad that allows more extensive coverage of other functional regions, such as the motor cortex, and ultimately a full head imaging cap. Our point spread functional analysis as conducted in **Chapter 5** and **6** can be easily extended along with the coverage (FOV) of the imaging array, therefore providing more comprehensive fDOT image quality mapping of the human brain function.
- **Atlas-based image quality evaluation using inflated brain.** Admittedly the MRI-guided routine as represented in **Chapter 5** still relies on subject-specific structural MRI datasets prior to HD-fDOT analysis, which could severely limit the chance of HD-fDOT as an alternative and standalone functional neuroimaging technique over fMRI. However as mentioned in **Chapter 4**, the development of atlas-based approach have shown promises in both *in silico* [7] and *in vivo* [89] studies. Therefore a future direction would be to evaluate the imaging performance of atlas-based HD-fDOT methods. However one major challenge that is worth mentioning in this case is the

evaluation method, which may require the transformation (or mapping) function from one (presumably inflated) cortical surface to the other in order to provide a more clinically meaning evaluation.

- **Singular value decomposition-based regularisation in nonlinear spectral diffuse optical tomography image reconstruction.** We have shown that conventional spectral techniques could cause significant crosstalk in linear imaging and this will inevitably be the same in nonlinear imaging. Therefore the inclusion of SVD-based regularisation in nonlinear DOT problems such as breast imaging should also help reducing crosstalk between the recovered chromophores as compared to conventional nonlinear spectral DOT method.

# Appendix A

# Additional Tutorials on Segmentation

## A.1 SPM

SPM is a Matlab-based package developed for the analysis of neuroimaging data sequence at UCL. It includes an atlas-based head segmentation tool which allows the segmentation of five tissue types to be performed on T1 dataset alone. The version used in this work is SPM8. Since the segmentation tool in SPM does not read DICOM images directly, first we need to convert the images from '.DICOM' format into SPM readable '.hdr' and '.img'. To do this, click the 'DICOM Import' button and select the 176 slices of .DICOM images. The loading will be started, and finished by generating a '.hdr' and a '.img' file.

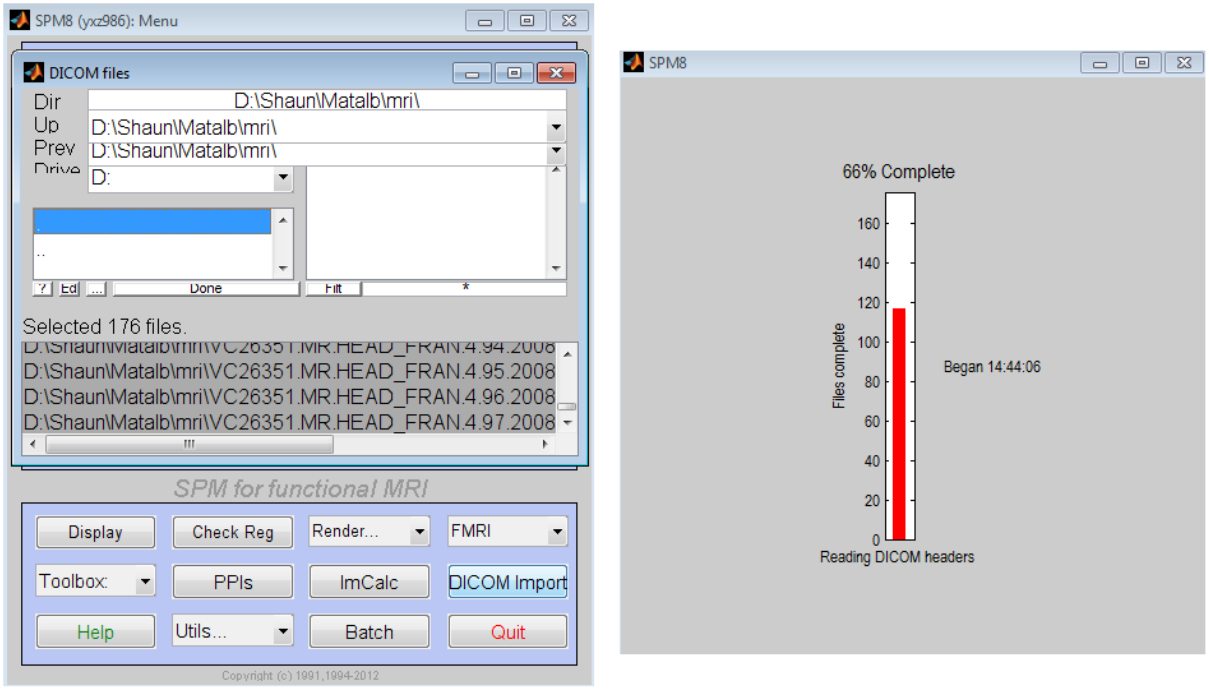


**Figure 59 SPM user interface for loading .DICOM images.**

Click 'Batch→SPM→Tools→New Segment'. Select the generated '.img' file in 'Data/Volumes'. The choice of atlas used is shown and can be changed in 'Warping & MRF/Affine Regularisation'. We use the default '*ICBM space template – European brains'. Once the settings are ready, click the green arrow Run bottom and the segmentation starts automatically. An animated window plotting 'Iteration versus Log-likelihood' are displayed during the segmentation, showing the likelihood between subject and atlas converges as iteration increases, and the algorithm terminates when a threshold is reached.

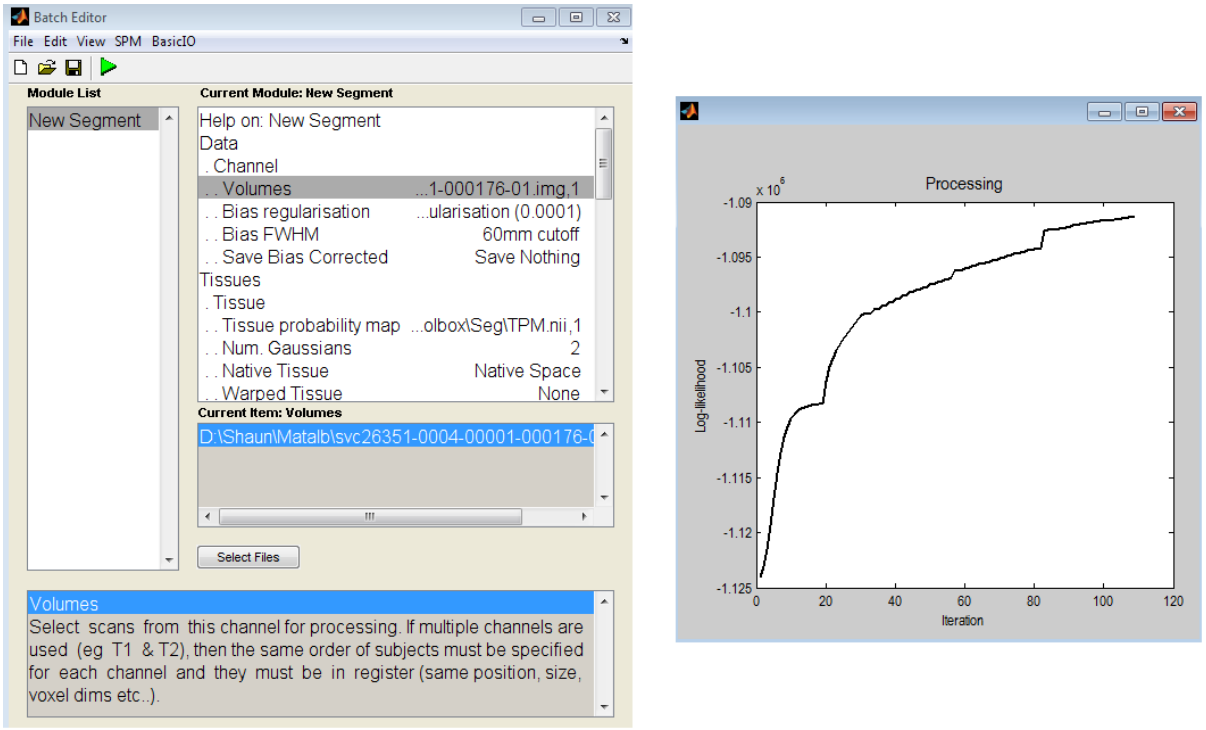


(a) (b)

**Figure 60 SPM user interface for performing atlas-based head tissue segmentation.**

The end products of the segmentation are five '.nii' files each containing the probability map of each tissue type. The probability map contains values ranging from 0 to 1, representing the probability (or confident level) of a given pixel to be a certain tissue type. Combining these five sets of data allows us to produce a segmented head anatomy.

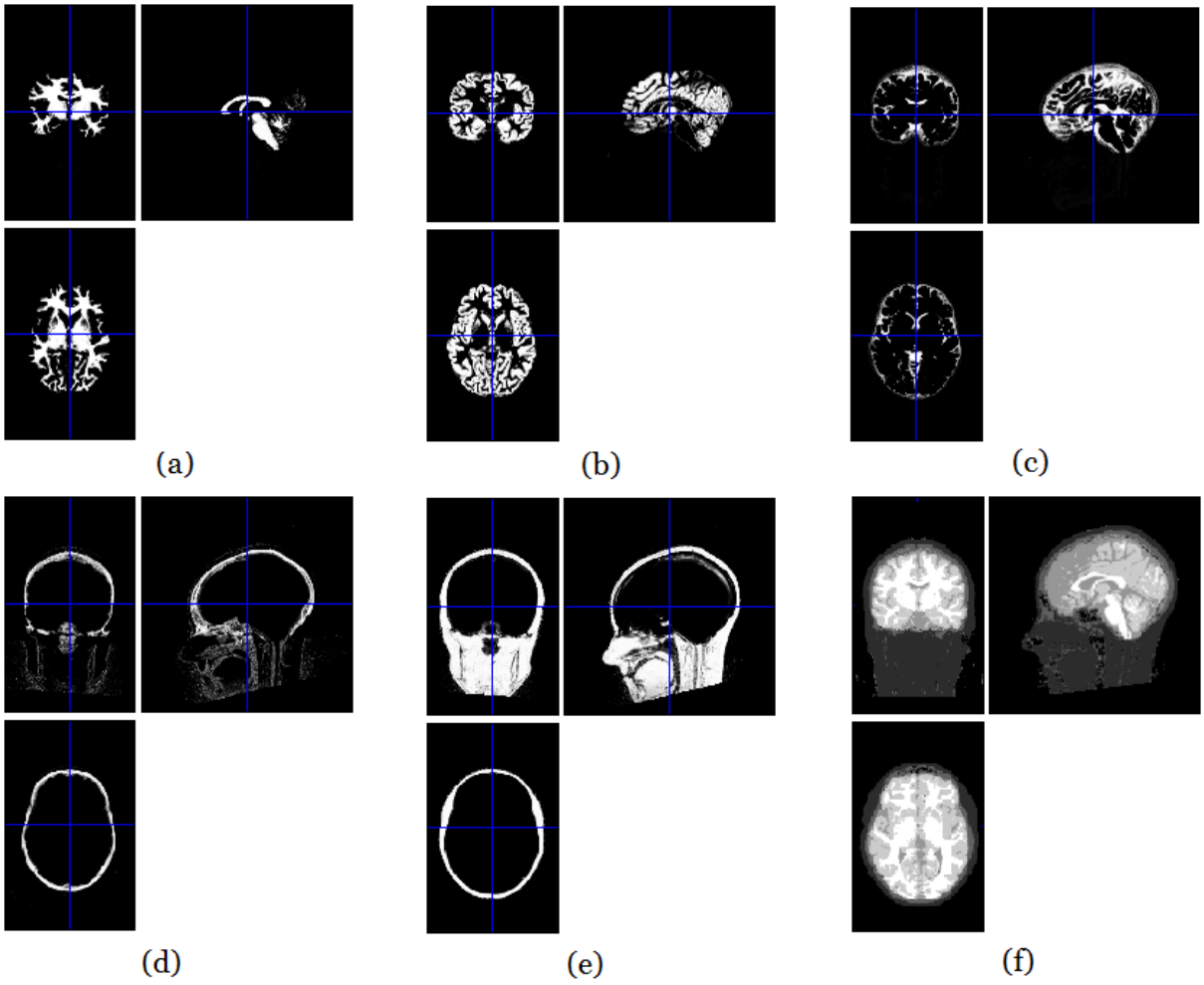


**Figure 61 SPM atlas-based segmentation outputs: segmented images for each of the five tissue types, namely (from a-e) white matter, grey matter, CSF, skull and scalp respectively, and the combination of them gives (f).**

# Appendix B

# Additional Tutorials on Mesh Generation

## B.1 Mimics

Mimics is a commercial 3D image processing and model generation software developed by Materialise [121]. The version used in this work is Mimics x64 15.01. First we load 176 slices of segmented images into Mimics, which automatically display the entire dataset in 4 views, namely coronal (top left), axial (top right), 3D (bottom right), and sagittal (bottom left) as shown in Figure 29. We then click 'Segmentation → Thresholding' on the toolbar to represent each tissue type with a colour mask. Although generating a finite element mesh for the entire head region is certainly practical, for our visual cortical mapping study we would like to focus on the posterior part of the head only. To do so, we click 'Segmentation → Crop Mask' to specify a region of our meshing interest.

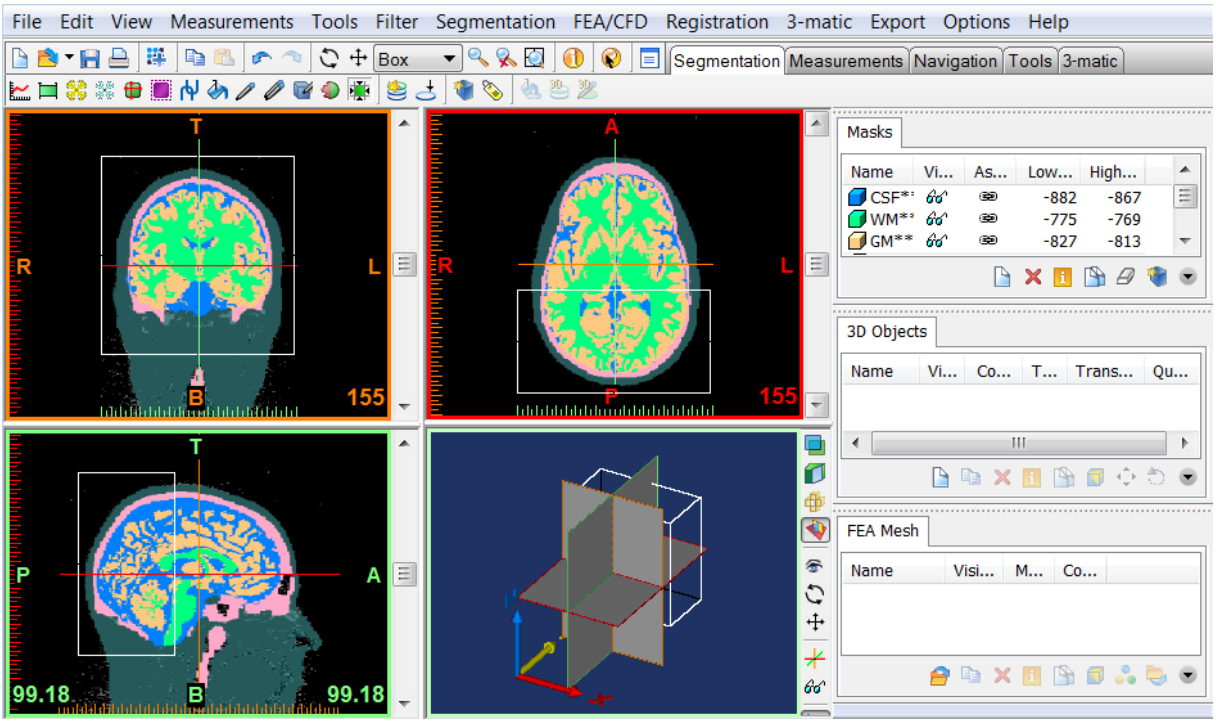


**Figure 62 Mimics user interface for cropping specific part of the head model.**

Next we generate a 1.0-mm voxel-based volume mesh for the defined region of interest. Select 'FEA/CFD → Create Voxel Mesh', there is a smaller window named 'Calculate Mesh' popping up which allows you to set a number of parameters. Follow the settings as shown in **Figure 53**. Mimics will then automatically generate a homogeneous volume mesh as shown in the 3D view window.

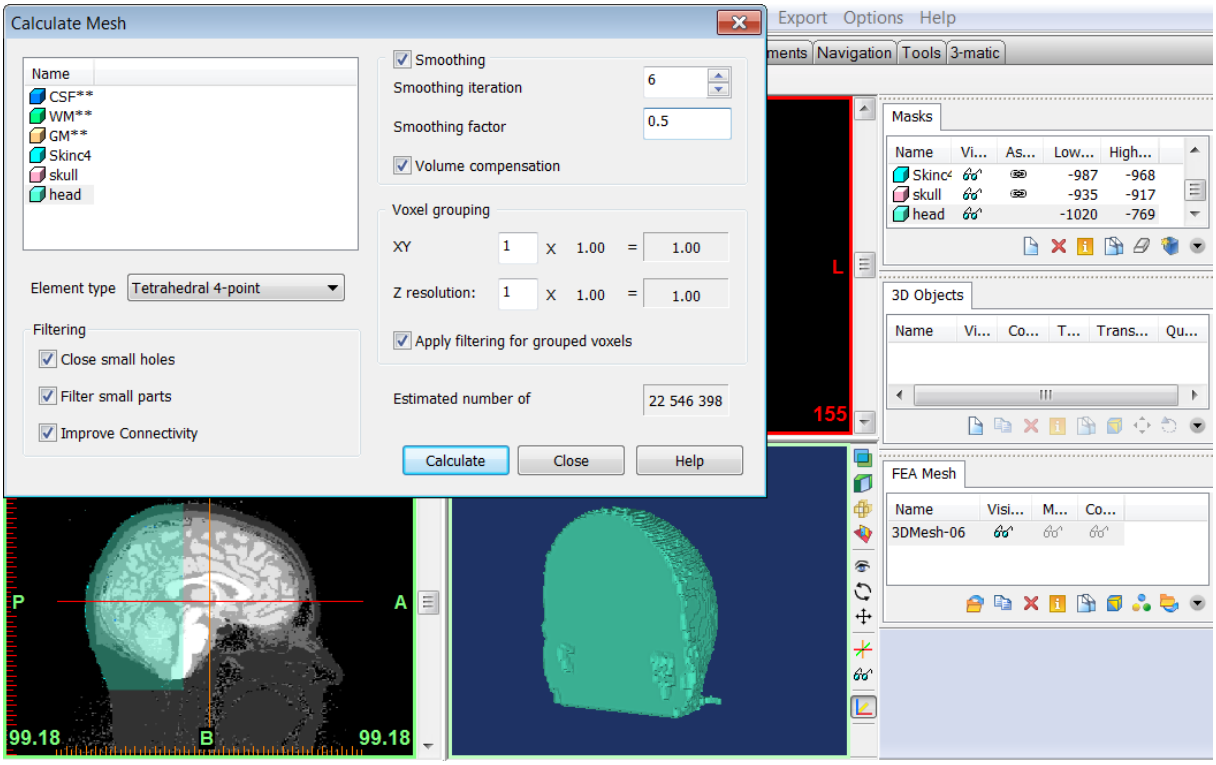


**Figure 63 Mimics user interface for performing volumetric mesh generation.**

To assign each node in the voxel mesh with their respective tissue type (represented by distinctive colour mask), click 'FEA/CFD → Material' and select the five colour masks, Mimics will automatically perform the assignment and complete with a colour-coded volume mesh displayed in the 3D view window.

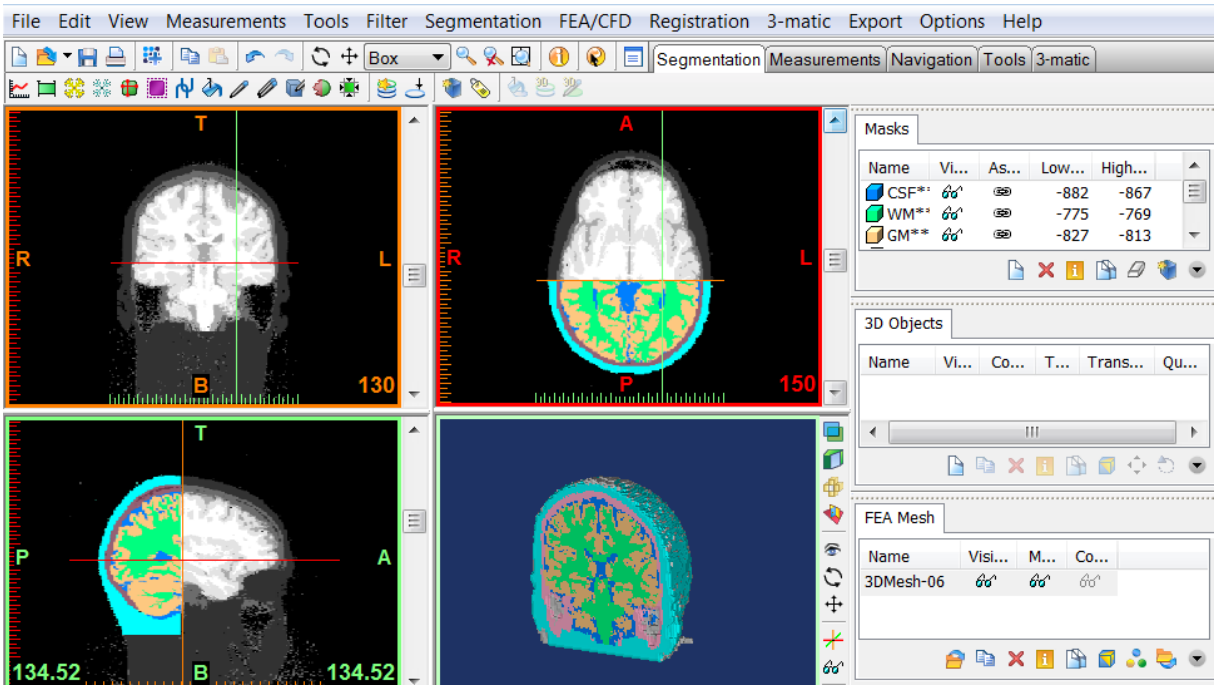


**Figure 64 Mimics user interface for performing tissue region labelling.**

Finally to export the mesh as description files, select 'FEA/CFD → Export', and export as 'Ansys Preprocessor files'. This would output a '.cdb' file containing node coordinates and element connectivity, and a '.txt'file containing nodal region information. Running a Matlab script named 'Mimics2Nirfast' would further translate these two files into Nirfast readable file formats.

## B.2 NIRView+Nirfast

NIRView is a free 3D image processing software developed by Kitware and jointly released with Nirfast [119], which is a Matlab-based open source, finite element meshing and analysis package developed at Dartmouth College. The two combined [160] provides a seamless workflow from segmented anatomical image dataset to finite element based imaging reconstruction and analysis. Similarly we first load 176 slices of segmented images into NIRView, which also display the entire dataset in 4 views. We then click 'Image Processing/Segmentation → K-Means+Markov Random Field (ITK)'. Set the 'Number of

Classes' to 6 as there are in total six regions in the entire image space, i.e. five tissues and background. Click 'Apply' and the dataset will be colour-coded as shown in Figure 55. This is known as 'label map' in NIRView and must be saved as a .mhd file before mesh generation.

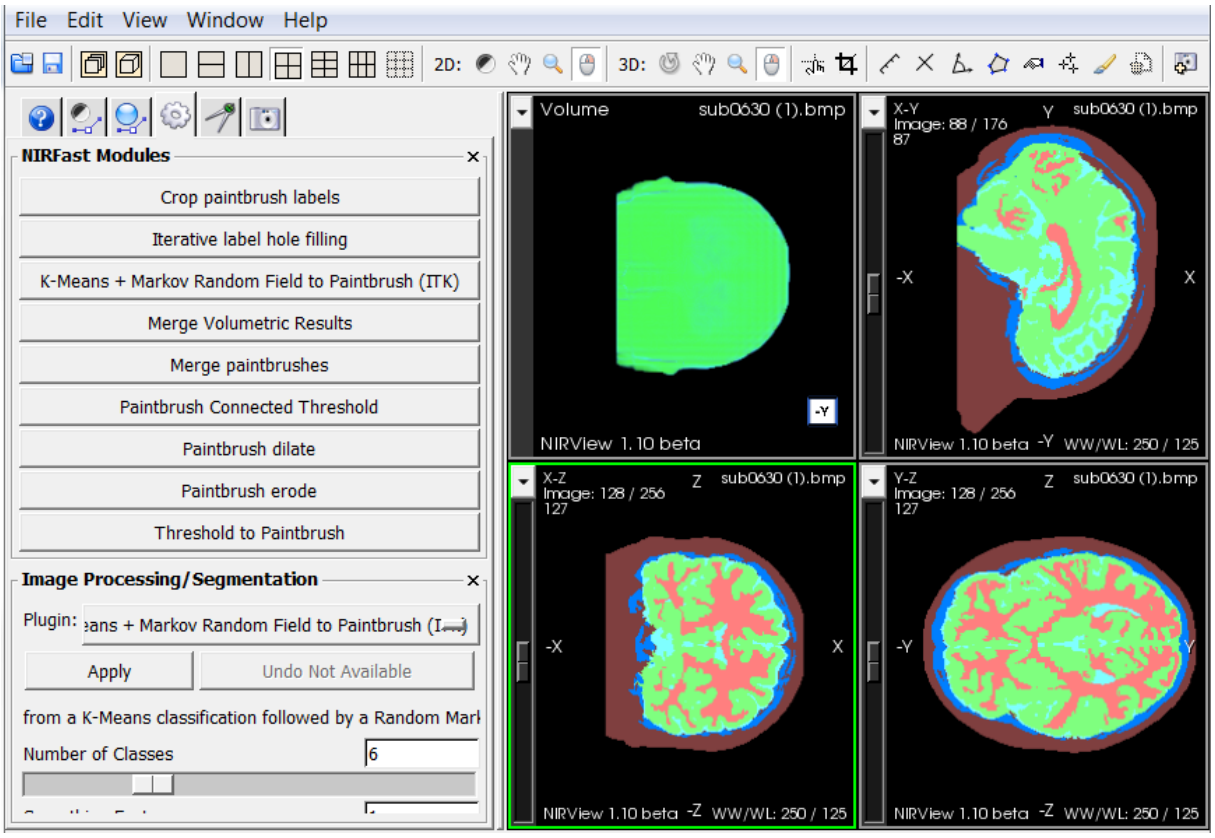


**Figure 65 NIRView user interface for loading segmented anatomical dataset.**

Go to 'File → Create Mesh' on the NIRView toolbar, this should start the Nirfast software with its mesh interface 'image2mesh_gui'. There are a number of parameters you can set regarding mesh generation. Under 'Image/Segmentation File name', load the '.mhd' file generated from NIRView. Follow the settings as shown in Figure 56. Nirfast will then automatically generate a Nirfast compatible segmented volume mesh that is ready for FEM analysis.

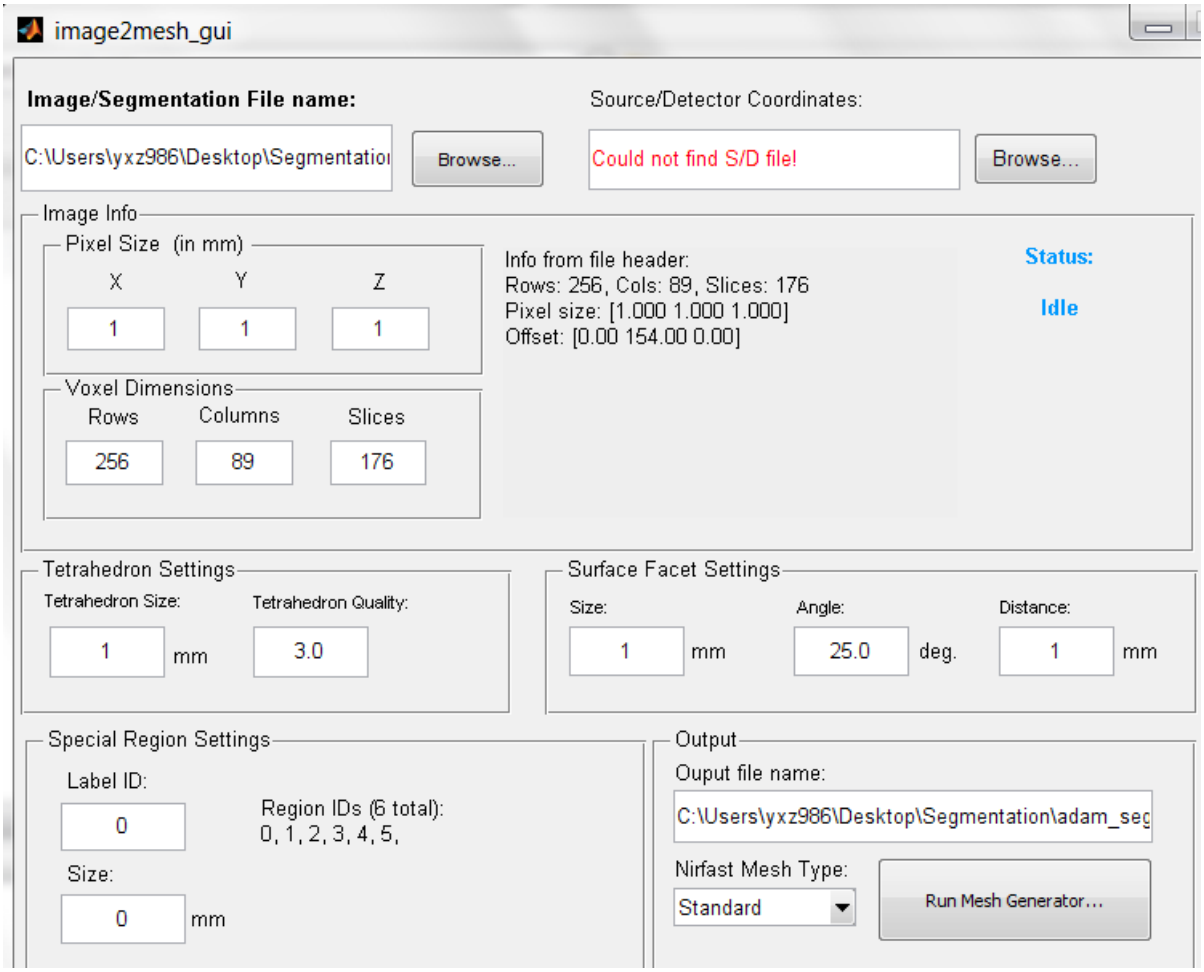


**Figure 66 Nirfast user interface for performing surface-based mesh generation.**

# Appendix C

# Additional Figures for Chapter 5

This appendix provides the scatter plots of metrics of image quality for Subject 2b-5b as described in **Chapter 5**.

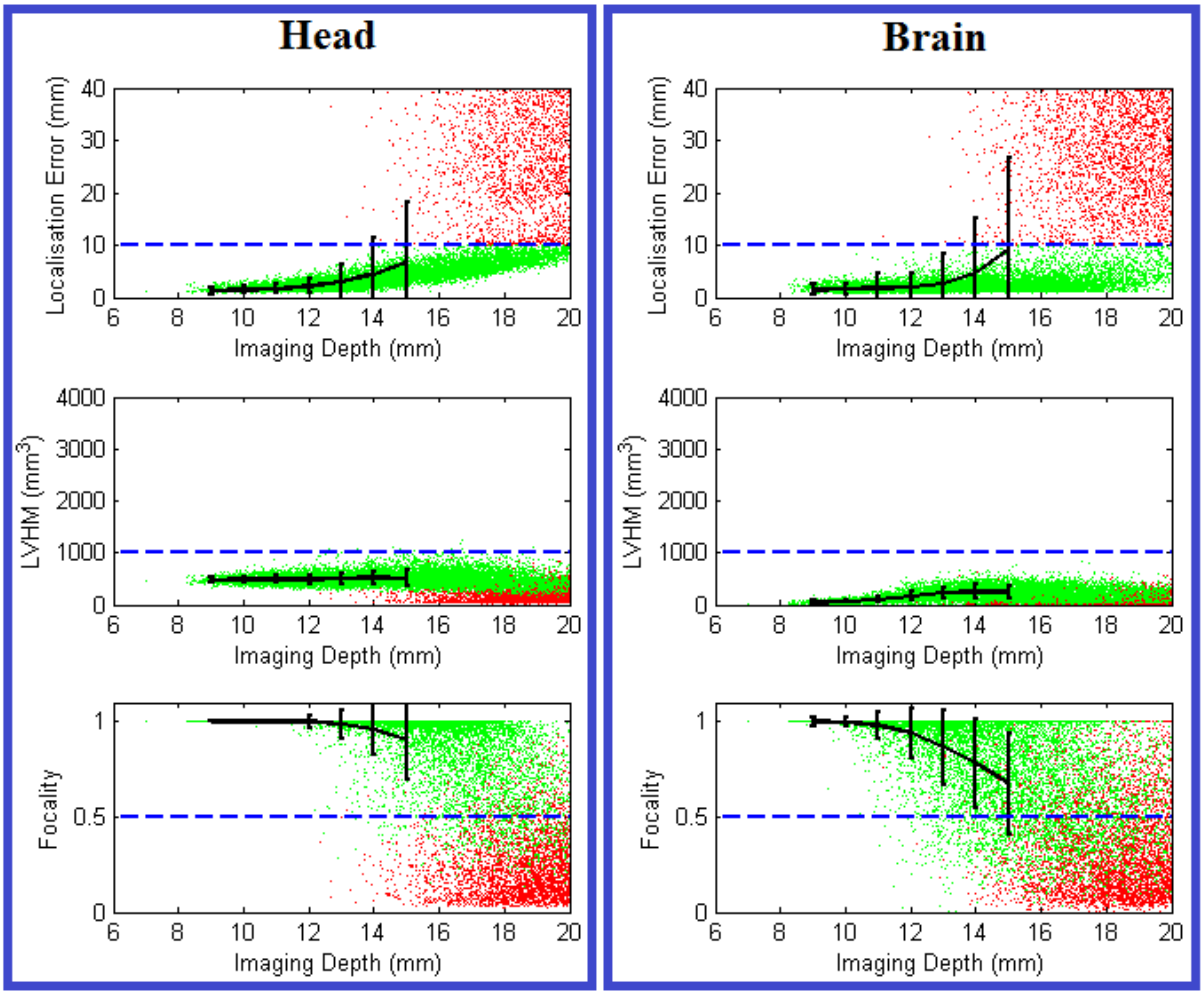


**Figure 67 Scatter plots of localisation error, LVHM and focality versus imaging depth (up to 20 mm) for all PSFs of Subject 2b.**

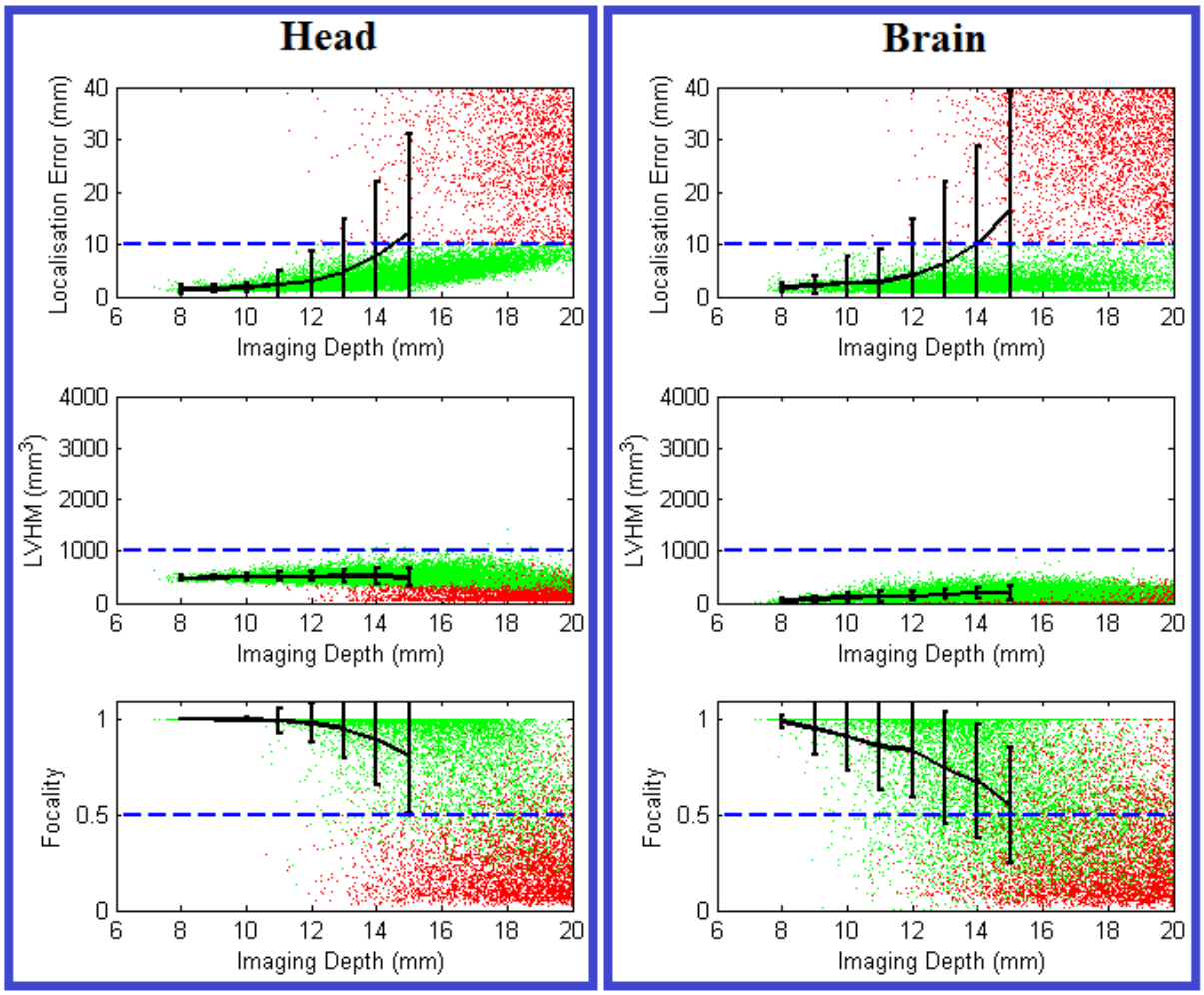


**Figure 68 Same as the last figure, but of Subject 3b.**

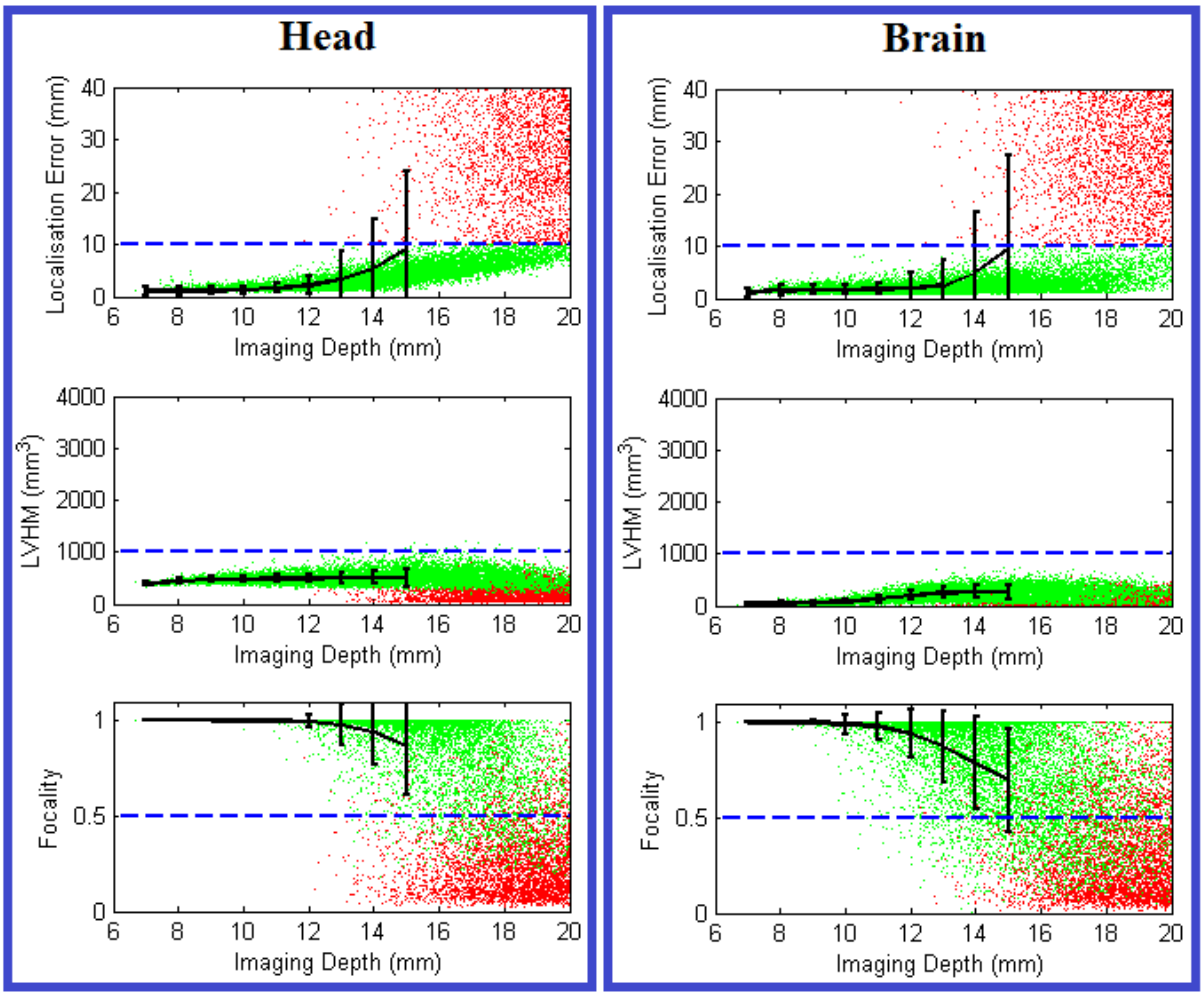


**Figure 69 Same as the last figure, but of Subject 4b.**

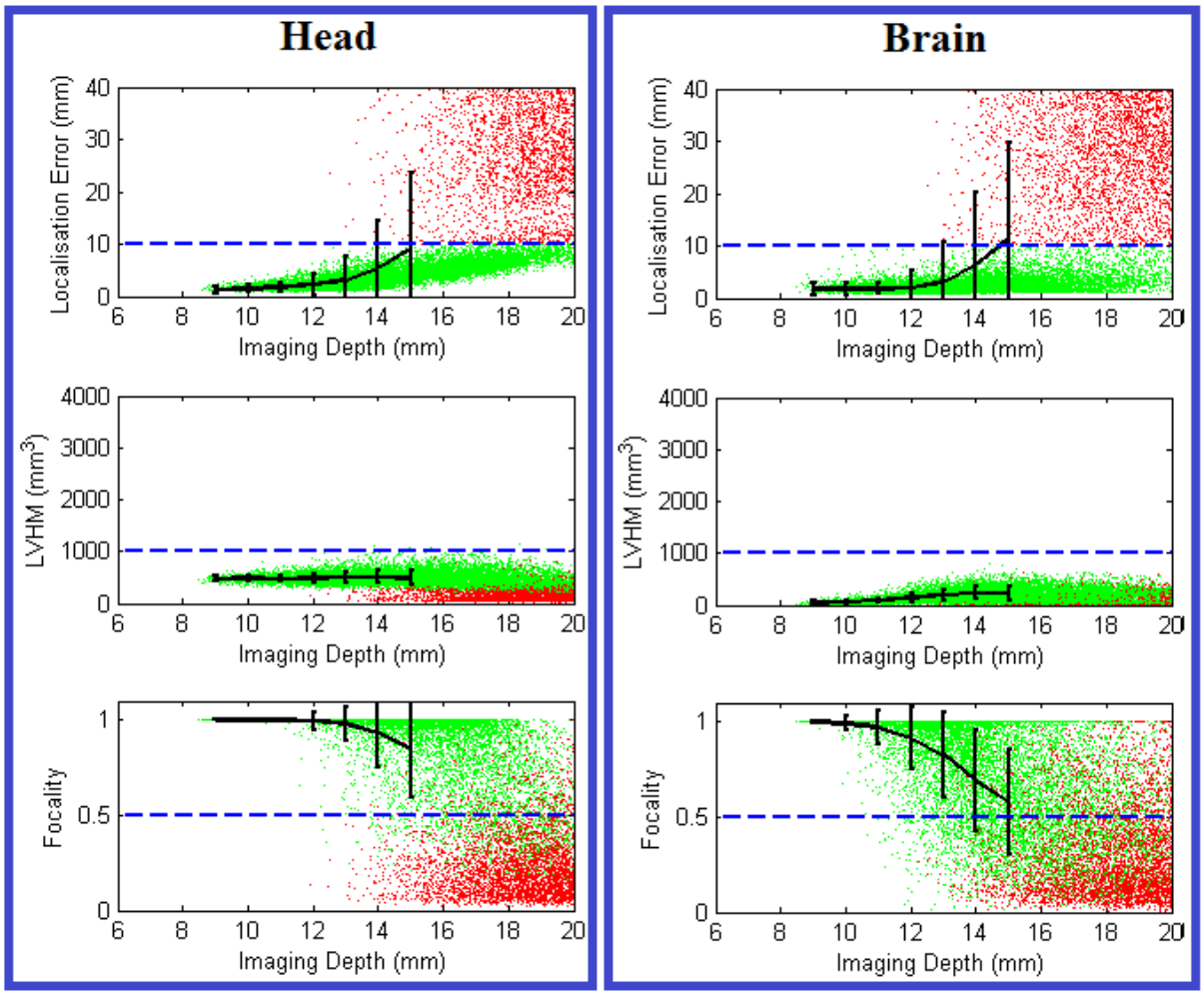


**Figure 70 Same as the last figure, but of Subject 5b.**

# Appendix D

# Additional Figures for Chapter 6

This appendix provides the scatter plots of metrics of image quality for Case A-E of Subject 1a, 1b-5b as described in **Chapter 6**.

## D.1 Head reconstruction

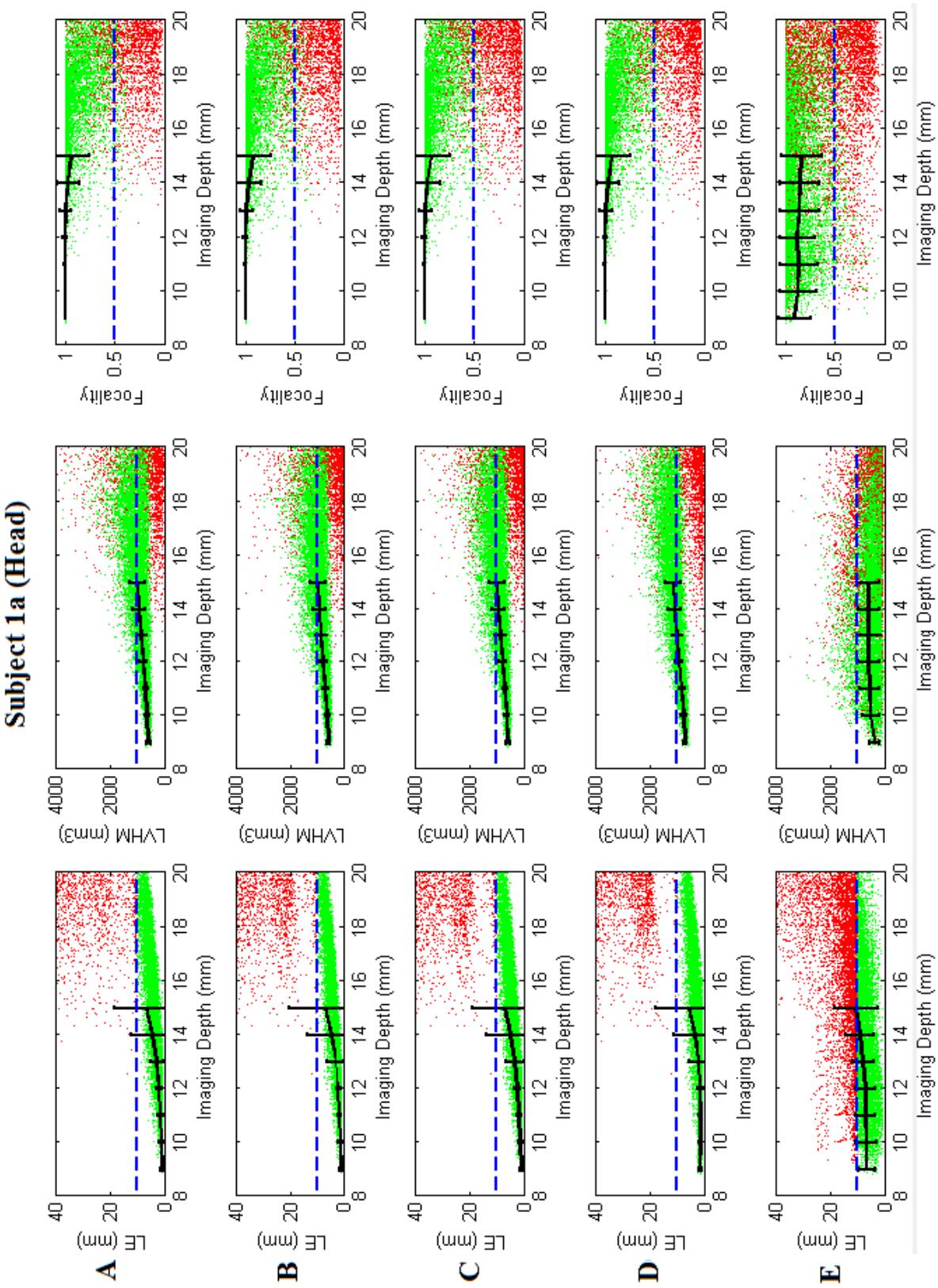


**Figure 71 Scatter plots of localisation error, LVHM and focality versus imaging depth (up to 20 mm) of Subject 1a using full head reconstruction in model A-E.**

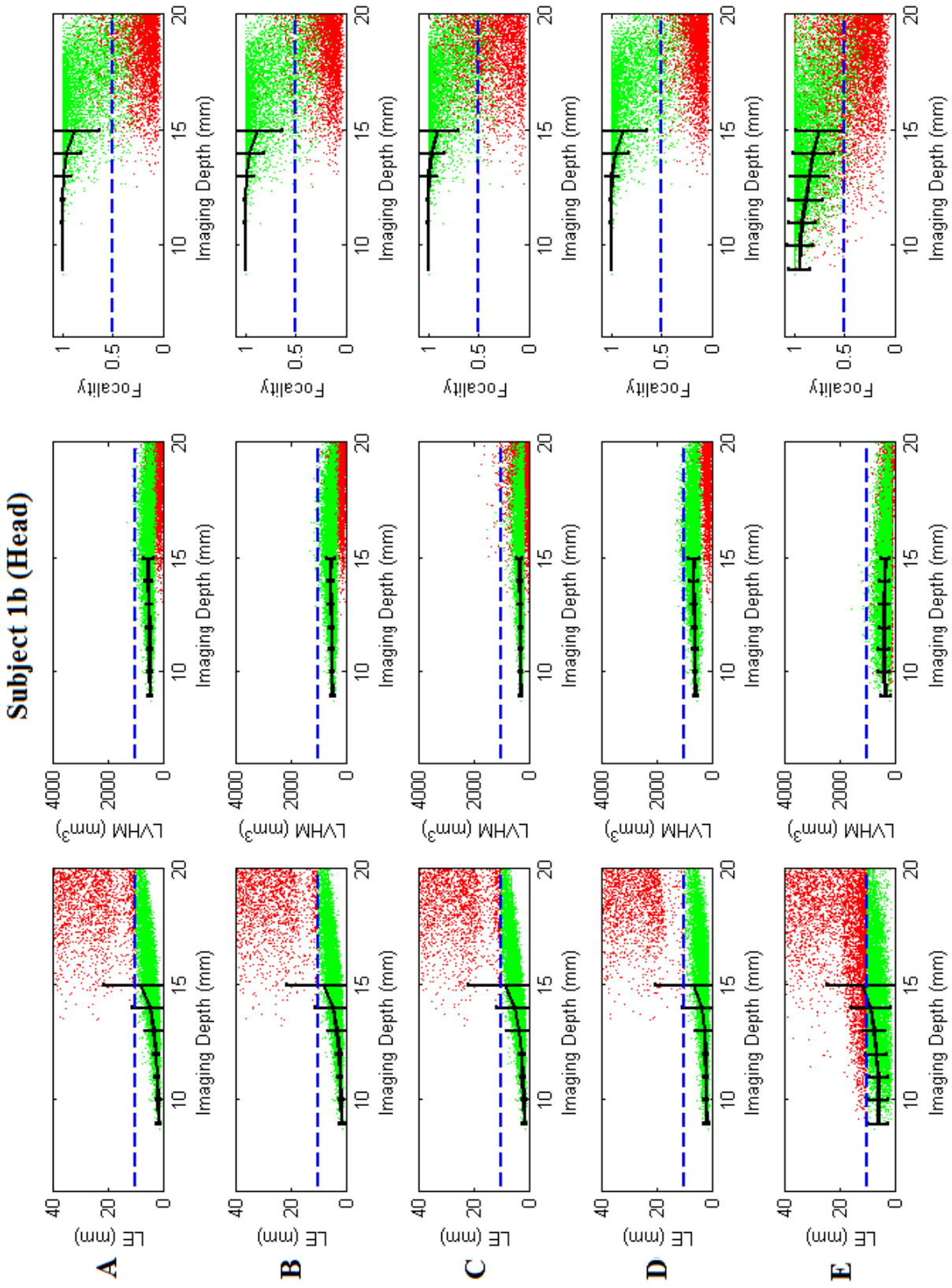


**Figure 72 Same as the last figure, but of Subject 1b.**

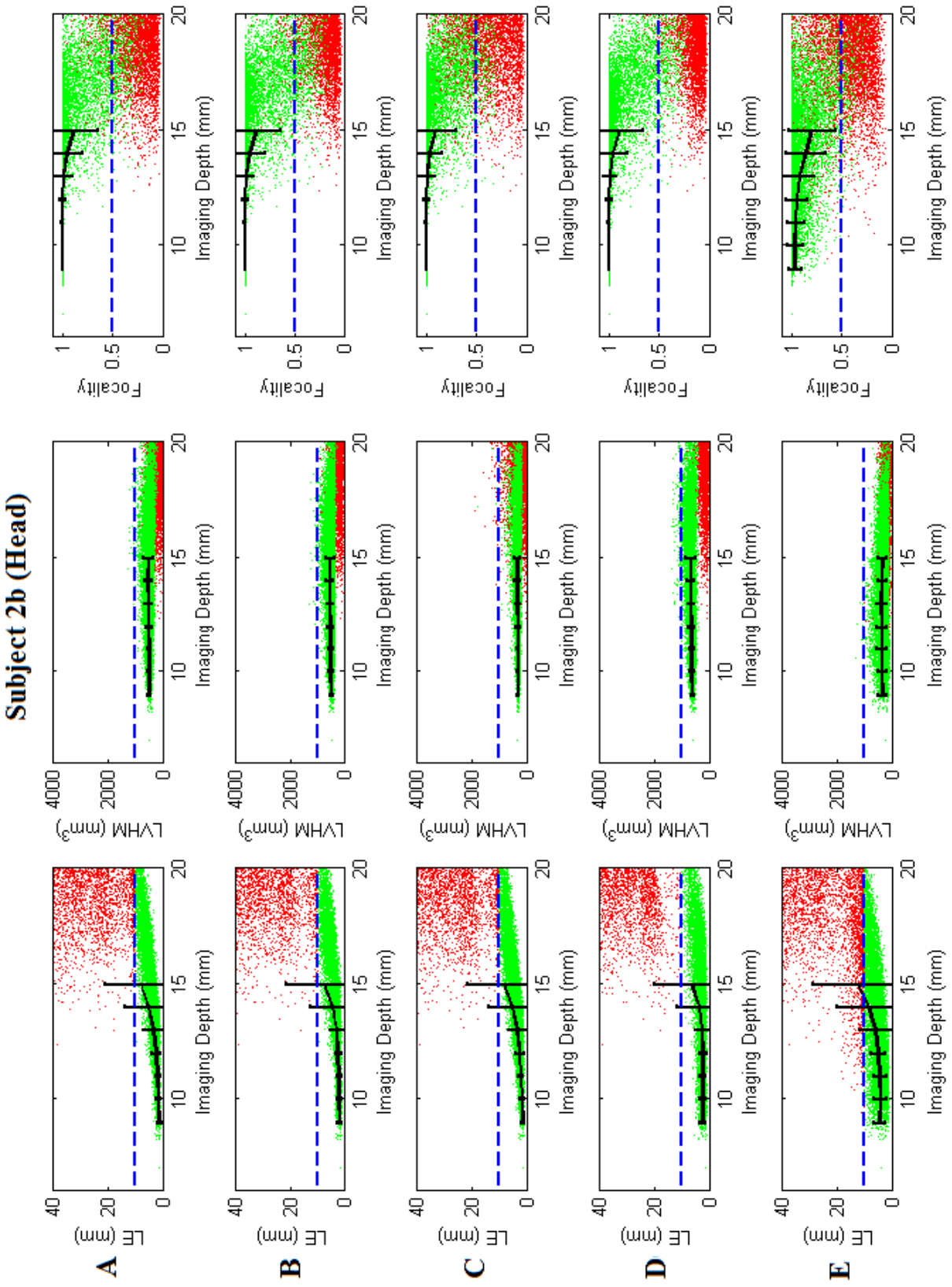


**Figure 73 Same as the last figure, but of Subject 2b.**

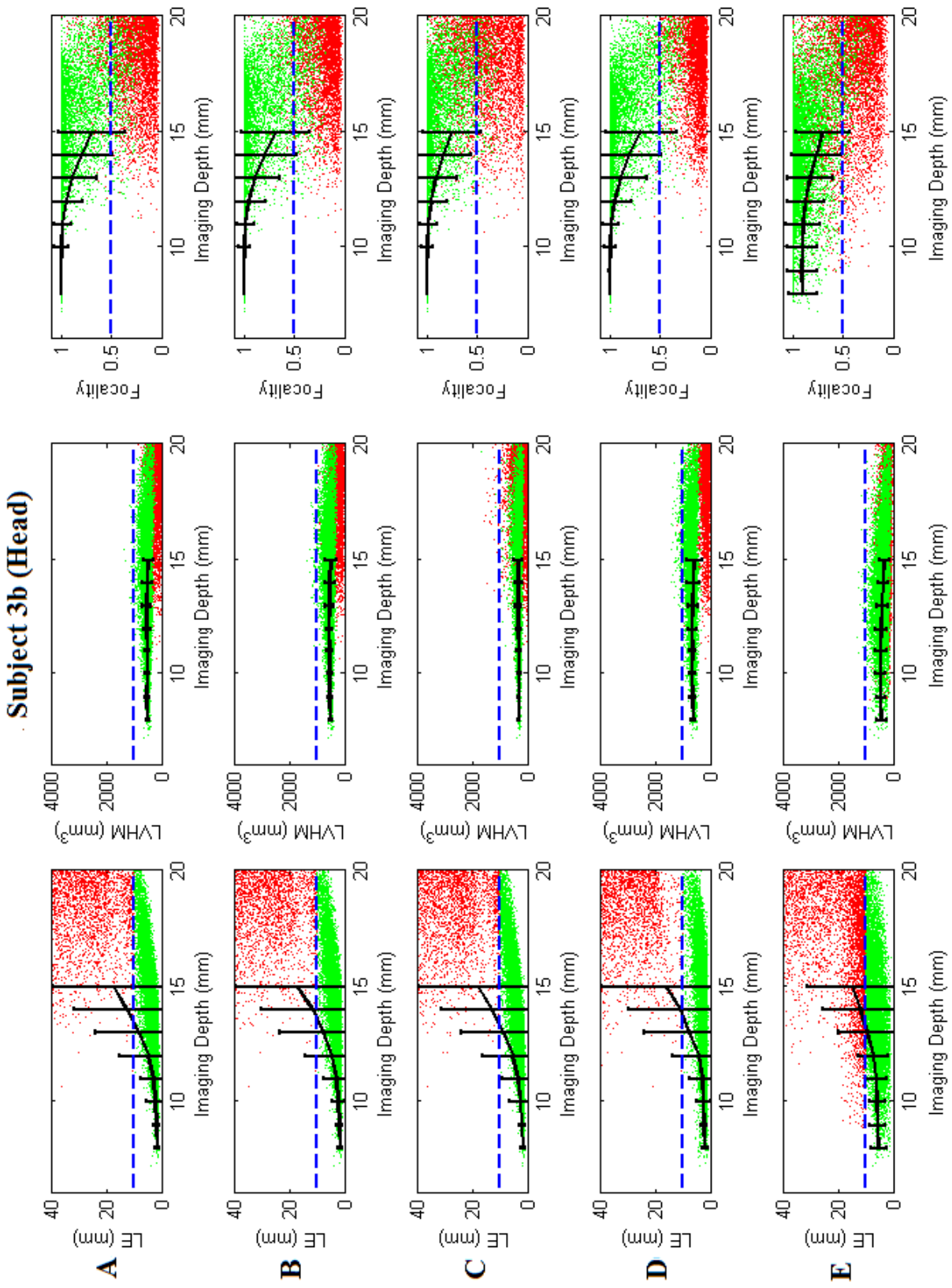


**Figure 74 Same as the last figure, but of Subject 3b.**

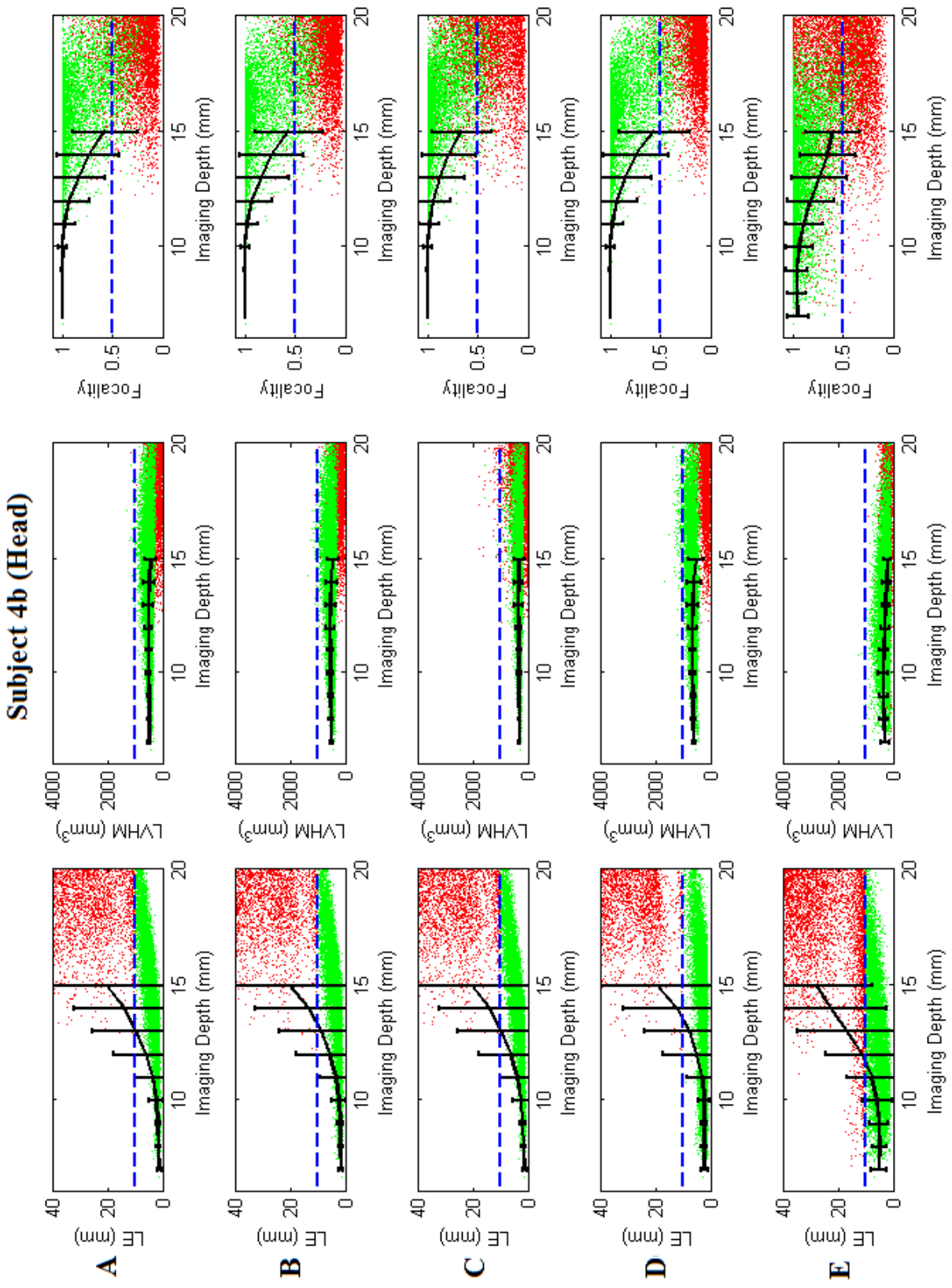


**Figure 75 Same as the last figure, but of Subject 4b.**

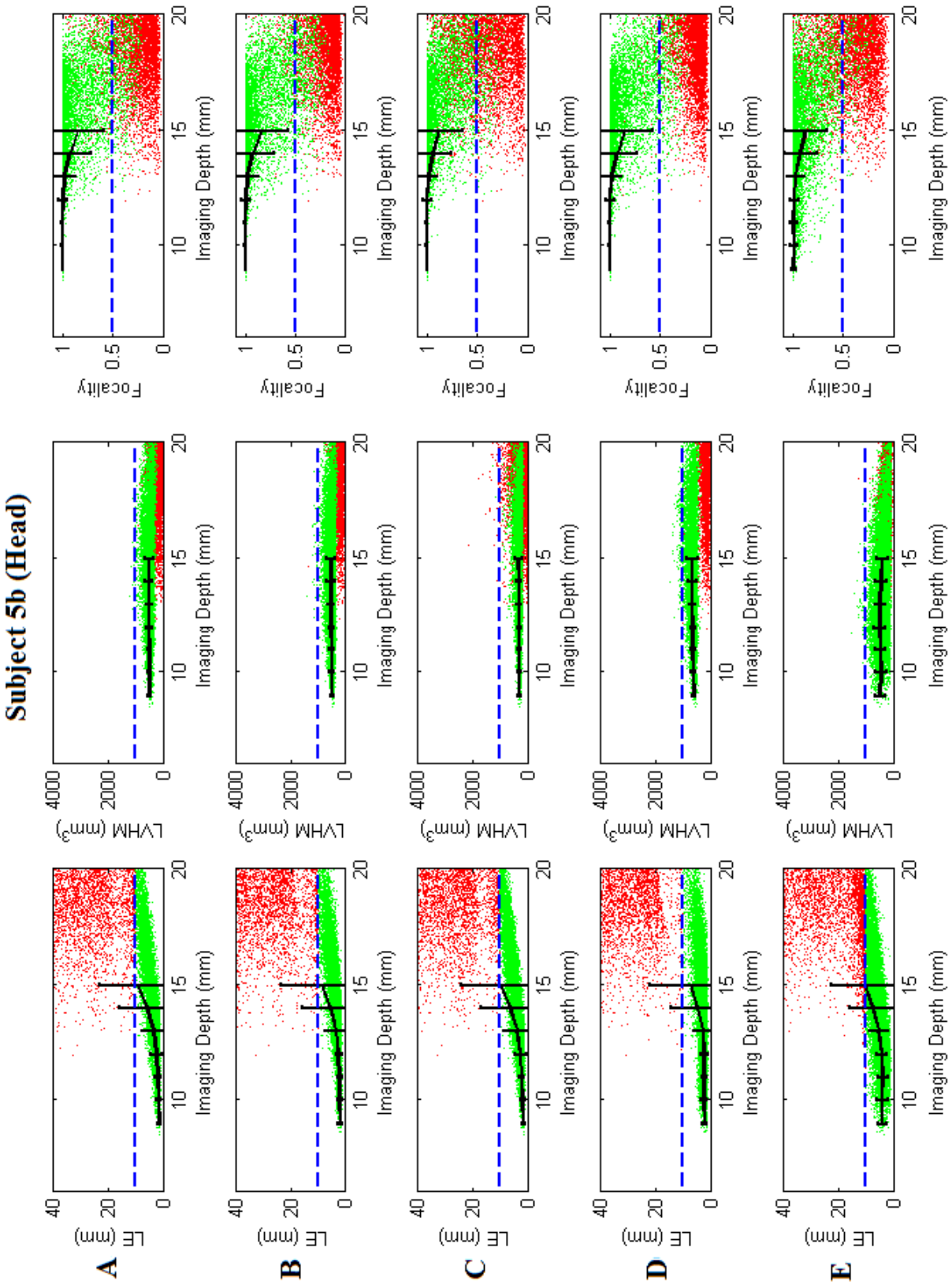


**Figure 76 Same as the last figure, but of Subject 5b.**

## D.2 Brain reconstruction

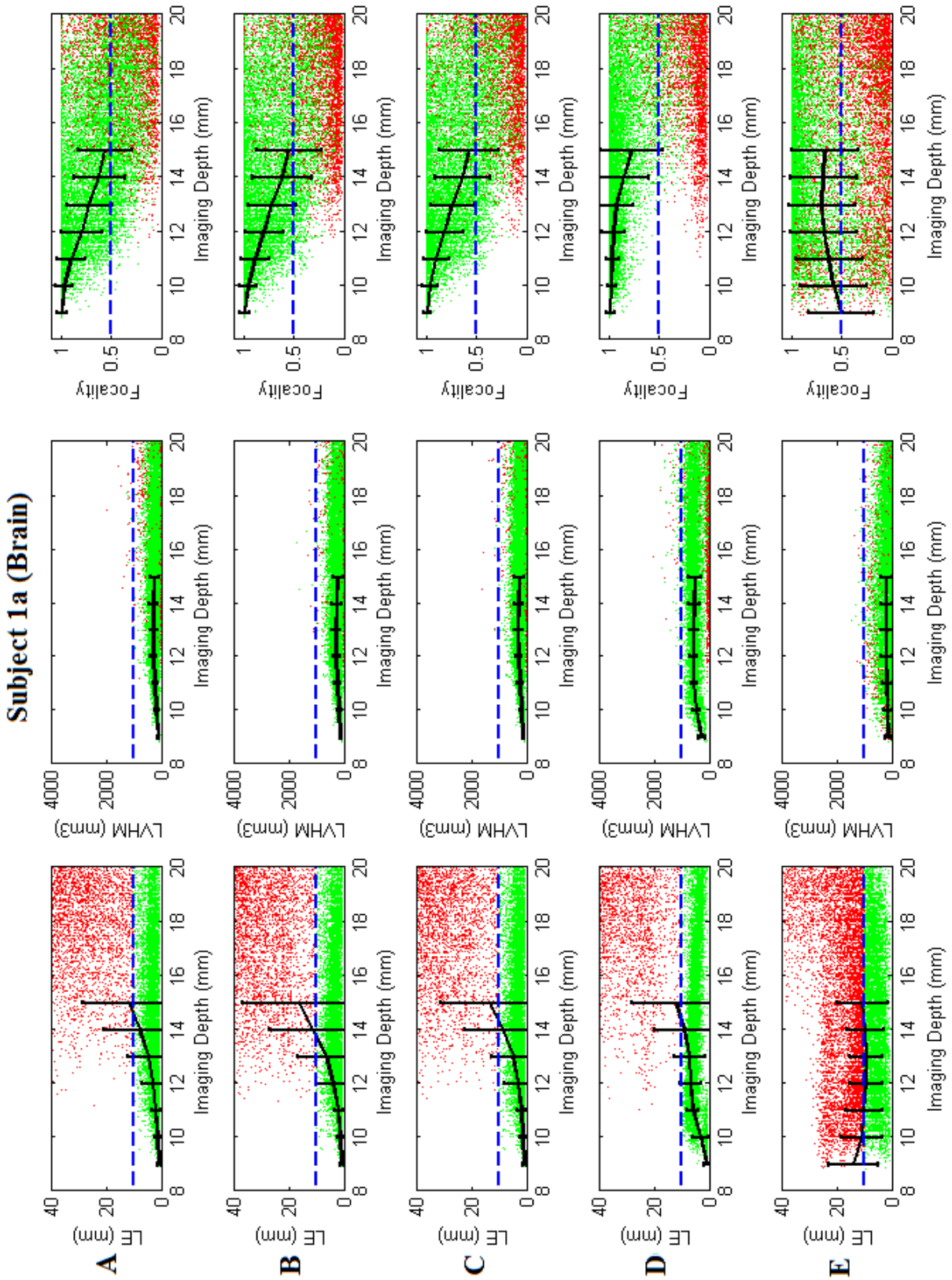


**Figure 77 Scatter plots of localisation error, LVHM and focality versus imaging depth (up to 20 mm) of Subject 1a using whole brain constrained reconstruction in model A-E.**

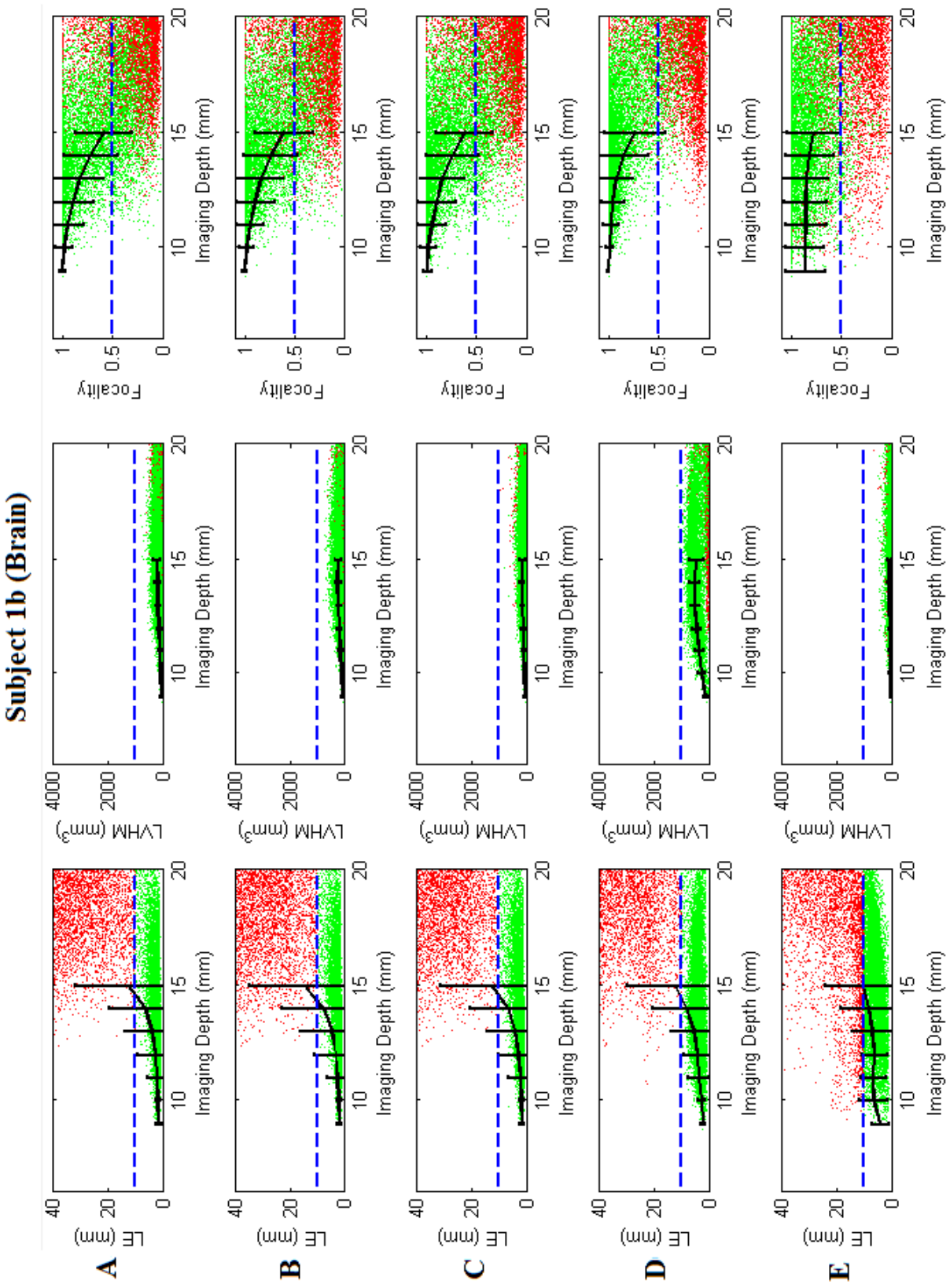


**Figure 78 Same as the last figure, but of Subject 1b.**

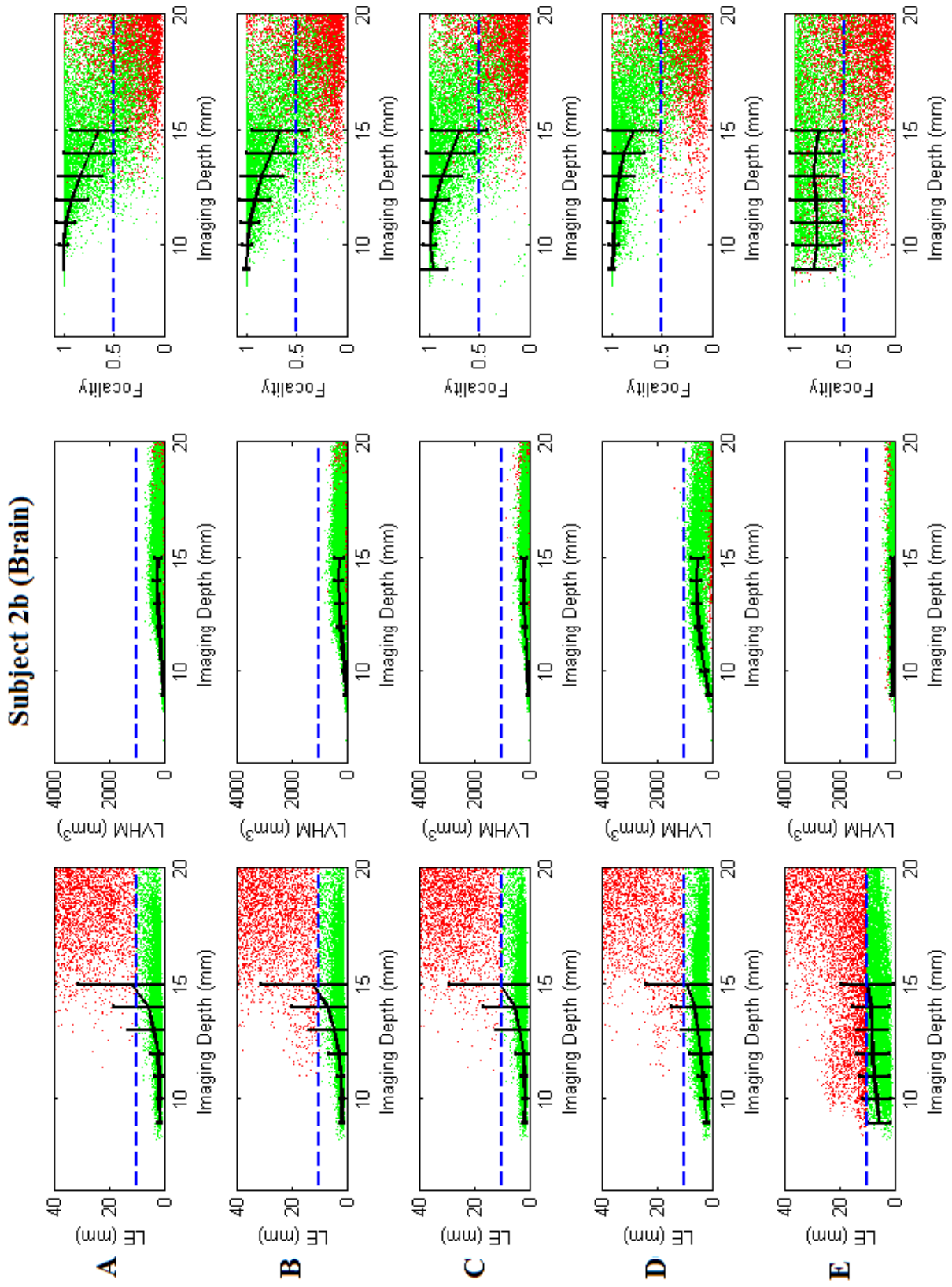


**Figure 79 Same as the last figure, but of Subject 2b.**

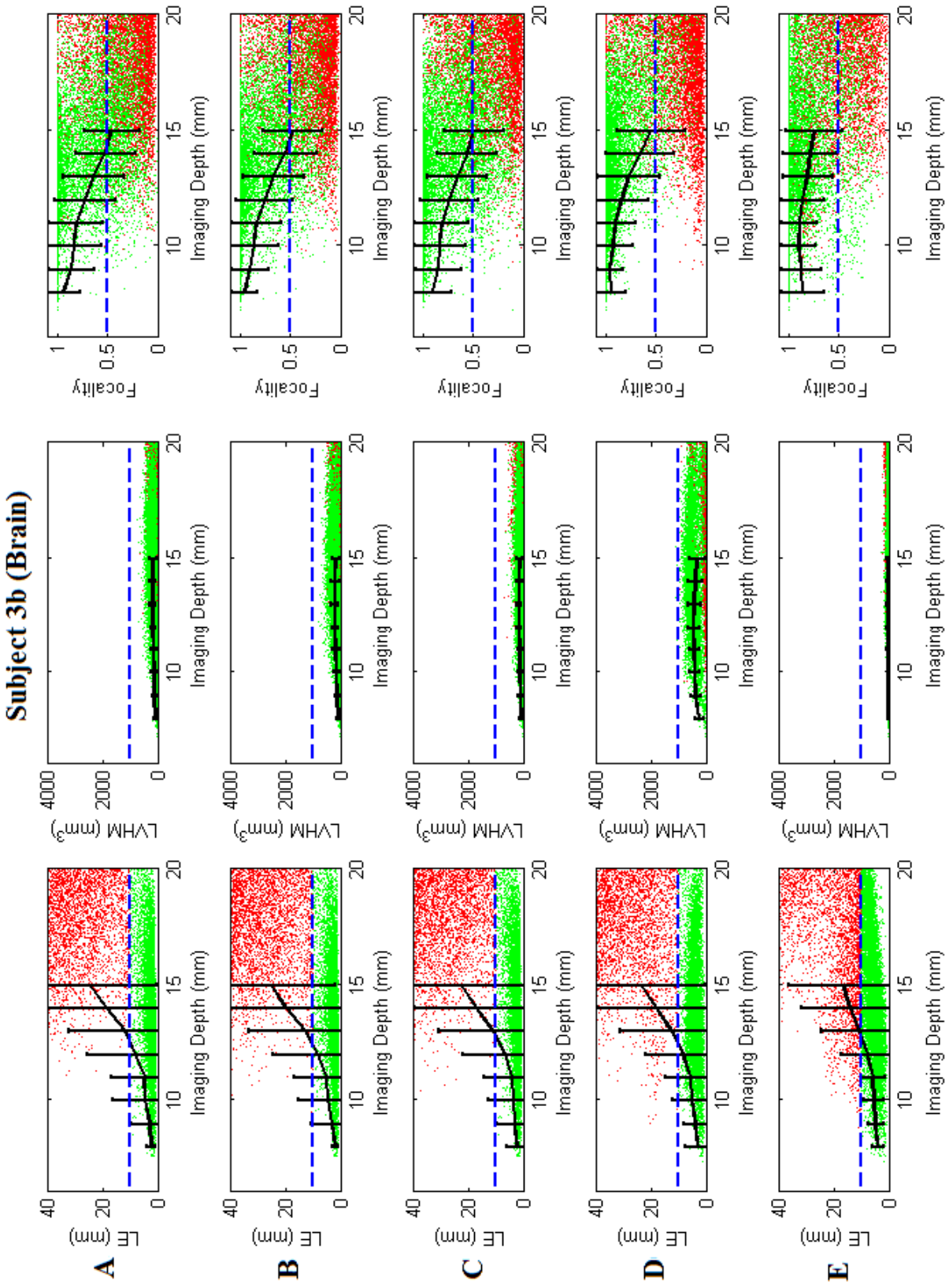


**Figure 80 Same as the last figure, but of Subject 3b.**

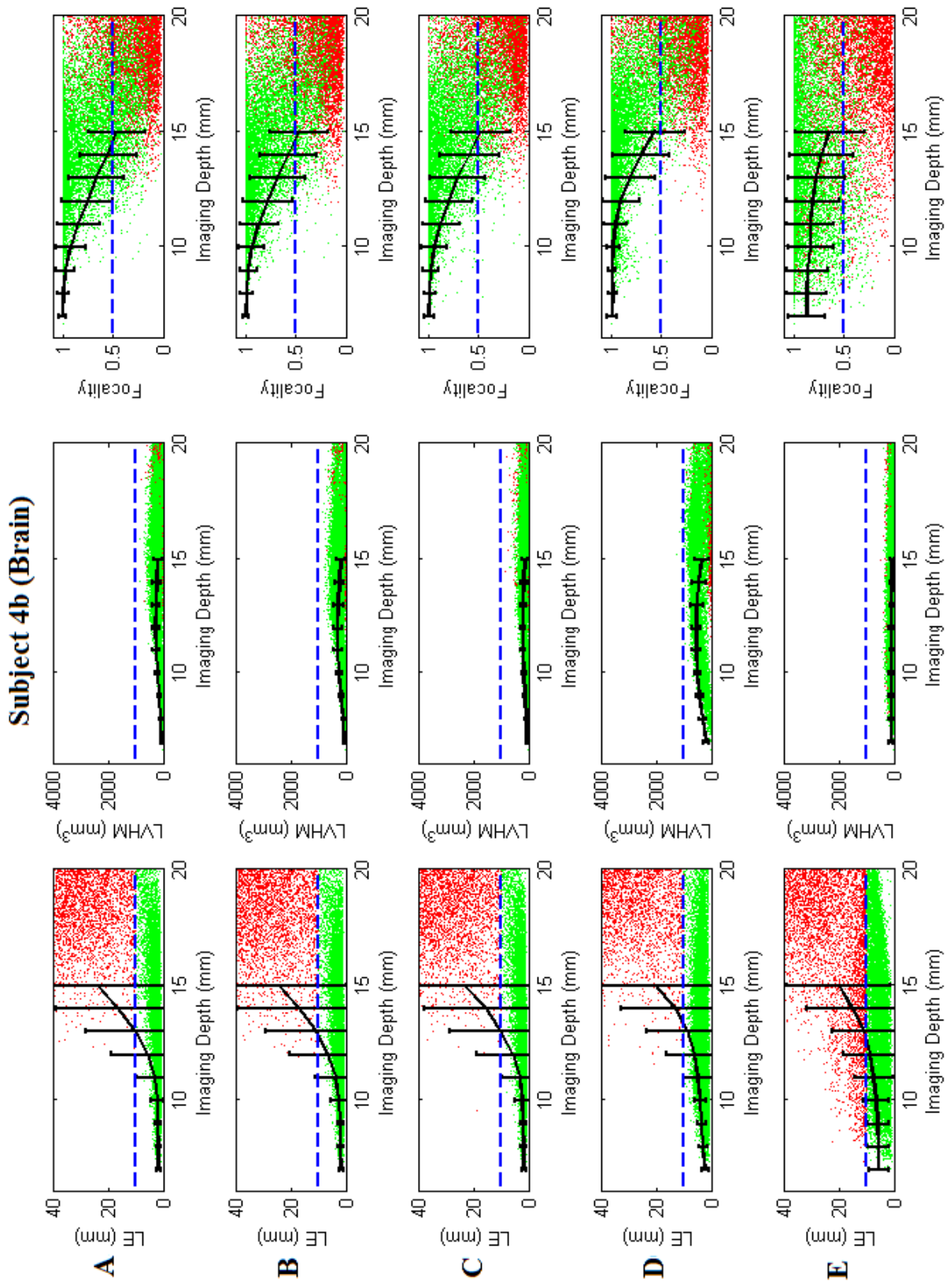


**Figure 81 Same as the last figure, but of Subject 4b.**

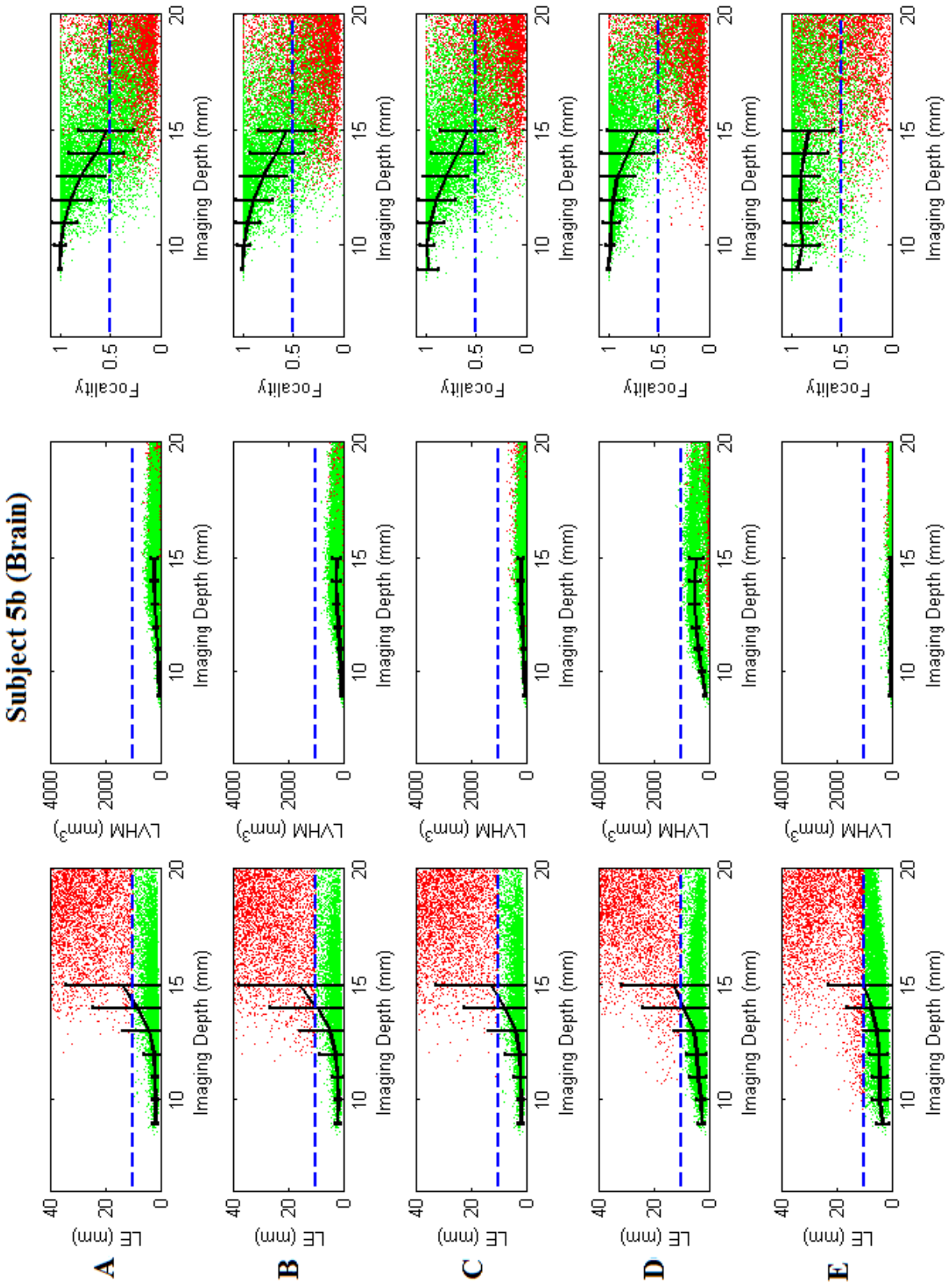


**Figure 82 Same as the last figure, but of Subject 5b.**

# Bibliography


1. Obrig, H. and A. Villringer, *Beyond the visible--imaging the human brain with light.* J Cereb Blood Flow Metab, 2003. **23**(1): p. 1-18.
2. Contini, D., et al., *Review: Brain and muscle near infrared spectroscopy/imaging techniques.* Journal of Near Infrared Spectroscopy, 2012. **20**(1): p. 15-27.
3. Ernst, L., et al., *Review: Functional near infrared spectroscopy in psychiatry: a critical review.* Journal of Near Infrared Spectroscopy, 2012. **20**(1): p. 93-105.
4. Boas, D.A., A.M. Dale, and M.A. Franceschini, *Diffuse optical imaging of brain activation: approaches to optimizing image sensitivity, resolution, and accuracy.* Neuroimage, 2004. **23 Suppl 1**: p. S275-88.
5. White, B.R. and J.P. Culver, *Quantitative evaluation of high-density diffuse optical tomography: in vivo resolution and mapping performance.* J Biomed Opt, 2010. **15**(2): p. 026006.
6. Heiskala, J., P. Hiltunen, and I. Nissila, *Significance of background optical properties, time-resolved information and optode arrangement in diffuse optical imaging of term neonates.* Phys Med Biol, 2009. **54**(3): p. 535-54.
7. Heiskala, J., et al., *Probabilistic atlas can improve reconstruction from optical imaging of the neonatal brain.* Opt Express, 2009. **17**(17): p. 14977-92.
8. Corlu, A., et al., *Uniqueness and wavelength optimization in continuous-wave multispectral diffuse optical tomography.* Opt Lett, 2003. **28**(23): p. 2339-41.
9. Eames, M.E., et al., *Wavelength band optimization in spectral near-infrared optical tomography improves accuracy while reducing data acquisition and computational burden.* J Biomed Opt, 2008. **13**(5): p. 054037.
10. Pelvig, D.P., et al., *Neocortical glial cell numbers in human brains.* Neurobiol Aging, 2008. **29**(11): p. 1754-62.
11. Rodgers, A.B., *Alzheimer's Disease: Unraveling the Mystery*, 2008, U.S. Department of Health and Human Services.
12. Jezzard, P., P.M. Matthews, and S.M. Smith, *Functional MRI : an introduction to methods*2001, Oxford: Oxford University Press. xiii, 390 p., [22] p. of col. plates.
13. Villringer, A. and U. Dirnagl, *Coupling of brain activity and cerebral blood flow: basis of functional neuroimaging.* Cerebrovasc Brain Metab Rev, 1995. **7**(3): p. 240-76.
14. Franceschini, M.A. and D.A. Boas, *Noninvasive measurement of neuronal activity with near-infrared optical imaging.* Neuroimage, 2004. **21**(1): p. 372-86.
15. Radhakrishnan, H., et al., *Fast optical signal not detected in awake behaving monkeys.* Neuroimage, 2009. **45**(2): p. 410-9.
16. Cuffin, B.N. and D. Cohen, *Comparison of the magnetoencephalogram and electroencephalogram.* Electroencephalogr Clin Neurophysiol, 1979. **47**(2): p. 132-46.
17. Niedermeyer, E. and F.H. Lopes da Silva, *Electroencephalography : basic principles, clinical applications, and related fields*. 5th ed2005, Philadelphia ; London: Lippincott Williams & Wilkins. xiii, 1309 p., [4] p. of plates.
18. Pylkkanen, L.; Available from: http://www.psych.nyu.edu/pylkkanen/Neural_Bases/07_slides/05_Methods.pdf.
19. Sharon, D., et al., *The advantage of combining MEG and EEG: comparison to fMRI in focally stimulated visual cortex.* Neuroimage, 2007. **36**(4): p. 1225-35.
20. Hoshi, Y., N. Kobayashi, and M. Tamura, *Interpretation of near-infrared spectroscopy signals: a study with a newly developed perfused rat brain model.* J Appl Physiol, 2001. **90**(5): p. 1657-62.

21. Strangman, G., et al., *A quantitative comparison of simultaneous BOLD fMRI and NIRS recordings during functional brain activation.* Neuroimage, 2002. **17**(2): p. 719-31.
22. MacIntosh, B.J., L.M. Klassen, and R.S. Menon, *Transient hemodynamics during a breath hold challenge in a two part functional imaging study with simultaneous near-infrared spectroscopy in adult humans.* Neuroimage, 2003. **20**(2): p. 1246-52.
23. Siegel, A.M., et al., *Temporal comparison of functional brain imaging with diffuse optical tomography and fMRI during rat forepaw stimulation.* Phys Med Biol, 2003. **48**(10): p. 1391-403.
24. Lim, R.; Available from: http://apps.snm.org/docs/CME/PresenterItems/EventID_85/PresenterItemTypeID_1/9.%20Lim%20-%20130.pdf.
25. Boss, A., et al., *Hybrid PET/MRI of intracranial masses: initial experiences and comparison to PET/CT.* J Nucl Med, 2010. **51**(8): p. 1198-205.
26. Langner, J.; Available from: http://www.jens-langner.de/ftp/langner_phdthesis_talk.pdf.
27. Boas, D.A., et al., *Handbook of Biomedical Optics.* Journal of Biomedical Optics, 2011. **16**(12): p. 129901-129901.
28. Habermehl, C., C.H. Schmitz, and J. Steinbrink, *Contrast enhanced high-resolution diffuse optical tomography of the human brain using ICG.* Opt Express, 2011. **19**(19): p. 18636-44.
29. Grosenick, D., et al., *Recent advances in contrast-enhanced near infrared diffuse optical imaging of diseases using indocyanine green.* J. Near Infrared Spectrosc., 2012. **20**(1): p. 203-221.
30. Pei, Y., H.L. Graber, and R.L. Barbour, *Influence of Systematic Errors in Reference States on Image Quality and on Stability of Derived Information for dc Optical Imaging.* Appl Opt, 2001. **40**(31): p. 5755-69.
31. Dehghani, H., et al., *Multiwavelength three-dimensional near-infrared tomography of the breast: initial simulation, phantom, and clinical results.* Appl Opt, 2003. **42**(1): p. 135-45.
32. Tian, F., et al., *Test-retest assessment of cortical activation induced by repetitive transcranial magnetic stimulation with brain atlas-guided optical topography.* Journal of Biomedical Optics, 2012. **17**(11): p. 116020-116020.
33. Fox, P.T., et al., *Mapping human visual cortex with positron emission tomography.* Nature, 1986. **323**(6091): p. 806-9.
34. Belliveau, J.W., et al., *Functional mapping of the human visual cortex by magnetic resonance imaging.* Science, 1991. **254**(5032): p. 716-9.
35. Ogawa, S., et al., *Intrinsic signal changes accompanying sensory stimulation: functional brain mapping with magnetic resonance imaging.* Proc Natl Acad Sci U S A, 1992. **89**(13): p. 5951-5.
36. Zeff, B.W., et al., *Retinotopic mapping of adult human visual cortex with high-density diffuse optical tomography.* Proc Natl Acad Sci U S A, 2007. **104**(29): p. 12169-74.
37. White, B.R. and J.P. Culver, *Phase-encoded retinotopy as an evaluation of diffuse optical neuroimaging.* Neuroimage, 2010. **49**(1): p. 568-77.
38. Eggebrecht, A.T., et al., *A quantitative spatial comparison of high-density diffuse optical tomography and fMRI cortical mapping.* Neuroimage, 2012. **61**(4): p. 1120-1128.
39. Bittar, R.G., et al., *Localization of somatosensory function by using positron emission tomography scanning: a comparison with intraoperative cortical stimulation.* J Neurosurg, 1999. **90**(3): p. 478-83.
40. Hammeke, T.A., et al., *Functional magnetic resonance imaging of somatosensory stimulation.* Neurosurgery, 1994. **35**(4): p. 677-81.
41. Koch, S.P., et al., *High-resolution optical functional mapping of the human somatosensory cortex.* Front Neuroenergetics, 2010. **2**: p. 12.
42. Habermehl, C., et al., *Somatosensory activation of two fingers can be discriminated with ultrahigh-density diffuse optical tomography.* Neuroimage, 2012. **59**(4): p. 3201-11.
43. Huppert, T.J., et al., *A temporal comparison of BOLD, ASL, and NIRS hemodynamic responses to motor stimuli in adult humans.* Neuroimage, 2006. **29**(2): p. 368-82.

44. Biswal, B., et al., *Functional connectivity in the motor cortex of resting human brain using echo-planar MRI.* Magn Reson Med, 1995. **34**(4): p. 537-41.
45. White, B.R., et al., *Resting-state functional connectivity in the human brain revealed with diffuse optical tomography.* Neuroimage, 2009. **47**(1): p. 148-56.
46. Niu, H., et al., *Resting-state functional connectivity assessed with two diffuse optical tomographic systems.* J Biomed Opt, 2011. **16**(4): p. 046006.
47. Adams, R. and A.S. David, *Patterns of anterior cingulate activation in schizophrenia: a selective review.* Neuropsychiatr Dis Treat, 2007. **3**(1): p. 87-101.
48. Watanabe, A. and T. Kato, *Cerebrovascular response to cognitive tasks in patients with schizophrenia measured by near-infrared spectroscopy.* Schizophr Bull, 2004. **30**(2): p. 435-44.
49. Ehlis, A.C., et al., *Cortical activation during two verbal fluency tasks in schizophrenic patients and healthy controls as assessed by multi-channel near-infrared spectroscopy.* Psychiatry Res, 2007. **156**(1): p. 1-13.
50. Shan, B., et al. *The Multi-center Study on Alzheimer's Disease Using FDG PET*. in *Complex Medical Engineering, 2007. CME 2007. IEEE/ICME International Conference on*. 2007.
51. Prvulovic, D., et al., *Functional imaging of visuospatial processing in Alzheimer's disease.* Neuroimage, 2002. **17**(3): p. 1403-1414.
52. Arai, H., et al., *A quantitative near-infrared spectroscopy study: a decrease in cerebral hemoglobin oxygenation in Alzheimer's disease and mild cognitive impairment.* Brain Cogn, 2006. **61**(2): p. 189-94.
53. Tomioka, H., et al., *Detection of hypofrontality in drivers with Alzheimer's disease by near-infrared spectroscopy.* Neurosci Lett, 2009. **451**(3): p. 252-6.
54. Schecklmann, M., et al., *Altered frontal brain oxygenation in detoxified alcohol dependent patients with unaffected verbal fluency performance.* Psychiatry Res, 2007. **156**(2): p. 129-38.
55. George, M.S., et al., *Daily left prefrontal transcranial magnetic stimulation therapy for major depressive disorder: a sham-controlled randomized trial.* Arch Gen Psychiatry, 2010. **67**(5): p. 507-16.
56. O'Reardon, J.P., et al., *Efficacy and Safety of Transcranial Magnetic Stimulation in the Acute Treatment of Major Depression: A Multisite Randomized Controlled Trial.* Biological psychiatry, 2007. **62**(11): p. 1208-1216.
57. Kozel, F.A., et al., *Using simultaneous repetitive Transcranial Magnetic Stimulation/functional Near Infrared Spectroscopy (rTMS/fNIRS) to measure brain activation and connectivity.* Neuroimage, 2009. **47**(4): p. 1177-84.
58. Hintz, S.R., et al., *Bedside imaging of intracranial hemorrhage in the neonate using light: comparison with ultrasound, computed tomography, and magnetic resonance imaging.* Pediatr Res, 1999. **45**(1): p. 54-9.
59. Austin, T., et al., *Three dimensional optical imaging of blood volume and oxygenation in the neonatal brain.* Neuroimage, 2006. **31**(4): p. 1426-33.
60. Gibson, A., et al., *Optical tomography of a realistic neonatal head phantom.* Appl Opt, 2003. **42**(16): p. 3109-16.
61. Hillman, E.M.C., *Optical brain imaging in vivo: techniques and applications from animal to man.* Journal of Biomedical Optics, 2007. **12**(5): p. -.
62. Dehghani, H., et al., *Numerical modelling and image reconstruction in diffuse optical tomography.* Philos Transact A Math Phys Eng Sci, 2009. **367**(1900): p. 3073-93.
63. Huppert, T.J., et al., *HomER: a review of time-series analysis methods for near-infrared spectroscopy of the brain.* Appl Opt, 2009. **48**(10): p. D280-98.
64. Durduran, T. and A.G. Yodh, *Diffuse correlation spectroscopy for non-invasive, micro-vascular cerebral blood flow measurement.* Neuroimage, (0).
65. Durduran, T., et al., *Transcranial optical monitoring of cerebrovascular hemodynamics in acute stroke patients.* Opt Express, 2009. **17**(5): p. 3884-902.
66. Durduran, T., et al., *Optical measurement of cerebral hemodynamics and oxygen metabolism in neonates with congenital heart defects.* J Biomed Opt, 2010. **15**(3): p. 037004.

67. Gibson, A.P., J.C. Hebden, and S.R. Arridge, *Recent advances in diffuse optical imaging.* Phys Med Biol, 2005. **50**(4): p. R1-43.
68. Hebden, J.C., S.R. Arridge, and D.T. Delpy, *Optical imaging in medicine: I. Experimental techniques.* Phys Med Biol, 1997. **42**(5): p. 825-40.
69. Wolf, M., et al., *Review: A review of near infrared spectroscopy for term and preterm newborns.* Journal of Near Infrared Spectroscopy, 2012. **20**(1): p. 43-55.
70. Boas, D.A. and A.M. Dale, *Simulation study of magnetic resonance imaging-guided cortically constrained diffuse optical tomography of human brain function.* Appl Opt, 2005. **44**(10): p. 1957-68.
71. Niu, H.J., et al., *Development of a compensation algorithm for accurate depth localization in diffuse optical tomography.* Optics Letters, 2010. **35**(3): p. 429-431.
72. Arridge, S.R. and W.R. Lionheart, *Nonuniqueness in diffusion-based optical tomography.* Opt Lett, 1998. **23**(11): p. 882-4.
73. System, C.; Available from: http://www.techen.com.
74. DYNOT. Available from: http://www.nirx.net/.
75. NIRO-200NX. Available from: www.hamamatsu.com.
76. ETG-4000. Available from: www.hitachi-medical-systems.eu.
77. 5100C, I.; Available from: www.somanetics.com.
78. Selb, J., A.M. Dale, and D.A. Boas, *Linear 3D reconstruction of time-domain diffuse optical imaging differential data: improved depth localization and lateral resolution.* Opt Express, 2007. **15**(25): p. 16400-12.
79. Hebden, J.C. and D.T. Delpy, *Enhanced time-resolved imaging with a diffusion model of photon transport.* Opt Lett, 1994. **19**(5): p. 311-3.
80. Patterson, M.S., B. Chance, and B.C. Wilson, *Time resolved reflectance and transmittance for the non-invasive measurement of tissue optical properties.* Appl Opt, 1989. **28**(12): p. 2331-6.
81. Torricelli, A., et al., *Time domain functional NIRS imaging for human brain mapping.* Neuroimage, (0).
82. Delpy, D.T., et al., *Estimation of optical pathlength through tissue from direct time of flight measurement.* Physics in medicine and biology, 1988. **33**(12): p. 1433.
83. TRS-20. Available from: www.hamamatsu.com.
84. Culver, J.P., et al., *Three-dimensional diffuse optical tomography in the parallel plane transmission geometry: evaluation of a hybrid frequency domain/continuous wave clinical system for breast imaging.* Med Phys, 2003. **30**(2): p. 235-47.
85. Duncan, A., et al., *Optical pathlength measurements on adult head, calf and forearm and the head of the newborn infant using phase resolved optical spectroscopy.* Physics in medicine and biology, 1995. **40**(2): p. 295.
86. OxiplexTS. Available from: www.iss.com.
87. Taga, G., et al., *Brain imaging in awake infants by near-infrared optical topography.* Proc Natl Acad Sci U S A, 2003. **100**(19): p. 10722-7.
88. Hofmann, M.J., et al., *Differential activation of frontal and parietal regions during visual word recognition: an optical topography study.* Neuroimage, 2008. **40**(3): p. 1340-9.
89. Custo, A., et al., *Anatomical atlas-guided diffuse optical tomography of brain activation.* Neuroimage, 2010. **49**(1): p. 561-7.
90. Jobsis, F.F., *Noninvasive, infrared monitoring of cerebral and myocardial oxygen sufficiency and circulatory parameters.* Science, 1977. **198**(4323): p. 1264-7.
91. Kocsis, L., P. Herman, and A. Eke, *The modified Beer-Lambert law revisited.* Physics in medicine and biology, 2006. **51**(5): p. N91-8.
92. Mesquita, R.C., M.A. Franceschini, and D.A. Boas, *Resting state functional connectivity of the whole head with near-infrared spectroscopy.* Biomed Opt Express, 2010. **1**(1): p. 324-336.
93. Khan, B., P. Chand, and G. Alexandrakis, *Spatiotemporal relations of primary sensorimotor and secondary motor activation patterns mapped by NIR imaging.* Biomed Opt Express, 2011. **2**(12): p. 3367-86.

94. Eggebrecht, A.T., et al., *A quantitative spatial comparison of high-density diffuse optical tomography and fMRI cortical mapping.* Neuroimage, 2012.
95. van Veen, R.L.P., et al. *Determination of VIS- NIR absorption coefficients of mammalian fat, with time- and spatially resolved diffuse reflectance and transmission spectroscopy*. 2004. Optical Society of America.
96. Eames, M.E. and H. Dehghani, *Wavelength dependence of sensitivity in spectral diffuse optical imaging: effect of normalization on image reconstruction.* Opt Express, 2008. **16**(22): p. 17780-91.
97. Boas, D.A., et al., *Improving the diffuse optical imaging spatial resolution of the cerebral hemodynamic response to brain activation in humans.* Opt Lett, 2004. **29**(13): p. 1506-8.
98. Joseph, D.K., et al., *Diffuse optical tomography system to image brain activation with improved spatial resolution and validation with functional magnetic resonance imaging.* Appl Opt, 2006. **45**(31): p. 8142-51.
99. Arridge, S.R. and J.C. Hebden, *Optical imaging in medicine: II. Modelling and reconstruction.* Phys Med Biol, 1997. **42**(5): p. 841-53.
100. Bassani, M., et al., *Independence of the diffusion coefficient from absorption: experimental and numerical evidence.* Opt Lett, 1997. **22**(12): p. 853-5.
101. Nakai, T., et al., *Expression of optical diffusion coefficient in high-absorption turbid media.* Phys Med Biol, 1997. **42**(12): p. 2541-9.
102. Custo, A., *Purely optical tomography: Atlas-based reconstruction of brain activation*, 2008, Massachusetts Institute of Technology: Cambridge.
103. Arridge, S.R., et al., *The finite element model for the propagation of light in scattering media: a direct method for domains with nonscattering regions.* Med Phys, 2000. **27**(1): p. 252-64.
104. Dehghani, H. and D.T. Delpy, *Linear single-step image reconstruction in the presence of nonscattering regions.* J Opt Soc Am A Opt Image Sci Vis, 2002. **19**(6): p. 1162-71.
105. Tarvainen, T., et al., *Coupled radiative transfer equation and diffusion approximation model for photon migration in turbid medium with low-scattering and non-scattering regions.* Phys Med Biol, 2005. **50**(20): p. 4913-30.
106. Custo, A., et al., *Effective scattering coefficient of the cerebral spinal fluid in adult head models for diffuse optical imaging.* Appl Opt, 2006. **45**(19): p. 4747-55.
107. Fukui, Y., Y. Ajichi, and E. Okada, *Monte Carlo prediction of near-infrared light propagation in realistic adult and neonatal head models.* Appl Opt, 2003. **42**(16): p. 2881-7.
108. Niu, H., et al., *Comprehensive investigation of three-dimensional diffuse optical tomography with depth compensation algorithm.* J. Biomed. Opt., 2010. **15**(4): p. 046005.
109. Xu, H., et al., *Near-infrared imaging in the small animal brain: optimization of fiber positions.* J Biomed Opt, 2003. **8**(1): p. 102-10.
110. Okada, E., et al., *Theoretical and experimental investigation of near-infrared light propagation in a model of the adult head.* Appl Opt, 1997. **36**(1): p. 21-31.
111. Zhan, Y., et al. *Application of Subject Specific Models for Mapping Brain Function with Diffuse Optical Tomography*. 2010. Optical Society of America.
112. Collins, D.L., et al., *Design and construction of a realistic digital brain phantom.* IEEE Trans Med Imaging, 1998. **17**(3): p. 463-8.
113. Zhang, S.X., et al., *The Chinese Visible Human (CVH) datasets incorporate technical and imaging advances on earlier digital humans.* J Anat, 2004. **204**(Pt 3): p. 165-73.
114. Li, T., H. Gong, and Q. Luo, *Visualization of light propagation in visible Chinese human head for functional near-infrared spectroscopy.* J Biomed Opt, 2011. **16**(4): p. 045001.
115. Kapur, T., et al., *Segmentation of brain tissue from magnetic resonance images.* Med Image Anal, 1996. **1**(2): p. 109-27.
116. Chen, M. and D.J. Mogul, *A structurally detailed finite element human head model for simulation of transcranial magnetic stimulation.* J Neurosci Methods, 2009. **179**(1): p. 111-20.
117. Fischl, B., et al., *Whole brain segmentation: automated labeling of neuroanatomical structures in the human brain.* Neuron, 2002. **33**(3): p. 341-55.

118. Frackowiak, R.S.J., *Human brain function*. 2nd ed2004, Amsterdam ; London: Elsevier Academic. xvi, 1144 p.
119. Dehghani, H., et al., *Near infrared optical tomography using NIRFAST: Algorithm for numerical model and image reconstruction.* Commun Numer Methods Eng, 2008. **25**(6): p. 711-732.
120. Fang, Q.Q. and D.A. Boas, *Tetrahedral Mesh Generation from Volumetric Binary and Gray-Scale Images.* 2009 Ieee International Symposium on Biomedical Imaging: From Nano to Macro, Vols 1 and 2, 2009: p. 1142-1145.
121. Materialise. Available from: http://www.materialise.com/mimics.
122. Tizzard, A., et al., *Generating accurate finite element meshes for the forward model of the human head in EIT.* Physiol Meas, 2005. **26**(2): p. S251-61.
123. Dehghani, H., et al., *Depth sensitivity and image reconstruction analysis of dense imaging arrays for mapping brain function with diffuse optical tomography.* Appl Opt, 2009. **48**(10): p. D137-43.
124. Fang, Q., *Mesh-based Monte Carlo method using fast ray-tracing in Plucker coordinates.* Biomed. Opt. Express, 2010. **1**(1): p. 165-175
125. Arridge, S.R., M. Cope, and D.T. Delpy, *The theoretical basis for the determination of optical pathlengths in tissue: temporal and frequency analysis.* Phys Med Biol, 1992. **37**(7): p. 1531-60.
126. Arridge, S.R., et al., *A finite element approach for modeling photon transport in tissue.* Med Phys, 1993. **20**(2 Pt 1): p. 299-309.
127. Boas, D., et al., *Three dimensional Monte Carlo code for photon migration through complex heterogeneous media including the adult human head.* Opt. Express, 2002. **10**(3): p. 159-170.
128. Wang, L., S.L. Jacques, and L. Zheng, *MCML—Monte Carlo modeling of light transport in multi-layered tissues.* Computer Methods and Programs in Biomedicine, 1995. **47**(2): p. 131-146.
129. Fang, Q. and D.A. Boas, *Monte Carlo simulation of photon migration in 3D turbid media accelerated by graphics processing units.* Opt. Express, 2009. **17**(22): p. 20178-20190.
130. Schweiger, M., et al., *The finite element method for the propagation of light in scattering media: boundary and source conditions.* Med Phys, 1995. **22**(11 Pt 1): p. 1779-92.
131. Xu, G., et al., *Trans-rectal ultrasound-coupled near-infrared optical tomography of the prostate, part I: simulation.* Opt Express, 2008. **16**(22): p. 17484-504.
132. Srinivasan, S., et al., *Interpreting hemoglobin and water concentration, oxygen saturation, and scattering measured in vivo by near-infrared breast tomography.* Proc Natl Acad Sci U S A, 2003. **100**(21): p. 12349-54.
133. Srinivasan, S., et al., *Near-infrared characterization of breast tumors in vivo using spectrally-constrained reconstruction.* Technol Cancer Res Treat, 2005. **4**(5): p. 513-26.
134. Dehghani, H., et al., *Effects of refractive index on near-infrared tomography of the breast.* Appl Opt, 2005. **44**(10): p. 1870-8.
135. Penrose, R., *A generalized inverse for matrices.* Proc. Cambridge Philos. Soc., 1955. **51**: p. 406-413.
136. Arridge, S.R. and M. Schweiger, *Photon-Measurement Density-Functions .2. Finite-Element-Method Calculations.* Applied Optics, 1995. **34**(34): p. 8026-8037.
137. O'Leary, M.A., *Imaging with diffuse photon density waves*, 1996, University of Pennsylvania: Philadelphia.
138. Arridge, S.R., *Optical tomography in medical imaging.* Inverse Problems, 1999. **15**(2): p. R41-R93.
139. Arridge, S.R., M. Schweiger, and D.T. Delpy, *Iterative reconstruction of near-infrared absorption images.* 1992: p. 372-383.
140. Gaudette, R.J., et al., *A comparison study of linear reconstruction techniques for diffuse optical tomographic imaging of absorption coefficient.* Phys Med Biol, 2000. **45**(4): p. 1051-70.

141. Culver, J.P., et al., *Optimization of optode arrangements for diffuse optical tomography: A singular-value analysis.* Opt Lett, 2001. **26**(10): p. 701-3.
142. Li, A., et al., *Reconstructing chromosphere concentration images directly by continuous-wave diffuse optical tomography.* Opt Lett, 2004. **29**(3): p. 256-8.
143. Li, A., et al., *Optimal linear inverse solution with multiple priors in diffuse optical tomography.* Appl Opt, 2005. **44**(10): p. 1948-56.
144. Culver, J.P., et al., *Volumetric diffuse optical tomography of brain activity.* Opt Lett, 2003. **28**(21): p. 2061-3.
145. Walker, S.A., S. Fantini, and E. Gratton, *Image reconstruction by backprojection from frequency-domain optical measurements in highly scattering media.* Appl Opt, 1997. **36**(1): p. 170-4.
146. Corlu, A., et al., *Diffuse optical tomography with spectral constraints and wavelength optimization.* Appl Opt, 2005. **44**(11): p. 2082-93.
147. Brooksby, B., et al., *Combining near-infrared tomography and magnetic resonance imaging to study in vivo breast tissue: implementation of a Laplacian-type regularization to incorporate magnetic resonance structure.* J Biomed Opt, 2005. **10**(5): p. 051504.
148. Strangman, G., M.A. Franceschini, and D.A. Boas, *Factors affecting the accuracy of near-infrared spectroscopy concentration calculations for focal changes in oxygenation parameters.* Neuroimage, 2003. **18**(4): p. 865-79.
149. Bevilacqua, F., et al., *In vivo local determination of tissue optical properties: applications to human brain.* Appl Opt, 1999. **38**(22): p. 4939-50.
150. Cheong, W.F., S.A. Prahl, and A.J. Welch, *A Review of the Optical-Properties of Biological Tissues.* Ieee Journal of Quantum Electronics, 1990. **26**(12): p. 2166-2185.
151. Cheng, X. and D. Boas, *Systematic diffuse optical image errors resulting from uncertainty in the background optical properties.* Opt Express, 1999. **4**(8): p. 299-307.
152. Okada, E., et al., *Theoretical and experimental investigation of the influence of frontal sinus on the sensitivity of the NIRS signal in the adult head.* Adv Exp Med Biol, 2010. **662**: p. 231-6.
153. McBride, T., *Spectroscopic reconstructed near infrared tomographic imaging for breast cancer diagnosis*, 2001, Dartmouth College.
154. Yalavarthy, P.K., et al., *Structural information within regularization matrices improves near infrared diffuse optical tomography.* Opt Express, 2007. **15**(13): p. 8043-58.
155. Zhan, Y., et al., *Quantitative evaluation of systematic imaging error due to uncertainty in tissue optical properties in high-density diffuse optical tomography*. Vol. 7896. 2011: SPIE. 78960O.
156. Srinivasan, S., et al., *Spectrally constrained chromophore and scattering near-infrared tomography provides quantitative and robust reconstruction.* Appl Opt, 2005. **44**(10): p. 1858-69.
157. Brooksby, B., et al., *Spectral priors improve near-infrared diffuse tomography more than spatial priors.* Opt Lett, 2005. **30**(15): p. 1968-70.
158. Yalavarthy, P.K., et al., *Critical computational aspects of near infrared circular tomographic imaging: Analysis of measurement number, mesh resolution and reconstruction basis.* Opt Express, 2006. **14**(13): p. 6113-27.
159. Zhan, Y., et al., *Image quality analysis of high-density diffuse optical tomography incorporating a subject-specific head model.* Frontiers in Neuroenergetics, 2012. **4**.
160. Jermyn, M., et al. *A User-Enabling Visual Workflow for Near-Infrared Light Transport Modeling in Tissue*. 2012. Optical Society of America.